ABSTRACT

Title of Dissertation: LONGITUDINAL DYNAMICS OF AN INTENSE ELECTRON BEAM

John Richardson Harris, Ph.D., 2005

Dissertation Directed By: Professor Patrick G. O'Shea, Department of Electrical and Computer Engineering

The dynamics of charged particle beams are governed by the particles' thermal velocities, external focusing forces, and Coulomb forces. Beams in which Coulomb forces play the dominant role are known as space charge dominated, or intense. Intense beams are of great interest for heavy ion fusion, spallation neutron sources, free-electron lasers, and other applications. In addition, all beams of interest are dominated by space charge forces when they are first created, so an understanding of space charge effects is critical to explain the later evolution of any beam. Historically, more attention has been paid to the transverse dynamics of beams. However, many interesting and important effects in beams occur along their length. These longitudinal effects can be limiting factors in many systems. For example, modulation or structure applied to the beam at low energy will evolve under space charge forces. Depending on the intended use of the beam and the nature of the modulation, this may result in improved or degraded performance.

To study longitudinal dynamics in intense beams, experiments were conducted using the University of Maryland Electron Ring, a 10 keV, 100 mA electron transport system. These experiments concentrated on space charge driven changes in beam length in parabolic and rectangular beams, beam density and velocity modulation, and space charge wave propagation. Coupling between the transverse and longitudinal dynamics was also investigated. These experiments involved operating the UMER gun in space charge limited, temperature limited, triode amplification, photon limited, and hybrid modes. Results of these experiments are presented here, along with a theoretical framework for understanding the longitudinal dynamics of intense beams.

LONGITUDINAL DYNAMICS OF AN INTENSE ELECTRON BEAM

By

John Richardson Harris.

Dissertation submitted to the Faculty of the Graduate School of the
University of Maryland, College Park, in partial fulfillment
of the requirements for the degree of
Doctor of Philosophy
2005

Advisory Committee:
Professor Patrick G. O'Shea, Chair
Professor Martin Reiser
Professor Victor Granatstein
Professor William Levine
Professor Adil Hassam

Dedication

To my parents.

Acknowledgements

I would like to thank the many people who provided their assistance, guidance, and encouragement to me during my time at Maryland. In particular, I would like to thank Prof. Patrick O'Shea for his guidance and the interest he took in me both at Maryland and at Duke University. Prof. Martin Reiser contributed greatly to this work by providing his advice and insight, and through the tradition of first-class graduate training in beam physics that he began and Prof. O'Shea has continued. I would like to thank Dr. Irving Haber for valuable discussions on electron guns and the dynamics of intense beams, Dr. Donald Feldman for his assistance with photoemission experiments, and Renee Feldman for her great help with image analysis. I am indebted to Dr. Agust Valfells for his participation in my early theoretical and experimental studies. I would also like to thank my fellow graduate students, both current and former, who contributed to my work, to the UMER project, and to the overall quality of the program at Maryland. In particular, I would like to thank Dr. Jonathan Neumann for his experimental contribution to this work, and Dr. Yupeng Cui for useful discussions on longitudinal dynamics. In addition, I would like to thank Bryan Quinn and all the other members of the UMER project who have worked for so long to build the machine and keep it running, no matter what the graduate students manage to do to it. I would also like to thank all the members of my dissertation committee for their time and service.

Finally, this work would not have been possible without the support of the Department of Energy, the Office of Naval Research, the Directed Energy Professional Society, and the Army Research Laboratory.

Table of Contents

Chapter 1: Introduction

1.1. Introduction and Motivation

Charged particle beams are used in many systems for generating electromagnetic radiation and inducing selected changes in matter. All of these applications require beams to be produced, accelerated, and transported to a particular location to interact with other matter or fields. In each of these stages, many fundamental and technological constraints impose limits on what can actually be accomplished. For high current and high quality beams, serious constraints are posed by the collective self forces between the charged particles that comprise the beam. Beams where these *space charge forces* govern the dynamics are referred to as *space charge dominated*, or *intense*. In these beams, the internal space charge forces are comparable in strength to the externally applied focusing forces, and they produce several interrelated effects that make beam control much more complicated. Space charge forces couple the beam dynamics in all three directions, so that *longitudinal* effects (parallel to the direction of beam travel) will affect *transverse* behavior (perpendicular to the direction of beam travel), and vice versa. In addition, space charge forces are dependent on the distribution of particles in the beam, which may vary over time. These effects result in instabilities and nonlinear behavior that degrade beam quality and make beam transport more difficult. Historically, longitudinal effects have not received as much attention as transverse effects, but this is changing as new systems using higher current and higher quality beams are being

developed where longitudinal space charge effects impact the beam's dynamics throughout its lifetime. As a result, issues of beam steering, quality, and evolution of intense beams cannot be adequately addressed without an understanding of effects occurring in the direction parallel to beam movement. All beams of interest are space charge dominated when first formed, and they also frequently contain unintended velocity or density modulation. This modulation will evolve under space charge forces until the beam is accelerated to high enough energy, when space charge will no longer be the dominant driving force in its evolution. This longitudinal structure can affect beam control and transport, may result in decreased beam quality as the beam tries to evolve towards equilibrium over long time scales, and at higher velocities can lead to the production of electromagnetic radiation. Depending on the intended application of the beam, these effects may be advantageous or harmful. It is therefore important to understand how these fluctuations arise, how they can be controlled, and how they evolve under space charge forces. In this dissertation I explore some aspects of these longitudinal effects in low energy space charge dominated beams.

1.2. Transverse Dynamics and Intense Beams

Before proceeding to discuss longitudinal dynamics in beams, it is useful to mention some key concepts in transverse dynamics. Many of the ideas and formalisms used to describe longitudinal dynamics were developed by analogy with those used for transverse dynamics. In addition, transverse effects can have an impact on longitudinal dynamics, as will be shown later.

1.2.1. Factors Affecting Beam Dynamics.

The overall dynamics of any charged particle beam is governed by three factors: emittance, space charge, and external focusing (Fig. 1). Emittance is a measure of the random thermal velocities of the particles in a beam. Any source of particles will have nonzero temperature, and many sources operate at elevated temperatures. The particles produced from these sources will also have nonzero temperatures, and therefore nonzero thermal velocities. Some of this thermal velocity will be in a direction perpendicular to the primary direction of travel of the beam, and (transverse) emittance is a measure of these velocities. This transverse velocity places a limit on how well the beam can be focused (Fig. 2), and therefore is a limit on the maximum current density that can be obtained in a particular system [1,2]. In this sense, emittance is also a measure of how "beam-like" the beam is -- particles in a low-emittance beam will follow more parallel paths, while particles in a high-emittance beam will follow paths that spread out from each other in space [3]. The expression for the (unnormalized effective) emittance in the x-direction is

$$\varepsilon_x = 4\sqrt{\langle x^2 \rangle \langle x'^2 \rangle - \langle xx' \rangle^2} \,. \qquad (1)$$

The brackets indicate an average over all the particles in the beam, or in a particular slice of the beam. Throughout this dissertation, a prime will denote differentiation with respect to s, the direction of travel (Fig. 1). Similar expressions can be written for emittance in the y-direction and the z-direction.

A second factor affecting beam dynamics, and the one on which we will concentrate, is space charge. Space charge refers to the fact that the beam is composed of similarly-charged particles which mutually repel each other. The

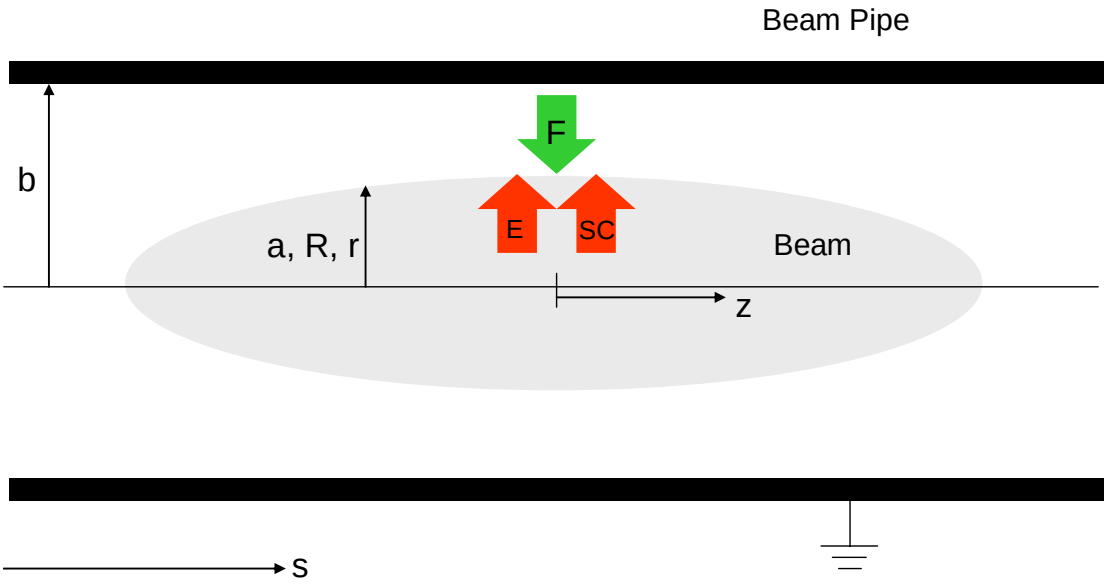

Fig. 1. Forces and coordinate system used in discussion of beam dynamics. Longitudinal distance in the beam frame is denoted by z, referenced to the beam center. Longitudinal distance in laboratory frame is denoted by s, referenced to the cathode location.

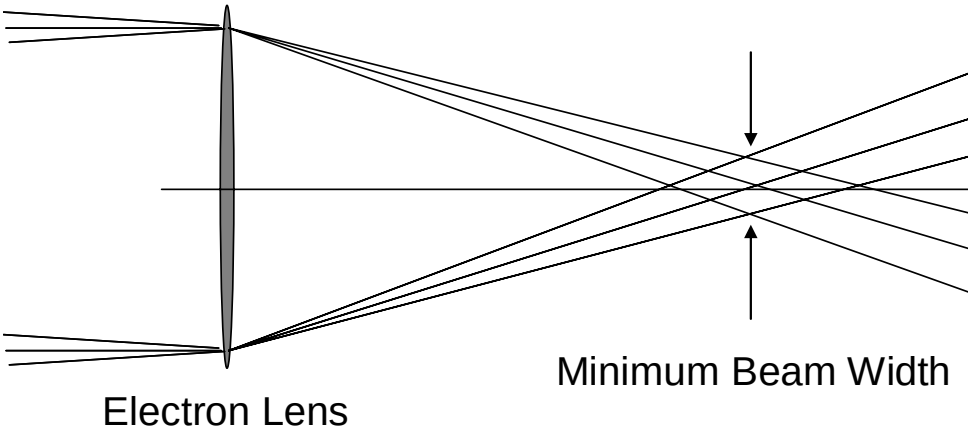

Fig. 2. Thermal velocity distribution (emittance) of beam causes particle trajectories to diverge, limiting minimum beam width [After 2].

strength of this Coulomb repulsion is determined by the number of charges and the distance between them. As a result, the effect of space charge should become stronger as the beam radius decreases or the beam current increases. The interaction of beam radius and current is expressed by the equation

$$R'' = \frac{K_T}{R}, \tag{2}$$

where R is the beam radius and K_T is the generalized perveance given by [1]

$$K_T = \frac{Iq}{2\pi\varepsilon_0 mc^3\beta^3\gamma^3}. \tag{3}$$

In Eq. (2) the beam is assumed to be axially symmetric, and the subscript "T" is used to emphasize that this is the expression for the *transverse* generalized perveance. In Eq. (3), I is the beam current, q is the charge of the particles in the beam, and ε_0 is the permittivity of free space. The quantity K_T is known as the *generalized perveance* to distinguish it from the *perveance* $\frac{I}{V^{3/2}}$; for a nonrelativistic beam, the generalized perveance is [1]

$$K_T = \frac{I}{V^{3/2}}\left[\frac{1}{4\pi\varepsilon_0\sqrt{2q/m}}\right]. \tag{4}$$

Eq. (2) can be solved numerically. The resulting curve is sometimes plotted in dimensionless "reduced variables" and known as the "Universal Beam Spread Curve" [1,2,4]. Note that as the radius becomes large ($R \to \infty$), the driving (and only!) term in Eq. (2) becomes small ($R'' \to 0$), and the beam radius growth becomes linear with distance ($R' \to const$).

Emittance and space charge both drive beam radius growth. To check this growth, external focusing is needed. This may be in the form of applied voltages or magnetic fields. Plasmas whose ions are charged oppositely to the particles in the beam may also be used [5], as may thin metal foils which serve to short the space charge field of the beam [3].

1.2.2. Transverse Envelope Equation and Transverse Intensity Parameter.

Eq. (2) only accounts for the effects of space charge on beam radius. A similar expression can be written which takes into account the effects of emittance and focusing, as well as space charge. This is the transverse envelope equation [1]:

$$R'' + k_0^2 R - \frac{K_T}{R} - \frac{\varepsilon^2}{R^3} = 0 . \qquad (5)$$

In this equation, k_0 is the (zero-current) betatron wave number, which describes the transverse oscillations of particles in the beam due to external focusing in the absence of space charge. Again, an axisymmetric beam is assumed. When this is not the case, Eq. (5) can be rewritten as two coupled equations in x and in y, where the coupling occurs in the space charge terms. Eq. (5) shows that space charge and emittance tend to increase beam radius, while the term containing k_0 -- a measure of the external focusing strength -- shows that external focusing tends to decrease the beam radius. If these three effects are in balance, the beam will be matched, so that

$$R'' = 0 \qquad (6)$$

and

$$k_0^2 R = \frac{K_T}{R} + \frac{\varepsilon^2}{R^3} . \qquad (7)$$

An intensity parameter χ_T can be defined as the ratio of the focusing term to the space charge term [6],

$$\chi_T = \frac{K_T}{k_0^2 R^2} . \tag{8}$$

When the external focusing is completely balanced by emittance, space charge is negligible so that $\chi_T \to 0$. When the external focusing is completely balanced by space charge, emittance is negligible and $\chi_T \to 1$. For $\chi_T < 0.5$, the beam radius is primarily governed by emittance, and the beam is considered *emittance dominated*. For $\chi_T > 0.5$, the beam radius is primarily governed by space charge, and the beam is considered *space charge dominated*, or *intense*. The transverse intensity parameter can be related to other measures of beam intensity [7]. For example, the presence of space charge will affect the transverse oscillations particles undergo due to transverse focusing. One measure of this effect is the ratio of the betatron wave number in the presence of space charge to the "zero-current" wave number in the absence of space charge. This ratio is related to the transverse intensity parameter by

$$\frac{k}{k_0} = \sqrt{1-\chi_T} . \tag{9}$$

The plasma frequency is also affected by space charge, and the ratio of the plasma frequency in the presence of space charge to the "zero-current" plasma frequency is related to the transverse intensity parameter by

$$\frac{\omega_P}{\omega_{P0}} = \sqrt{2\chi_T} . \tag{10}$$

Eqs. (9) and (10) are plotted against χ_T in Fig. 3. The transverse intensity parameters for some charged particle beam systems are given in Table 1.

1.3 Overview of Dissertation

The remainder of this dissertation will describe the longitudinal dynamics of intense beams, and experiments performed on such beams in the University of Maryland Electron Ring (UMER). Chapter 2 describes UMER itself, emphasizing its diagnostics and modes of operation. Chapter 3 introduces key theoretical descriptions of longitudinal dynamics in intense beams and experiments performed on UMER to test those descriptions. Chapter 4 describes the nonideal triode behavior of the UMER gun, and experiments using this behavior to generate and study wave propagation in intense beams. Chapter 5 covers the generation and propagation of perturbations and waves in intense beams, and describes an apparatus developed to produce flexible perturbation trains in the UMER beam. Finally, Chapter 6 will summarize the work described in this dissertation, and suggest some future areas for study.

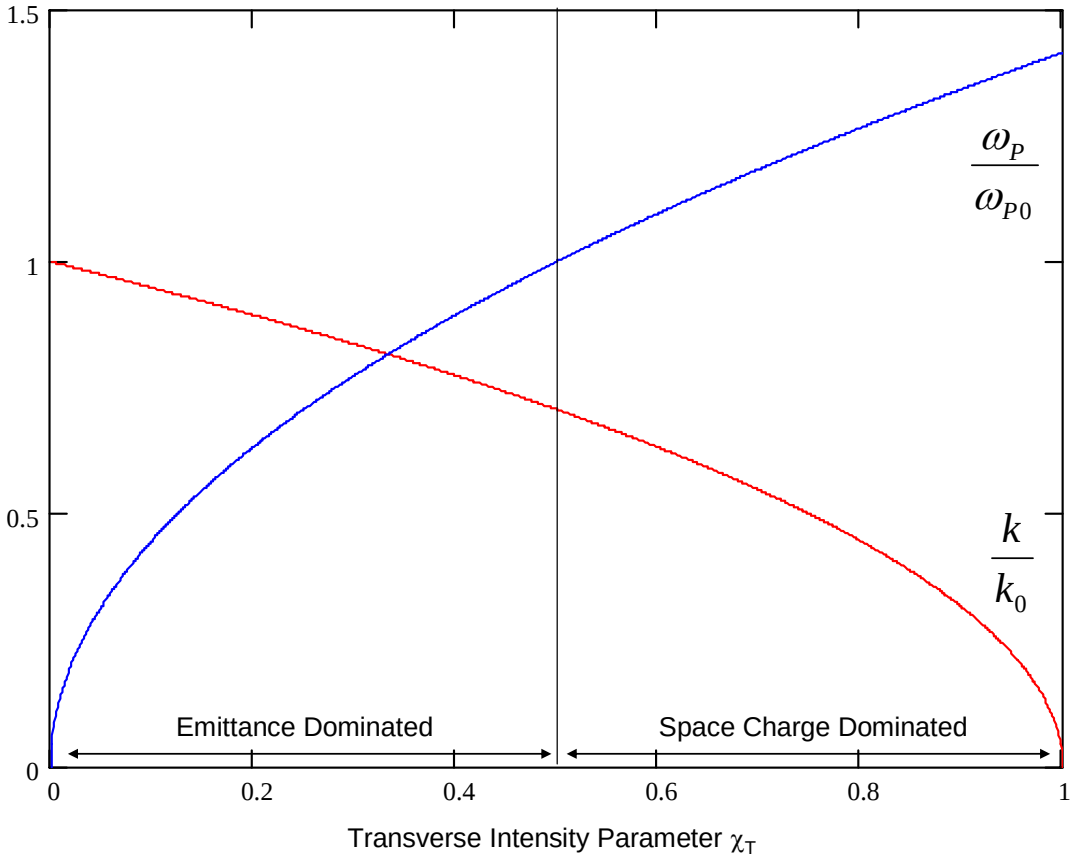

Fig. 3. Dependence of scaled plasma frequency and depressed betatron wave number on space charge intensity parameter.

Table 1. Machine parameters for selected beam transport systems.

Machine	Location	Species	Energy	γ	β	Current	ε [μm] [a]	K_T [b,h]	R [mm]	χ_T
ETA II	LLNL	e^-	2.4 MeV [8]	5.7 [b]	0.98 [b]	1.5 kA [8]	38.2 [9]	1.01×10^{-3}	8.8 [b]	0.84 [b]
HCX	LBNL	K^+	1 MeV [10]	1 [b]	0.007 [b]	175 mA [10]	197 [10] [c]	8.44×10^{-4}	10 [10]	0.685 [b]
SNS MEBT	ORNL	H^-	2.5 MeV [11]	1.0027 [11]	0.0728 [11]	40 mA [12]	8.6 [c]	6.63×10^{-6}	6 [12] [c,d]	0.76 [b]
SNS Ring	ORNL	H^+	1 GeV [11]	2.066 [11]	0.875 [11]	90 A [11]	301 [11] [c]	9.83×10^{-7}	17.5 [13]	0.003 [b]
UMER [6]	UMCP	e^-	10 keV	1.02	0.20	100 mA	50	1.39×10^{-3}	10	0.98
UMER [6]	UMCP	e^-	10 keV	1.02	0.20	1 mA	5	1.39×10^{-5}	13	0.51
UMER [6]	UMCP	e^-	50 keV [e]	1.10	0.41	1 mA	2.2	1.28×10^{-6}	0.95	0.20
PTSX [f]	Princeton	Cs^+	(0)	(1)	(0)	7–30μA [14] [g]	N/A	N/A	10 [15]	1-0.1 [15]
Duke FEL Storage Ring	Duke	e^-	1 GeV [16]	1958 [16] [b]	1 [16] [b]	3.5 mA [16]	0.0099 [17] [d]	5.49×10^{-17} [16]	0.102 [16] [d]	5.83×10^{-9} [b]

[a] unnormalized, non-RMS
[b] calculated from published data
[c] converted from published value to unnormalized, non-RMS value
[d] average of x and y values
[e] future upgrade
[f] Paul Trap Simulator Experiment is an electrically-confined plasma used to simulate a beam's behavior in its rest frame
[g] ion source current
[h] dimensionless

Chapter 2: The University of Maryland Electron Ring

2.1. Introduction

The University of Maryland Electron Ring (UMER) is the latest in a series of experiments conducted at Maryland to study the physics of intense electron beams. Previous experiments [18] looked at the evolution of these beams as they propagated along straight-line transport systems. In order to look at effects which occur on a longer time scale, as well as effects due to curved transport systems, it was decided to design UMER as a recirculator. Although physically small, UMER is complex (Figs. 4 and 5). It contains over 153 magnetic elements and over 30 individual diagnostics for measuring beam properties, all in a circular machine that is only 3.7 m in diameter. The low energy (10 keV) means that negligible amounts of radiation are produced by UMER, and there is no activation of the machine. This, along with the small size make UMER particularly well suited for a university environment. (A full listing of machine parameters is given in Table 2.) In this chapter, we will discuss the major components of UMER.

2.2. Electron Gun

The beam in UMER is produced by a gridded, variable perveance Pierce-type electron gun built by FM Technologies [21]. (A full list of gun parameters is given in Chapter 4). Electrons are produced by thermionic emission or

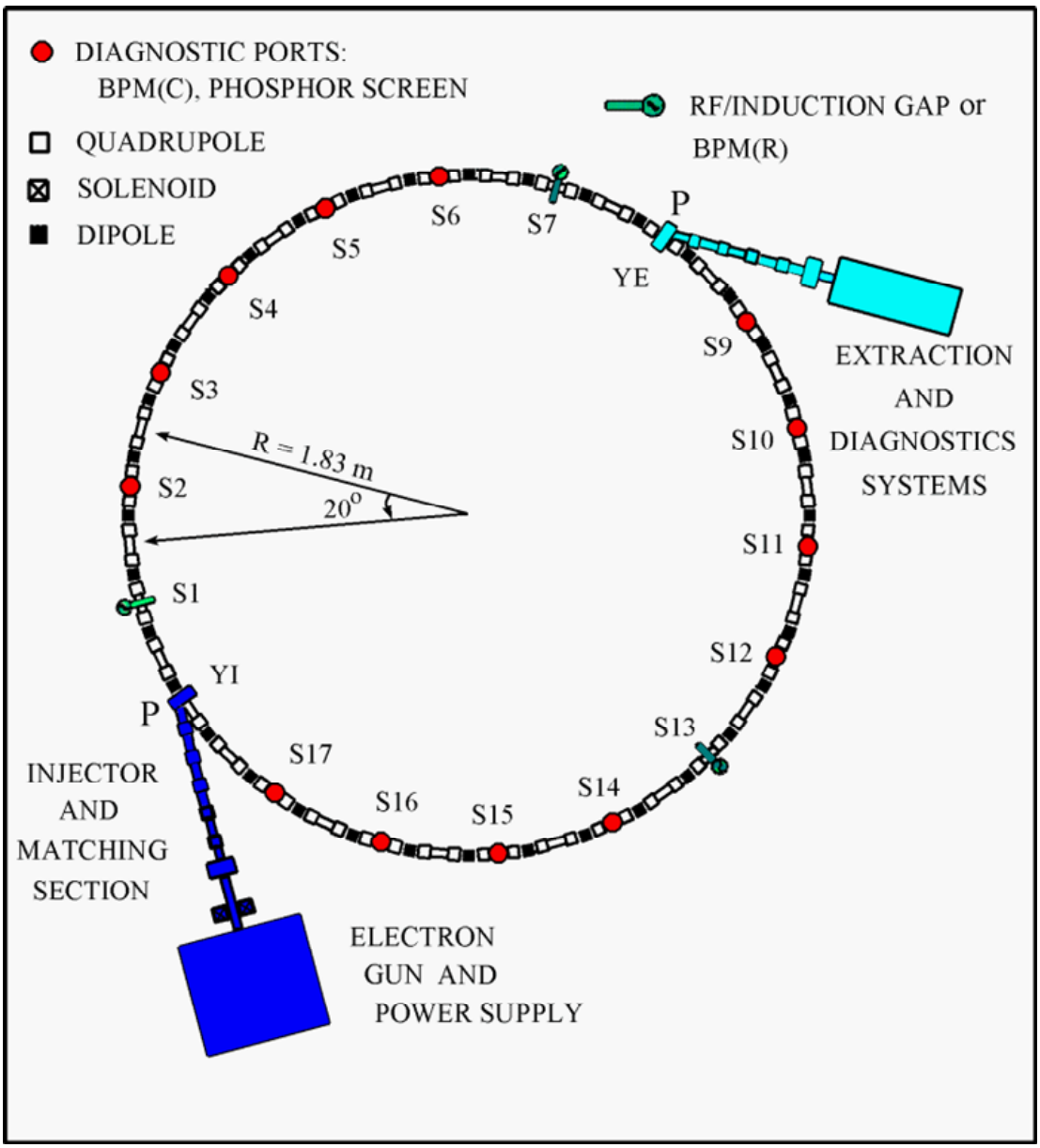

Fig. 4. Plan of UMER design [19].

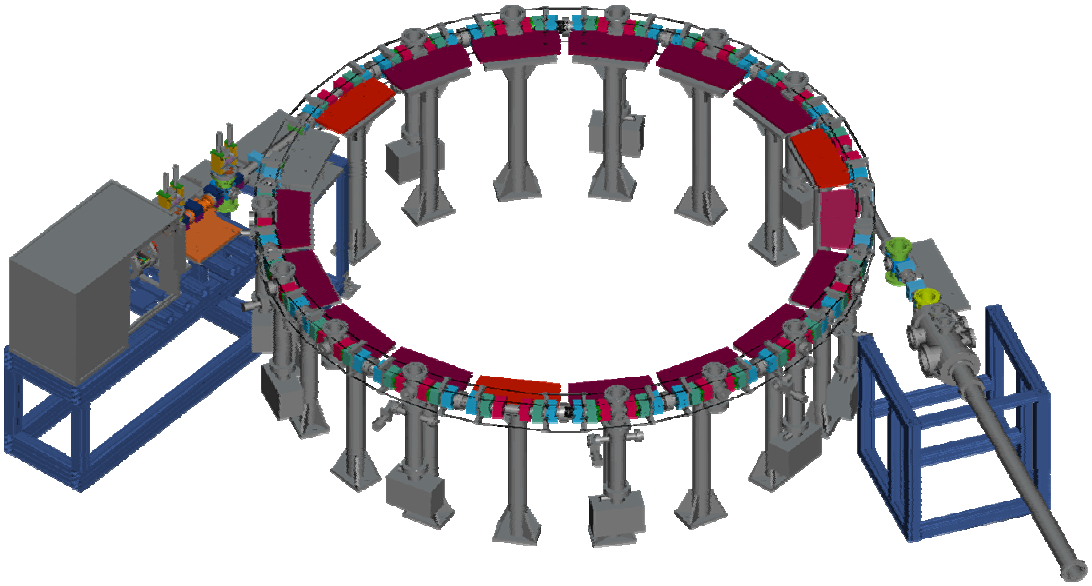

Fig. 5. Three-dimensional rendering of UMER design [20].

Energy	10 keV
β	0.2
γ	1.02
Current	0-100 mA
Generalized Perveance at 100 mA	1.5×10^{-3}
Normalized Emittance	2 μm
Circumference	11.52 m
Lap Time	197 ns
Pulse Length	100 ns
Rep Rate	10 Hz
FODO Period	0.32 m
Dipole Magnets (Bending)	36
Dipole Magnets (Steering)	> 36
Quadrupole Magnets	> 78
Mean Beam Radius at 100 mA	0.01 m

Table 2. Nominal Parameters for UMER.

photoemission (Fig. 6) from an Eimac Y-646B dispenser cathode. They are prevented from leaving the cathode by a bias voltage of approximately 40 V applied between the cathode and the grid, which holds the grid at a more negative potential than the cathode (Fig. 7). To generate beam, a 60 V pulse produced in a pulse forming line is applied directly to the cathode, which causes the cathode to become more negative than the grid, allowing electrons to escape. The cathode pulse is nominally 100 ns long, but can be easily adjusted by changing the length of the pulse forming line. The grid and cathode float at -10 kV with respect to the anode, which is kept at ground. Electrons passing through the grid are swept towards the anode, passing through the anode aperture. To counteract the defocusing effects of space charge, a Pierce-type gun geometry is used. Pierce-type geometry uses electrodes at the anode and cathode which are shaped to provide a transverse focusing force to prevent the beam from expanding transversely under the influence of space charge [2,4,22]. In the UMER gun, a wire mesh is used at the anode aperture to simulate the presence of a continuous anode, which is needed to generate the correct potential in the gun to prevent aperture-lens defocusing of the beam [1,2].

The current produced from the gun may be controlled in several ways. (Table 3) First, the cathode-anode spacing may be adjusted by use of three micrometers located on the backplane of the gun. By adjusting this distance, the perveance $\frac{I}{V^{3/2}}$ of the gun may be changed, and therefore the amount of current produced by a given accelerating voltage will change. Alternatively, the accelerating voltage itself may be adjusted from 0 kV to approximately 13 kV. This presents several problems, including the potential for damaging components at high voltages, and the need to

Fig. 6. UMER beam current. (Top) Thermionic emission only. (Center) Combined thermionic emission and photoemission. (Bottom) Photoemission only. In early experiments, the location of the photoemission pulse within the thermionic pulse was fixed at the beam center [23].

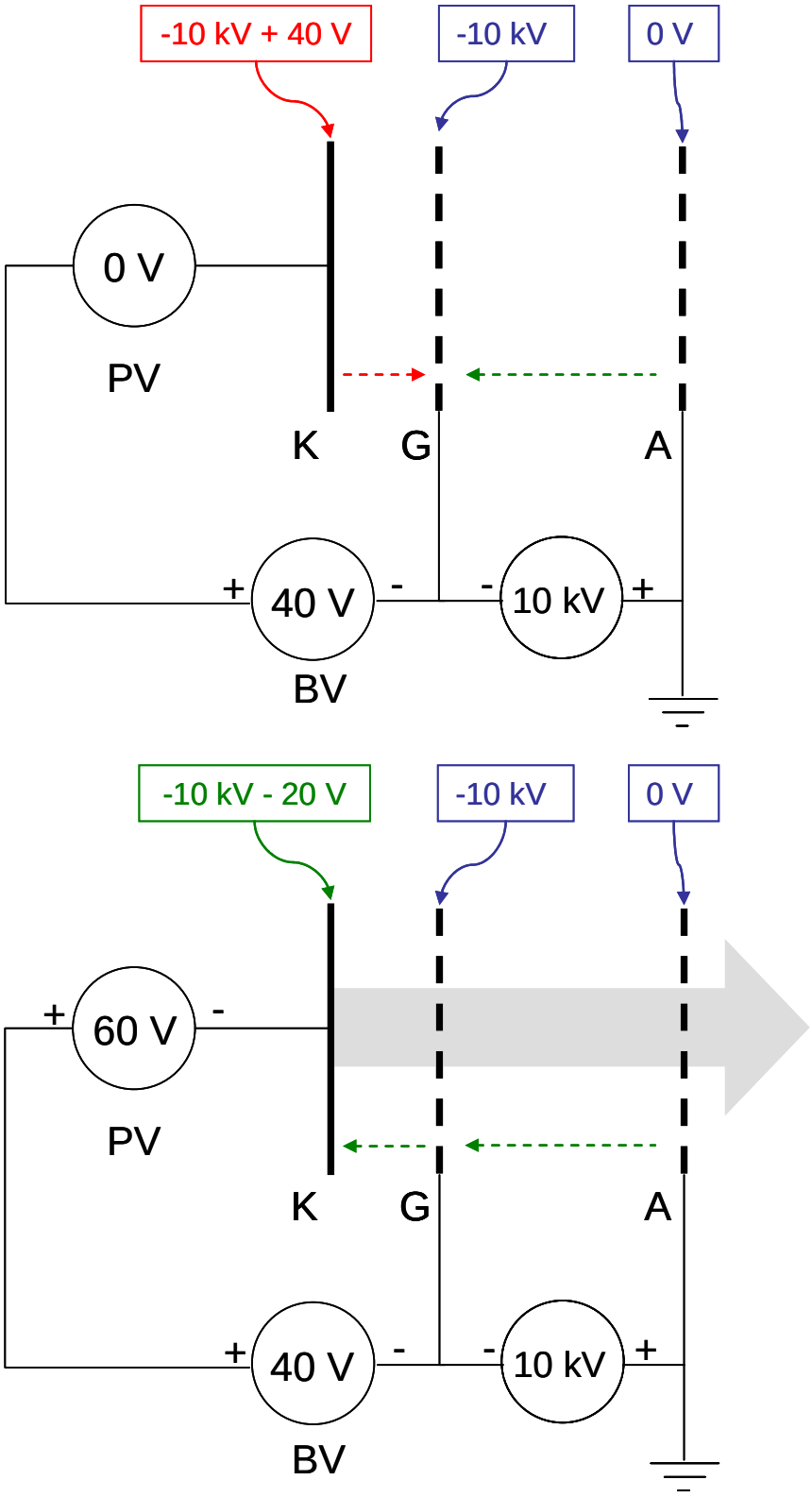

Fig. 7. Action of grid in suppressing (top) and allowing (bottom) current flow in the UMER gun.

Table 3. Principle Modes of Operation of the UMER Gun.

Mode	Main Control Variable	Governing Equation	Characteristics	Applications
Space Charge Limited (Diode Saturation)	Anode-Cathode Voltage	Child-Langmuir $J = P(V_{AK})^{3/2}$	•Flat Top Pulse •Max Current for "Long" Pulses	•Conventional Mode of operation •Beam end studies •Background pulse for wave studies
Bias Voltage Limited (Triode Amplification)	Grid-Cathode Voltage	Triode $J = K_T\left(V_{GK} + \frac{V_{AK}}{\mu}\right)^{3/2}$	•Reduced Current •Amplifier Effect •Fast Response to voltage changes •Velocity modulation	•Generation of waves •Novel pulse shapes
Temperature Limited (Source Limited)	Cathode Temperature	Richardson-Dushman $J = A_{RD}T^2 \exp\left[\frac{-W}{k_B T}\right]$	•Reduced Current •Flat Top Pulse •Slow response to temperature changes	•Reduced-current operation without apertures
Photon Limited (Source Limited)	Laser Power	"Photon Counting" $I = \frac{\lambda \cdot P_{laser} \cdot QE}{124 \cdot 10^8}$	•Fast Response to laser power changes •Variable Pulse Shape •"Short" pulse current may exceed space charge limit •Density modulation	•High peak current •Short pulse length •Generation of perturbations, waves

readjust the strength of the bending magnets in UMER to provide the correct curvature for the beam and prevent it from hitting the beam pipe. Second, the gun may be operated in the temperature-limited regime, where the current density produced from the cathode is given by the Richardson-Dushman equation

$$J = A_{RD} T^2 \exp\left[\frac{-W}{k_B T}\right], \tag{11}$$

where $A_{RD} = 1.2 \times 10^6 \, A/m^2 K^2$, T is the cathode temperature, W is the work function of the cathode material, and k_B is the Boltzmann constant [1]. This mode is useful in conjunction with photoemission, which will be discussed in more detail in Chapter 5. The grid bias voltage can be changed, although this causes a series of related effects which are the subject of Chapter 4. This flexibility is very unusual, and UMER's is the only known gun capable of operating in all these different modes, and combinations of these modes [3]. In practice, an aperture is generally used to block some of the beam (Fig. 8). This was an original design feature of the UMER gun, and works quite well because it allows the current to be changed while maintaining the gun at a single stable operating point. However, there are cases when it is desirable to use other means to control the current, as will be shown.

There are also several ways of changing the electron beam pulse shape at the gun. These include combined thermionic and photoemission at the cathode, altering the pulse forming line, triode amplification, and hybrid techniques. These methods will be discussed in Chapters 4 and 5.

The physics occurring in the gun region is singularly rich. The gun is capable of operating in several distinct modes, each of which has its own nuances. Effects of

the grid and bias voltage, nonideal pulser behavior, cathode temperature, transverse-longitudinal coupling, transients, and nonideal transverse focusing all come into play in the gun, and change the downstream behavior of the beam. We will also address some of these issues in more detail in Chapters 4 and 5.

2.3. Transport System

The bulk of UMER consists of the transport system, which may be divided into three parts: the injection line, the ring, and the extraction line. When the beam emerges from the gun, it immediately begins to expand transversely under the influence of space charge. The injection system, consisting of a solenoid and quadrupole magnets, serves to check this expansion, and match the beam into the ring focusing lattice. The "unit cell" of the ring lattice consists of pairs of quadrupoles separated by a dipole (Fig. 9). One of these quadrupoles will focus the beam in the x-direction and defocus the beam in the y-direction, while the next quadrupole will focus the beam in the y-direction and defocus the beam in the x-direction. Each dipole bends the beam 10º. Between each of these quadrupole-dipole-quadrupole cells is either a diagnostics port (which will be discussed below), or a bellows. The bellows serve to connect adjacent ring sections, each of which carries one diagnostics port and two focusing unit cells (Fig. 10). The bellows are also used for mounting short steering dipoles, which provide additional control over the beam. The extraction section serves to carry the beam out of the ring and into the final diagnostics chamber.

One unique feature of UMER is the use of printed circuit magnets [24]. Iron-core magnets are problematic at very small field strengths due to remnant fields and

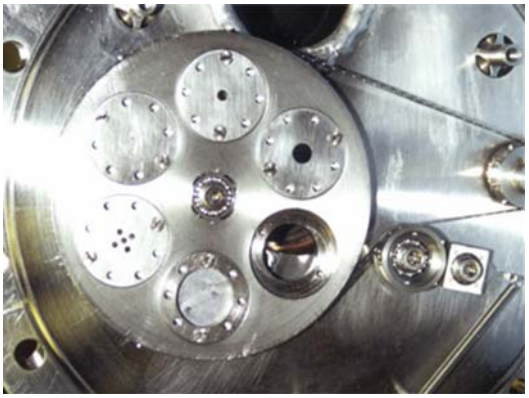

Fig. 8. Aperture wheel in UMER gun [25].

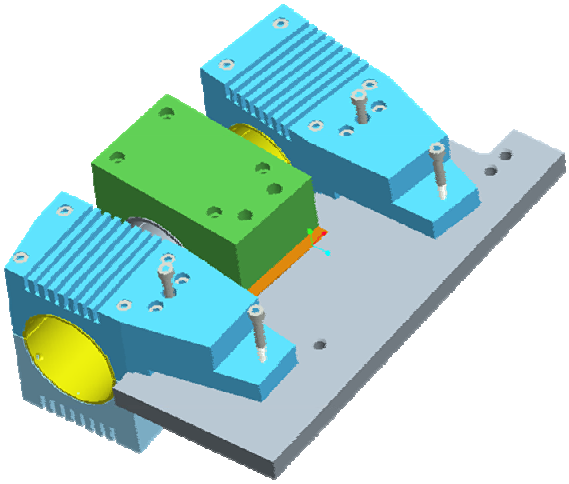

Fig. 9. Focusing lattice unit cell, consisting of quadrupole magnets (blue) and dipole magnet (green) [25].

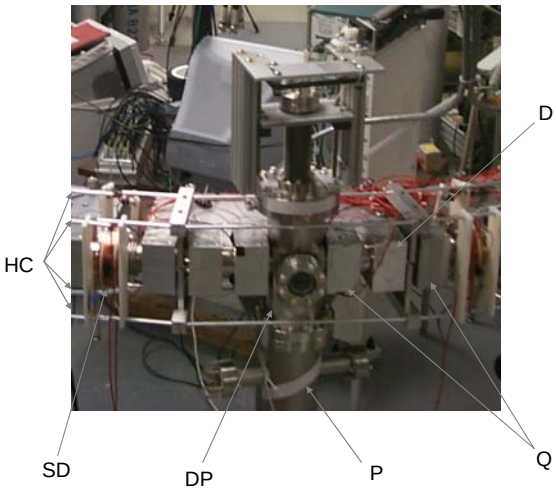

Fig. 10. Ring section, with Helmholtz coils (HC), steering dipoles (SD), diagnostics port (DP), vacuum pumping port (P), quadrupoles (Q), and dipole (D) [25].

hysteresis. The low-energy beam in UMER requires a very small field strength to bend it with the radius of the UMER ring. If this bending field were uniformly distributed about the ring, only 1.8 G would be needed[1]; in practice the needed field is closer to 17 G because each of the 36 dipoles only fills about 0.3% of the ring circumference. To obviate the need for iron-core magnets, air-core printed circuit magnets were developed that use a double-layer copper spiral embedded in kapton to produce the needed magnetic fields. Each magnet consists of two such printed circuits, held in place by aluminum heat sink mounts. Dipoles have one spiral per magnet half, and quadrupoles have two spirals per half.

2.4. Diagnostics

UMER was always designed as an accelerator physics testbed, and as such was designed with an unusually large number of diagnostics. When completed, UMER will have over 42 individual measurement devices, and will be capable of measuring the beam's properties in the full 6-D phase space. The most important diagnostics are discussed here.

2.4.1. Bergoz Fast Current Transformers

UMER employs up to two Bergoz [26] FCT-082-20:1 fast current transformers (FCTs) for monitoring beam current and pulse shape. These are passive coils that detect the magnetic field produced by the passing beam. Because the beam pipe carries a return or image current which is opposite to the beam current, the Bergoz FCTs must be placed over glass gaps to ensure that only the magnetic field from the beam is detected. To reduce the discontinuity seen by the image currents,

[1] Calculated from the cyclotron radius.

wire mesh straps are fastened to the beam pipe on either side of the Bergoz FCT, allowing the wall current to flow around the coil relatively unimpeded (Fig. 12). Glass gaps for use with Bergoz FCTs are located in the injection section (s = 62.6 cm) and in the extraction section just before the diagnostics end station. This allows a quick comparison of the beam profile and current at injection and at extraction to determine if beam loss is occurring. The FCT-082-20:1 coils used on UMER have a sensitivity of 1.25 V/A.

2.4.2. Phosphor Screens

Every 64 cm along the ring, and at two locations in the extraction section and the injection section, space is reserved for diagnostics ports. These ports allow for either a phosphor screen or a beam position monitor to be inserted into the beam. Phosphor screens will glow where they are struck by the electron beam, and can be used to determine the transverse beam location, size, and shape for diagnostic and steering purposes. The configuration of a phosphor screen in a diagnostics port is shown in Fig. 13, and a black and white camera image of the beam taken with the phosphor screen is shown in Fig. 14. Fig. 14 shows the supporting structure for the phosphor screen; this structure will be removed from most phosphor screen images used in this dissertation.

2.4.3. Beam Position Monitors

Beam Position Monitors (BPMs) are the primary diagnostic tool for studying longitudinal effects on UMER, and will be key for transverse steering of the beam during multiturn operation of UMER. Each BPM consists of four plates arranged along a cylinder which can be positioned so that it is coaxial with the beam pipe (Fig.

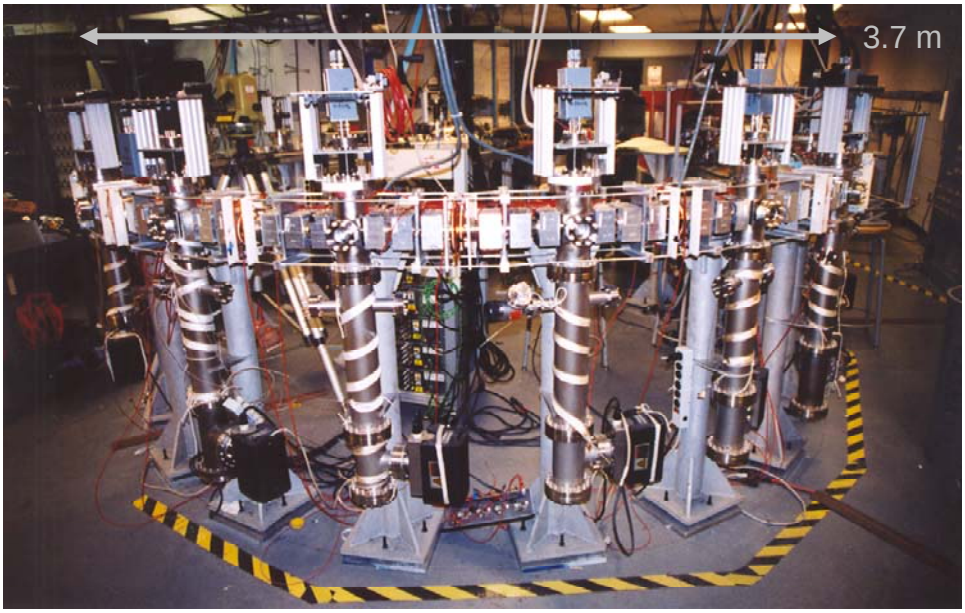

Fig. 11. The University of Maryland Electron Ring.

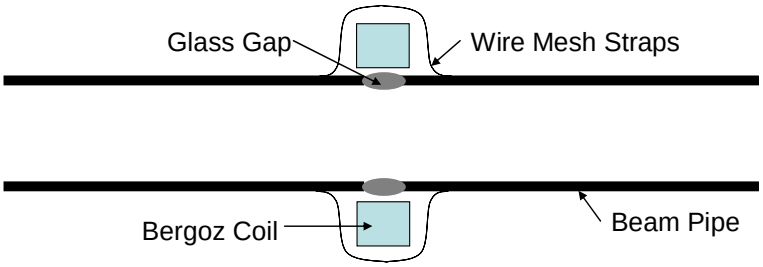

Fig. 12 Bergoz FCT configuration.

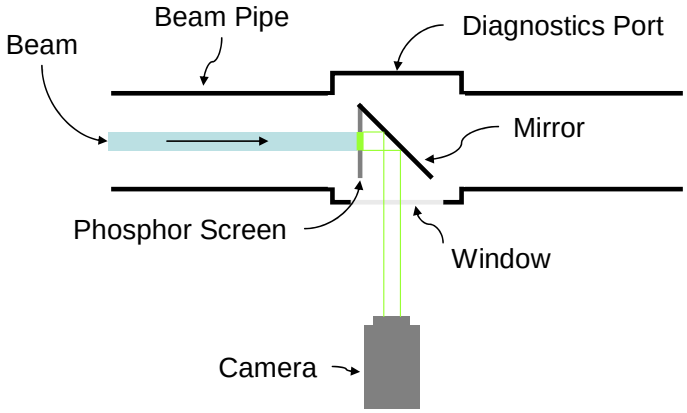

Fig. 13. Phosphor screen configuration.

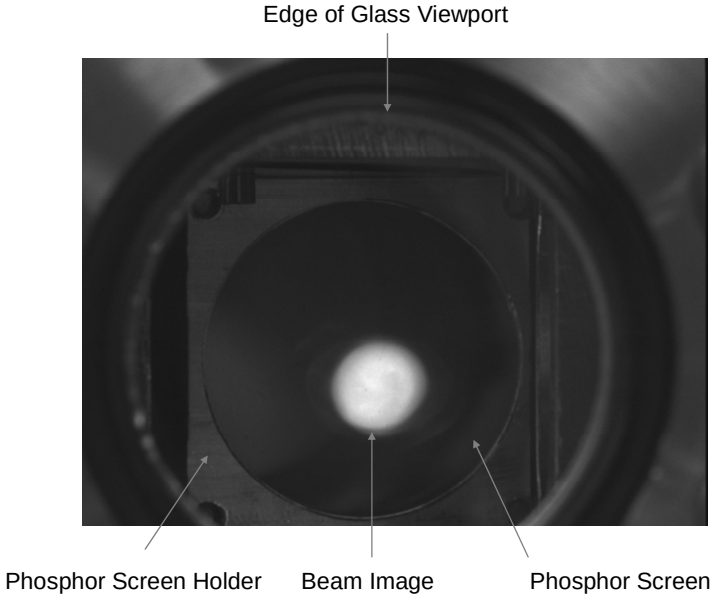

Fig. 14. Typical phosphor screen image.

15). Each BPM is carried in an assembly, along with a phosphor screen, which can be raised or lowered to bring either the BPM or the phosphor screen into the path of the beam (Fig. 16). When a beam passes by one of the plates, an image charge is induced on the plate. This changes the voltage on the plate, which is detected. The voltage detected on each plate will depend in part on the beam current and on the location of the beam centroid relative to the BPM center. In general, the signal on any given plate depends on both the horizontal and vertical position of the beam. However, it can be shown that if the angle Φ subtended by each plate is 76.99°, then the signals on the left and right plates will depend only on the horizontal displacement of the beam centroid, and the signals on the top and bottom plates will depend only on the vertical displacement of the beam centroid [29]. Thus, the horizontal and vertical signals are decoupled, and the displacement of the beam centroid in a particular direction is given by the ratio of the voltages on the corresponding plates. For example, if x is the beam centroid displacement in the horizontal direction, then the ratio of voltages on the left and right plates is given by

$$20\log\left[\frac{V_R}{V_L}\right] = 32.2\frac{x}{b}, \qquad (12)$$

where b is the beam pipe radius and 32.2 is a constant determined from geometry. By suitable combinations of the plate voltages, other information, such as beam current, can be obtained from the BPM [30].

The plate voltage is measured through an op amp buffer circuit [28]. The resistances used in this circuit help determine the temporal response, sensitivity to transverse displacements, and plate discharge time of the BPM. Because the BPM was intended for use both as a longitudinal and as a transverse diagnostic,

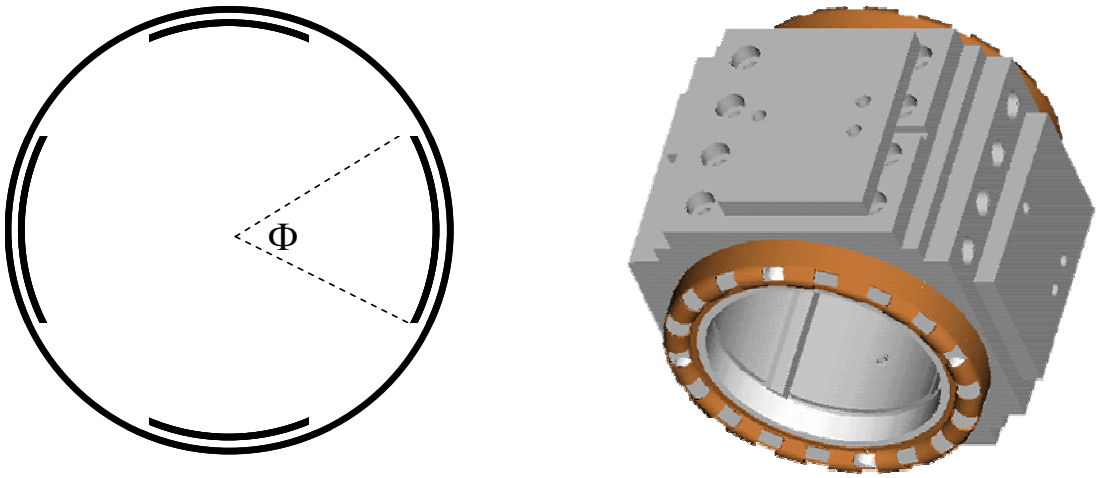

Fig.15. Beam position monitor geometry [27].

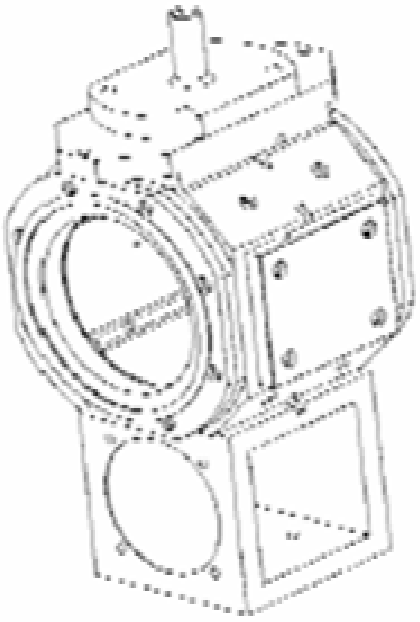

Fig. 16. Beam position monitor mount (top) and phosphor screen mount (bottom) [28].

compromise resistance values were used. This provided a spatial resolution of 0.1 mm, a highly linear response to transverse displacements, and a rise time of 1.7 ns. The BPM rise time may actually be less than this measured value, because the measurement was made using the UMER beam, which also has a rise time of approximately 2 ns. Therefore, 1.7 ns is only an upper bound on the BPM temporal resolution.

2.5. Other Systems

The UMER subsystems discussed thus far play a major role in the experiments to be described later. However, UMER consists of several other important systems, some of which are still under development. These systems will be mentioned here.

2.5.1. Induction Gaps

Three ring sections have been built with glass gaps replacing the diagnostics ports. These are intended for installing induction modules to provide longitudinal focusing and acceleration for the UMER beam.

These glass gaps can also be used for resistive BPMs, which detect transverse misalignment of the beam by measuring asymmetries in the wall or image currents associated with the beam. Resistive BPMs are discussed in reference [31].

2.5.2. Y-sections

Multiturn operation in UMER requires fast, pulsed magnets to switch from injection mode to recirculation mode to extraction mode. The speed required for these transitions is on the order of tens of nanoseconds, which is much faster than the

speed at which magnetic field changes can diffuse through the steel beam pipe used throughout UMER. To allow these fast changes in magnetic field strength and configuration to be felt by the beam, a junction section including a glass cylinder has been designed and installed on UMER. The nonconductive glass allows magnetic field changes to propagate through to the beam quickly, while a thin layer of metal has been deposited inside the glass to minimize the discontinuity for the return wall current. This effort has also included design of fast pulsers and low-inductance, high-quality printed circuit magnets. The Y-section development is described in detail in reference [32]. Most of the experimental work to be described in this dissertation occurred before the Y-section was installed in the injection line.

2.5.3. Energy Analyzers

A high-resolution energy analyzer has been under development for use with UMER. This device uses electric fields to retard the beam, and detects the amount of current passing through the retarding field. By appropriate analysis, this can be used to determine the longitudinal velocity of the particles in the beam, as well as the distribution of longitudinal velocities (energy spread). This is essentially a detector of longitudinal emittance. In testing, it has shown sub-eV resolution when used with a 5 keV beam. Ultimately, energy analyzers will be installed in the diagnostics end station on UMER, and perhaps in selected diagnostics ports in the ring. The energy analyzer is described in detail in references [33-39].

2.5.4. Diagnostics End Station

At the end of the extraction section is a diagnostics station, containing several additional measurement tools. Fig. 17 shows the inside of the diagnostics station,

with the upstream flange and beam pipe removed. This station includes a pepperpot (perforated foil) and slit-wire systems for measuring beam emittance, a Faraday cup for measuring beam current, and a phosphor screen on a sliding mount.

The measurement tools in the end station were not used to take data in the experiments to be described below. However, the slit-wire system could potentially be useful for longitudinal studies. Ordinarily, each of the slits is used with a corresponding, parallel wire (Fig. 18). The slit blocks all of the beam except that falling within a narrow band. The portion of the beam passing through the slit expands under emittance and space charge, and this expansion is measured by scanning the pickup wire across the beamlet passing through the slit. This technique yields a transverse emittance for the beam at the location of the slit.

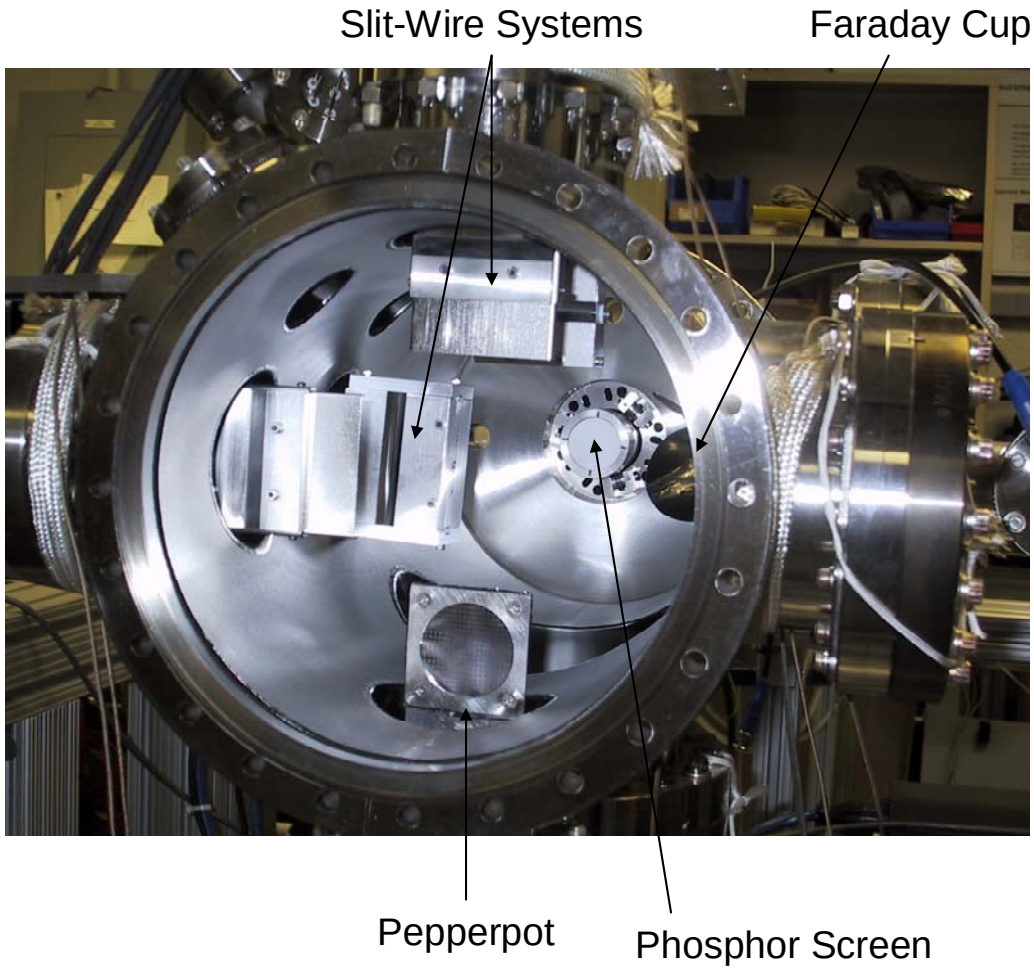

Fig. 17. Diagnostics end station [25].

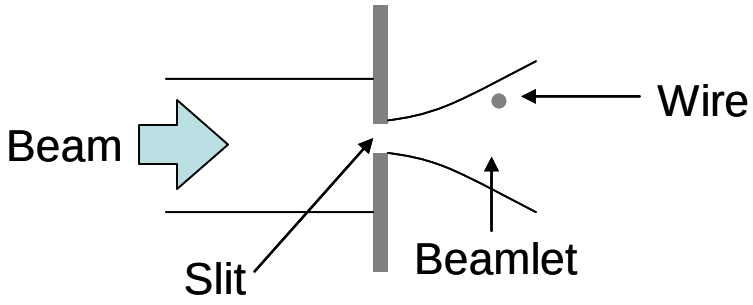

Fig. 18. Slit-wire system.

Chapter 3: Longitudinal Expansion

3.1. Introduction

We now turn our attention to the longitudinal dynamics of charged particle beams. Many of the essential concepts of longitudinal dynamics can be understood in a framework analogous to that used for transverse dynamics in Chapter 1. For example, the three effects that govern transverse dynamics -- space charge, emittance, and focusing -- also govern longitudinal dynamics. As in transverse dynamics, longitudinal space charge forces consist of the repulsive Coulomb interactions between the particles in the beam. These interactions occur through the longitudinal electric field, which can drive the longitudinal expansion of a beam, and also participates in the propagation of space charge waves along a beam. The value of the longitudinal electric field is given by

$$E_z = -\frac{g}{4\pi\varepsilon_0\gamma^2}\frac{\partial\lambda}{\partial z}, \tag{13}$$

where λ is the local line charge density in the beam, γ is the relativistic factor, and

$$g = \alpha + 2\ln\left(\frac{b}{a}\right) \tag{14}$$

is a geometry factor depending on the ratio of the beam pipe diameter b to the beam diameter a. The value of α is generally quoted as being between zero and one, depending on the theoretical assumptions made and whether the geometry factor being considered is the local value, or an approximate single value used to treat the dynamics of an entire bunch. Note that the geometry factor provides coupling

between the longitudinal and transverse dynamics. For example, varying the beam current not only changes the longitudinal electric field by providing more space charge in the beam, but also through the geometry factor by increasing the beam diameter. A derivation of the longitudinal electric field is given in Appendix A.

Longitudinal emittance, like transverse emittance, is a measure of the random, thermal velocity spread of the particles in a beam. The transverse emittances (in x and y) measure the components of that thermal velocity spread which is perpendicular to the overall direction of travel of the beam, while the longitudinal emittance measures that component of the thermal velocity spread which is parallel to the direction of travel of the beam. For this reason, the visualization of the transverse emittance and the longitudinal emittance differs (Fig. 19). Since the velocity spread measured by the longitudinal emittance is parallel to the direction of travel of the beam, it also implies a spread of kinetic energy in the beam. It should be noted that the energy spread associated with the thermal distribution of velocities in the beam, which is measured by longitudinal emittance, is not the same as an overall variation in energy or velocity along the beam pulse, which is sometimes known as the "coherent energy spread." This difference can be seen more clearly by looking at a plot of energy vs. location in a beam (Fig. 20). The longitudinal emittance relates to the "thickness" of the distribution, while the coherent energy spread or velocity tilt is a comparison of the average energy at the head and tail. As with transverse emittance, longitudinal emittance will have a defocusing effect. This can be seen by considering only the particles at the extreme head and tail of a beam; for simplicity, consider only three particles at each location (Fig. 21). If the particles at the head and

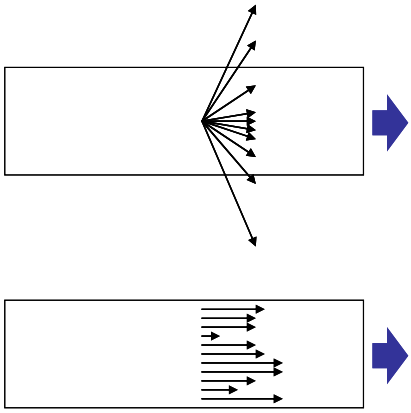

Fig. 19. Effect of transverse velocity spread (top) and longitudinal velocity spread (bottom).

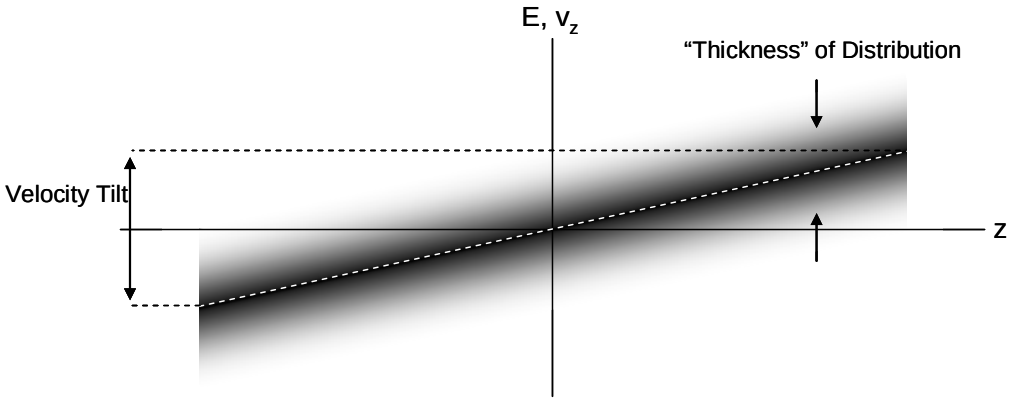

Fig. 20. Coherent energy spread ("velocity tilt") and incoherent energy spread (emittance).

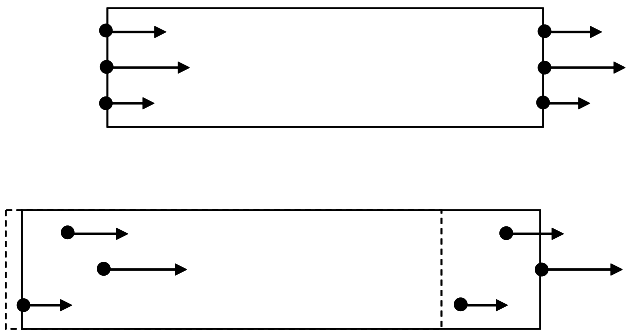

Fig. 21. Defocusing effect of longitudinal emittance.

at the tail have a distribution of velocities, and the beam is allowed to drift without focusing, the beam length after a given amount of time will be defined by the location of the fastest particle at the head, and the slowest particle at the tail. As a result, the length of the beam will expand. To counteract beam expansion driven by longitudinal space charge and emittance, longitudinal focusing may be applied. Implementation of longitudinal focusing is planned for a future upgrade of UMER.

The rest of this chapter will be devoted to a study of the overall longitudinal behavior of bunched beams, with an emphasis on longitudinal expansion of intense beams. The longitudinal envelope equation, analogous to the transverse envelope equation, will be introduced and used to derive a longitudinal intensity parameter. Experimental results of expanding parabolic beams in UMER will be presented. Then another model for longitudinal expansion of beams, the cold fluid model, will be introduced and compared to experiments on UMER. Finally, the longitudinal envelope equation and the cold fluid model will be compared.

3.2. Longitudinal Envelope Equation

To simultaneously consider the effects of space charge, emittance, and external focusing on the longitudinal evolution of a beam, we need a longitudinal equivalent of Eq. (5), the transverse envelope equation. This is found in the form of the *longitudinal* envelope equation [1]:

$$z_m'' + \kappa_{z0} z_m - \frac{K_L}{z_m^2} - \frac{\varepsilon_{zz'}^2}{z_m^3} = 0 \,. \qquad (15)$$

Here, z_m is the half-length of the beam, measured from the beam center to the extreme head of the beam; κ_{z0} is the longitudinal focusing function, which in

general will be a function of the distance s traveled along the beam line; $\varepsilon_{zz'}$ is the unnormalized effective emittance, given by

$$\varepsilon_{zz'} = 5\sqrt{\langle z^2 \rangle \langle z'^2 \rangle - \langle zz' \rangle^2}\ ; \tag{16}$$

And K_L is the longitudinal generalized perveance, given by

$$K_L = \frac{3}{2}\frac{g_b N}{\beta^2 \gamma^5}\frac{q^2}{4\pi\varepsilon_0 mc^2}, \tag{17}$$

where g_b is the geometry factor for bunched beams and N is the total number of particles in the bunch. As before, primes denote differentiation with respect to s, the distance traveled in the laboratory frame.

The longitudinal envelope equation was first derived by Smith [40]. It was then rederived in a self-consistent manner by Neuffer [41,42]. Neuffer's derivation used a distribution function defined by

$$f(z, z', s) = \frac{3N}{2\pi\varepsilon_L}\sqrt{1 - \frac{z^2}{z_m^2} - \frac{z_m^2}{\varepsilon_L^2}\left(z' - \frac{z_m'}{z_m}z\right)^2}\ , \tag{18}$$

wherever the argument of the square root is positive, and $f(z, z', s) = 0$ otherwise. This distribution is a solution of the Vlasov equation, and yields a parabolic line charge density of the form

$$\lambda(z) = \lambda_0\left(1 - \frac{z^2}{z_m^2}\right) \tag{19}$$

in free space. (The effect of boundary conditions is discussed in Appendix A.) This parabolic line charge density provides for linearity of the space charge forces in the beam (again, in free space), and with the assumption of linear external focusing will preserve the emittance ε_L.

3.2.1. General Comparison to Transverse Envelope Equation.

Like the transverse envelope equation, the longitudinal envelope equation consists of four terms – a dynamical or acceleration term consisting of the second derivative of the beam size with respect to the distance traveled, a defocusing term for emittance, a defocusing term for space charge, and a term for applied focusing. However, several differences should be noted.

The transverse generalized perveance K_T is dimensionless while the longitudinal generalized perveance K_L has units of meters. As a result, the denominator of the space charge term in the longitudinal envelope equation also has a higher power. In addition, the transverse generalized perveance (Eq. (3)) scales with γ^{-3} while the longitudinal generalized perveance (Eq. (17)) scales with γ^{-5}. This occurs because in each case two factors of γ are required to Lorentz-contract the acceleration term during the derivation, while one additional factor is associated with the use of the "transverse mass" γm in the transverse case and three additional factors are associated with the use of the "longitudinal mass" $\gamma^3 m$ in the longitudinal case[1, 43].

The relationship between RMS quantities of length and emittance and their non-RMS counterparts is also different. Specifically, the relationship for the longitudinal envelope equation are $z_m = \sqrt{5}\tilde{z}$ and $\varepsilon_{zz'} = 5\tilde{\varepsilon}_{zz'}$, while those for the transverse envelope equation are $x_m = 2\tilde{x}$ and $\varepsilon_x = 4\tilde{\varepsilon}_x$. This is a result of the difference between the longitudinal envelope equation, which is derived for a bunched beam, and the transverse envelope equation, which assumes an unbunched

beam. This discrepancy can be eliminated by using a modified transverse envelope equation which assumes a bunched beam [1,44].

3.2.2. Longitudinal Intensity Parameter

Just as the intensity parameter χ_T of Eq. (8) can be derived to compare the relative strengths of space charge and emittance in governing the transverse evolution of a beam, a longitudinal intensity parameter χ_L can be derived to compare the relative strengths of space charge and emittance in governing the longitudinal evolution of a beam [45].

By analogy with the transverse intensity parameter, we begin by assuming that longitudinal focusing exists, and that the beam is longitudinally matched. In this case, the longitudinal envelope becomes

$$k_{0L}^2 z_m - \frac{K_L}{z_m^2} - \frac{\varepsilon_{zz'}^2}{z_m^3} = 0 . \tag{20}$$

In Eq. (20), the focusing function κ_{z0} is replaced by the square of the zero-current synchrotron wave number k_{0L} because focusing is assumed to be continuous [1]. The synchrotron wave number, and the synchrotron frequency $\omega_l = k_{0L} c\beta$, describe the longitudinal oscillations made by the particles within the beam bunch under the influence of external focusing, and are analogous to the betatron wave number and frequency for transverse focusing. By analogy with the definition of the transverse intensity parameter, we take

$$\chi_L = \frac{\text{longitudinal space charge term}}{\text{longitudinal focusing term}} \tag{21a}$$

or

$$\chi_L = \frac{K_L}{k_{0L}{}^2 z_m{}^3}. \tag{21b}$$

In a machine where external longitudinal focusing was present, and where the resulting synchrotron wave number could be calculated, Eq. (21b) would be sufficient to determine the longitudinal intensity of the beam. In the case of UMER, however, longitudinal focusing is not present, and therefore Eq. (21b) is not appropriate. Like the transverse intensity parameter, the longitudinal intensity parameter is derived by assuming a matched beam, which in turn requires focusing. Strictly speaking, an intensity parameter, therefore, should not be stated in the absence of focusing. However, we can calculate from Eq. (21b) a longitudinal intensity parameter, assuming that longitudinal focusing was being used and was exactly strong enough to maintain a given beam half-length z_m. For this purpose, it is more convenient to combine Eqs. (20) and (21b) to eliminate the synchrotron wave number. This gives

$$\chi_L = \frac{K_L}{K_L + \frac{\varepsilon_{zz'}^2}{z_m}}. \tag{22}$$

To further express the longitudinal intensity parameter in terms of experimentally-observable quantities, the longitudinal emittance can be replaced with the longitudinal energy spread, as follows [1,45]. First, express the unnormalized total emittance in terms of the unnormalized RMS emittance $\tilde{\varepsilon}_{zz'}$,

$$\varepsilon_{zz'} = 5\tilde{\varepsilon}_{zz'}. \tag{23a}$$

Replace the unnormalized RMS emittance with the normalized RMS emittance $\tilde{\varepsilon}_{nz}$,

$$\varepsilon_{zz'} = 5\frac{\tilde{\varepsilon}_{nz}}{\beta\gamma^3}. \tag{23b}$$

The normalized RMS emittance is invariant under acceleration (assuming linear forces), and makes the dependence on the relativistic factors explicit. Next, rewrite the normalized RMS emittance in terms of the Boltzmann constant k_B and the longitudinal temperature $T_{\|}$ [1],

$$\varepsilon_{zz'} = \frac{5}{\beta\gamma^3}\tilde{z}\left(\frac{\gamma^3 k_B T_{\|}}{mc^2}\right)^{1/2}. \tag{23c}$$

Replace the longitudinal temperature by the RMS incoherent energy spread $\Delta\tilde{E}$,

$$\varepsilon_{zz'} = \frac{5}{\beta\gamma^3}\tilde{z}\left(\frac{\gamma}{\beta Ec}\Delta\tilde{E}\right). \tag{23d}$$

Replace the RMS half length $\tilde{z}$ with the actual half length z_m, and collect terms,

$$\varepsilon_{zz'} = \frac{5}{\beta^2\gamma^3}\frac{z_m}{\sqrt{5}}\frac{\Delta\tilde{E}}{mc^2}. \tag{23e}$$

Together with Eq. (22), this gives

$$\chi_L = \frac{K_L}{K_L + \left[\frac{\sqrt{5}}{\beta^2\gamma^3}\frac{\Delta\tilde{E}}{mc^2}\right]^2 z_m}, \tag{24}$$

a convenient expression of the effective longitudinal intensity parameter in terms of experimental quantities.

As with the transverse intensity parameter, the longitudinal intensity parameter varies from 0 to 1; a beam is considered longitudinally space charge dominated or intense if $\chi_L > 0.5$, and longitudinally emittance dominated if $\chi_L < 0.5$. Table 4 shows the values of the longitudinal intensity parameter in UMER for several operating regimes. The resulting values indicate that UMER is

	Case 1	Case2	Case3	Case4	Case5
Current	100 mA	100 mA	1 mA	1 mA	1 mA
Pulse Length	100 ns	70 ns	70 ns	70 ns	70 ns
Energy Spread	10 eV	10 eV	10 eV	50 eV	100 eV
χ_L	0.99979	0.99979	0.97957	0.65734	0.3241
$\varepsilon_{zz'}$	0.00345 m	0.00241 m	0.00241 m	0.0121 m	0.0241
$T_{\parallel}$	53.26 K	53.26 K	53.26 K	1331.6 K	5326.3 K

Table 4. Longitudinal Intensity Parameter for UMER. In Cases 1, 2, and 3, the beam is almost totally space charge dominated. Cases 4 and 5 cannot be realized with UMER, but were included to show examples of operating parameters which would result in a longitudinal intensity different from $\chi_L \approx 1$. Note that the perpendicular temperature $T_{\perp}$ is 1453.7 K, which shows that the beam will not normally be in thermal equilibrium between its transverse and longitudinal properties. Thermal equilibrium is approximately achieved in Case 4. Operating parameters assumed for UMER were: $\beta = 0.2$, beam radius 1 cm, transverse normalized effective emittance 10 μm [45].

longitudinally space charge dominated under all accessible regimes. As a result, the emittance term in the longitudinal envelope equation can be neglected when studying the beam in UMER.

Like the transverse intensity parameter, the longitudinal intensity parameter can be related to other measures of beam intensity. Of particular interest are the relationships between the longitudinal intensity parameter, the longitudinal tune depression, and the scaled plasma frequency. The relationship between the longitudinal intensity parameter and the longitudinal (synchrotron) tune depression is the same as the relationship between the transverse intensity parameter and the transverse (betatron) tune depression [45]:

$$\frac{k_L}{k_{0L}} = \sqrt{1-\chi_L}\ . \tag{25}$$

Notice the similarity with Eq. (9). Here, k_{0L} is the synchrotron oscillation wave number in the absence of space charge, while

$$k_L = \sqrt{{k_{0L}}^2 - \frac{K_L}{{z_m}^3}} \tag{26}$$

is the synchrotron oscillation wave number in the presence of space charge.

Unlike the longitudinal and transverse tune depressions, the expressions for the longitudinal and transverse scaled plasma frequencies differ. The transverse expression, Eq. (10), relates the transverse intensity parameter to the ratio of the transverse plasma frequency ω_p with the zero-current betatron frequency $\omega_0 = k_0 c\beta$. A similar expression can be derived for the longitudinal intensity parameter,

longitudinal plasma frequency, and zero-current synchrotron frequency. The transverse equation of motion due to space charge is

$$\ddot{x} = \omega_p{}^2 x = \frac{qE_s}{\gamma^3 m}, \tag{27}$$

in which the location of the particle is x, $\ddot{x}$ is the particle's acceleration, and E_s is the electric field due to space charge [1]. An equivalent longitudinal equation would be [45],

$$\ddot{z} = \omega_{pL}{}^2 z = \frac{qE_{sz}}{\gamma^3 m}, \tag{28}$$

where ω_{pL} is the longitudinal plasma frequency, z is the longitudinal location of the particle, and the space charge field is taken as

$$E_{sz} = -\frac{g_b}{4\pi\varepsilon_0\gamma^2}\frac{\partial\lambda}{\partial z}. \tag{29}$$

With the parabolic line charge density of Eq. (19), the longitudinal plasma frequency becomes

$$\omega_{pL}{}^2 = \frac{2qg\lambda_0}{m\gamma^5 4\pi\varepsilon_0 z_m{}^2}. \tag{30}$$

This can be further rewritten by noticing that the peak line charge density λ_0 can be replaced by an “RMS average” line charge density

$$\tilde{\lambda} = \frac{4}{\sqrt{30}}\lambda_0, \tag{31}$$

which in turn has the value

$$\tilde{\lambda} = \frac{qN}{2z_m}. \tag{32}$$

Using these relations, the longitudinal plasma frequency becomes

$$\omega_{pL}{}^2 = \left(\frac{3}{2} \frac{gNq^2}{\beta^2 \gamma^5 4\pi\varepsilon_0 mc^2} \right) \frac{\sqrt{30}}{6} \frac{v^2}{z_m{}^3} \tag{33}$$

or

$$\omega_{pL}{}^2 = \sqrt{\frac{5}{6}} \frac{K_L v^2}{z_m{}^3}. \tag{34}$$

The ratio of the longitudinal plasma frequency to the zero-current synchrotron frequency $\omega_{0L} = k_{0L} v$ [1] then becomes the scaled longitudinal plasma frequency

$$\frac{\omega_{pL}}{\omega_{0L}} = \sqrt{\sqrt{\frac{5}{6}} \chi_L} \approx \sqrt{0.91 \chi_L}\,, \tag{35}$$

which differs from the scaled transverse plasma frequency Eq. (10) in the prefactor of the intensity parameter. A comparison of some transverse and longitudinal relations is given in Table 5, and the longitudinal intensity parameter is plotted against the longitudinal tune depression and the scaled longitudinal plasma frequency in Fig. 22.

3.2.3. Solutions of the Longitudinal Envelope Equation

The longitudinal envelope equation can be used to determine the beam length as a function of distance traveled under a variety of focusing conditions and beam parameter values. The design of UMER calls for longitudinal focusing to be installed. Although this longitudinal focusing is not continuous, the change in beam length during travel between focusing elements will be small. This allows us to make an approximation of smooth focusing. For smooth longitudinal focusing, an approximate stationary solution for beam length, taking into account focusing, emittance, and space charge, has been found previously to be [46]

Transverse Envelope Equation	Longitudinal Envelope Equation
$R'' + {k_0}^2 R - \frac{K}{R} - \frac{\varepsilon_x^2}{R^3} = 0$	$z_m'' + \kappa_{z0} z_m - \frac{K_L}{{z_m}^2} - \frac{\varepsilon_{zz'}^2}{{z_m}^3} = 0$
Transverse Intensity Parameter	Longitudinal Intensity Parameter
$\chi = \frac{K}{k_0^2 R^2}$	$\chi_L = \frac{K_L}{{k_{0L}}^2 {z_m}^3} = \frac{K_L}{K_L + \left[\frac{\sqrt{5}}{\beta^2\gamma^3}\frac{\Delta\tilde{E}}{mc^2}\right]^2 z_m}$
Transv. Intensity and Tune Depression	Long. Intensity and Tune Depression
$\frac{k}{k_0} = \sqrt{1-\chi}$	$\frac{k_L}{k_{0L}} = \sqrt{1-\chi_L}$
Transv. Intensity and Plasma Frequency	Long. Intensity and Plasma Frequency
$\frac{\omega_p}{\omega_0} = \sqrt{2\chi}$	$\frac{\omega_{pL}}{\omega_{0L}} = \sqrt{\sqrt{\frac{5}{6}}\chi_L} \approx \sqrt{0.91\chi_L}$

Table 5. Comparison of longitudinal and transverse relations [45].

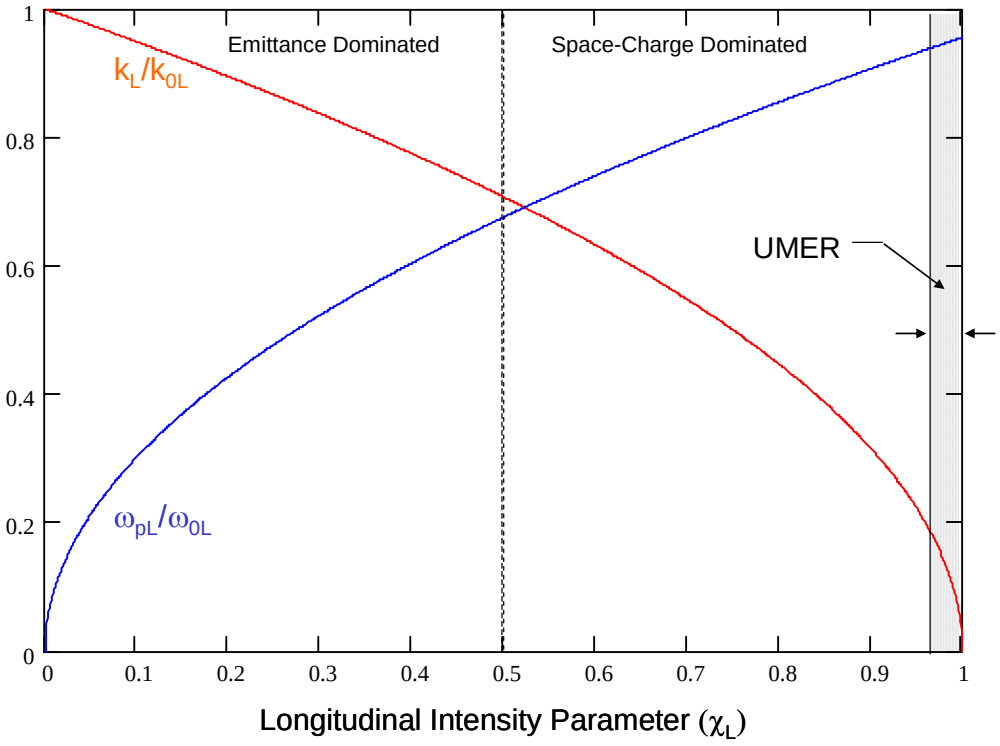

Fig. 22. Longitudinal Space charge Intensity Parameter (χ_L). This graph relates the intensity parameter for longitudinal beam physics with the longitudinal tune depression (k_L/k_{0L}) and the longitudinal plasma frequency (ω_{pL}). Beams with $0 \le \chi_L < 0.5$ are considered emittance dominated, while beams with $0.5 < \chi_L \le 1$ are considered space charge dominated. Space charge forces dominate the longitudinal physics of UMER for all practical operating parameters. The operating range for UMER is indicated by the arrows at the extreme right of the graph [45].

$$z_m \approx \left(\frac{\varepsilon_{zz'}{}^{3/2}}{k_{0L}{}^{3/2}} + \frac{K_L}{k_{0L}{}^2} \right)^{1/3} . \tag{36}$$

In the current configuration of UMER, no longitudinal focusing is present, and emittance is negligible. Under these conditions, the longitudinal envelope equation of Eq. (15) can be reduced to

$$\frac{d^2 z_m}{ds^2} = \frac{K_L}{z_m^2} . \tag{37}$$

To solve this equation, multiply both sides by $2\frac{dz_m}{ds}$ and integrate, which gives [45,47]

$$\frac{dz_m}{ds} = \pm \sqrt{-\frac{2K_L}{z_m} + \frac{2K_L}{z_{m0}} + \left(\left[\frac{dz_m}{ds} \right]_{z_{m0}, s_0} \right)^2} . \tag{38}$$

In Eq. (38), the upper sign is taken when the beam is expanding, and the lower sign is taking when the beam is contracting; z_{m0} is the initial value of the beam half length; and $\left[\frac{dz_m}{ds} \right]_{z_{m0}, s_0}$ is the initial value of the longitudinal divergence of the beam. Eq. (38) can be integrated further , to yield

$$s = s_0 + \left[\pm \frac{\sqrt{c_1 z_m{}^2 - 2K_L z_m}}{c_1} \pm \frac{K_L}{c_1^{3/2}} \ln \left| 2\sqrt{c_1}\sqrt{c_1 z_m{}^2 - 2K_L z_m} + 2c_1 z_m - 2K_L \right| \right]_{z_{m0}}^{z_m} . \tag{39}$$

The constant c_1 is the sum of the squared initial rate of expansion $\left(\left[\frac{dz_m}{ds} \right]_{z_{m0}, s_0} \right)^2$ and the initial value of the space charge term $\frac{2K_L}{z_{m0}}$, and as before the upper sign is taken

when the beam is expanding so that $\frac{dz_m}{ds} \geq 0$ and the lower sign is taken when the beam is contracting so that $\frac{dz_m}{ds} \leq 0$. Notice that Eq. (39) gives the beam half length z_m as the independent variable and the beam position s as the dependent variable. When actually plotting beam expansion curves this causes no trouble whatsoever, and the independent variable is plotted on the vertical axis while the dependent variable is plotted on the horizontal axis.

In practice, Eq. (38) is usually used to calculate beam expansion curves instead of Eq. (39); Eq. (38) is directly numerically integrated using the computer program Mathcad. An example of this is shown in Fig. 23, where the full length of a representative beam in UMER is plotted against distance traveled from the cathode. In Figs. 24 - 29, the effects of varying beam current, beam energy, beam diameter, beam pipe diameter, initial longitudinal divergence, and α on the beam expansion are shown.

In any longitudinal focusing system which is not continuous, the beam length will have its maximum values at the focusing elements, and will reach a minimum length somewhere in between those elements. If the longitudinal focusing forces are assumed to act only over a very short distance (longitudinal thin lens approximation) , this minimum beam length can be calculated from Eq. (38) by recognizing that the minimum beam length will occur when $\frac{dz_m}{ds} = 0$ [45]. The minimum half length is then given by

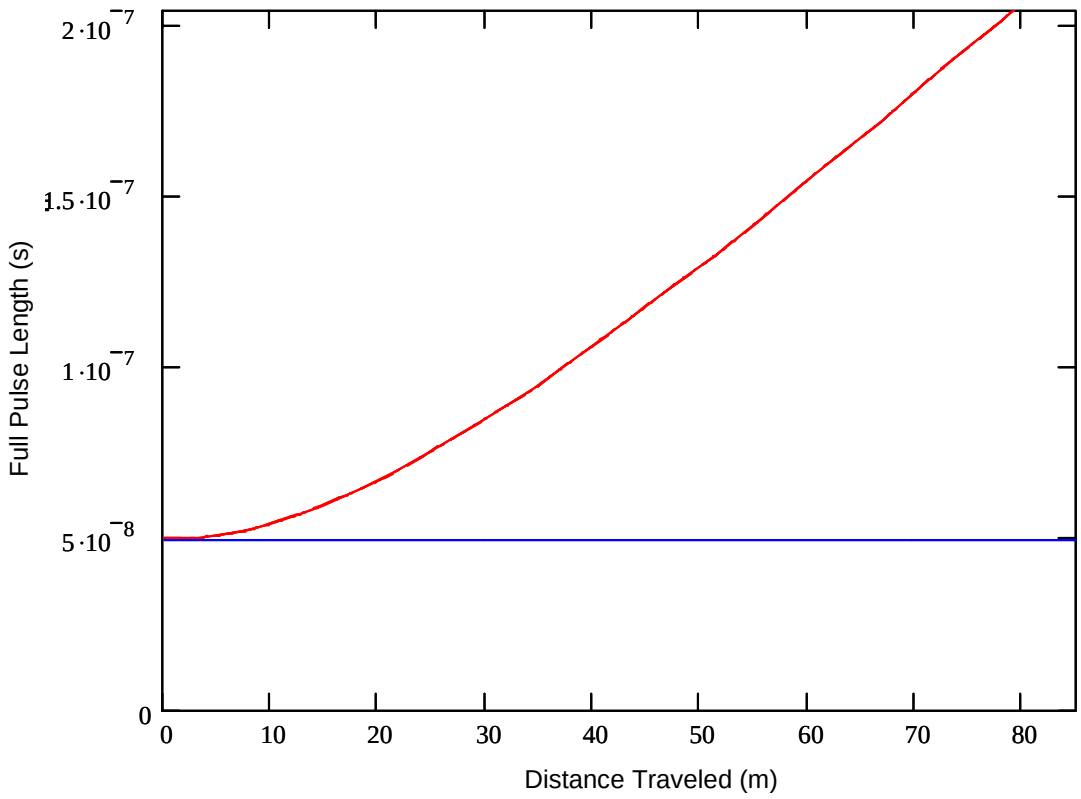

Fig. 23. Longitudinal expansion of parabolic beam in UMER. Red line is full pulse length of the beam, blue line is initial full pulse length of the beam. Parameters assumed were 100 mA peak current, 10 keV energy, 50 ns initial full length, 2 cm beam diameter, 5.08 cm beam pipe diameter, $\alpha = 1$ ($g = 2.864$), and no initial longitudinal divergence.

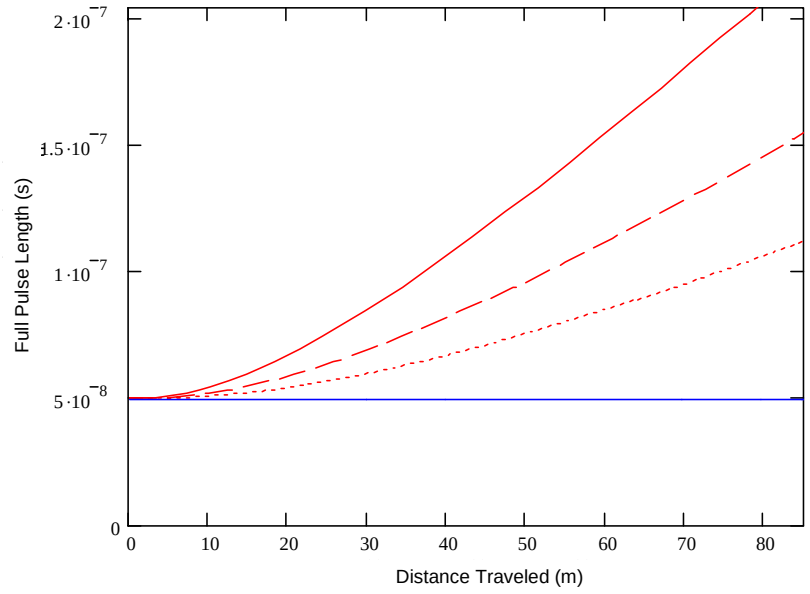

Fig. 24. Effect of varying beam current on longitudinal expansion of parabolic beam in UMER. Full pulse length plotted for 24 mA peak current (dotted red line), 50 mA peak current (dashed red line), and 100 mA peak current (solid red line). Initial full pulse length is 50 ns (blue line). All other parameters remain as in Figure 23.

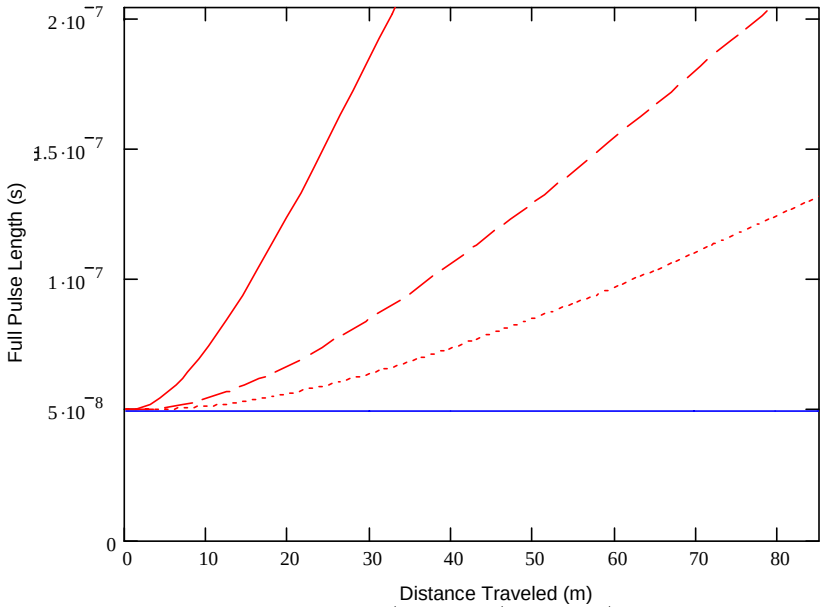

Fig. 25. Effect of varying beam energy on longitudinal expansion of parabolic beam in UMER. Full pulse length plotted for 5 keV beam (solid red line), 10 keV beam (dashed red line), and 15 keV beam (dotted red line). Initial full pulse length is 50 ns (blue line). All other parameters remain as in Figure 23.

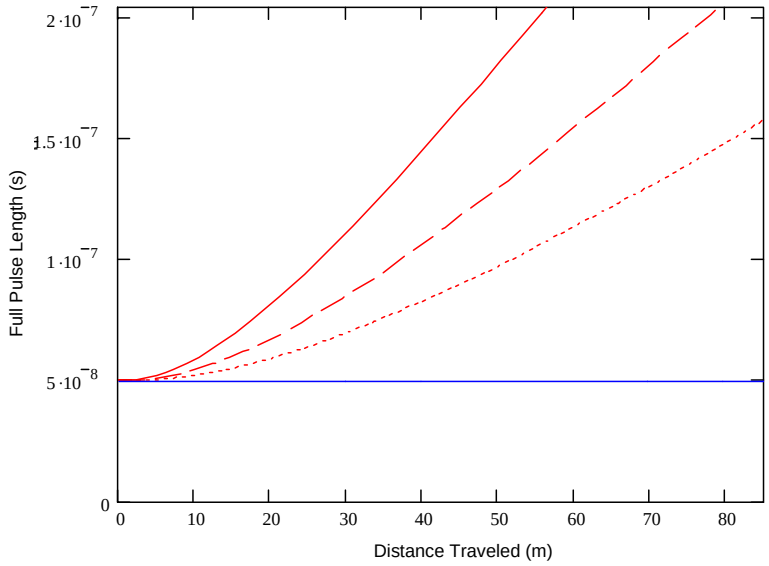

Fig. 26. Effect of varying beam diameter on longitudinal expansion of parabolic beam in UMER. Full pulse length plotted for beam diameters of 0.5 cm (solid red line), 2 cm (dashed red line), and 4 cm (dotted red line). Initial full pulse length is 50 ns (blue line). All other parameters are as given in Figure 23.

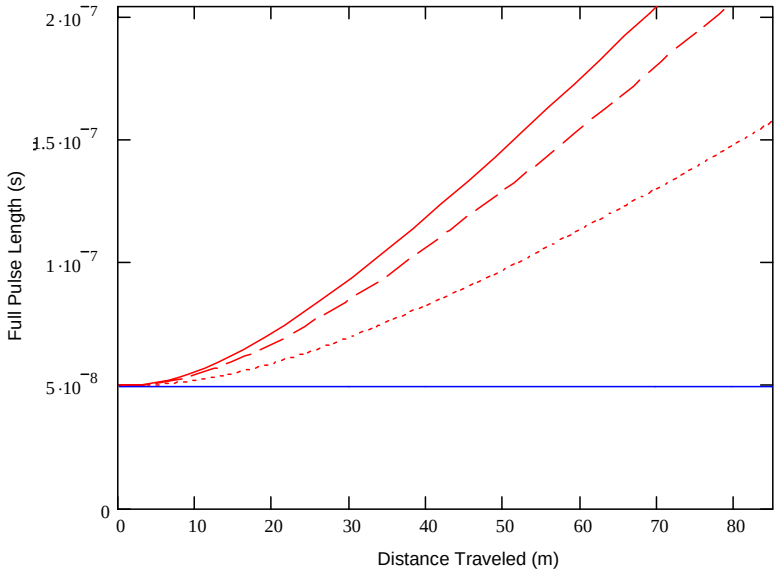

Fig. 27. Effect of varying beam pipe diameter on longitudinal expansion of parabolic beam in UMER. Full pulse length plotted for beam pipe diameters of 7.62 cm (solid red line), 5.08 cm (dashed red line), and 2.54 cm (dotted red line). Initial full pulse length is 50 ns (blue line). All other parameters are as given in Figure 23.

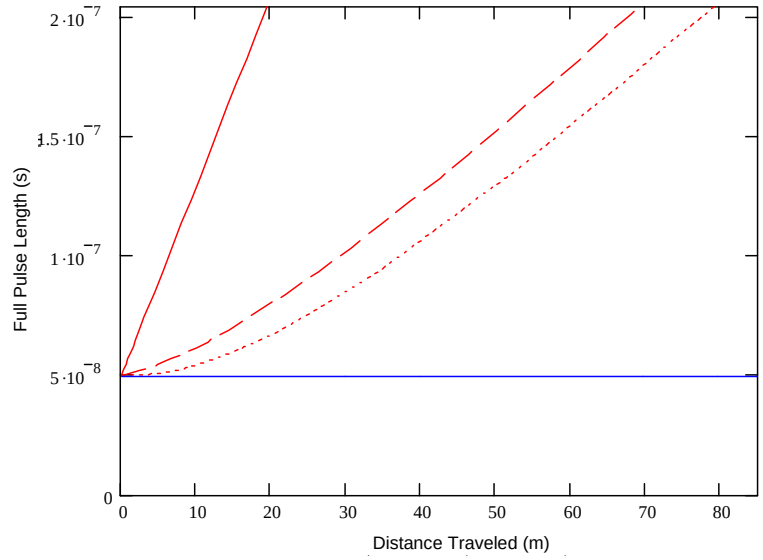

Fig. 28. Effect of varying initial longitudinal divergence on longitudinal beam expansion of parabolic beam in UMER. Full pulse length plotted for initial longitudinal RMS divergences (dz_{rms}/ds) of 0 (dotted red line), 0.01 (dashed red line), and 0.1 (solid red line). Initial full pulse length is 50 ns (blue line). All other parameters are as given in Figure 23.

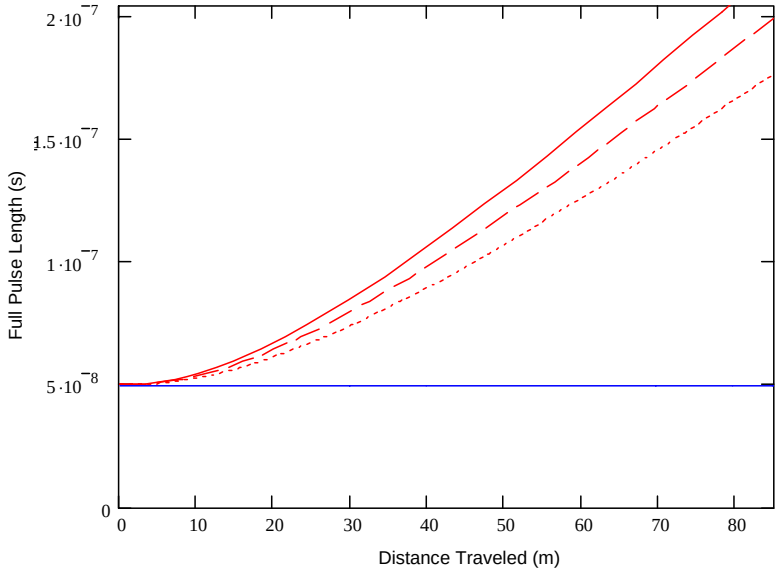

Fig. 29. Effect of alpha on longitudinal expansion of parabolic beam in UMER. Full pulse length plotted for alpha of 0 (g = 1.864) (dotted red line), 0.5 (g = 2.364) (dashed red line), and 1 (g = 2.864) (solid red line). Initial full pulse length is 50 ns (blue line). All other parameters are as given in Figure 23.

$$z_{mw} = \frac{2K_L}{\frac{2K_L}{z_{m0}} + \left(\left[\frac{dz_m}{ds} \right]_{z_{m0}, s_0} \right)^2}. \qquad (40)$$

3.3. Expansion of Parabolic Beam in UMER

To test the longitudinal envelope equation in UMER, a parabolic beam was produced at the gun and allowed to freely expand as it traveled through the UMER transport lattice. The longitudinal expansion of parabolic beams was previously studied at Maryland in the early 1990's [48-50]. In those experiments, the parabolic beam was produced in a gridded electron gun by applying an appropriate voltage to the grid, and a typical beam had an energy of 2.5 keV, a peak current of 28 mA, and a full length of 25 ns. This beam was allowed to expand through a 0.5 m injection section, and a 5 m transport section. Both the injection and transport were achieved using solenoid focusing. Beam current and velocity as a function of position in the beam were measured at several points along the beamline. The motivation for conducting new experiments to verify the longitudinal envelope equation for parabolic beams in UMER was to test the longitudinal envelope equation in a quadrupole focusing channel, rather than the solenoid channels used previously; to test the longitudinal envelope equation over longer distances; and to take advantage of the improved and more numerous diagnostics available on UMER.

In UMER, parabolic pulses can be produced in several ways. Originally, parabolic beams were intended to be produced in UMER in a manner similar to that used in previous experiments. The grid pulse in UMER is supplied by a pulse forming line, which is switched by a transistor. In normal operation, the trigger signal applied to this transistor is high enough that it operates in avalanche mode,

providing quick switching times. By reducing the voltage applied to the transistor, its switching operation is slower, providing a parabolic grid pulse, and therefore a parabolic beam [51]. However, this capability was not retained when the original pulser provided by FMT was replaced by one provided by R.F. Koontz [52]. More recently, parabolic beams have been produced in UMER by using low-pass filters on the pulse forming line [53]. However, this capability was not available when longitudinal experiments began on UMER.

Instead, we chose to take advantage of work being done by D. Feldman and others on using thermionic dispenser cathodes as photocathodes [54]. By illuminating the cathode with laser light, photoelectrons can be produced, and since the dispenser cathodes used are prompt photoemitters, the pulse of photoelectrons produced has the same pulse shape as the laser pulse. This allows a dispenser thermionic cathode, such as the one used in UMER, to produce a beam due to thermionic emission alone, due to photoemission alone, or due to both thermionic emission and photoemission simultaneously (Fig. 6). The Nd:YAG laser used in these experiments naturally produces a pulse shape which is approximately Gaussian or parabolic in shape, and so it produces a photoelectron beam which is ideal for studying the longitudinal envelope equation in UMER. In this experiment, the laser was shifted into the green by nonlinear crystals, and directed onto the cathode by a mirror in the beamline, in a manner similar to the more complicated system discussed in Chapter 5. (The evolution of hybrid beams and rectangular thermionic beams will be discussed in later sections.)

The 10 keV, approximately 5 ns long photoemission beam thus produced was injected into the UMER beamline. At the time of the experiment, the injector section and approximately 180° of the ring were completed, and the extraction section was in use, providing a total travel distance of approximately 7.7 m from the cathode to the final current monitor. The beam transport system was set for 25 mA, using settings optimized for use with the nominal 25 mA UMER beam by H. Li and S. Bernal. In order to ensure a transversely matched beam, the laser intensity was adjusted to maintain 25 mA peak current, as measured at the injection Bergoz fast current transformer (FCT). Because of a progressive decay in the quantum efficiency of the cathode, the laser power was manually increased to maintain 25 mA as the experiment progressed. This rate of decay was fast enough that two people were required for the experiment -- one to operate the laser, and one to take the data. In addition to the Bergoz FCT, ten BPMs in the injection and transport sections and one Bergoz FCT in the extraction section were used to monitor beam pulse shape. Mathcad spreadsheets were written to aid in extracting the beam length and estimating the experimental error (see Appendix B for more details). The beam length quoted from these experiments is usually the full width half maximum (FWHM) or 10%-10% length; Table 6 lists conversions between different beam length measures used for parabolic beams. To ensure that no significant beam loss was occurring under these conditions, the beam current, bunch charge, and beam length were compared at the upstream and downstream Bergoz FCTs. Typical data traces at the upstream and downstream Bergoz FCTs are shown in Fig. 30, and beam loss data is shown in Table 7. The current in a parabolic bunch is given by [1]

	Distance	Time
Full Length (z_F or τ_F)	$z_F = 2\sqrt{5}\tilde{z}$	$\tau_F = \frac{2\sqrt{5}}{c\beta}\tilde{z}$
Half Length (z_m or τ_m)	$z_m = \sqrt{5}\tilde{z}$	$\tau_m = \frac{\sqrt{5}}{c\beta}\tilde{z}$
FWHM Length (z_{FWHM} or τ_{FWHM})	$z_{FWHM} = \sqrt{10}\tilde{z}$	$\tau_{FWHM} = \frac{\sqrt{10}}{c\beta}\tilde{z}$
10%-10% Length ($z_{10\,pc}$ or $\tau_{10\,pc}$)	$z_{10\,pc} = 2\sqrt{4.5}\tilde{z}$	$\tau_{10\,pc} = \frac{2\sqrt{4.5}}{c\beta}\tilde{z}$

Table 6. Beam length measure conversions for parabolic. All pulse lengths referenced to RMS pulse length $\tilde{z}$.

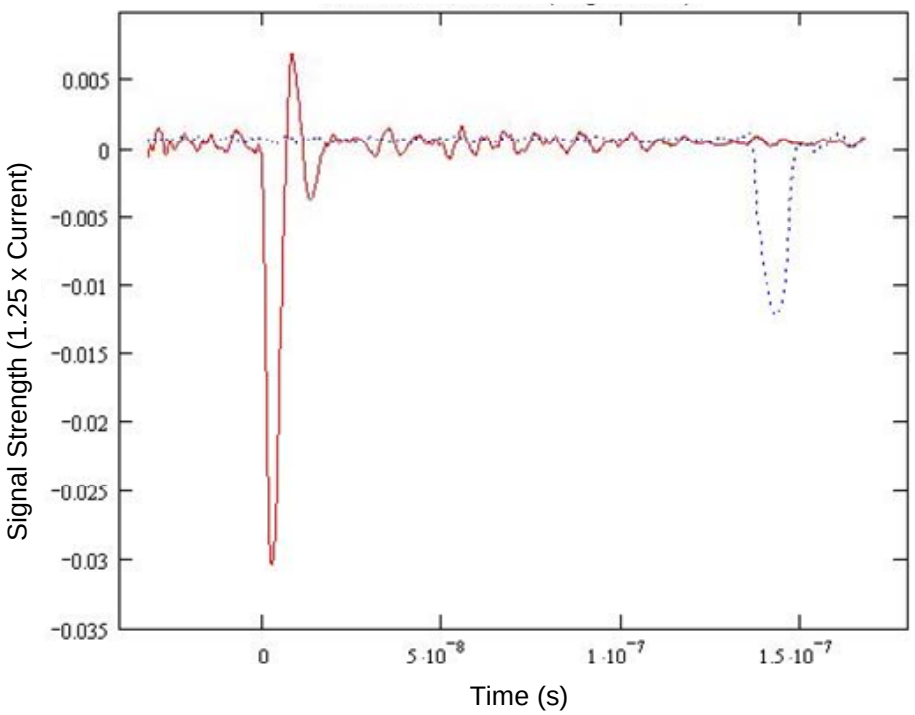

Fig. 30. Typical parabolic beam current measured by upstream (red) and downstream (blue) Bergoz fast current transformers. Note that the beam expands and the peak current decreases while approximately preserving the parabolic pulse shape

	Upstream Charge	Upstream Current	Upstream Length	Downstream Charge	Downstream Current	Downstream Length
Set 2	0.1152 nC	24.0 mA	3.401 ns	0.1184 nC	10.4 mA	7.717 ns
Set 3	0.1074 nC	24.8 mA	3.401 ns	0.1184 nC	10.4 mA	7.717 ns

Table 7. Upstream and Downstream Bergoz FCT Data. Upstream Bergoz FCT was located at 0.626 m, downstream Bergoz FCT at 7.697 m. Net charge was found by integrating over the entire recorded data set for each location. Currents are peak current measured in each data set. Bergoz FCT gives data as voltage, and the conversion factor is 1.25 V/A. Upstream length shown is length recorded at BPM 0 (0.826 m), because length found from upstream Bergoz FCT data is not consistent with other lengths measured. Only data sets 2 and 3 are shown; Set 1 was a trial run, set 2 immediately preceded taking the BPM data, and set 3 immediately followed taking the BPM data. All data used was internally averaged over several shots by the Lecroy scope.

$$I(z,s) = I_0\left(1 - \frac{z^2}{z_m^2}\right) \tag{41}$$

where I_0 is the peak current in the bunch, z is the position in the bunch, and z_m is the bunch half length. If the total charge in the bunch is constant and the beam length is changing, then I_0 must be a function of distance traveled, or equivalently, of beam length. The bunch length and peak current at two locations will be related by

$$\frac{I_0(1)}{I_0(2)} = \frac{z_{BL}(2)}{z_{BL}(1)}, \tag{42}$$

where z_{BL} is the bunch length measure in any system (FWHM, RMS, etc.). The beam in UMER expanded from 3.401 ns to 7.717 ns. This expansion ratio of 2.27 agrees well with the observed 2.35 factor of reduction in peak beam current, suggesting that beam loss was negligible.

Typical beam expansion results are shown in Fig. 31 for the FWHM and the 10%-10% beam length. Note that while both data sets show the same overall dependence, the lower curve, corresponding to the FWHM length, shows several discrepancies. First, the data point at 62 cm is significantly above the value expected based on the other data points. During this experiment, two different scopes were used, with the faster scope being used for BPM data, and the slower scope being used for Bergoz FCT data. In addition, the data from the first Bergoz FCT showed more ringing than most of the other data sets (Fig. 32). BPM 8, located 6.42 m from the cathode, also exhibited severe ringing in this experiment, which is probably responsible for the artificially low beam length reported there (Fig. 33). Note that

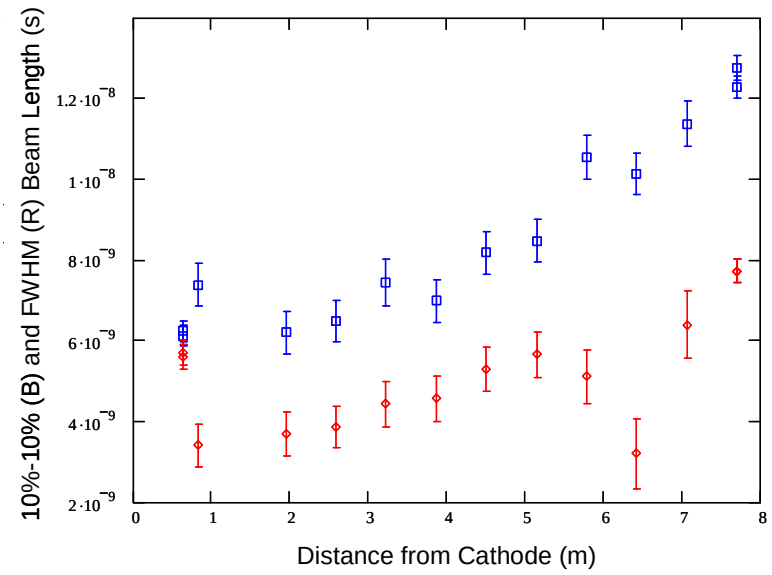

Fig. 31. Beam length vs. distance traveled. Red diamonds indicate FWHM length, and blue squares indicate 10% lengths. FWHM data and 10% length data were calculated from the same measured beam traces. Vertical scale is beam length in seconds and horizontal scale is distance traveled in meters.

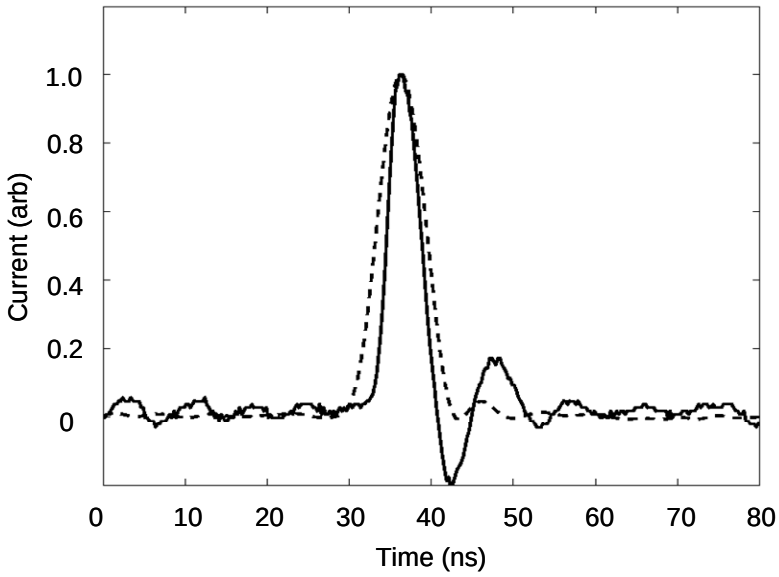

Fig. 32. Beam profile at Bergoz fast current transformer (solid) and at BPM 6 (s = 5.14 m, dash). Curves are scaled to provide equal height to emphasize changes in pulse shape.

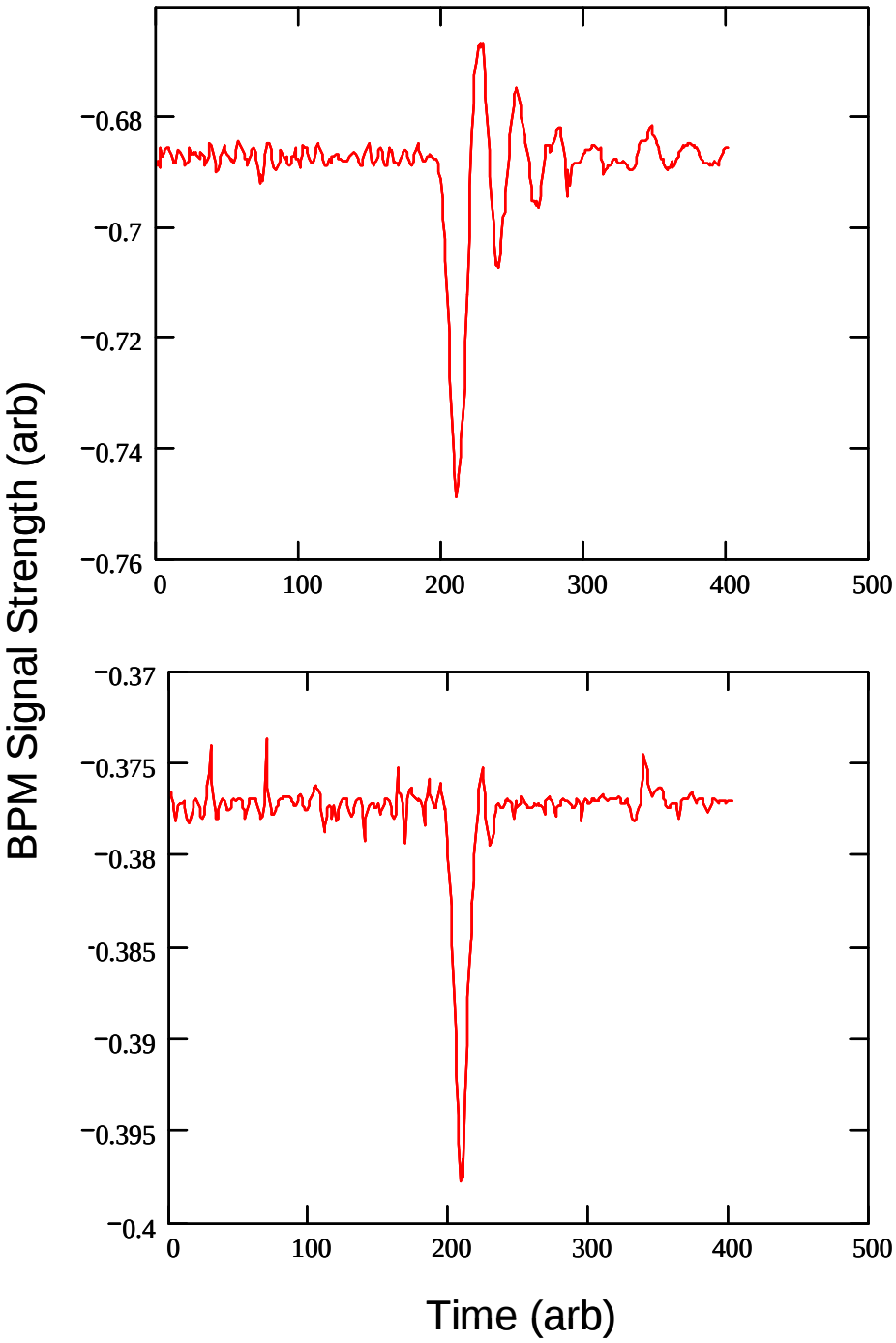

Fig. 33. Signals from BPM 8(T+B) (top) and BPM 7(T) (bottom). Notice significant ringing in BPM 8 trace.

for both the first Bergoz FCT and BPM 8, the anomalous pulse length measurements were only seen in the FWHM length, but not in the 10%-10% length, both of which were extracted from the same data set. This indicates that the detector issues are causing changes in the observed pulse shape, not just the observed pulse length, since the proportionality relations of Table 6 seem not to hold for the anomalous data points.

During the experiment, it was observed that the Bergoz FCT and several of the BPMs closest to the gun showed a sinusoidal "noise" signal even before the arrival of the electron beam (Fig. 34). The average amplitude of this noise signal was taken into account when estimating the experimental error. When the photoinjection laser was blocked, so that no electron beam was produced, this signal remained, but it would disappear when the pulser system was disabled. On detectors further downstream, the signal became much fainter. This suggests that the noise source was the UMER pulser. Data from the upstream Bergoz FCT and BPMs 0, 1, and 2 was analyzed with a fast Fourier transform in Mathcad, which revealed that the signal's frequency content peaked at around 150 MHz to 200 MHz. Note that this is approximately the frequency of the density modulation seen in the UMER beam when the gun is operating in the triode amplifying regime, as will be discussed in Chapter 4.

To compare the data to the longitudinal envelope equation, the FWHM data was plotted against the expected FWHM length calculated from the longitudinal envelope equation (Fig. 35). To obtain the theoretical curve, 24 mA current, 10 keV

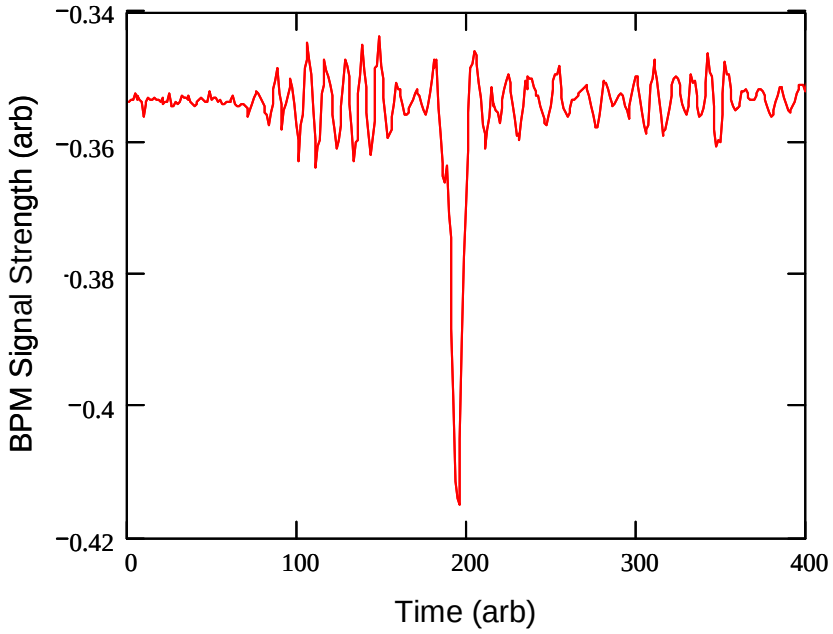

Fig. 34. Data from BPM 0 (IC2) (0.826 m).

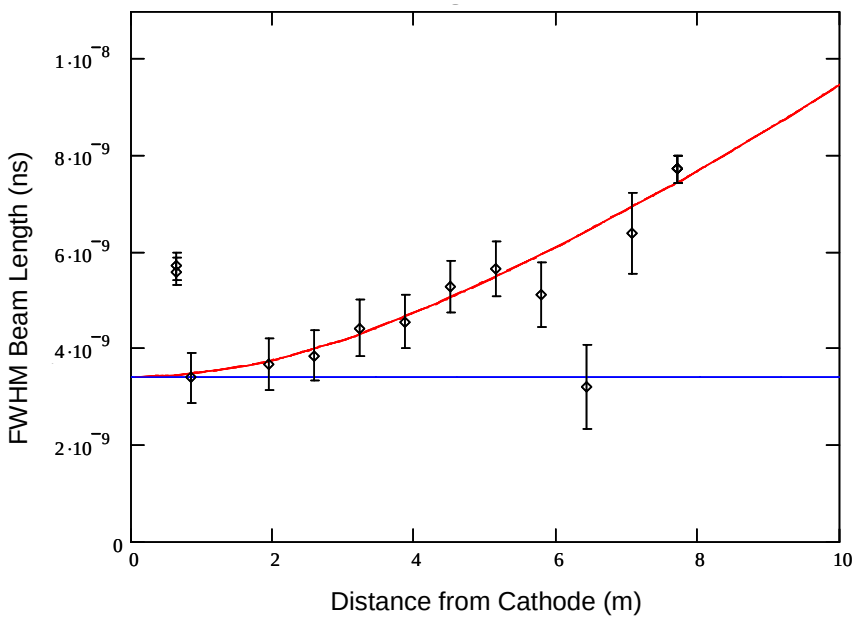

Fig. 35. Comparison of FWHM data to FWHM beam length calculated from longitudinal envelope equation. A beam radius of 1.7 cm (g = 3.189) was used, with all other parameters having their standard values.

energy, 3.4 ns initial FWHM length, an initial longitudinal divergence (dz/ds) of zero, and a geometry factor of 3.189 were used. This geometry factor corresponds to a beam diameter of 1.7 cm, a beam pipe diameter of 5.08 cm, and an alpha of 1. Since no phosphor screen pictures were taken, the actual beam diameter is unknown. To show the effect of varying alpha, the same data is plotted with the geometry factor reduced by 0.5 and 1 to simulate changes in alpha (Fig. 36). From this graph it is clear that this experiment does not yet have the resolution to determine alpha, although with a longer beam (and therefore smaller relative errors) and multiturn operation, it should be possible.

In these experiments, the peak beam current was limited to 25 mA. This is a result of the limitations associated with the photoemission system used in UMER. In order to produce beams which are parabolic in shape, the cathode must be operated at low temperature in order to suppress thermionic emission. However, the Eimac Y-646B cathode used in UMER was designed for thermionic emission, and therefore for operation at higher temperatures. At low temperature, the cathode becomes contaminated more quickly, and the rate of replenishment of barium on the surface of the cathode is also reduced. The result is that the quantum efficiency of the cathode falls over time, and therefore the current falls also (Fig. 37). In order to maintain a given current, it was necessary to continually raise the applied laser power. The longer the experiment took, the greater an increase in laser power would be required, and the lower the current that could be sustained throughout the experiment. A 25 mA current could be sustained during an experiment, but only if the only measurements taken were on the relatively quick BPMs and Bergoz FCTs. The 25

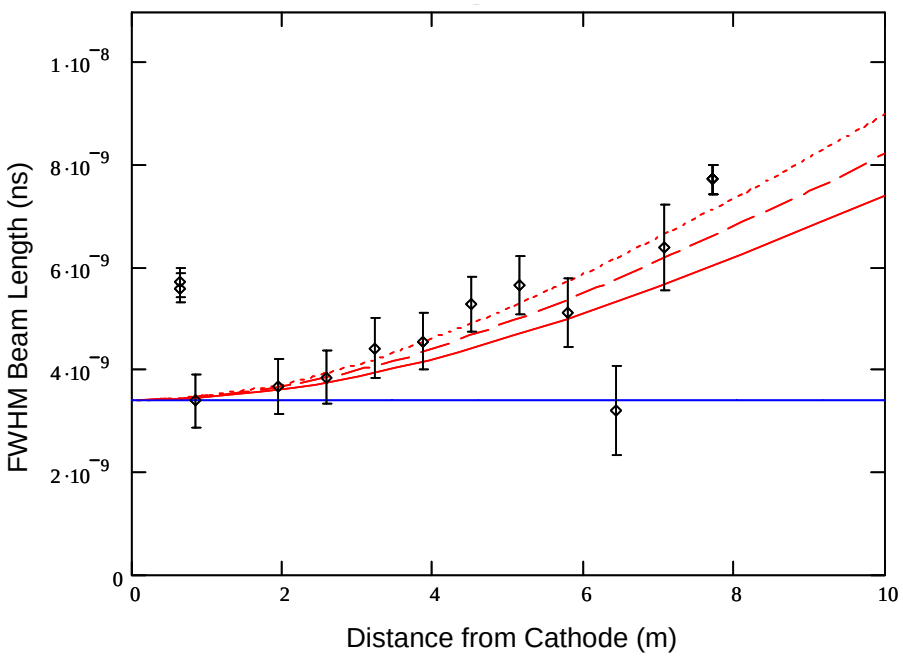

Fig. 36. Effect of varying alpha. Dotted line is alpha of 1, dashed line is alpha of 0.5, solid line is alpha of 0. All other parameters standard.

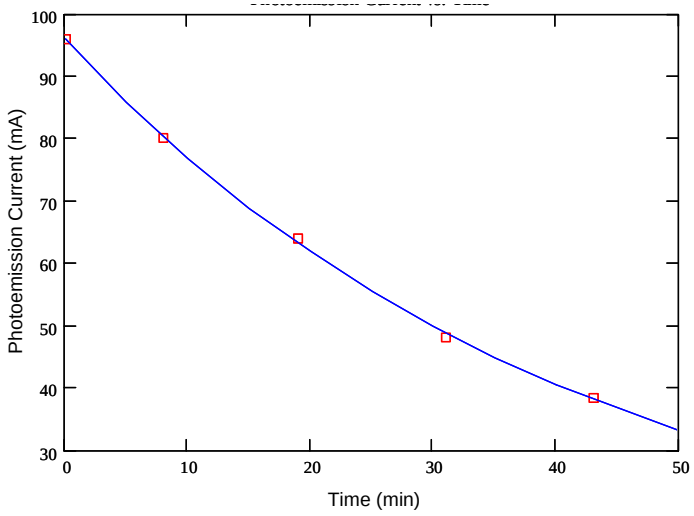

Fig. 37. Measured the decay in photoemission current, as seen at the first Bergoz fast current transformer. The data is shown with the red boxes, while the blue line is an exponential fit to the data. In this experiment, the fit was given by:

$$I(t) = 90.899 \times \exp(-0.024t) + 5.051 \quad \text{mA}.$$

Time is measured in minutes.

mA current could not be sustained for long enough to use phosphor screens along the beamline to measure the beam radius because of the extra time needed to raise and lower the phosphor screen mounts. An 85 mA beam could not be sustained long enough even if only current measurements were taken. As a result, only 25 mA data is presented, and while the geometry factor can be measured experimentally, theoretical values for comparison must be based on beam radius values predicted from envelope codes or experiments with beams having very different longitudinal profiles. As a result, while the data does agree well with the longitudinal envelope equation, future near-term experiments on parabolic beams in UMER should be carried out using the filter technique developed by I. Haber. This will also have the benefit of providing a longer parabolic pulse, which will reduce the relative error in measuring the beam length. A longer term solution is the development of low-temperature dispenser photocathodes, which is currently in progress at Maryland [3].

3.4. One-Dimensional Cold Fluid Model

The longitudinal envelope equation was developed specifically to describe the evolution of beams whose longitudinal current distribution is parabolic. However, the beams used in many applications do not have a parabolic distribution. Beams with rectangular line charge profiles are of particular interest. For induction linacs, rectangular line charge profiles would provide a constant impedance, which increases efficiency [55]. In UMER, the standard beam profile is rectangular, both to simulate the beams produced by induction linacs, and to provide a constant background current for studying the propagation of space charge waves [56].

To describe the evolution of intense rectangular beams, the one-dimensional cold fluid model is often used. In this model, the beam is described by two equations, which are analogous to the equations used to describe the evolution of cold, compressible fluids. The first of these equations is the one-dimensional continuity equation

$$\frac{\partial \lambda}{\partial t} + \frac{\partial}{\partial z} v\lambda = 0, \tag{43}$$

where λ is the line charge density, t is time, z is the longitudinal position in the beam, and v is the particle velocity within the beam. This equation can be derived from the familiar three-dimensional continuity equation

$$\frac{\partial \rho}{\partial t} + \vec{\nabla} \cdot \vec{J} = 0 \tag{44}$$

by assuming that at a particular location the beam has a constant cross-sectional area A and a velocity v, and using relations for line charge density ($\lambda = A\rho$) and current density ($J = \rho v$).

The second equation used in the cold fluid model is the momentum equation, which relates particle velocity v in the beam to the local electric field due to space charge. The electric field due to space charge, in the long-wavelength limit, is

$$E_z = -\frac{g}{4\pi\varepsilon_0\gamma^2}\frac{\partial \lambda}{\partial z} \tag{45}$$

as derived in Appendix A. The space charge field will result in an acceleration $\frac{dv}{dt}$, which is the sum of a stationary term $v\frac{\partial v}{\partial z}$ due to particle flow through regions with

different properties, and a nonstationary term $\frac{\partial v}{\partial t}$ due to flow changes at any given location [45,57]. Newton's second law gives

$$\frac{F}{m_l} = \ddot{z} = \frac{\partial v}{\partial t} + v\frac{\partial v}{\partial z} = \frac{q}{m\gamma^3}E_z, \tag{46}$$

where $m_l = m\gamma^3$ is the longitudinal mass of the particles in the beam. Eq. (46) becomes the momentum equation [58,59]

$$\frac{\partial v}{\partial t} + v\frac{\partial v}{\partial z} = -\frac{qg}{4\pi\varepsilon_0 m\gamma^5}\frac{\partial \lambda}{\partial z}. \tag{47}$$

Together, the continuity and momentum equations fully describe the evolution of an intense (cold) beam. To solve these equations, the method of characteristics may be used. This method was originally developed to describe supersonic gas flow, and calculates the evolution of a fluid by considering the effects of incremental changes in the fluid state as they propagate through the fluid as waves [60-62]. In the case of a beam with rectangular line charge density, the particles far from the beam ends will experience no net force because the line charge density is constant, and therefore the longitudinal electric field is also zero. At the beam ends, the line charge density changes very rapidly, resulting in a very strong electric field (Fig. 38). This can be seen intuitively by recognizing that the particles far from the beam ends experience the electric field contributions from other particles both ahead and behind them in the beam, and so those contributions should tend to cancel out. Particles at the beam ends only experience the electric field contributions from one side, resulting in a strong net field.

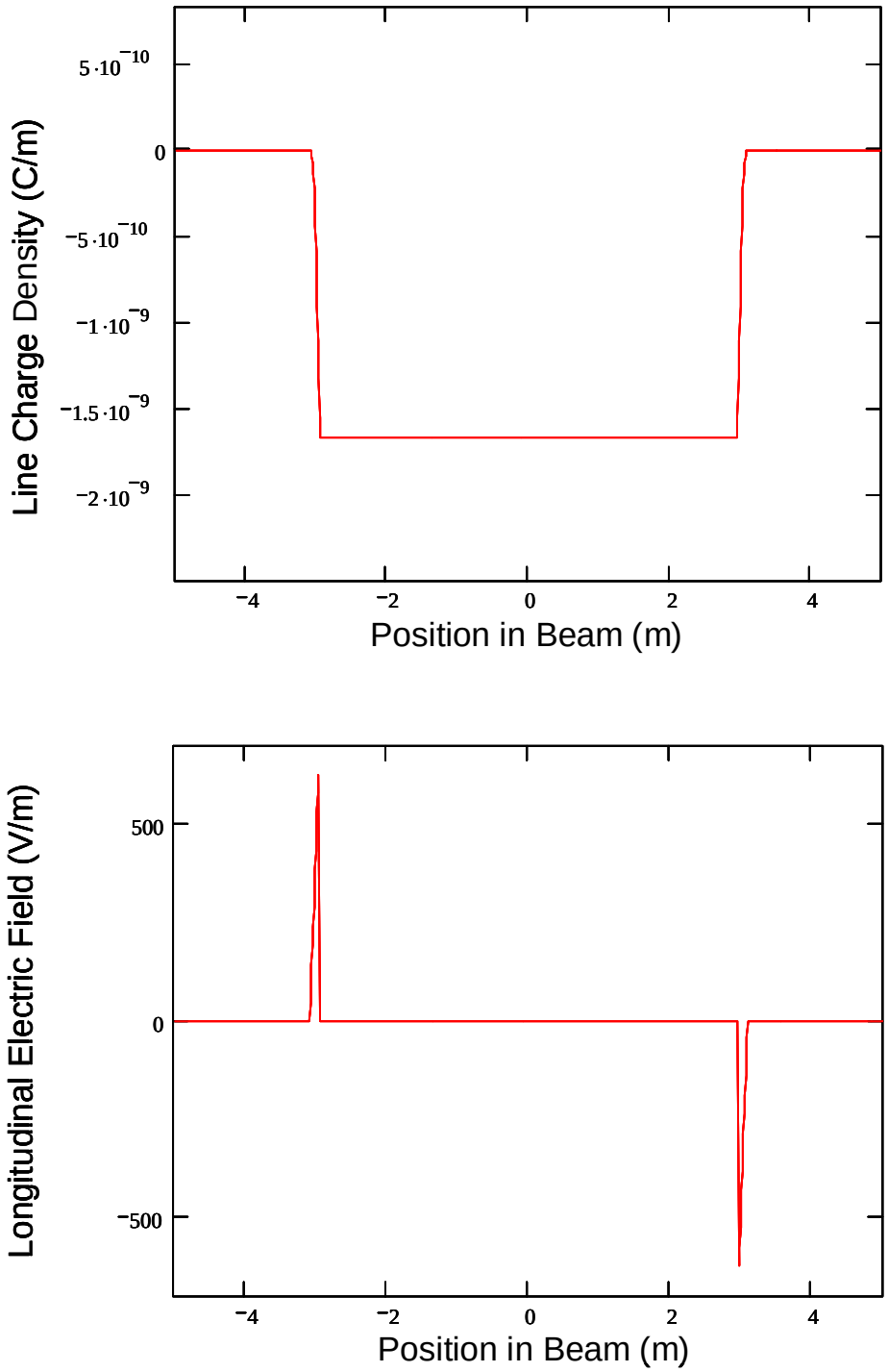

Fig. 38. Line charge density and longitudinal electric field for a 100 mA beam traveling at 0.2 c, g of 3. Beam began as rectangular pulse and expanded for 1 m.

An analogous situation occurs in compressible fluids, where the fluid is separated from a region of vacuum by a thin foil (Fig. 39). When the foil is ruptured, the fluid will flow into the vacuum at a rate known as the escape velocity. This depletes the fluid density near the old fluid-vacuum boundary. A shock wave traveling at the speed of sound in the fluid will flow back into the bulk of the fluid. This shock wave can be thought of as carrying the information that the fluid is undergoing expansion into the vacuum. In the region between the vacuum and the shock wave, the fluid density will be reduced compared to its initial value. This process is known as cavitation [45]. When the method of characteristics is used to solve the continuity and momentum equations for an initially rectangular beam, a similar effect occurs [58,59]. The beam expands by launching particles into the vacuum at its escape velocity and launching a wave into the bulk of the beam at the sound speed. In a charged particle beam, the sound speed is given by [58,63]

$$c_0 = \sqrt{\frac{Zqg\lambda_0}{4\pi\varepsilon_0 m\gamma^5}}, \tag{48}$$

where Z is the charge state of the particles in the beam (1 for electrons), q is the fundamental charge, m is the mass of the particles, g is the geometry factor, and λ_0 is the initial line charge density of the beam. In UMER, the sound speed is on the order of 10^6 m/s. Notice that any change in beam radius will affect the geometry factor, and result in a change in the sound speed. In fact, in UMER the beam radius will change due to the quadrupole focusing used for transverse focusing of the beam. However, the timescale for longitudinal evolution of the beam is much greater than the timescale for transverse evolution of the beam, and so it is assumed that these

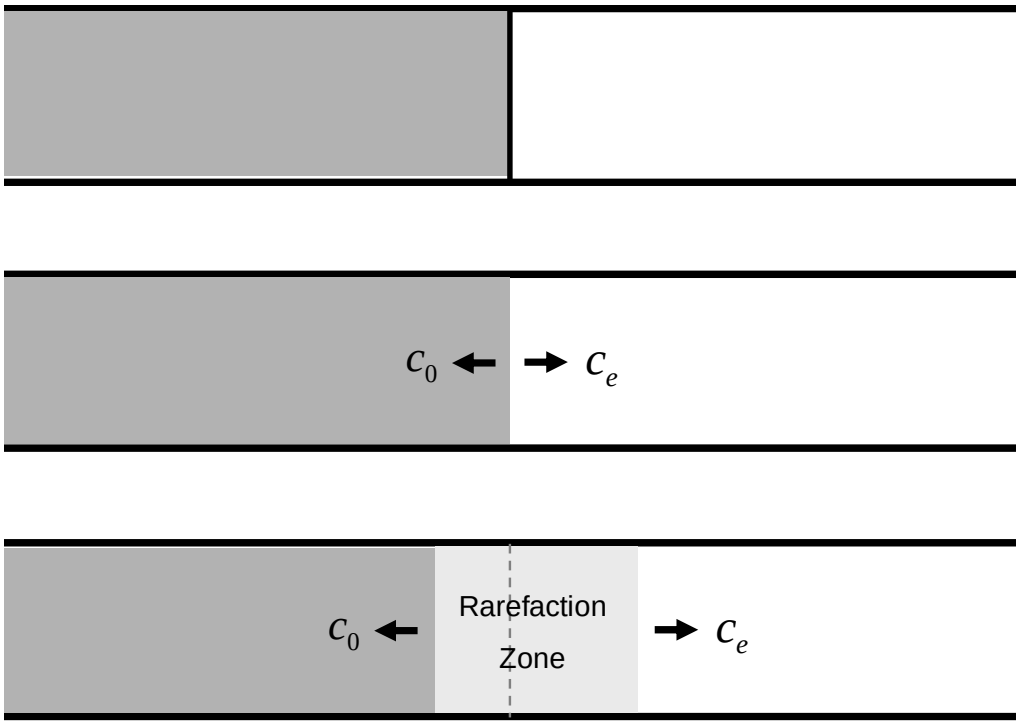

Fig. 39. Cavitation.

quadrupole "breathing modes" of the beam average out when considering the longitudinal dynamics. This will be addressed experimentally in section 3.5.2.

In general, the sound speed and the escape velocity are related, and this relation is based on fundamental properties of the fluid concerned [61]. In the case of an electron beam, the escape velocity is twice the sound speed [63]. The method of characteristics can be used to calculate the line charge and particle velocity for a beam expanding in this way [58,59]; the results are given here for the three regions of the expanding beam in the beam frame:

Zone I (Dead Zone) $$\lambda = \lambda_0 \tag{49}$$

$$v = v_0 = 0 \tag{50}$$

Zone II (Rarefaction Zone) $$\lambda(z,t) = \left(\frac{2}{3} \pm \frac{1}{3} \frac{z \pm z_0}{t c_0} \right)^2 \lambda_0 \tag{51}$$

$$v(z,t) = \frac{2}{3} \left(\frac{z \pm z_0}{t} \mp \sqrt{\frac{Zqg\lambda_0}{4\pi\varepsilon_0 m}} \right) \tag{52}$$

Zone III (Vacuum) $$\lambda = 0 \tag{53}$$

In these equations, λ_0 is the initial line charge density of the rectangular pulse, v_0 is the initial (beam frame) velocity of the particles, z is the location in the beam measured from the beam center, z_0 is the initial half length of the beam, and t is time measured from the beginning of the expansion. Since the beam has both a head and a tail undergoing expansion, the $\pm$ and $\mp$ symbols are used; the upper symbol is used for erosion from the rear end (tail), while the lower sign is used for erosion from the

front end (head). The signs used here differ slightly from those used elsewhere, because we take z_0 to always be positive. These curves are plotted for a sample case in UMER in Fig. 40.

Eventually, the two shockwaves traveling towards the center of the beam at the sound speed will meet. When this occurs, the flat top will have entirely eroded, and the line charge density will form a cusp at the beam center. After this occurs, the shockwaves will overlap, and the beam evolution becomes nonlinear. Only an approximate solution is possible after this time, and that solution is given elsewhere [60,63].

3.5. Expansion of Rectangular Beam in UMER

In this section, we describe experiments on the longitudinal expansion of beams in UMER with initial line charge distributions that are close to rectangular in shape. The expansion of such beams should be described by the cold fluid model discussed in the previous section. We will show that the cold fluid model is a good approximation for the behavior of these beams.

3.5.1. Expansion of Matched Beam

The longitudinal expansion of intense initially-rectangular beams is a subject of great importance for the ultimate success of the UMER project. This is the standard longitudinal beam profile used in UMER, and it is the expansion of such beams that longitudinal focusing will ultimately have to correct in UMER. In order to properly design a longitudinal focusing system, it is critical to first understand how these beams evolve, so that the correct fields can be applied to focus the beam

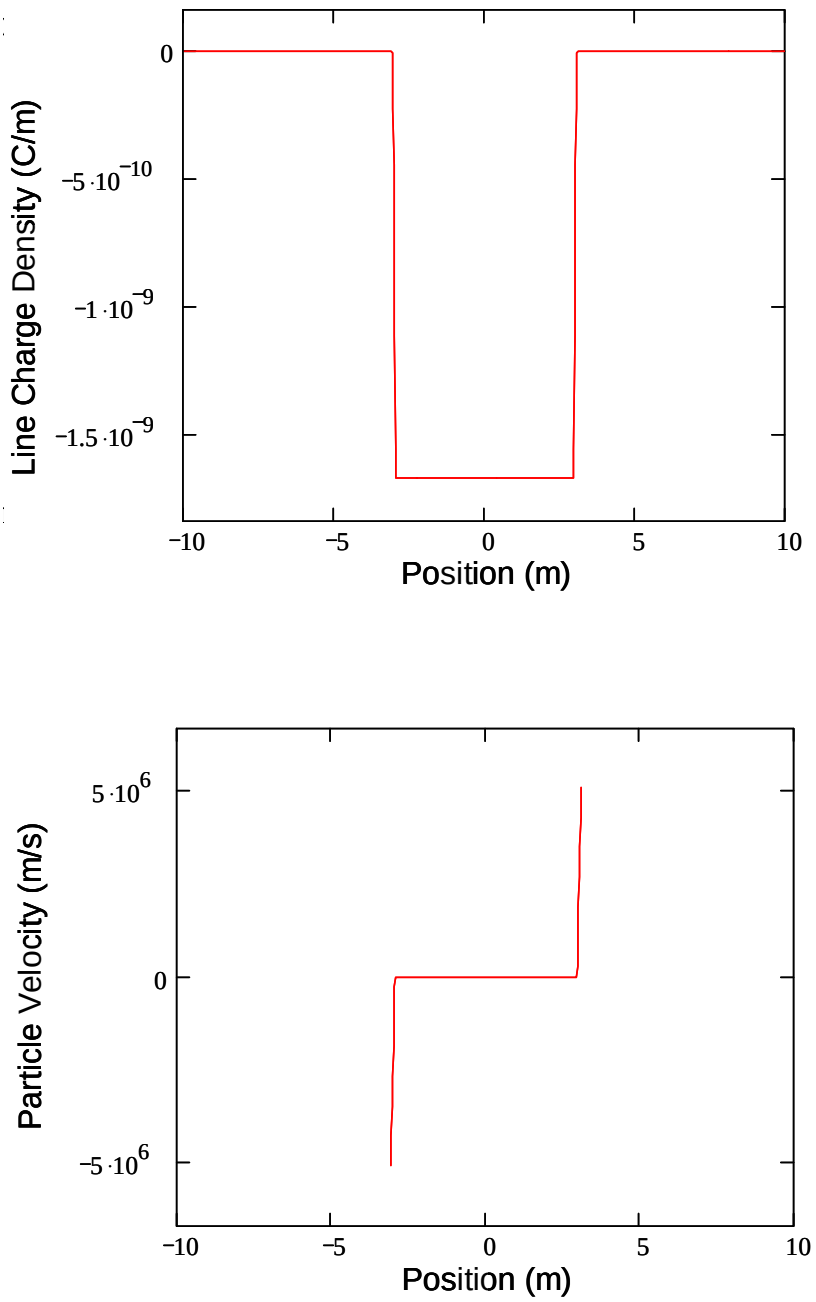

Fig. 40a. Line charge density and particle velocity for a 100 mA, 6 m long beam which has traveled for 1 m. Beam velocity is 0.2 c, g = 3.

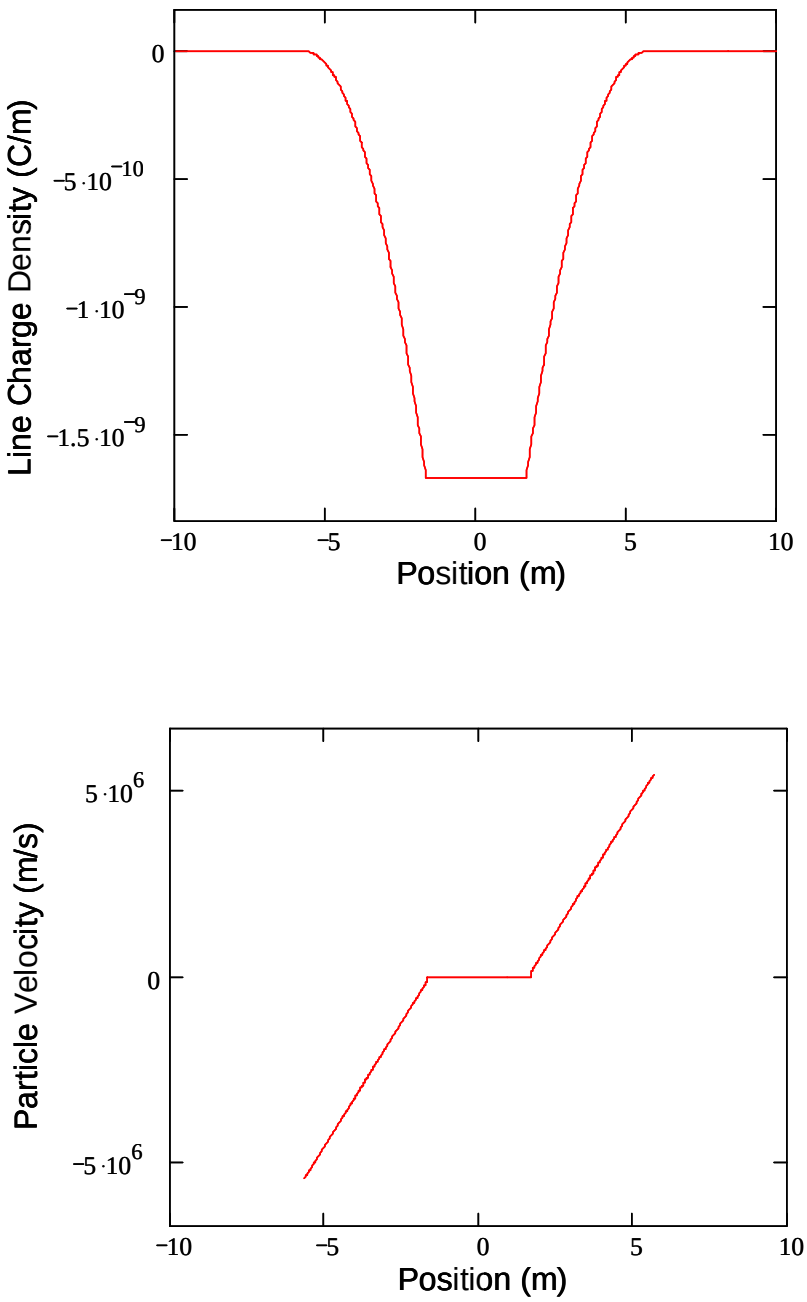

Fig. 40b. Line charge density and particle velocity for a 100 mA, 6 m long beam which has traveled for 30 m. Beam velocity is 0.2 c, g = 3.

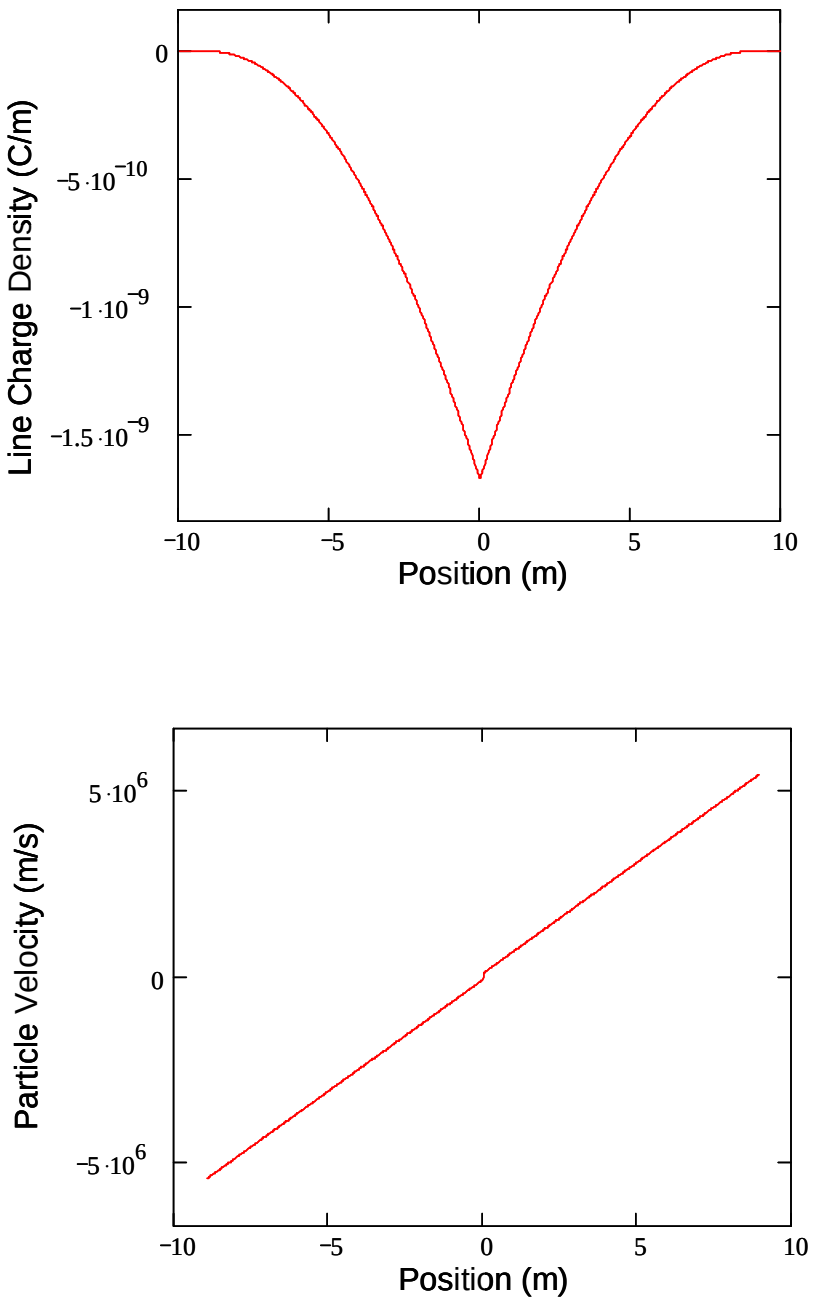

Fig. 40c. Line charge density and particle velocity for a 100 mA, 6 m long beam which has traveled for 67 m. Beam velocity is 0.2 c, g = 3.

without inducing harmful space charge waves or emittance growth. Some previous experimental work has been done on the longitudinal expansion of intense beams with initial rectangular line charge distributions. Prior experiments have looked at both the changes in the beam current profile [64-65] and the beam velocity distribution [33,66] as it evolves under space charge forces. In these experiments, the cold fluid model was found to give a good description of the expansion of these beams. However, there are several important reasons to study these beams in UMER as well. UMER offers a longer propagation distance for the beam than previous experiments with electrons. This allows the beam to expand further, and therefore to make measurements on the expanded beam profile easier and more reliable. Previous experiments were conducted on machines with electrostatic quadrupole focusing [64] or solenoid focusing [33,58,65], while the cold fluid model itself assumes a beam with uniform radius. Because there is coupling between the longitudinal and transverse dynamics, notably through the geometry factor, it is conceivable that the transverse focusing system may affect the longitudinal dynamics. In addition, UMER has more diagnostics, and better diagnostics, than any previous experiment on longitudinal beam expansion. But the most important reason to verify the descriptions for longitudinal beam expansion in UMER is because these descriptions will be critical in designing a longitudinal focusing system for UMER, which in turn will be required for achieving high-revolution operation without beam loss.

For these experiments on UMER, standard 100 ns long beams with currents of 25 mA, 85 mA, or 100 mA were used. These beams were produced from the UMER gun by aperturing the full 100 mA beam from the gun down to the desired current.

This allowed the gun to operate in space charge limited mode, which provides stable, reproducible beams, and which is the mode in which the gun was originally intended to operate. Standard beam currents were used not only because that allowed the most stable operation, but also because that allowed the use of transverse focusing settings developed by H. Li, S. Bernal, and M. Walter during their transverse beam transport experiments. Early longitudinal expansion experiments on UMER [66] concentrated on 25 mA and 85 mA beams because of the lack of good matching solutions for the more intense 100 mA beam. Later experiments concentrated on 100 mA beams after the UMER group developed more experience with matching those beams. Operation with the 100 mA beam is more challenging because the beam will expand faster and will have larger coherent energy spread due to longitudinal space charge, and will have larger radius and therefore be more susceptible to image charge forces that tend to distort the beam transverse profile and affect the longitudinal dynamics through longitudinal-transverse coupling.

For longitudinal experiments on UMER, the primary diagnostics used were the BPMs and the injection Bergoz FCT. During early experiments, the extraction section was also present on the UMER beamline, and the extraction Bergoz FCT was also in use. Phosphor screens were also available in the beamline for measuring the beam radius, but in early experiments, beam radius values were obtained from beam transport and matching codes used by H. Li for use in calculating the geometry factor. During later experiments with the more intense 100 mA beam for which matching is more difficult, more use was made of the phosphor screens, together with image analysis software developed by R. Feldman, to extract beam radius values (Fig. 41).

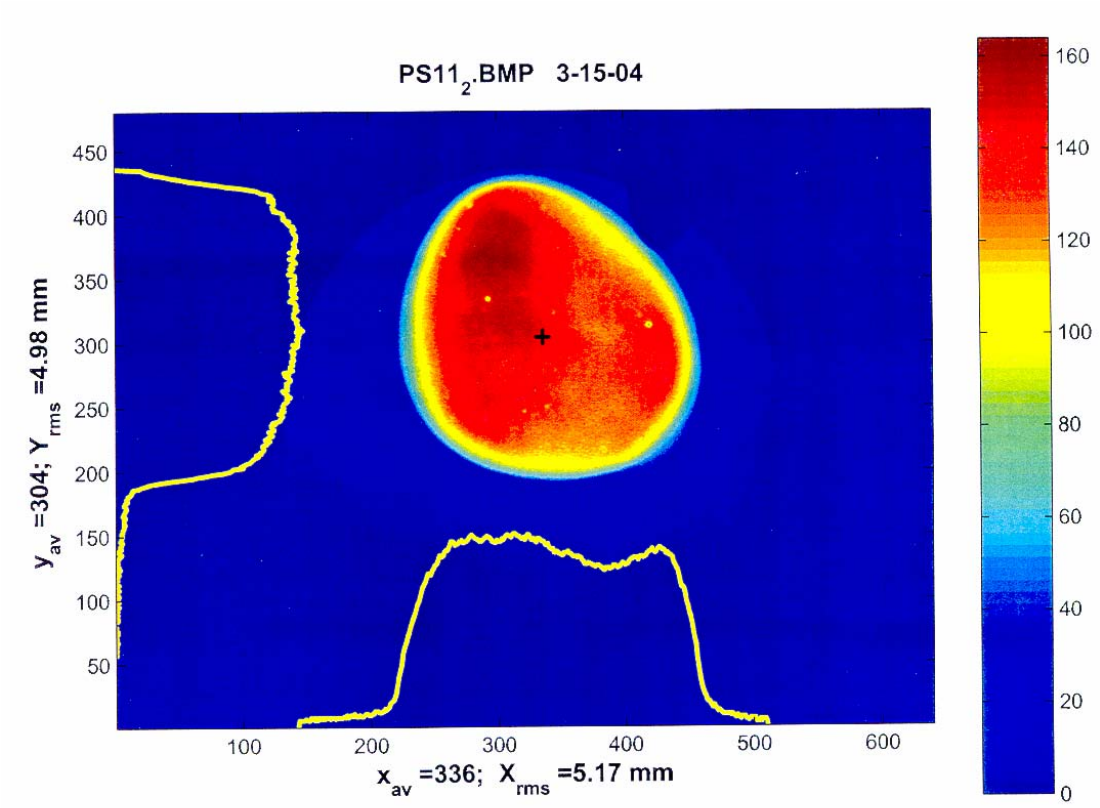

Fig. 41. Typ. false color beam image from R. Feldman software.

Unfortunately, energy analyzers were not available on UMER during these experiments, preventing direct measurement of beam velocity changes due to longitudinal space charge forces as predicted by the cold fluid model.

Most prior experiments on longitudinal expansion of intense beams compared the theoretical predictions and the experimental results by plotting both on the same axes to facilitate a qualitative comparison. In order to obtain a more quantitative comparison, we chose to measure the beam length and rise time, and compare these values to those predicted by the cold fluid theory. In order to avoid complications introduced by detector ringing and other effects at the head and tail that might obscure the behavior of the beam, we chose to use the 80% and 20% current levels. This provides two measures of beam length (20%-20% length and 80%-80% length) and two measures of rarefaction zone length (80%-20% rise time [head] and 80%-20% rise time [tail]) (Fig. 42). These beam lengths can be derived from Eq. (51), and are found to give

$$\tau_{80-20}(s) = \frac{3(0.447)c_0}{c^2\beta^2}s \tag{54}$$

for the 80%-20% rise times,

$$\tau_{20-20}(s) = \tau_0 + \left|6\left(\sqrt{0.2} - \frac{2}{3}\right)\right|\frac{sc_0}{c^2\beta^2} \tag{55}$$

for the 20%-20% beam length, and

$$\tau_{80-80}(s) = \tau_0 - \left|6\left(\sqrt{0.8} - \frac{2}{3}\right)\right|\frac{sc_0}{c^2\beta^2} \tag{56}$$

for the 80%-80% beam length. All lengths are quoted in units of seconds, s is the distance from the cathode, c_0 is the sound speed, and τ_0 is the initial beam length in

seconds. These equations assume that the initial length of the rarefaction regions or beam ends is zero; in fact, experiments indicate that this length is less than approximately 1.5 ns.

Figure 43 shows typical results for the 80%-20% rise time at the head of 24 mA and 85 mA beams in UMER. The data shown was taken in experiments over approximately 7.7 m of the UMER beamline, including the injection section, 9 ring sections, and the extraction section. Beam measurements were made using injection and extraction Bergoz FCTs, and eight BPMs; the BPM at 5.78 m was not available during this experiment. The 80%-20% rise time at the head was extracted from the data for the two beams, and found to increase linearly with distance from the cathode beyond $s \approx 4m$. This linear dependence is expected, as shown in Eq. (54). Before $s \approx 4m$, the 80%-20% rise time for the 24 mA beam flattens to approximately 1.7 ns, while the rise time for the 85 mA beam flattens to approximately 1 ns. This is believed to be due to the detector resolution, rather than the intrinsic rise time in the beam. In the regions where the rise time exhibits a linear dependence on distance ($s > 4.5m$ for the 85 mA beam and $s > 3.9m$ for the 24 mA beam), a least-squares fit of Eq. (54) to the data was made, holding the geometry factor in the sound speed as the free parameter. The resulting geometry factors (2.82 for the 85 mA beam and 4.25 for the 24 mA beam) were used with the average beam radii (9.5 mm for the 85 mA beam and 5.3 mm for the 24 mA beam, as determined by H. Li from matching codes) to determine experimental values for alpha of $\alpha = 0.85 \pm 0.25$ for the 85 mA beam and $\alpha = 1.12 \pm 0.25$ for the 24 mA beam. (More details on data extraction and error analysis are given in Appendix B.) Note that the data for the 24 mA beam

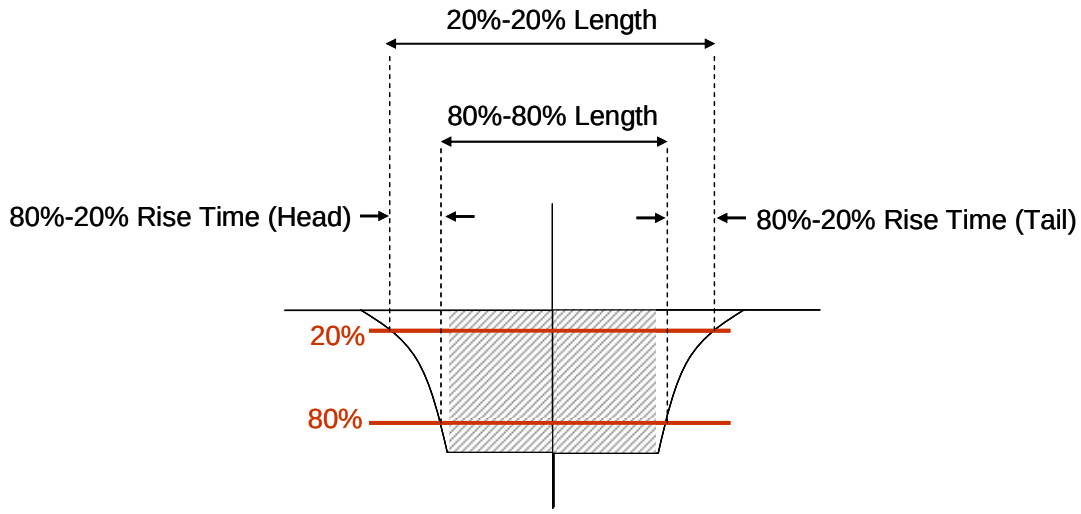

Fig. 42. 80% and 20% quantities.

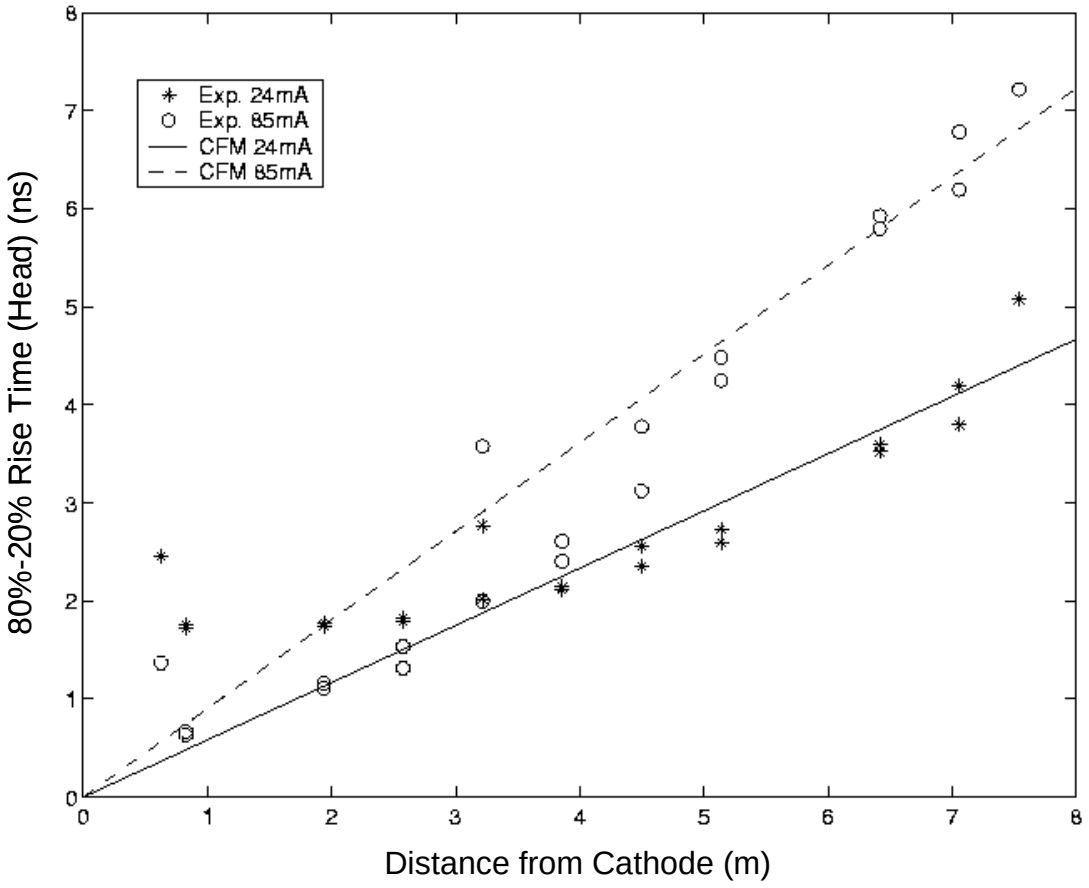

Fig. 43. Typical results for 80%-20% rise time for 24 mA and 85 mA beams. Error at each data point is approximately ± 0.7 ns [66].

makes a smooth transition from a linear dependence far from the cathode to a flat dependence close to the cathode. This smooth transition can be reproduced by adding the theoretical value from Eq. (54) in quadrature with a detector resolution of 1.7 ns; this results in a hyperbolic curve, which is a typical result when detector resolution becomes important. Note also that the first and last data points for each beam seem to give somewhat higher rise times than the adjacent points or the theoretical curve. These points come from data extracted from the Bergoz FCTs, which were used with a different oscilloscope than the BPMs. It is believed that the use of a different oscilloscope accounts for this small discrepancy.

As discussed in this chapter, the geometry factor plays a very important role in longitudinal dynamics. In theory, it is given by Eq. (13), with the value of alpha depending on the assumptions made, as described in Appendix A. For the geometry factor used in the cold fluid model, an alpha of zero is found by assuming that the beam volume charge density is constant and its radius is variable, while an alpha of one is found by assuming that the beam radius is constant and its volume charge density is variable. The former condition is usually assumed for space charge dominated beams, while the latter condition is usually assumed for emittance dominated beams [53]. This suggests that alpha relates to the three dimensional shape of the beam, and therefore also to the potential (configuration) energy stored in the beam. In addition, it suggests that the alpha -- and therefore the energy stored in the beam -- may change as the beam evolves, since our intense beam is expected to have a uniform density (and therefore an alpha of zero), but it must begin life at the cathode with a uniform radius (and therefore an alpha of one). Early in this research,

the question of measuring and interpreting alpha was deemed to be important. However, it became clear that the uncertainty in measurements of alpha in UMER was high, and that the significance of a given measurement was unclear. For parabolic beams, as shown in section 3.3, we are not yet able to determine alpha in UMER, although this is easier in the initially rectangular beam. More significant is the question of measuring the beam radius. In deriving the longitudinal electric field and the geometry factor, the beam is always assumed to have a uniform density in each slice, and to have a well-defined edge. Also the beam is assumed to be on-axis and cylindrically symmetric. In practice, beams often have varying density and halos, and they are rarely on-axis, and are usually not cylindrically symmetric. In order to determine the geometry factor, therefore, the experimenter must make choices about how to measure the beam radius. The choice of beam radius measure -- for example, FWHM or RMS -- will have the effect of modifying the observed alpha [67]. In a system with periodic focusing, the location of phosphor screens in the lattice may also introduce a systematic distortion in the measured radius, which will affect the measured alpha. In addition, the beam radius may vary along the beam length, but phosphor screens do not measure this variation. This will result in a modification to the measured value of alpha compared to its theoretical value. Perhaps most interestingly, the effect of transverse displacement of the beam in the beam pipe or quadrupole breathing modes on the geometry factor are not known. The result of all these effects is to muddy the waters with respect to the significance of alpha. In practice, alpha must be specified experimentally for a given system, for given matching and steering, and for a given beam measurement technique.

Later experiments focused on higher current beams. Typical data from an expanding 100 mA beam in UMER is shown in Fig. 44. During these experiments, several different transverse matching solutions were used. A detailed analysis of the longitudinal expansion of 100 mA beams in UMER using two different matching solutions is given here. These matching solutions used are shown in Fig. 45. In this figure, the RMS beam radius is given as a function of phosphor screen location. RMS radii were extracted from phosphor screen images using image analysis software developed by R. Feldman.

The 80%-20% rise times (head) for the two cases are shown in Fig. 46. The error indicated at each point is ± 0.7 ns, which arises from the sampling rate of the oscilloscope used (see Appendix B). The lines shown are from Eq. 54, with alpha of zero (solid) and one (dash). The logarithmic term in the geometry factor was calculated using twice the average of the RMS radii in x and y as an approximate single hard-edge radius; the relationship $2\tilde{x} = X$ between an RMS radius and a hard-edge radius is correct for beams which have uniform transverse density, and is a good approximation in UMER [1]. As with previous experiments, the agreement between theory and experiment is very good for an alpha of one. Notice that there are no resolution effects in this data as were seen in the 24 mA data. This suggests that the 1.7 ns resolution limit seen in the 24 mA experiment is not due to the intrinsic rise time of the UMER beam, but rather due to intrinsic temporal resolution in the BPMs, and that the BPM resolution improves with higher beam current.

The 80%-80% beam length measurements for the two matching solutions are shown in Fig. 47. The lines are theoretical predictions from Eq. 56, with the

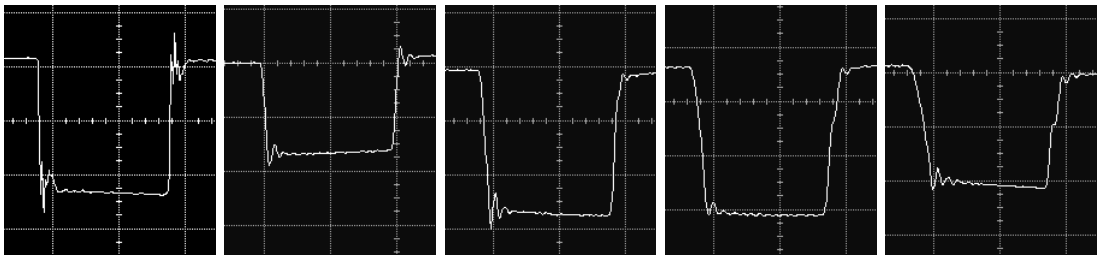

Fig. 44. Typical results for expanding 100 mA beam in UMER.

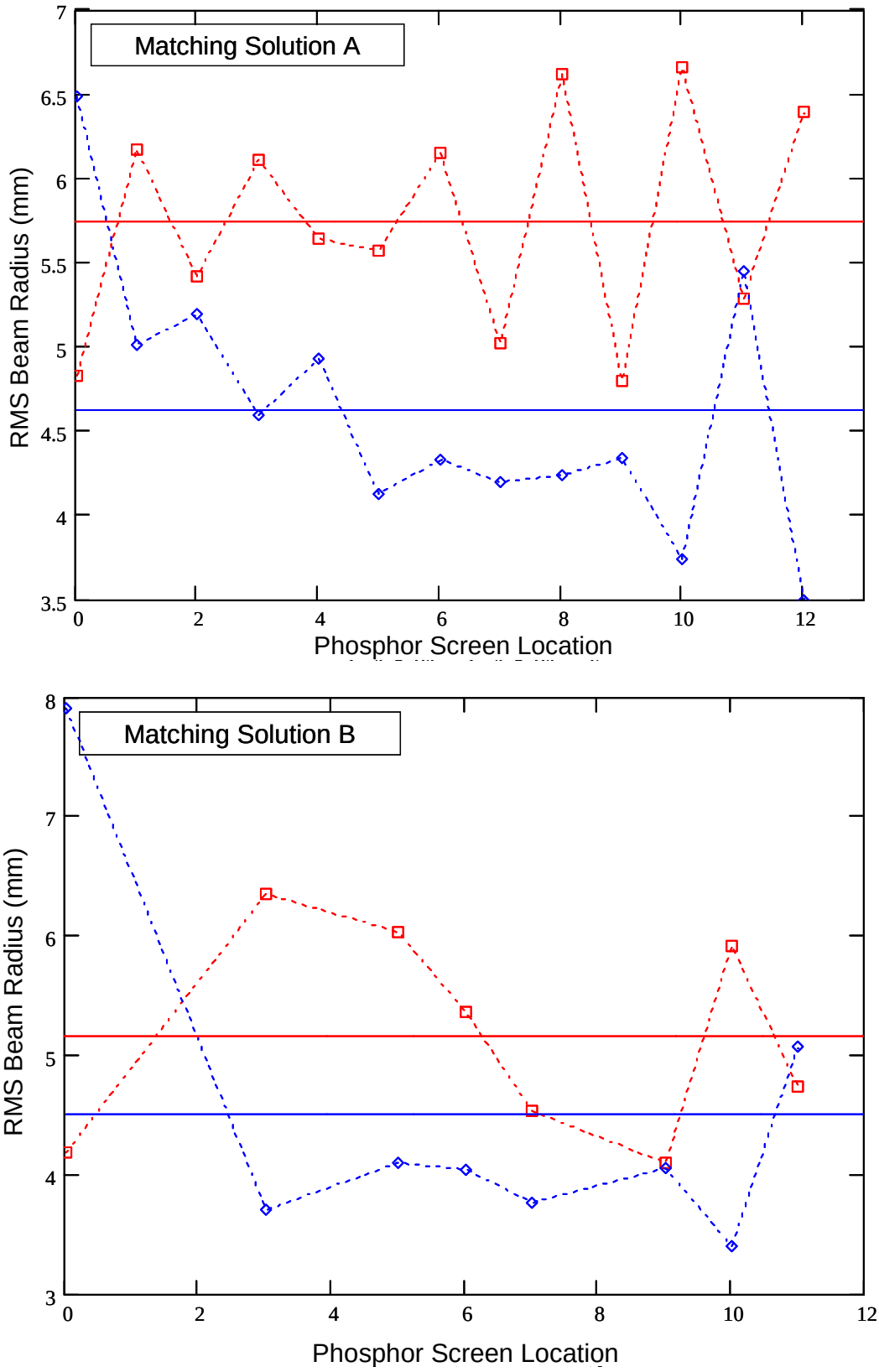

Fig. 45. Two transverse matching solutions in UMER.

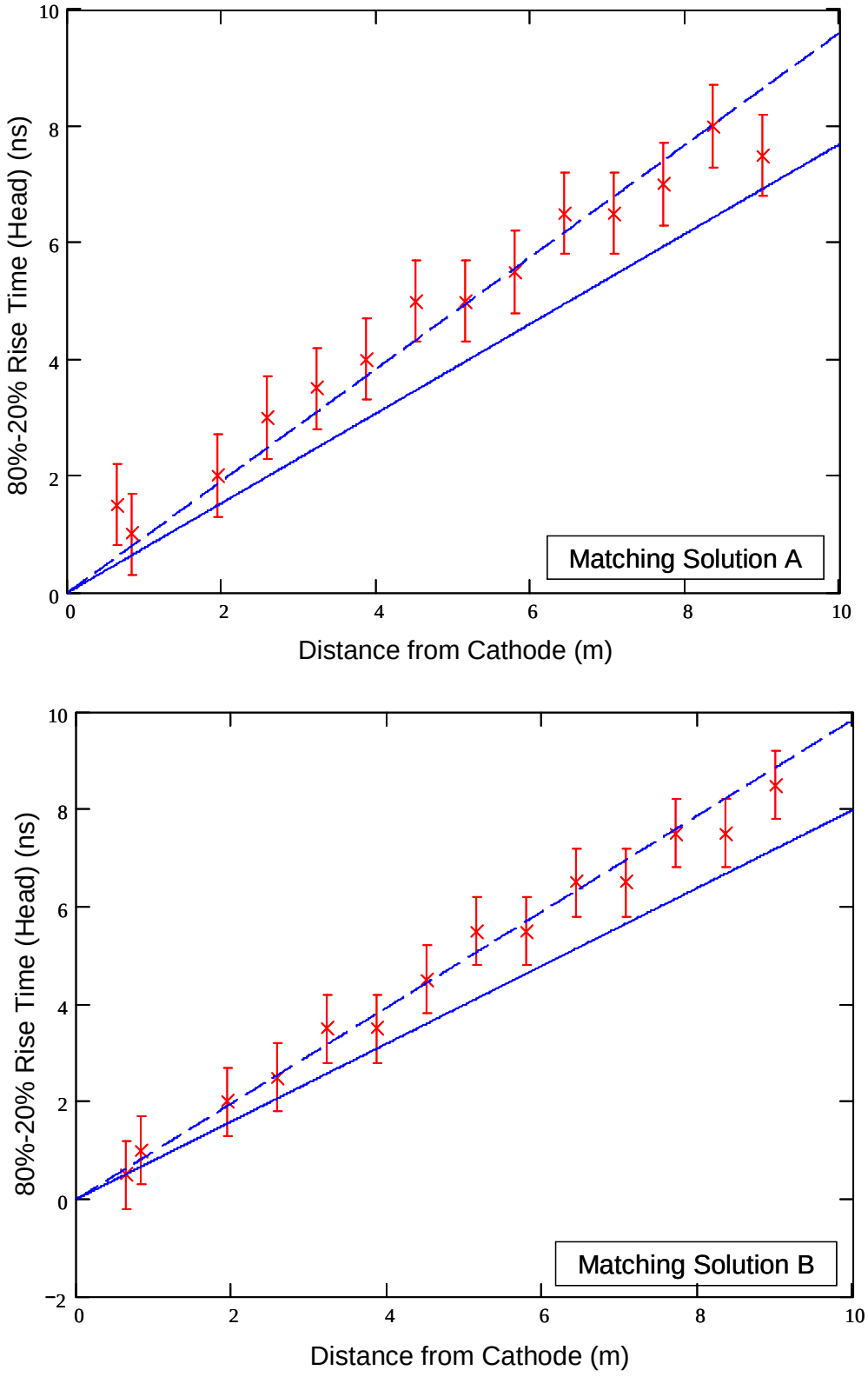

Fig. 46. 80%-20% Rise times (head) for two matching solutions.

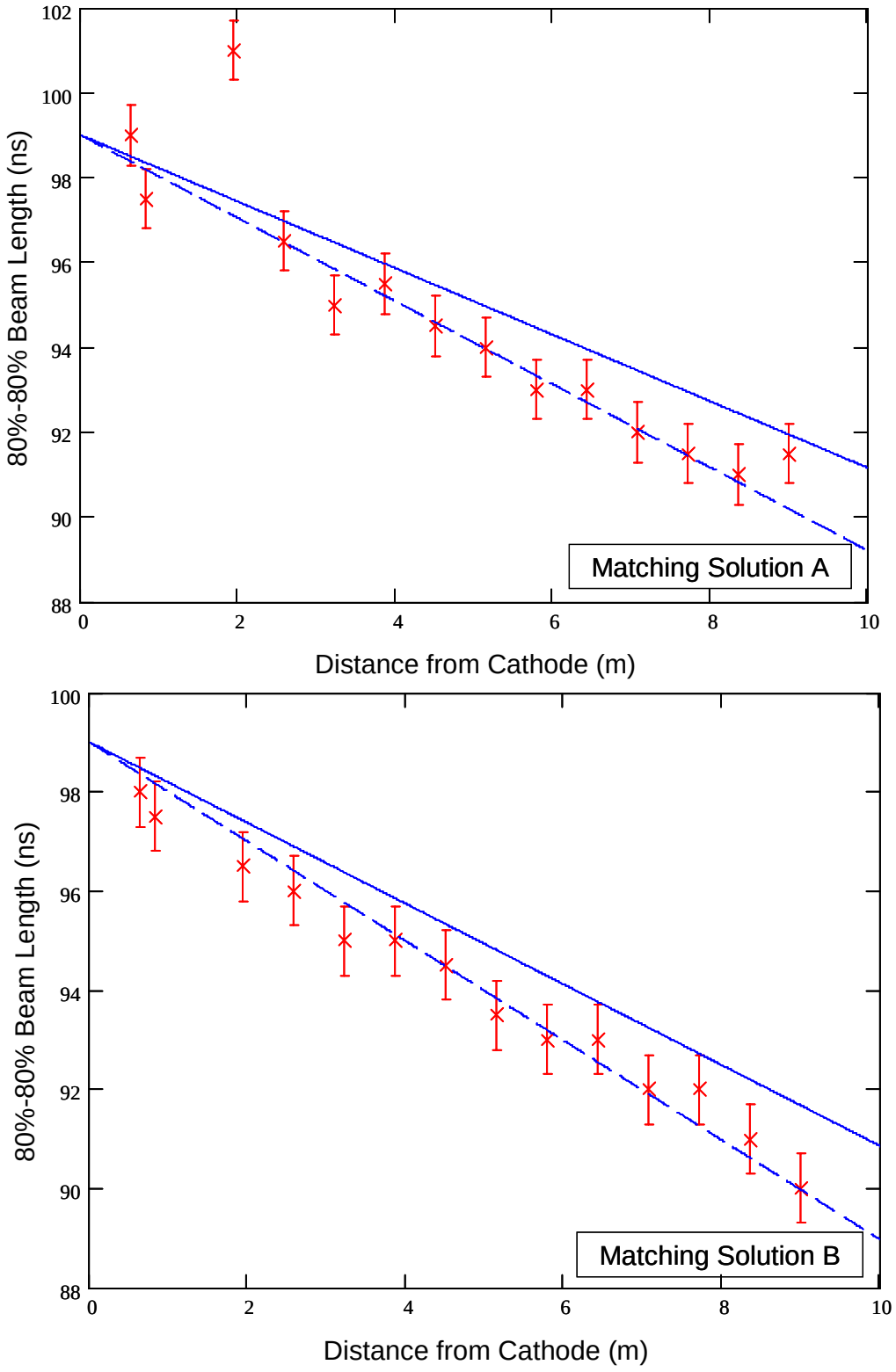

Fig. 47. 80%-80% Beam length for two matching solutions.

logarithmic term for the geometry factor calculated as mentioned in the previous paragraph, and the initial beam length set to 99 ns. Good agreement is again shown with an alpha of one (dashed line).

The measured 80%-20% rise times (tail) are shown in Fig. 48. The theoretical predictions, geometry factors, and data analysis techniques used to extract this data were identical to those used for the 80%-20% rise times (head) presented previously. Although the general trend in the 80%-20% rise time (tail) data is correct, there is significant variation above and below the theoretical values. Notice that similar variation is seen in the 20%-20% beam length data, shown in Fig. 49. Note that the pattern of these variations is different for each matching solution. Since the data for the rise time at the beam head and the 80%-80% beam length agrees so well with theory, but the rise time at the beam tail and the 20%-20% beam length exhibits these variations, whatever is causing them must be present at the 20% level on the beam tail, but not at the 80% level on the beam tail and not at the beam head. In fact, in more recent experiments, a "bump" has been consistently observed at approximately this location in the beam (Fig. 50). The exact source of this effect is not known, but several observations have been made. First, the effect is not observed before BPM 4 (s = 3.857 m). In addition, at a given BPM location, the bump does not appear to have equal strength on all channels. In fact, in some cases the bump will be very visible on one channel and totally absent on another channel at the same BPM. This suggests that a transverse "sloshing" of charge is occurring within the beam, in the form of changes in beam shape, density, or both. Finally, the only "knob" on UMER that was found to significantly affect the strength of the bump was the gun bias

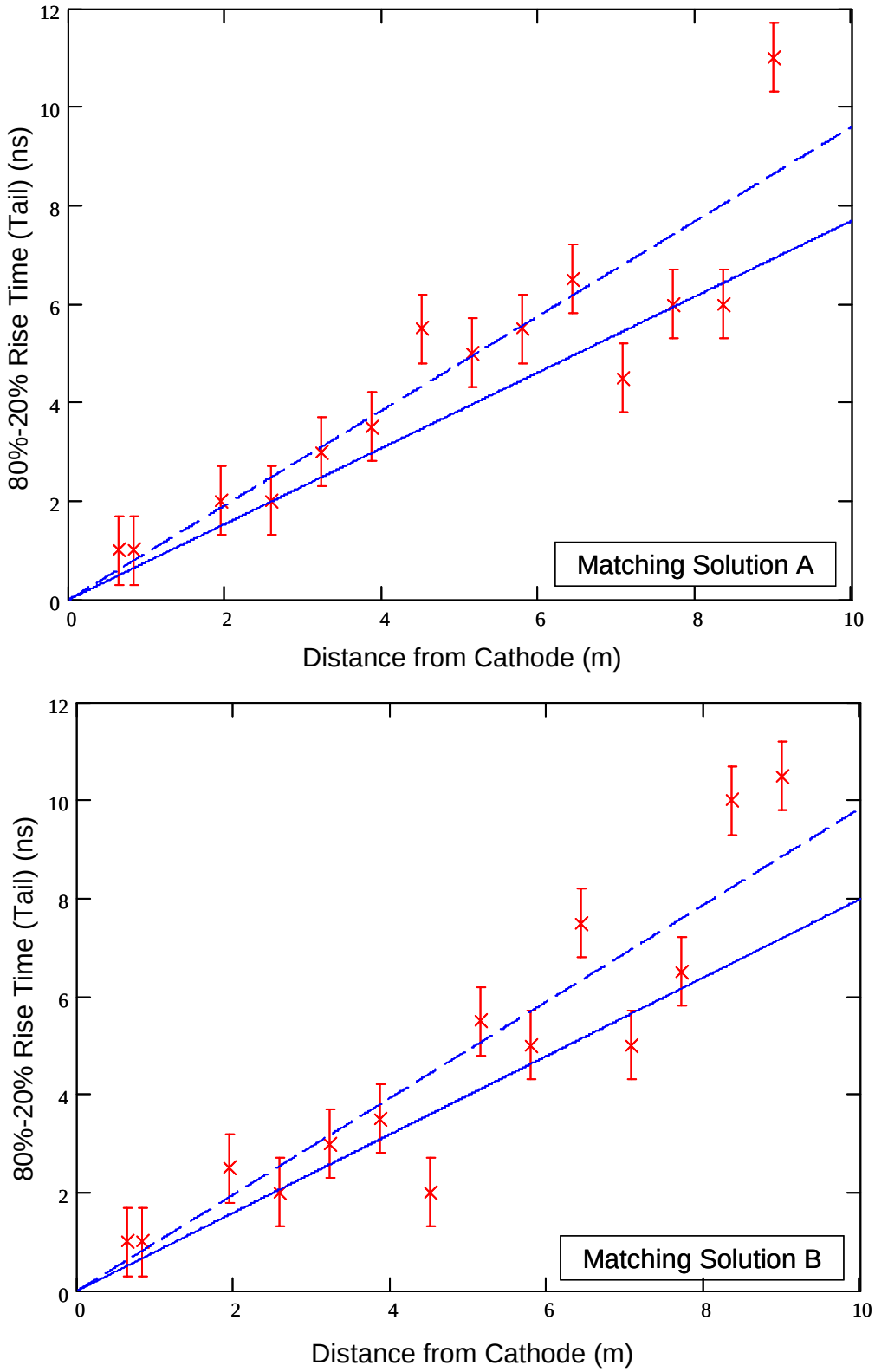

Fig. 48. 80%-20% Rise time (tail) for two matching solutions.

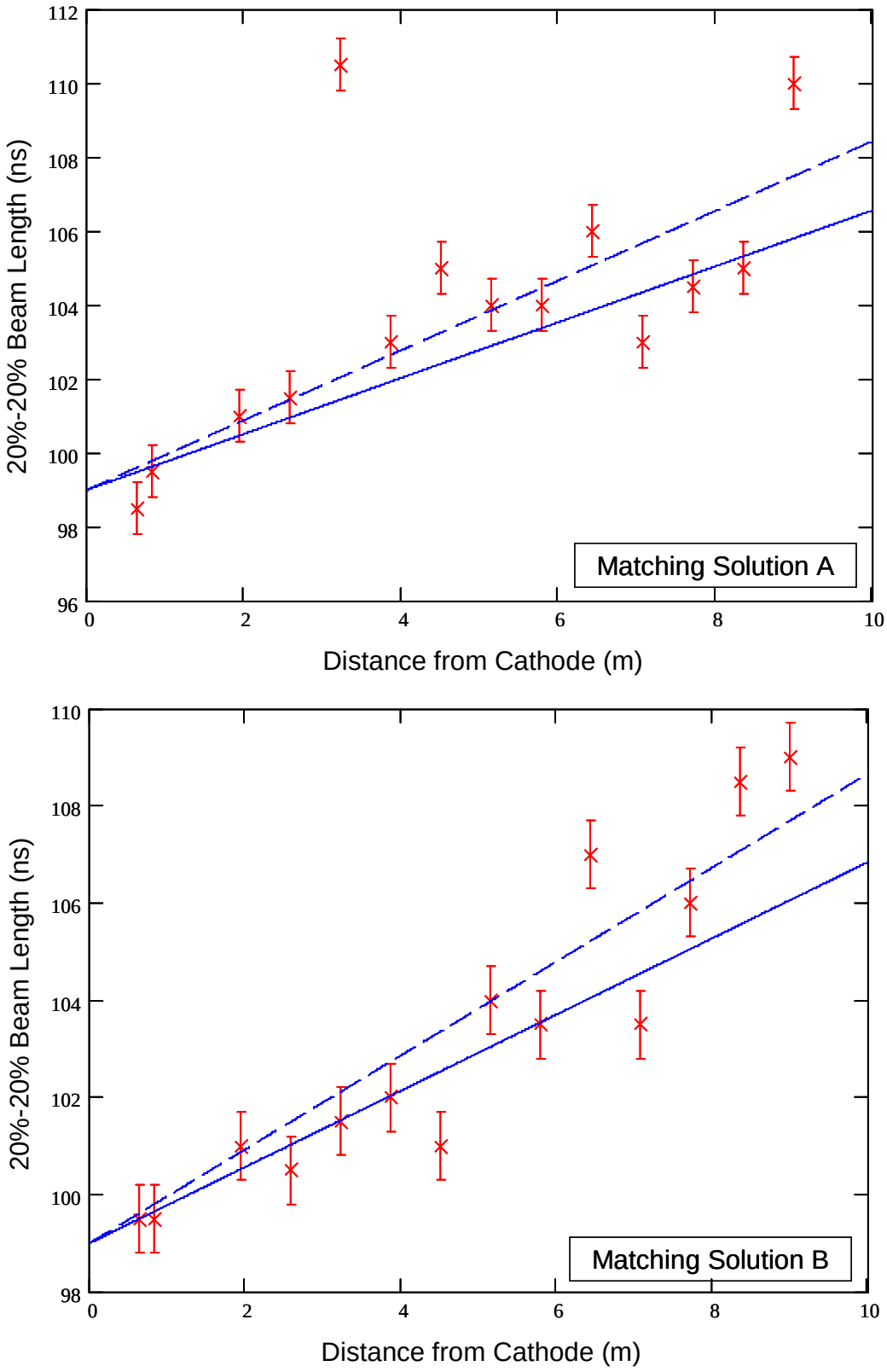

Fig. 49. 20%-20% Beam length for two matching solutions.

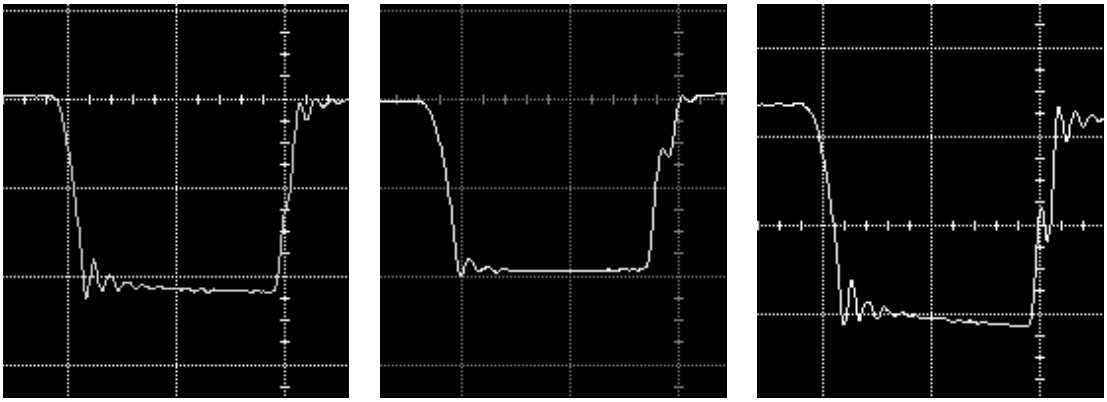

Fig. 50. "Bumps" of varying strength.

voltage. Increasing the bias voltage to suppress beam current does decrease the bump amplitude, as shown in Fig. 71. If an initial cathode pulse including a "bump" is assumed as shown in Fig. 77, the decrease of the bump in the actual beam with increasing bias voltage can be predicted by treating the UMER gun as a triode (Fig. 78). (Triode effects in the UMER gun are the subject of Chapter 4.) This suggests that the bump observed on the beam is an artifact built into the beam at its creation. However, this does not explain why the bump is not seen until after BPM 4, and why it is not seen with equal strength on all BPM plates. To verify that the anomalies seen in the 80%-20% rise time (tail) data are associated with the bump, the data for the two cases was plotted, and data points were marked if a bump was seen in the BPM data at that location (Fig. 51). Black circles indicate that a bump was seen, but not on the BPM channel used to measure the rise time at the tail; red circles indicate that a bump was seen, and was present on the channel use to measure the rise time at the tail; and no circle indicates that no bump was seen on any channel (or at the Bergoz FCT). In each case where the measured 80%-20% rise time (tail) was significantly different than the value predicted by the cold fluid model, a bump was observed, and in almost all cases it was observed on the channel used for the measurement.

The bump, then, is created at the gun, but not observed until 4 m downstream. When it is observed, it is observed on different channels at different BPMs. It affects the measured rise time at the beam tail. And its presence at a given location and on a given channel, and its effect in increasing or reducing the rise time, are all sensitive to the details of the transverse matching solution used. This is strong evidence for a complicated and unexpected longitudinal-transverse coupling effect.

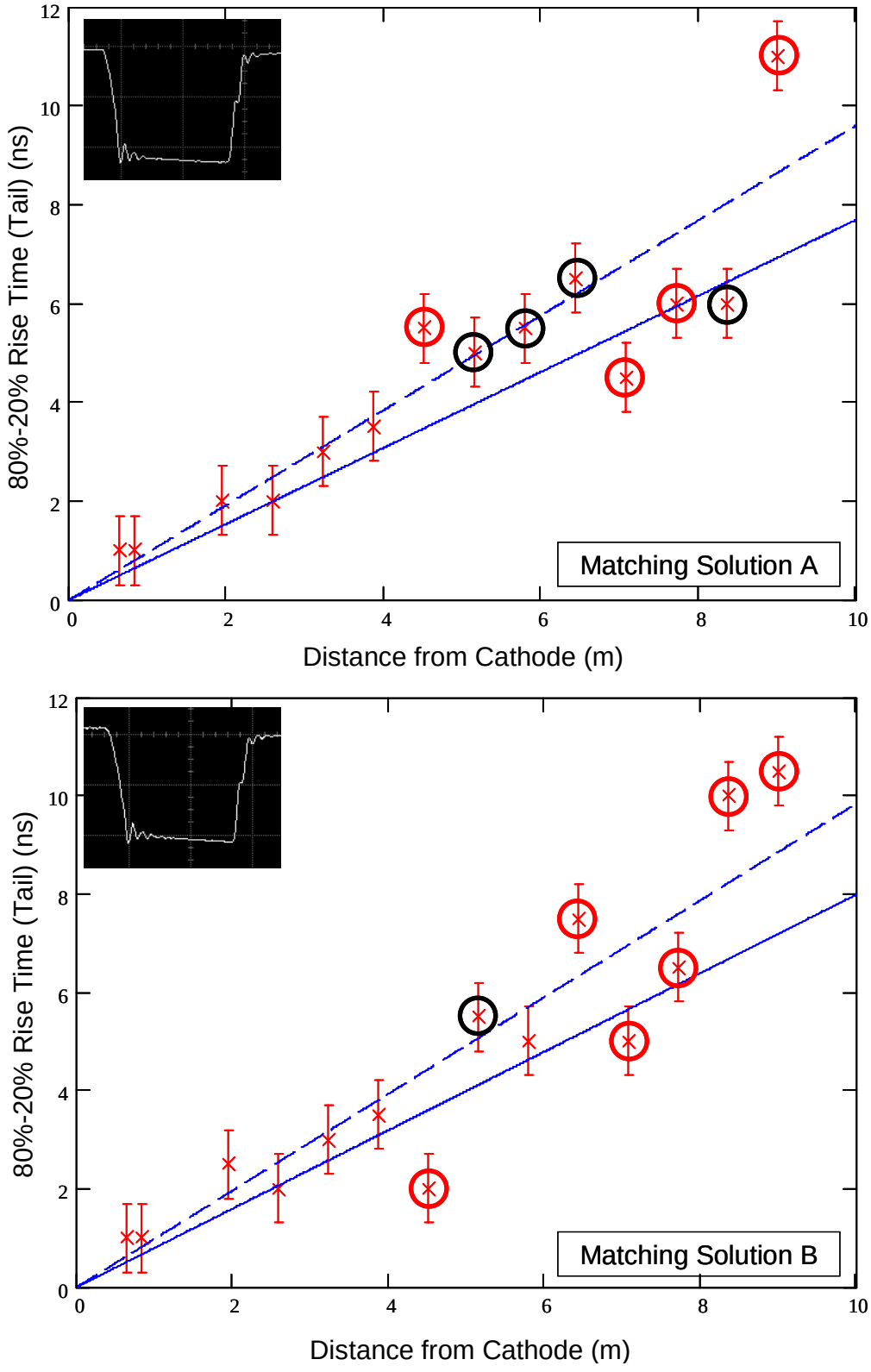

Fig. 51. 80%-20% Rise time (tail), compared to observed locations of "bumps"

3.5.2. Effect of Transverse Mismatch

The experiments described previously in this chapter involved beams which were well matched to the transverse focusing system in UMER. However, beams are often mismatched. This can be caused by mispowering focusing elements, changing beam current or energy, or incorrect assumptions about beam radius. If a beam is not correctly matched to its focusing system, it will undergo transverse mismatch oscillations, in which the beam radius will oscillate due to under- or over-focusing of the beam. It has always been assumed that for the purpose of longitudinal dynamics the breathing modes due to quadrupole focusing could be neglected as averaging out, since the longitudinal evolution occurs on a very long timescale compared to transverse evolution. Logically, this should be the case for mismatches as well, so long as the mismatch envelope was small enough to prevent beam loss.

In order to experimentally explore the sensitivity of longitudinal expansion to transverse mismatch, we deliberately mismatched beams in UMER [68]. To achieve this the gun was operated in temperature-limited mode with the full aperture, providing a current that was variable from 100 mA to approximately 2 mA, while the transverse focusing system was set for 85 mA. The 80%-20% rise time of the beam was observed, and used to calculate an experimental geometry factor from Eq. 54 (see Appendix B for details). This data is shown in Fig. 52 for the beam head; similar results were seen for the beam tail.

To predict the geometry factor under these conditions, we note that changing the beam current will change the average beam size as well as inducing mismatch

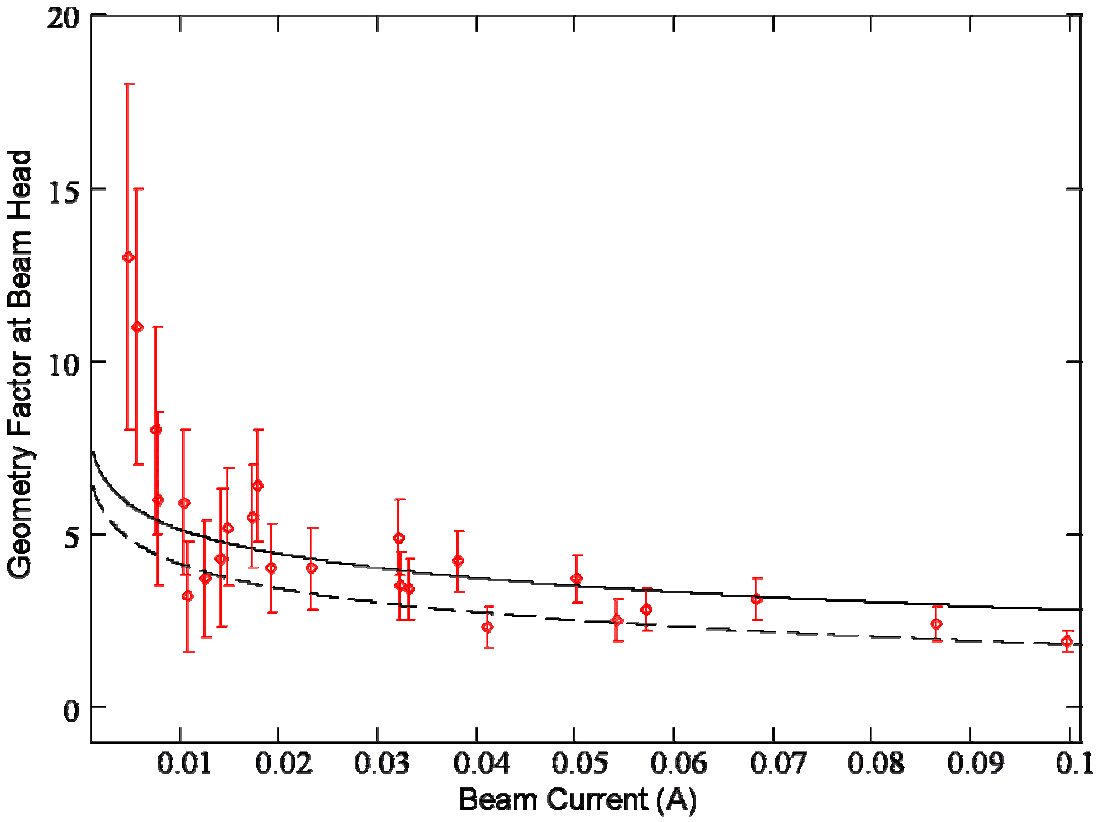

Fig. 52. Variation of geometry factor at head with beam current in mismatched beam. Beam matching was fixed for 85 mA [68].

oscillations. As a result, the geometry factor becomes a value which can only be specified locally, and varies as the beam travels along the beam pipe. However, by taking certain simplifying assumptions, an approximate, average value of the geometry factor can be calculated as a function of beam current for fixed focusing settings. The transverse envelope equation for a matched space charge dominated beam gives the following relation for beam radius:

$$R = \sqrt{\frac{K}{k_0^2}}, \tag{57}$$

where K is the generalized perveance,

$$K = 1.515 \times 10^4 \frac{I}{V^{\frac{3}{2}}} \tag{58}$$

for electrons. Since the beam voltage was not changing during our experiments, we can rewrite the expression for beam radius as a function of current as

$$R = \sqrt{\frac{AI}{k_0^2}}, \tag{59}$$

where A is a constant. The variable k_0 is the zero-current betatron oscillation wave number, which is related to the transverse focusing. Since the focusing in our system was always set for 85 mA, k_0 is fixed and can be calculated from

$$R_{matched} = \sqrt{\frac{AI_{matched}}{k_0^2}}. \tag{60}$$

Substituting this into the general expression for beam radius gives

$$R = R_{matched} \sqrt{\frac{I}{I_{matched}}}. \tag{61}$$

Again, it should be pointed out that we are only trying to find the average beam radius. The actual beam will be ellipsoidal due to quadrupole focusing, and will undergo mismatch oscillations due to operation at other than the matched current. However, since longitudinal effects evolve much slower than transverse effects, only the average beam radius is important for our purposes. The geometry factor g becomes

$$g = \alpha + 2\ln\left(\frac{b}{R_{matched}}\sqrt{\frac{I_{matched}}{I}}\right). \qquad (62)$$

The first term is a constant to be determined, and the second can be evaluated by using the previously-measured beam radius for an 85 mA matched beam, which is 9.5 mm, and the beam pipe radius of 24.5 mm [69]. The geometry factor, in an average sense, is now a function of actual beam current, and can be compared to experiment. This geometry factor is plotted in Fig. 52 for alpha of one (solid line) and zero (dashed line).

At currents above 10 mA, the measured values of the geometry factor for the head and tail agree fairly well with the theoretical geometry factors calculated from Eq. 62. In a sense, this is surprising because the theory assumes conditions which are not present, namely a matched beam. But, for the reasons explained above, this should not be a total surprise, because for the purposes of longitudinal evolution of the beam we are only interested in the average transverse behavior.

At currents below 10 mA, the observed geometry factors have pronounced scatter away from the theoretical curve. Some of this is simply due to the larger error bars. But to a certain extent, this scatter may be a result of the assumption of a matched, on-axis beam. The beam size at 85 mA was used as a benchmark, which

allowed the beam size at higher and lower currents to be estimated. The further the beam current gets from 85 mA, the more incorrect these assumptions become, and the less faith we must have in the theoretical curve. At lower currents, not only will the beam become more severely mismatched, but transverse steering adjustments may no longer be correct. Both effects may cause beam loss or other pronounced problems which the simple theory presented in this section does not take into account.

3.6. Comparison of Longitudinal Envelope Equation and Cold Fluid Model

The longitudinal envelope equation was derived specifically to model the evolution of a beam having the Neuffer distribution, which yields a parabolic line charge density. It has been believed that the Neuffer distribution, which always produces linear space charge fields, can serve as an equivalent beam to analytically model the evolution of beams having different distributions [1,55,66]. In this way, it would serve the same role in longitudinal dynamics that the Kapchinsky-Vladimirsky (K-V) distribution serves in transverse dynamics. For this purpose, the RMS version of the longitudinal envelope equation is used:

$$\tilde{z}'' + \kappa_{z0}\tilde{z} - \frac{K_L}{5\sqrt{5}\tilde{z}^2} - \frac{\tilde{\varepsilon}_{zz'}^2}{\tilde{z}^3} = 0\,, \qquad (63)$$

where $\tilde{z}$ is the RMS value of the beam length. In the equivalent beam approach, the RMS length of a beam with any given distribution should be modeled correctly by a beam having the Neuffer distribution if the two beams have the same RMS emittance, RMS length, and number of particles.

As a test of this, we can directly compare the results given from the longitudinal envelope equation with those given by the one-dimensional cold fluid

theory for free expansion of a beam. Since the cold fluid theory only applies to perfectly intense beams in which emittance is negligible, and since no longitudinal focusing is applied, the RMS form of the longitudinal envelope equation reduces to

$$\tilde{z}'' - \frac{K_L}{5\sqrt{5}\tilde{z}^2} = 0\,. \tag{64}$$

This equation can be solved completely, although for the purposes of numerical calculations it is preferable to leave it in the form

$$s(\tilde{z}) = \int_{\tilde{z}_0}^{\tilde{z}} \frac{d\tilde{z}}{\sqrt{\frac{-2K_L}{5\sqrt{5}\tilde{z}} + \frac{2K_L}{5\sqrt{5}\tilde{z}_0} + (\tilde{z}_0')^2}}\,. \tag{65}$$

The initial divergence of the beam $\tilde{z}_0'$ is assumed to be zero.

For comparison, an RMS beam length must be calculated from the cold fluid model. The RMS length will be

$$\tilde{z}_{CFM}(s) = \sqrt{\frac{\int \lambda(z,s) z^2 dz}{\int \lambda(z,s) dz}}\,. \tag{66}$$

When the correct values of $\lambda(z,s)$ are used from the cold fluid model, this becomes

$$\tilde{z}_{CFM}(s) = \sqrt{\frac{\int_{-z_e(s)}^{-z_c(s)} \left(\frac{2}{3} + \frac{1}{3}\frac{z+z_0}{sc_0}c\beta\right)^2 \lambda_0 z^2 dz + \int_{-z_c(s)}^{z_c(s)} \lambda_0 z^2 dz + \int_{z_c(s)}^{z_e(s)} \left(\frac{2}{3} - \frac{1}{3}\frac{z-z_0}{sc_0}c\beta\right)^2 \lambda_0 z^2 dz}{\int_{-z_e(s)}^{-z_c(s)} \left(\frac{2}{3} + \frac{1}{3}\frac{z+z_0}{sc_0}c\beta\right)^2 \lambda_0 dz + \int_{-z_c(s)}^{z_c(s)} \lambda_0 dz + \int_{z_c(s)}^{z_e(s)} \left(\frac{2}{3} - \frac{1}{3}\frac{z-z_0}{sc_0}c\beta\right)^2 \lambda_0 dz}} \tag{67}$$

where

$$z_e(s) = z_0 + \frac{2c_0 s}{c\beta} \tag{68}$$

is the location of the extreme edge of the beam and

$$z_c(s) = z_0 - \frac{c_0 s}{c\beta} \tag{69}$$

is the location of the shock wave traveling into the bulk of the beam.

Notice that cold fluid model and the longitudinal envelope equation implicitly rely on the geometry factor g. However, the two theories call for different values of g, as discussed in Appendix A. For the moment, we will neglect this and proceed as if both theories called for the same value of g.

The RMS beam length for an initially-rectangular beam is plotted in Figs. 53 - 57 using both theories and varying values for initial pulse length, beam current, geometry factor, and beam energy. The curves are only plotted for values of s which occur before the cusp condition is reached in the cold fluid model, since that model breaks down at this point. In all of these cases, the longitudinal envelope equation and the cold fluid model produce curves which are qualitatively similar, although the cold fluid model produces RMS beam lengths which are slightly greater than those produced by the longitudinal envelope equation. For $\beta >> 0.005$, the cold fluid model gives lengths which are consistently 3.5298% longer than those from the longitudinal envelope equation, regardless of beam current, initial pulse length, or geometry factor value. This can be corrected by assuming that the geometry factor used in the longitudinal envelope equation is greater than that used in the cold fluid model by a factor of 1.1106. For $\beta << 0.005$, the cold fluid model gives lengths which are consistently 2.8141% longer than those from the longitudinal envelope equation, regardless of beam current, initial pulse length, or geometry factor value. This can be corrected by assuming that the geometry factor used in the longitudinal

envelope equation is greater than that used in the cold fluid model by a factor of 1.0875. For $\beta \sim 0.005$, the error between the cold fluid model and longitudinal envelope equation varies with beam energy, beam current, initial pulse length, and geometry factor value.

The source of these discrepancies is not clear at this time. The geometry factors used for the cold fluid model and the longitudinal envelope equation should be different, based on the discussion in Chapter 3. However, that variation should be in α only, which would not be reflected as a constant ratio between the two geometry factors. Nevertheless, it seems safe to say that in the absence of longitudinal emittance and focusing, the longitudinal envelope equation and the cold fluid model yield results for an intense expanding rectangular beam (which has not reached the cusp) that agree to within about 3.5%, which should be close enough for many purposes.

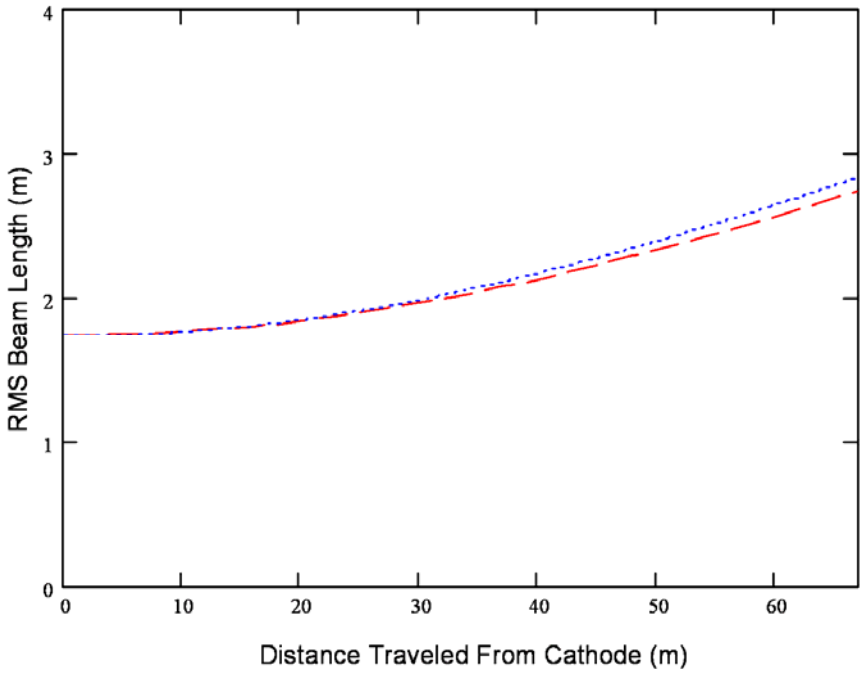

Fig. 53. RMS Beam Length calculated from longitudinal envelope equation (blue) and cold fluid model (red). Beam parameters: g = 3, beta of 0.2, initial length 100 ns, current 100 mA.

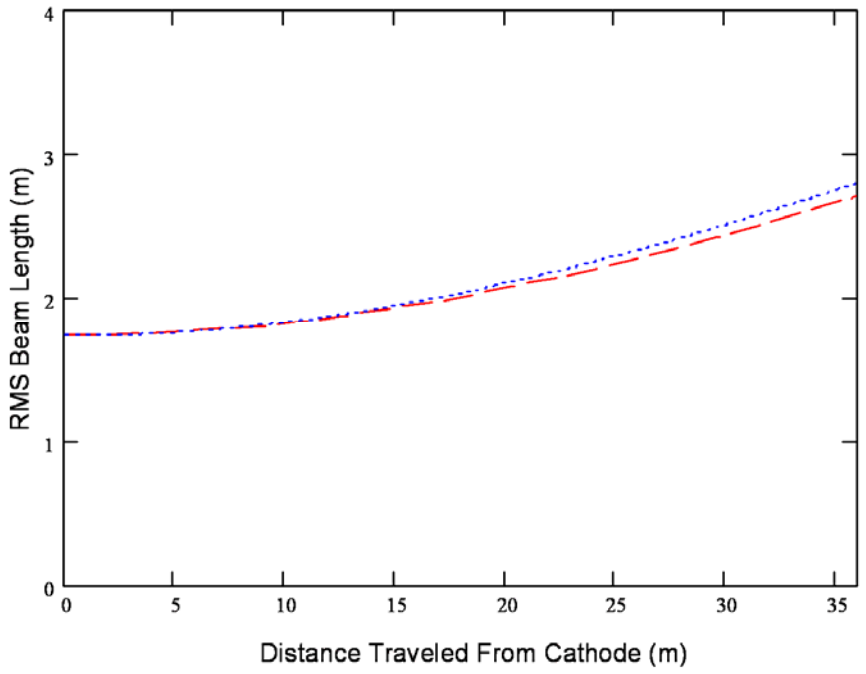

Fig. 54. RMS Beam Length calculated from longitudinal envelope equation (blue) and cold fluid model (red). Beam parameters: g = 10, beta of 0.2, initial length 100 ns, current 100 mA.

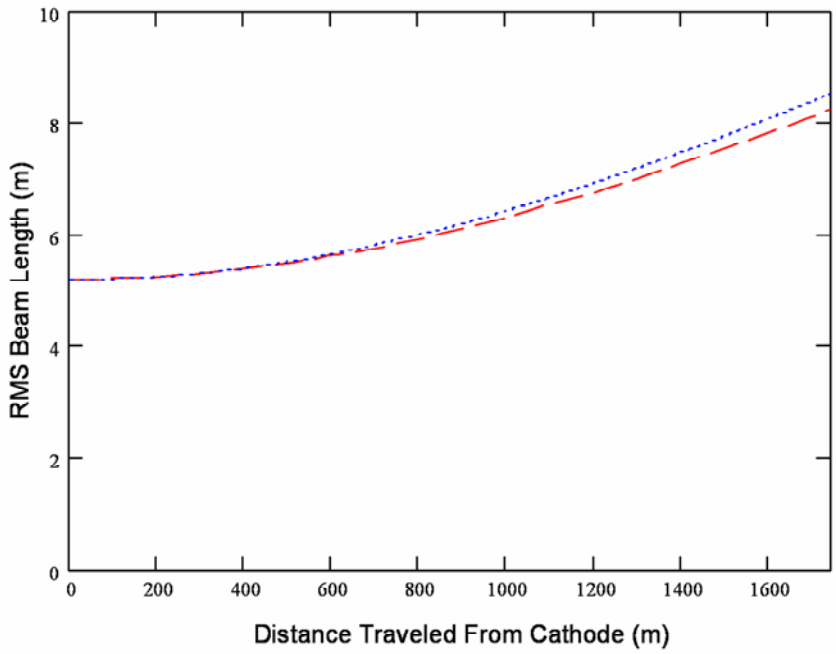

Fig. 55. RMS Beam Length calculated from longitudinal envelope equation (blue) and cold fluid model (red). Beam parameters: g = 3, beta of 0.6, initial length 100 ns, current 100 mA.

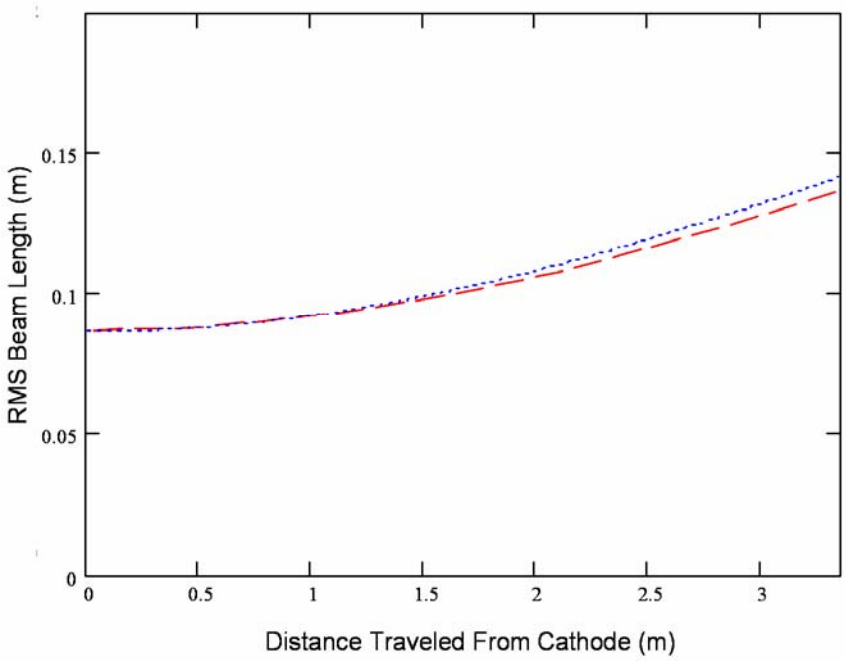

Fig. 56. RMS Beam Length calculated from longitudinal envelope equation (blue) and cold fluid model (red). Beam parameters: g = 3, beta of 0.2, initial length 5 ns, current 100 mA.

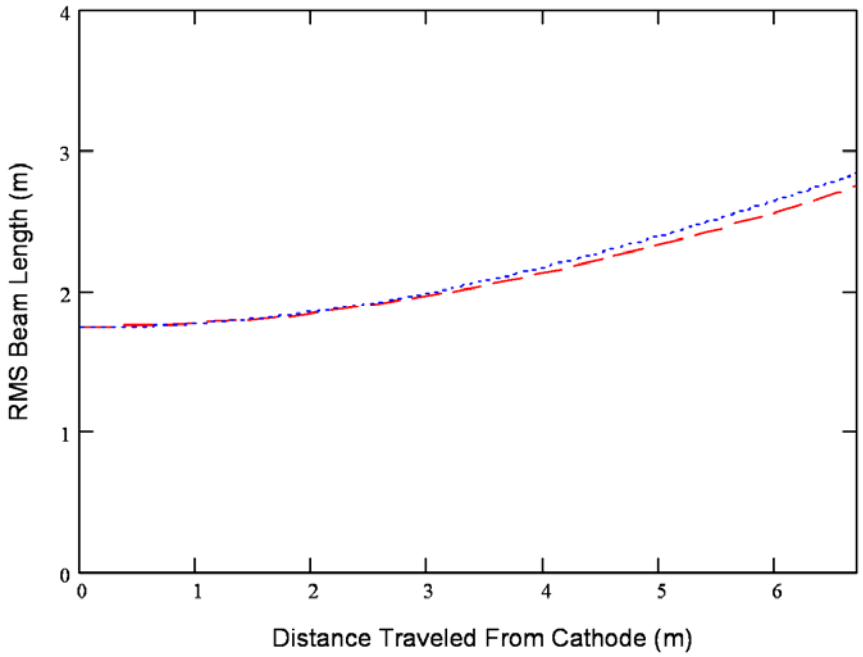

Fig. 57. RMS Beam Length calculated from longitudinal envelope equation (blue) and cold fluid model (red). Beam parameters: g = 3, beta of 0.2, initial length 100 ns, current 10 A.

3.7. Conclusions

In this chapter, we discussed the role played in longitudinal dynamics by external focusing, longitudinal emittance, and longitudinal space charge forces, and derived an intensity parameter to compare the importance of emittance and space charge in governing the beam length. Longitudinal space charge forces act through the longitudinal electric field, which we introduced along with the geometry factor, which provides coupling between the longitudinal and transverse dynamics of the beam. We presented experimental data which verified the applicability of the longitudinal envelope equation to the expansion of parabolic beams in UMER. We introduced the one-dimensional cold fluid theory, which governs the expansion of intense beams which are created with rectangular line charge profiles. Experimental results were shown to verify that the cold fluid model accurately describes the expansion of such beams in UMER, but which showed evidence for an unexpected longitudinal-transverse coupling effect. This effect requires additional study, especially with energy analyzers, in order to design appropriate longitudinal focusing fields for UMER. Experimental data was shown indicating that the long-scale longitudinal expansion of intense beams is insensitive to local transverse envelope oscillations due to mismatch. Finally, calculations were presented showing that the RMS version of the longitudinal envelope equation is a good approximation to describe the increase in RMS beam length of an intense, initially-rectangular beam, as calculated from the cold fluid model.

Chapter 4: Triode Effects and Space Charge Waves

4.1. Introduction

This chapter discusses the UMER gun and describes how the details of its construction result in unusual behavior, especially when operated in atypical regimes. One of the results of such operation is the production of a modulated beam, even though no modulating signal is deliberately applied to the gun. The evolution of this modulated beam as it travels along the UMER ring returns us to a consideration of the sound speed and longitudinal wave propagation in intense beams. But first, we begin with the vacuum diode.

4.2. The UMER Gun: A "Pierce-Focusing Triode"

4.2.1. Vacuum Diodes and Pierce Guns

In conventional high-current electron guns, electrons are generated at the cathode by thermionic emission, governed by the Richardson-Dushman equation,

$$J = A_{RD} T^2 \exp\left[\frac{-W}{k_B T}\right], \tag{70}$$

where $A_{RD} = 1.2 \times 10^6 \, A/m^2 K^2$, T is the cathode temperature, W is the work function of the cathode material, and k_B is the Boltzmann constant. Dispenser cathodes of the type used in UMER typically have effective work functions of about 1.6 eV and are designed to operate at about 1400 K ($k_B T \sim 0.12$ eV) [1]. The electrons are then

accelerated towards the anode, which is held at positive potential relative to the cathode, and leave the gun through an aperture in the anode. Except for the aperture, this is essentially a vacuum diode, of the type once used widely in electronics. The maximum current density that can be transported across a diode is given by the Child-Langmuir limit

$$J = \frac{4}{9}\varepsilon_0\left(\frac{2e}{m}\right)^{1/2}\frac{V^{3/2}}{d^2}, \tag{71}$$

where ε_0 is the permittivity of free space, e is the charge, m is the mass of the electron, V is the potential difference between the cathode and anode, and d is the distance between the cathode and anode. At this current density, the potential gradient at the cathode is zero, so that an electron produced at the cathode would feel no force directing it towards the anode. This assumes that the electrons produced from the cathode have zero initial velocity. In fact, they have small but nonzero initial velocities due to the cathode temperature, typically less than 0.5 V for thermionic cathodes [70]. Electrons produced from the cathode with some nonzero axial velocities will be able to penetrate into the diode region some distance even if the current density already in the diode is the maximum predicted by the Child-Langmuir equation. This will produce a region of excess space charge, and depressed potential, known as a virtual cathode. Additional electrons injected into the diode region will reach the area of the virtual cathode, with their initial kinetic energy being converted to potential energy as they approach it. The region between the virtual cathode and the anode behaves as an idealized diode, and will only pass that amount of current predicted by the Child-Langmuir equation. Excess electrons, having been

produced at the physical cathode and sent into the diode with nonzero axial velocity, are reflected from the virtual cathode and return to the physical cathode. Thus, the current flowing through a vacuum diode may be temperature-limited if the current density predicted by Richardson-Dushman is less than that predicted by Child-Langmuir, or space charge-limited and in saturation otherwise.

The Child-Langmuir equation was derived for ion flow between infinitely-large parallel plates [72]. In this case, there is no variation of potential perpendicular to the flow of current, resulting in straight-line particle motion with no divergence. This type of motion is of great use in optimizing charged-particle devices and deriving scaling laws for the operation of guns. But any realizable beam is of limited extent, and space charge forces will exist transverse to the direction of motion of the particles, causing the beam to diverge as discussed in Chapter 1. However, the beam can be "tricked" into behaving as if it were of infinite extent if a suitable potential is applied at the beam edges to simulate the presence of the "missing" space charge. Pierce used this principle to determine shapes for electrodes at the cathode and anode, which produce just such a potential, giving rectilinear electron flow [22]. The action of these electrodes can also be thought of as providing a transverse focusing force to maintain the beam diameter during its passage through the gun. A variety of configurations are possible, but all have the common feature that the electrode at the cathode makes an angle of 67.5° with the edge of the electron beam. Guns using these electrodes are known as "Pierce guns," and are the standard for high-current electron and ion guns [1,2,4,22,70,71].

4.2.2. Triodes

For diodes in space charge limited operation, the current flowing through the tube must be controlled by changing the voltage applied across the tube. To control this current without changing the applied voltage, a grid may be placed between the anode and cathode, forming a triode. Current flow then depends on the electric field at the cathode, which is affected by both the potential of the grid, and the potential of the anode "leaking" through the spaces in the grid. However, because the grid is closer to the cathode than the anode, and because of the partial shielding effect of the grid, it will have a much stronger influence on the electric field at the cathode than does the anode. This allows control of a large current by the application of a small voltage. By analogy with the diode, the current density in a triode in space charge limited operation is [70,73,74]

$$J = K_T\left(V_G + \frac{V_A}{\mu}\right)^{3/2}, \tag{72}$$

where V_G is the potential applied between the grid and cathode, V_A is the potential between the cathode and anode, μ is the amplification factor, and

$$K_T = \frac{2.335\times10^{-6}}{d_{cg}^2\left[1+\frac{1}{\mu}\left(\frac{d_{ca}}{d_{cg}}\right)^{4/3}\right]^{3/2}} \tag{73}$$

is a constant depending on the amplification factor, the distance between cathode and grid (d_{cg}), and the distance between cathode and anode (d_{ca}). The amplification factor is a measure of how much stronger the influence of the grid on the field at the cathode is compared to that of the anode. No single formula exists for the

amplification factor, but exact solutions or approximate formulas exist within certain parameter ranges [70]. The amplification factor is found to increase with increasing grid-anode distance, and with increasing screening factor. Typical triodes have amplification factors between 2.5 and 200 [70].

In general, the grid of a triode is kept negatively biased, which prevents electrons from reaching the grid and serves to counteract the action of the anode[2]. Note that current may flow in a triode even when the grid is more negative than the cathode because of penetration of the anode field through the spaces in the grid mesh. When the grid is biased sufficiently negatively such that $V_G + \frac{V_A}{\mu}$ is zero, the triode reaches cutoff and the current through the tube becomes zero. Experimentally, this technique may be used to determine the amplification factor. However, near cutoff the amplification factor begins to decrease. This is because the single amplification factor of Eq. (72) is really an average amplification factor for the entire tube. The local amplification factor will tend to vary with location on the cathode due to edge effects and grid-cathode spacing errors. As the grid is made increasingly negative with respect to the cathode, the high-μ regions of the cathode will reach cutoff first, while the low-μ regions will continue to emit. Thus, the average amplification factor of the emitting regions of the cathode will fall as cutoff is approached, sometimes by up to 20% [70].

[2] Because no electrons may reach the grid when it is biased negatively with respect to the cathode, there will be no grid current, and therefore a grid voltage alone can control the triode current, without significant power dissipation in the grid circuit [70]. In triodes where the grid is held at a very large positive voltage, exceeding that of the anode, the "dynamic plate resistance" [70] may become negative and spontaneous oscillations are observed to occur [75-78].

In the case of a tube with grid-cathode spacing equal to or smaller than the distance between wires in the grid, no true cutoff will exist. Near "cutoff" the electric field on areas of the cathode adjacent to the grid wires will become negative, while areas between grid wire locations will still have positive fields allowing electrons to escape. In this case, a phenomenon known as *Insel Bildung* ("island formation") may occur, in which "islands" of the cathode will continue to emit while other regions of the cathode will not (Fig. 58) [70].

When Eq. (72) holds, the device is said to be in "triode amplification" mode. In this mode, small voltages applied at the grid will cause strong changes in the current flowing through the tube. But the triode can be thought of as a pair of diodes, and so the Child-Langmuir equation will also come into play. If the grid voltage is adjusted to increase the current flowing through the triode, as predicted by Eq. (72), eventually an upper limit on the current will be found. This limit is the value given by the Child-Langmuir equation for the cathode-anode "diode." Once this current has been reached, varying the grid potential no longer has any effect on the current in the triode, and the device is said to be in "saturation." Once the triode is in saturation, any modulating voltages applied to the grid will have no effect on the current flowing through the triode.

4.2.3. UMER's Gridded Gun: Triode with Pierce Focusing

The UMER gridded gun combines Pierce focusing electrodes with a planar triode geometry. The anode is kept a ground, while the grid floats at -10 kV. A DC bias voltage is applied between the grid and cathode to suppress emission, except during a nominal 100 ns long pulse applied to the cathode (Fig. 59). Note that we

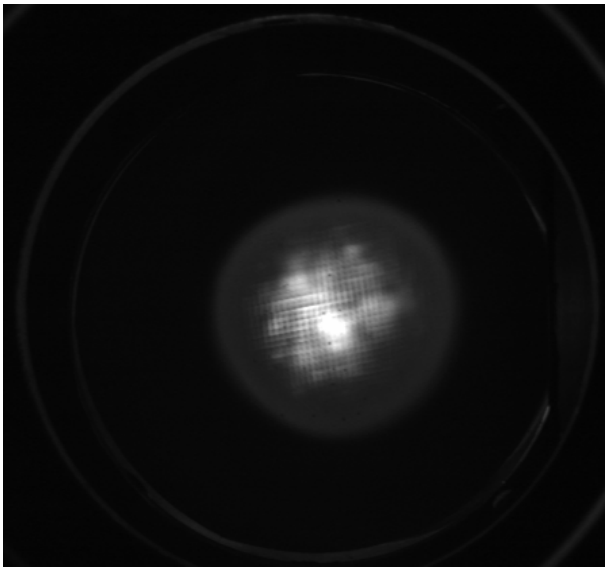

(a)

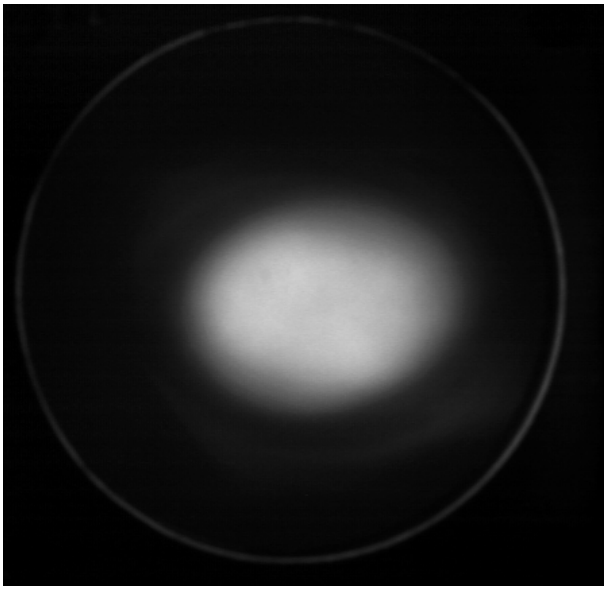

(b)

Fig. 58. (a) *Insel Bildung* observed in UMER. Bias voltage is approximately 5.5 V. Darker regions of the cathode represent those that are emitting during the cathode pulse but are in cutoff otherwise. Brighter regions are those that do not reach cutoff at all. Note that this is a phosphor screen image of the beam, produced from the cathode, while Fig. 76 is a photograph of the hot glowing cathode taken through the anode and cathode meshes. The effect in Fig. 76 is a "shadow" of the grid and anode mesh wires, while the effect shown here is due to nonuniform emission from the cathode. (b) Typical emission far from cutoff.

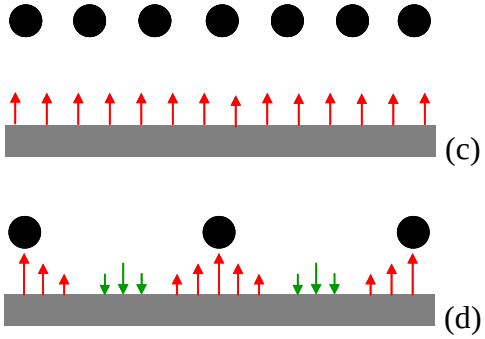

Fig. 58 (continued). (c) Grid wire and grid-cathode spacing to provide uniform electric field at cathode, and no *Insel Bildung*. (d) Grid wire and grid-cathode spacing to provide nonuniform electric field at cathode due to enhanced penetration between

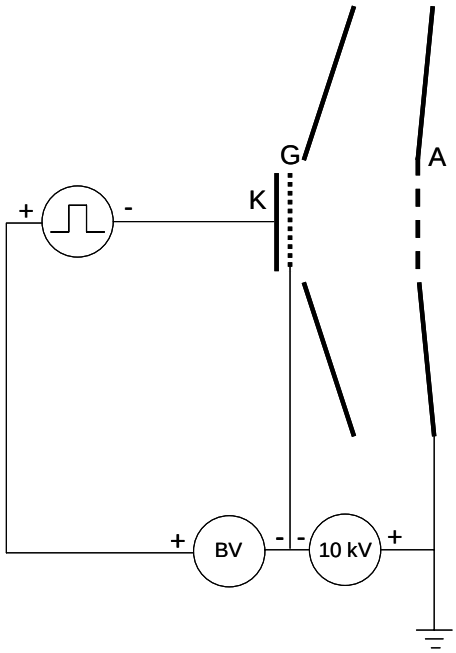

Fig. 59. UMER gun diagram (simplified)

typically think of controlling the current in a triode by pulsing the grid and holding the cathode constant. In UMER, the reverse is done, although the effect is the same. A grid at the anode aperture serves to provide uniform potential across the anode aperture and prevent defocusing of the beam. The UMER gun was designed to operate in a space charge limited mode, with output current being adjustable by placing aperture plates of various radii in front of the anode aperture. A full set of UMER gun parameters are shown in Table 8.

The amplification factor of UMER has been found experimentally to be 910. This value was found by changing the bias voltage to bring the gun into cutoff, as described in the previous section. There is some uncertainty in this number due to differences between the values for the bias voltage and accelerating voltage displayed on UMER and the actual voltages applied to the gun, errors in determining the pulser voltage due to ringing, and the lack of a clearly-defined cutoff due to the effects described in the previous section. The amplification factor for UMER is larger than is typical for triodes, but this is due to the very large grid-anode spacing in UMER, which is between 170 and 270 times greater than the spacing between grid wires.

4.2.4. Anomalous Behavior and Transverse Effects

Among the many effects that have been observed in the UMER gun is the anomalous dependence of beam current on cathode temperature [79]. As cathode temperature is increased from zero, the current produced from the gun increases, as expected from the Richardson-Dushman equation. However, as the expected space charge limited current level is reached, the current produced from the gun continues to increase above the level predicted by the Child-Langmuir equation as cathode

Table 8. Nominal UMER gun parameters

Type	Triode-type gridded gun, Pierce focusing
Cathode	Eimac Y-646B
Cathode type	Barium dispenser, indirectly heated
Cathode radius	4 mm
Cathode heater power (nominal)	7.8 Watts
Cathode-grid distance (nominal)	0.15 mm
Grid type	Rectangular mesh
Grid wire radius	0.0254 mm
Grid wire spacing	0.15 mm
Grid transparency	66%
Grid screening factor	0.34
Cathode "aperture"	4 mm radius aperture in Pierce electrode
Cathode-Pierce electrode spacing	< 0.30 mm
Anode-cathode gap	25 - 41 mm

Table 8. Nominal UMER gun parameters (continued)

Anode grid type	Rectangular mesh
Anode grid transparency	87%
Accelerating voltage	10 kV
Cathode-grid voltage	Bias voltage variable from 0 V to 66 V
Pulser type	Transistor-switched coaxial PFL
Pulse length	100 ns nominal
Pulser voltage	approx. 55 V average
Aperture type	wheel-mounted aperture plates
Aperture plate types	Single-hole, pepperpot, pinhole, five - beamlet
Aperture sizes	8.13 mm - 0.25 mm radius

temperature is increased. Eventually a maximum current is produced from the gun, after which increasing the cathode temperature *decreases* the output current, until the diode saturation current predicted by Child-Langmuir is reached. After this point, continuing to increase the cathode temperature has no effect on current. Additionally, using the photoemission techniques described in Chapter 5, it has been found that the injection of additional electrons produced at the cathode by photoemission has different effects depending on cathode temperature [80]. At low temperatures, where the current is clearly emission-limited, producing photoelectrons at the cathode results in an increased current, sometimes exceeding the Child-Langmuir limit. At high temperatures, where the current is clearly space charge limited, producing photoelectrons at the cathode does not result in any change in the current produced by the gun. Presumably, these additional photoelectrons are reflected from a virtual cathode, and therefore cannot escape the gun. However, producing photoelectrons at the cathode while the gun is in the anomalous transition between emission and space charge limited operation results in a *decrease* in current produced from the gun (Fig. 60).

A seemingly related effect also occurs with changes in bias voltage [59]. Measurements of beam current (with the 25 mA aperture) and beam radius (with 85 mA settings) as a function of bias voltage are shown in Fig. 61 and Fig. 62. The measured current at the injection Bergoz FCT (red) agrees very well with the expected current until the Bias Voltage passes 50 V. At this time, the measured current drops, then increases greatly, and then finally falls away.

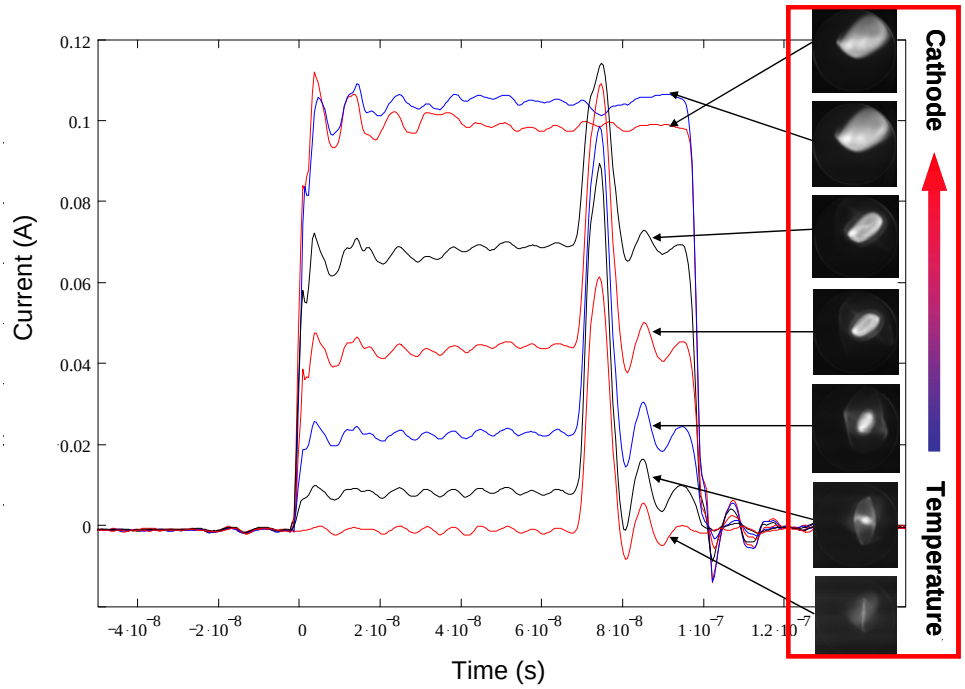

Fig. 60. Variation of beam pulse with cathode temperature.

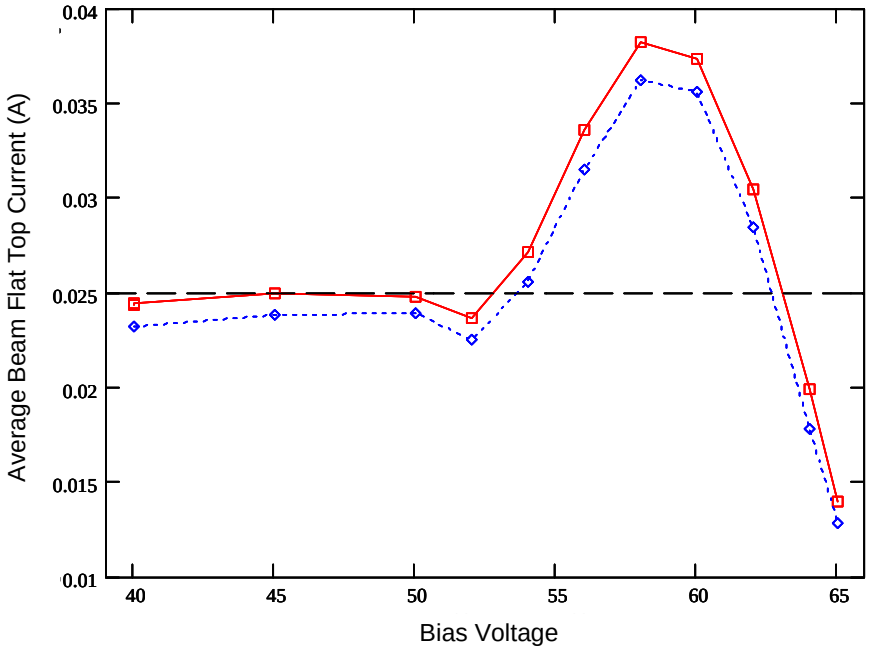

Fig. 61. Beam current measured at injection Bergoz fast current transformer (s = 0.626 m, red) and extraction Bergoz fast current transformer (s = 7.54 m, blue) as a function of applied bias voltage for 25 mA aperture. Nominal 25 mA current shown with black line.

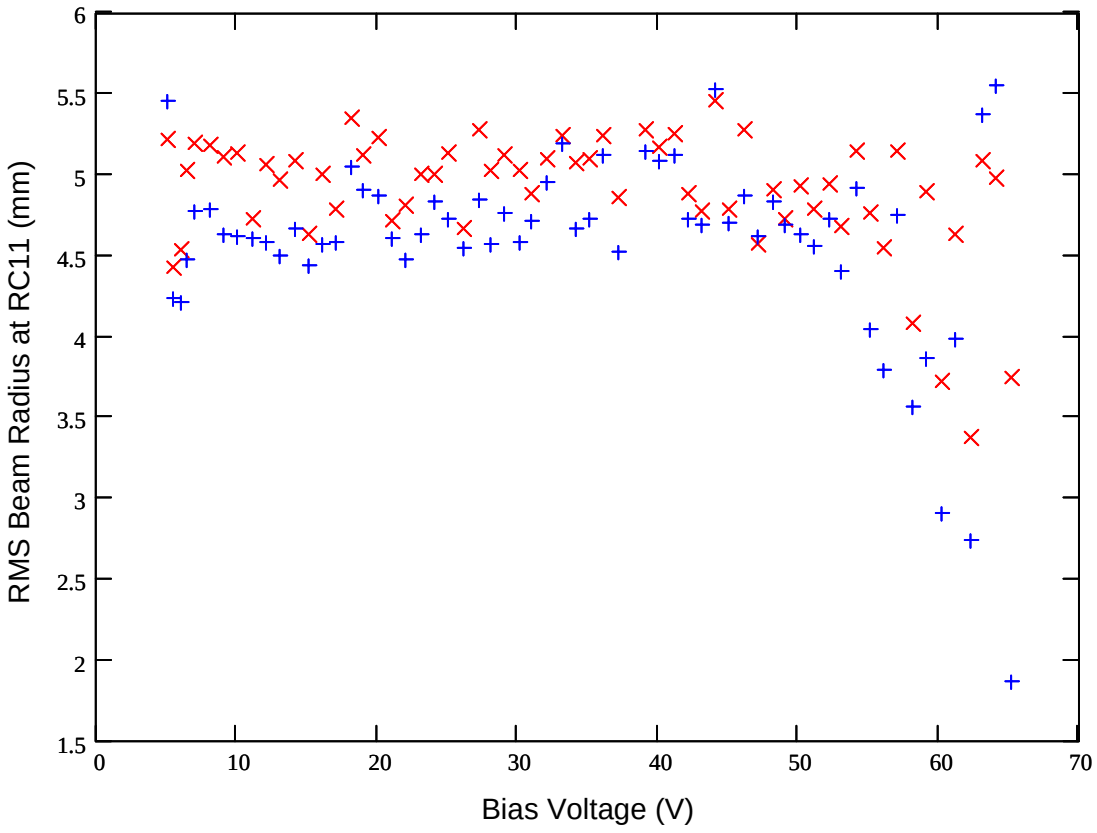

Fig. 62. RMS beam radius measured at ring chamber 11 as a function of bias voltage. Standard settings for 85 mA beam transport were used, except for the bias voltage, which was varied across its entire dynamic range. Beam image was recorded at ring chamber 11 (s = 8.34 m from cathode), and RMS radius in x (red) and y (blue) were extracted (see Appendix B). Beam radius is fairly insensitive to bias voltage over most of its range, although variation due to mismatch oscillations is seen below 10 V and above 50 V. As shown in Fig. 61, 50 V marks the onset of anomalous bias-voltage-dependent current variation in UMER.

This is not the current vs. bias voltage curve that is expected in UMER. Since UMER has a gridded gun, it should behave like a triode. Figure 63 compares the measured beam current at the injection Bergoz FCT (red) to the expected beam current based on triode behavior (black). The two black lines use different values of the triode amplification factor – the solid curve is approximately 1500, while the dotted curve uses the measured value of 910. This shows that the UMER gun behaves like a triode in saturation between bias voltages of 40 V and 50 V. A triode in saturation is just a diode, so the current in this region obeys the Child-Langmuir law. After 50 V, strange things happen, and we need a new picture to understand this region.

It has long been believed that this effect is due to transverse focusing effects in the gun [81]. UMER uses a Pierce gun, which is designed to provide transverse focusing for the beam at full current. Thus, the beam size and beam current density remain constant in the diode region. When an aperture is used, the final output current is the product of the beam current density and the aperture area. Figure 64 shows the UMER gun in saturation. When the bias voltage is increased past 50 V, the gun is no longer in saturation and the triode law should apply. The triode law says that the current in the device will decrease with increasing bias voltage. Unlike conventional triode tubes, the UMER gun has Pierce-type focusing, which is designed to keep the full-current beam uniform. At lower currents, the transverse focusing is too strong. The beam is not matched, and it will be compressed transversely, as shown in Fig. 65. The beam may be compressed so much at the aperture that the current density at the aperture actually increases, even though the total current in the

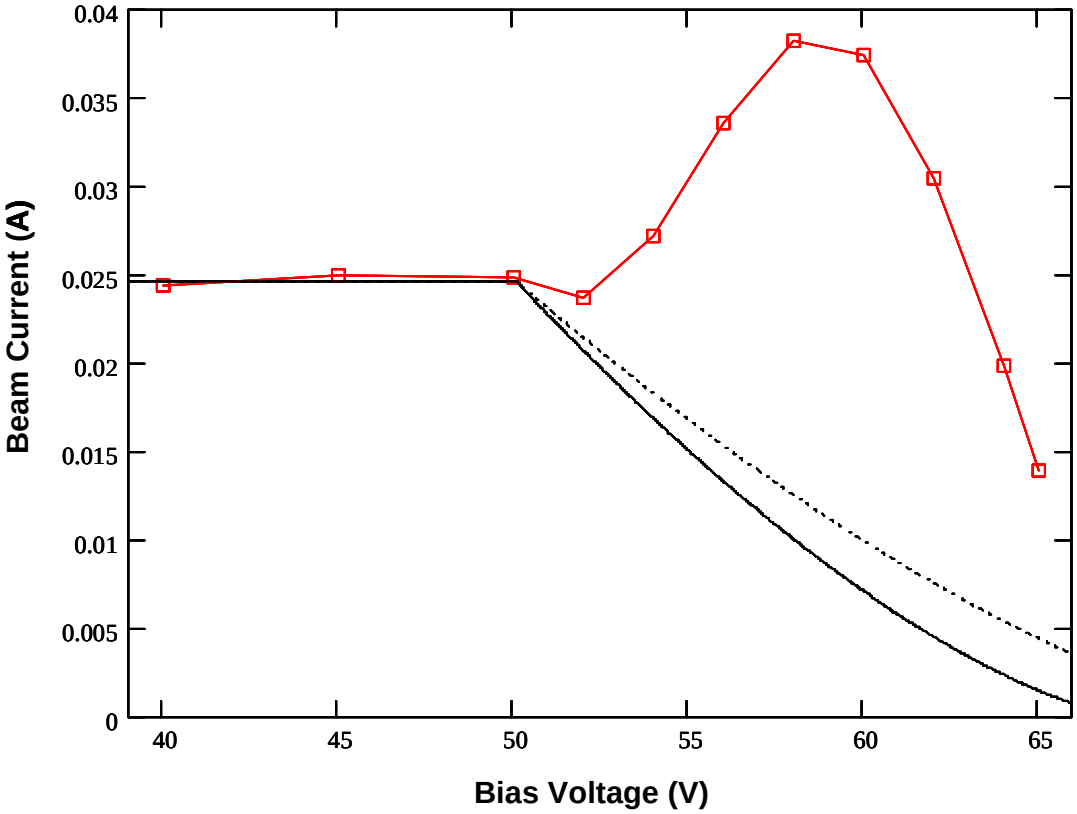

Fig. 63. Variation of average beam current with bias voltage (red), and theoretical current from ideal triode. Calculation and data are for 25 mA aperture.

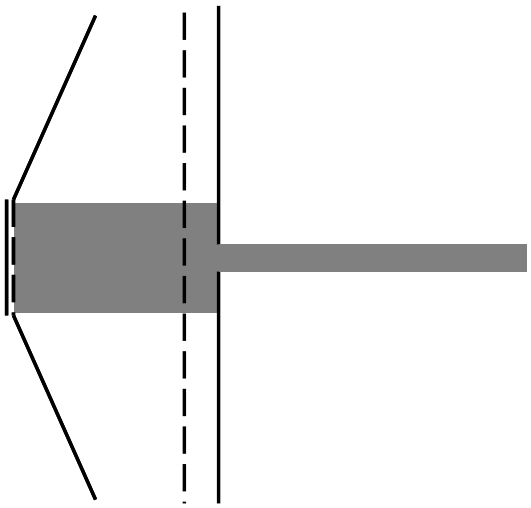

Fig. 64. Full-current operation of "Pierce-focusing triode."

gun has decreased. Since the net output current is the product of the current density at the aperture and the aperture area, the net output current may *increase*. This can continue until the beam radius just before the aperture is equal to the aperture radius. At this point, the full current in the gun will be able to leave the gun. This condition should give maximum current, and is shown in Fig. 66. From now on, increasing bias voltage will decrease the observed beam current, as shown in Fig. 67. This will continue until the gun reaches triode cutoff.

If this picture is right, we can write down some equations based on the beam size, the gun geometry, and the triode law to describe the situation. (For simplicity, we will denote quantities at the cathode with a "0" subscript, quantities just before the aperture with a "1" subscript, and quantities at or just after the aperture with a "2" subscript.) When the gun is in saturation, life is easy, and the current produced from the gun is just given by Child-Langmuir, with the current density produced at the gun multiplied by the area of the aperture:

$$I_2 = J_0 \pi R_2^2 = P V^{\frac{3}{2}} \pi R_2^2 , \qquad (74)$$

where R_2 is the aperture radius and P is the perveance of the gun. Conversely, when the beam radius at the aperture is smaller than the aperture radius, the whole beam gets through, and the current should be given by the triode law for the *full beam without apertures*. In between these two regions, life is more complicated. As the bias voltage is increased, the gun will leave the saturation region and enter the triode amplifying region. In this region, the current density which is produced by the cathode and makes it past the grid is given by the Triode law:

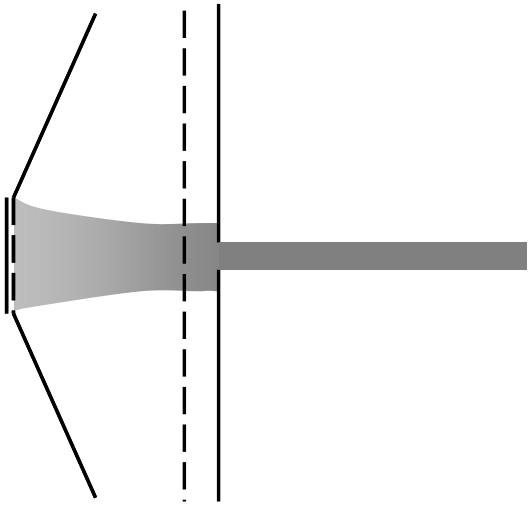

Fig. 65. Reduced-current operation of "Pierce-focusing triode." Onset of over-focusing.

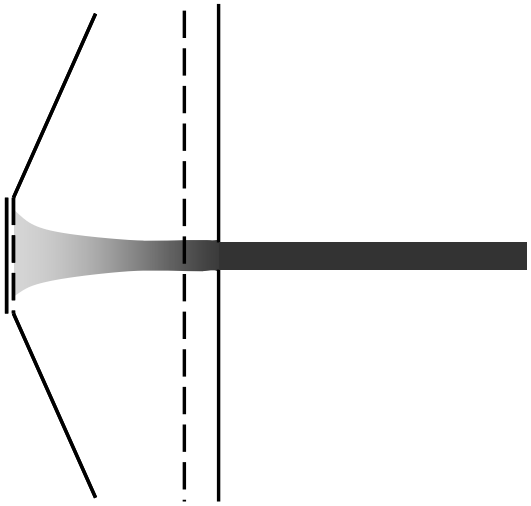

Fig. 66. Reduced-current operation of "Pierce-focusing triode." Beam radius equal before and after aperture is equal. This condition will result in maximum output current, even though current in the diode region is reduced.

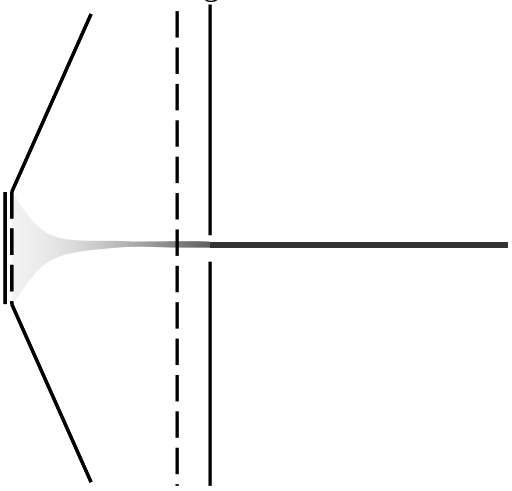

Fig. 67. "Pierce-focusing triode" near triode cutoff.

$$J_0 = K_T\left[\frac{10kV}{\mu} - BV\right]^{3/2}. \tag{75}$$

So the total amount of current produced *from the cathode* depends on this, and on the cathode radius:

$$I_0 = K_T\left[\frac{10kV}{\mu} - BV\right]^{3/2}\pi R_0^2. \tag{76}$$

Because charge is conserved, this is the total amount of current which reaches the aperture($I_0 = I_1$). However, the beam radius will not necessarily stay the same as the cathode radius; for a gun current less than the design current the external focusing should exceed the space charge force, and the beam should shrink to a new radius R_1, so that the current density at the aperture is now

$$J_1 = K_T\left[\frac{10kV}{\mu} - BV\right]^{3/2}\frac{R_0^2}{R_1^2}. \tag{77}$$

However, because of the aperture (radius R_2), the amount of current that can actually leave the gun and enter the transport system is

$$I_2 = K_T\left[\frac{10kV}{\mu} - BV\right]^{3/2}\frac{R_0^2}{R_1^2}\pi R_2^2. \tag{78}$$

The key factor which will determine if the net current will increase or decrease is the beam area compression ratio

$$\frac{R_0^2}{R_1^2}. \tag{79}$$

It is not clear how to determine an exact analytical solution for this ratio. However, it is possible to find an approximate value by treating the Pierce gun as a beam transport system in which there are mismatch oscillations (Fig. 68). Assume that the Pierce

geometry provides constant transverse focusing to the beam in the gun. All beams are produced at the cathode, and therefore have an initial radius R_0 equal to that of the cathode. Also assume that the beam emerges from the cathode at normal incidence, so $R_0' = 0$. The function of a Pierce gun is to maintain the beam radius, so the transverse focusing strength can be calculated from the transverse envelope equation:

$$k_{0,Pierce}{}^2 = \frac{K_{full}}{R_0{}^2}. \tag{80}$$

If the beam current is reduced due to triode action, the beam will no longer be matched and will perform mismatch oscillations. If the mismatch is not severe, the beam envelope will be sinusoidal with mismatch period [1]

$$k_e = \sqrt{k_0^2 + \frac{K_{reduced}}{R_{match}^2} + 3\frac{\varepsilon^2}{R_{match}^4}} = \frac{2\pi}{\lambda_e}. \tag{81}$$

For our purposes, emittance in (81) can be ignored. From the transverse envelope equation, the matched beam radius at the reduced current is

$$R_{match}^2 = \frac{K_{reduced}}{k_{0,Pierce}{}^2} = \frac{K_{reduced}}{K_{full}} R_0^2 \ , \tag{82}$$

which gives a mismatch wave number in the Pierce gun of

$$k_e = \sqrt{k_{0,Pierce}^2 + \frac{K_{full}}{R_0{}^2}} = \sqrt{2\frac{K_{full}}{R_0^2}} = \sqrt{2\frac{1.515\times 10^4 I_{full}}{V^{3/2} R_0^2}}. \tag{83}$$

In the UMER gun (where the current is 0.118 A), this gives

$$k_e = 14.9 m^{-1} \tag{84}$$

and

$$\lambda_e = 0.420m. \tag{85}$$

Note that the calculated wavelength is much longer than the cathode-anode distance of 0.025 m. This, and the fact that this calculation is not intended to apply to beam radius changes of more than 50%, suggest that the first-order mismatch approximation being used may work.

$$R(s) = R_{match} - (R_0 - R_{match})\sin\left(k_e s + \frac{\pi}{2}\right), \tag{86}$$

which gives

$$R(0) = R_0 \tag{87}$$

and

$$R'(0) = 0 \tag{88}$$

as desired. Rewriting (86) in terms of generalized perveance in the gun gives

$$R(s) = \sqrt{\frac{K_{reduced}(I)}{K_{full}}}R_0 - \left(R_0 - \sqrt{\frac{K_{reduced}(I)}{K_{full}}}R_0\right)\sin\left(k_e s + \frac{\pi}{2}\right) \tag{89}$$

or

$$R(s) = R_0\sqrt{\frac{I(BV)}{I_{\max}}} - R_0\left(1 - \sqrt{\frac{I(BV)}{I_{\max}}}\right)\sin\left(k_e s + \frac{\pi}{2}\right). \tag{90}$$

For UMER, evaluated at $s_A = 0.025m$, this becomes

$$R(s_A) = 0.004m\left(-0.932 + 1.932\sqrt{\frac{I(BV)}{0.118}}\right). \tag{91}$$

When this value is used as R_1 in Eq. (79), the current density just the left of the aperture can be calculated. When this is multiplied by the aperture size corresponding to the 25 mA beam, the output current in the transition region can be

calculated. Combined with the Child-Langmuir law for the saturation region and the triode law for higher value of the bias voltage, a fairly good match to experiment is found with a transmission factor of 0.63 and an amplification factor of 910. This is shown in Fig. 69. In this plot, the experimental data is shown in red, the mismatch approximation curve is shown with black dashes, and the full beam triode law curve is shown with black dots. The total theory for all regions is shown in blue.

The saturation region and the full-beam triode regions are in very good agreement with the data, as expected. The transition region (50 V < BV < 58 V) is approximately right compared to experiment, but seems to be shifted to the left by 2.5 V. If we shift it to the right by 2.5 V, it exactly predicts the data points at BV = 52 V, 54 V, and 56 V. This makes the plot look nicer, but there is not a clear theoretical reason to do that. The theoretical curve is peaked at BV = 58 V. The data is actually peaked at 59 V, which is not obvious in this data set, but is clearly shown in other data sets. This is reproduced exactly if the transition region curve is shifted right by 2.5 V. Even if the transition region curve is shifted right by 2.5 V, the theoretical peak is still sharply pointed, while the data is rounded. Near the predicted maximum, the shape of the current curve as a function of bias voltage should be very sensitive to the transverse beam distribution, and particularly to the current density near the beam edges. In the theory presented here, the current density in the beam was assumed to be uniform. However, if the beam (at bias voltages higher than ~ 55 V) has higher current density in the center than near the beam edges, the transition region curve would become rounded near peak current. Also, it has been pointed out that this

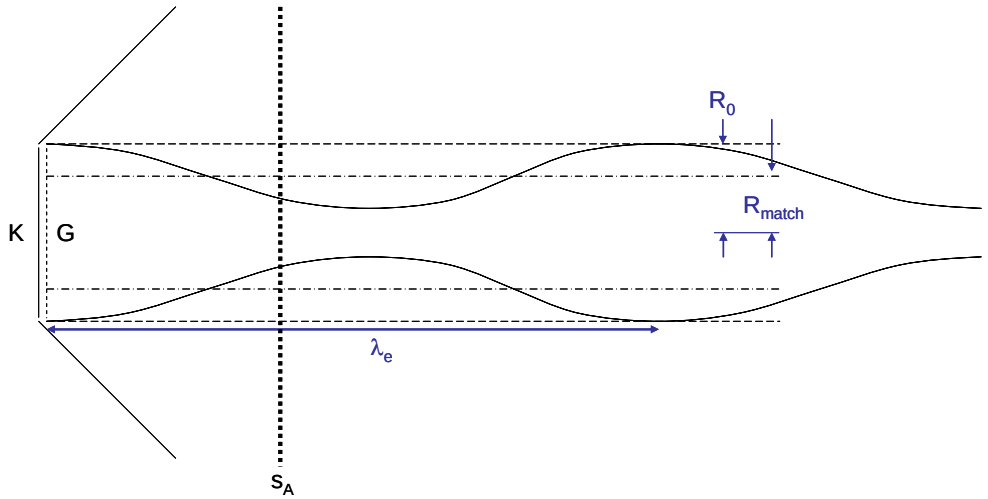

Fig. 68. Over-focusing due to decreased current in Pierce gun will result in transverse mismatch oscillations because the new matched-beam radius (R_{match}) is less than the cathode radius (R_0), which was the matched-beam radius for full-current operation. Distance from cathode (K) to the plane of the anode aperture plate (s_A) is much less than the mismatch oscillation wavelength (λ_e).

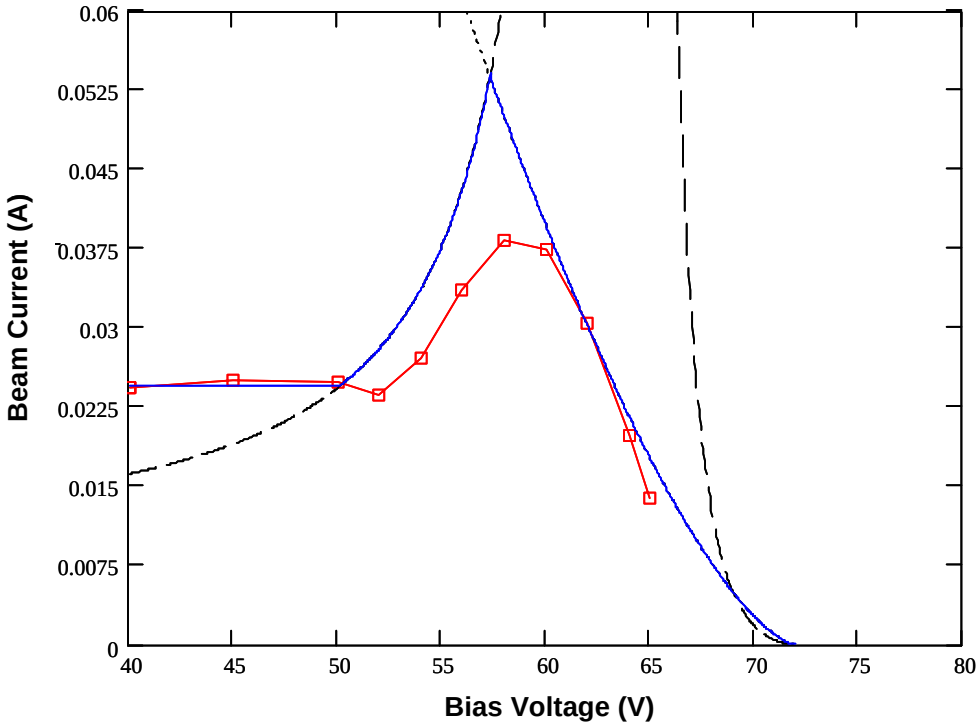

Fig. 69. Average beam current variation due to change in bias voltage. Experiment (red) and theory (blue). Overall trends are reproduced well, but there is some discrepancy, especially near the peak beam current, where the effect is very sensitive to transverse beam profile. A uniform transverse beam profile was assumed for the theory. The actual transverse beam profile is centrally-peaked, which will account for the rounding of the curve seen in the experimental data.

model of Pierce over-focusing should apply anytime the beam transitions from space charge limited to source limited operation, and therefore should be able to explain the anomalous dependence of beam current on cathode temperature mentioned at the beginning of this section [52]. Note also that mismatch oscillations can result in emittance growth and halo formation [1]. Finally, it is very important to remember that the physics in the gun, both transverse and longitudinal, is extremely complex [53], while the model presented here is quite simple. This model does not include key details about the beam behavior in the gun, such as transverse density variation or virtual cathodes. These details can be expected to have a strong influence on the actual output characteristics of the UMER gun.

4.3. Beam Modulation and Longitudinal Effects

In the first part of this chapter, we discussed some principles of triode operation as they relate to the UMER gun, and described some unusual effects that occur in UMER as a result. However, the effects discussed so far do not have a strong relation to longitudinal dynamics. In the rest of this chapter, we will return our focus to longitudinal effects. We first describe a beam modulation that appears "spontaneously" in the UMER beam under certain operating conditions, and explain this in terms of the triode nature of the UMER gun. Then we will discuss the evolution of this modulation in the UMER beamline in the context of the sound speed for longitudinal space charge wave propagation.

4.3.1. Observation

The modulation discussed here had been discovered soon after delivery of the UMER gun [79]. At that time, it was considered that the effect was of no interest, and simply an operating point to be avoided. Having decided on a "better" operating point that avoided these effects, they were largely forgotten.

The modulation was "rediscovered" during longitudinal expansion experiments. A bump was observed on the beam tail which had not been seen before. In an attempt to understand the source of this bump, various machine settings were changed. These controls had no influence on the bump, but a profound change in the beam was noticed when the bias voltage was increased from 40 V to about 60 V. When this was done, the beam no longer had a rectangular pulse shape, but rather showed a strong modulation at the head followed by significant droop throughout the rest of the pulse. The region containing the droop could be eliminated by using a shortened pulse forming line (Fig. 70). This condition occurred just before cutoff (Fig. 71). The research group had previously been tasked to develop a way to produce a modulated beam in one of our existing machines, in hopes of observing an expected shift from density modulation to energy modulation, and back again [3]. In fact, our beam *was* evolving as it traveled along the beamline, with the modulation at first nearly disappearing, then reappearing, and then beginning to disappear again (Fig. 72). The immediate issue became to determine if this was a real effect, or some sort of detector problem. The most significant reason to believe it was a real effect is the systematic nature of the change from one detector to the next. The modulation detected by the BPMs changes slowly from one device to the next as the beam goes

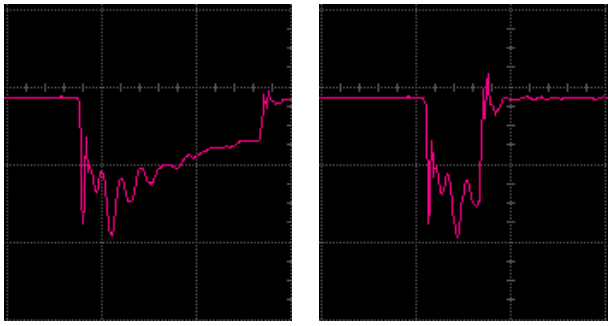

Fig. 70 Bergoz FCT trace showing modulation; (l) 100 ns beam, (r) ~40 ns beam.

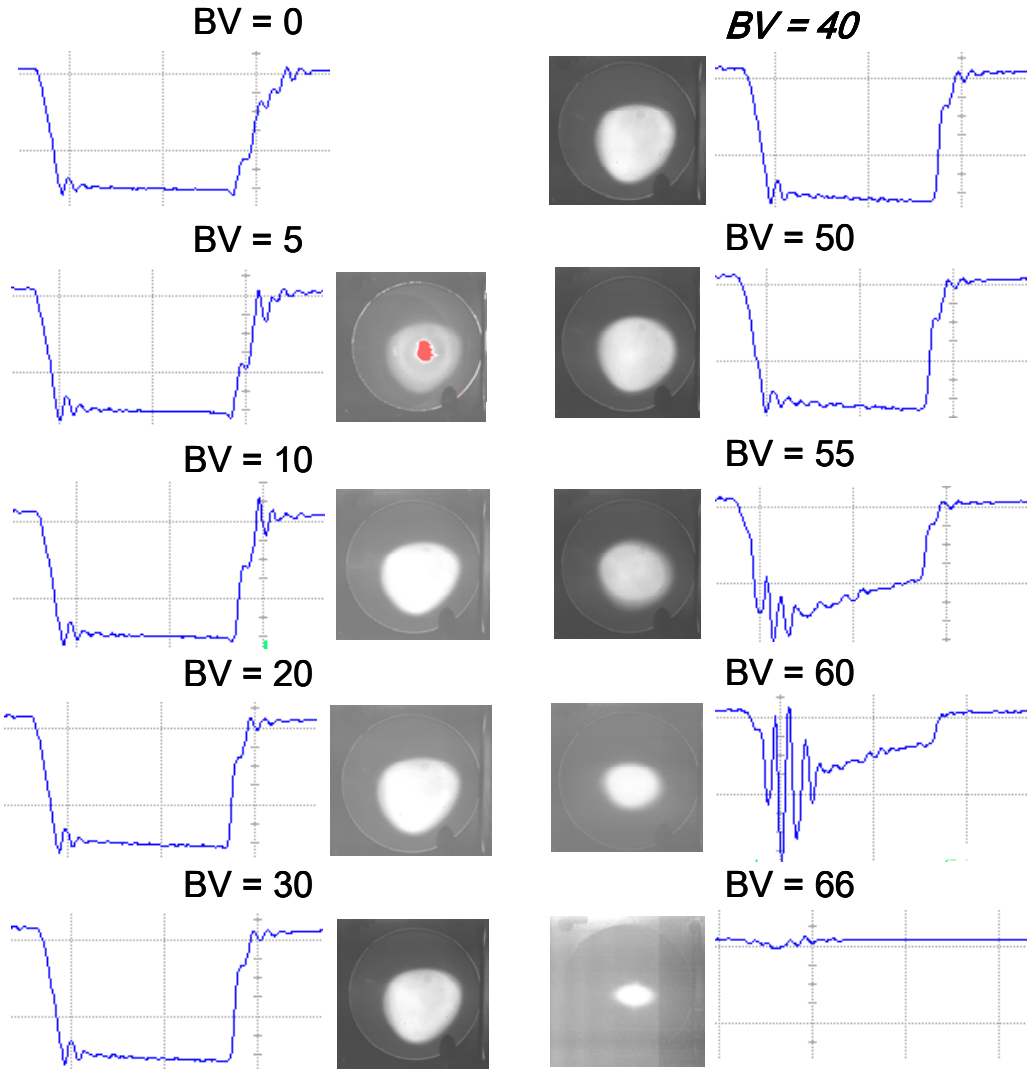

Fig. 71. UMER Measurements (3-29-04). BPM 10 (new electronics), Phosphor Screen at RC 11, 85 mA standard settings. around the ring.

If this was a detector effect, it is most likely that there would be more randomness in the modulation strength detected from one BPM to the next, or that the "ringing" in the detector circuit would fall with distance along the beamline, as space charge driven longitudinal expansion increased the beam rise time and therefore would provide less of an impulse to drive the ringing. Neither of these was the case. In addition, the modular nature of the BPM electronics allowed different electronics packages to be attached to a particular BPM to see if changing the specific output circuits significantly changed the output signal. First, the electronics packages of the locations with most and least detected modulation were swapped, but the modulation measured at each specific location remained approximately the same. Next, a single electronics module was used to take data at each location. These results, shown in Fig. 72, show that the modulation was still seen. Finally, a comparison was made between the modulation seen with the new faster-risetime electronics modules recently installed, as compared to that seen with the old, slower modules (Fig. 73). It is clear that the new BPM electronics respond more strongly to the modulation than the old electronics, or the Bergoz FCT. In fact, the trace at BPM 0 with the new electronics is actually seen to cross the zero-current line during the modulation, which suggests a resonance in the electronics is being driven. However, the modulation is observed on both detector types and with both types of BPM electronics, and the trend of decreasing and then increasing modulation strength is seen in all cases. This strongly suggests that there is a real modulation on the beam, and that the modulation is disappearing and then reappearing. In addition, this modulation was found to be relatively insensitive to changes in focusing and bending magnet strengths, although

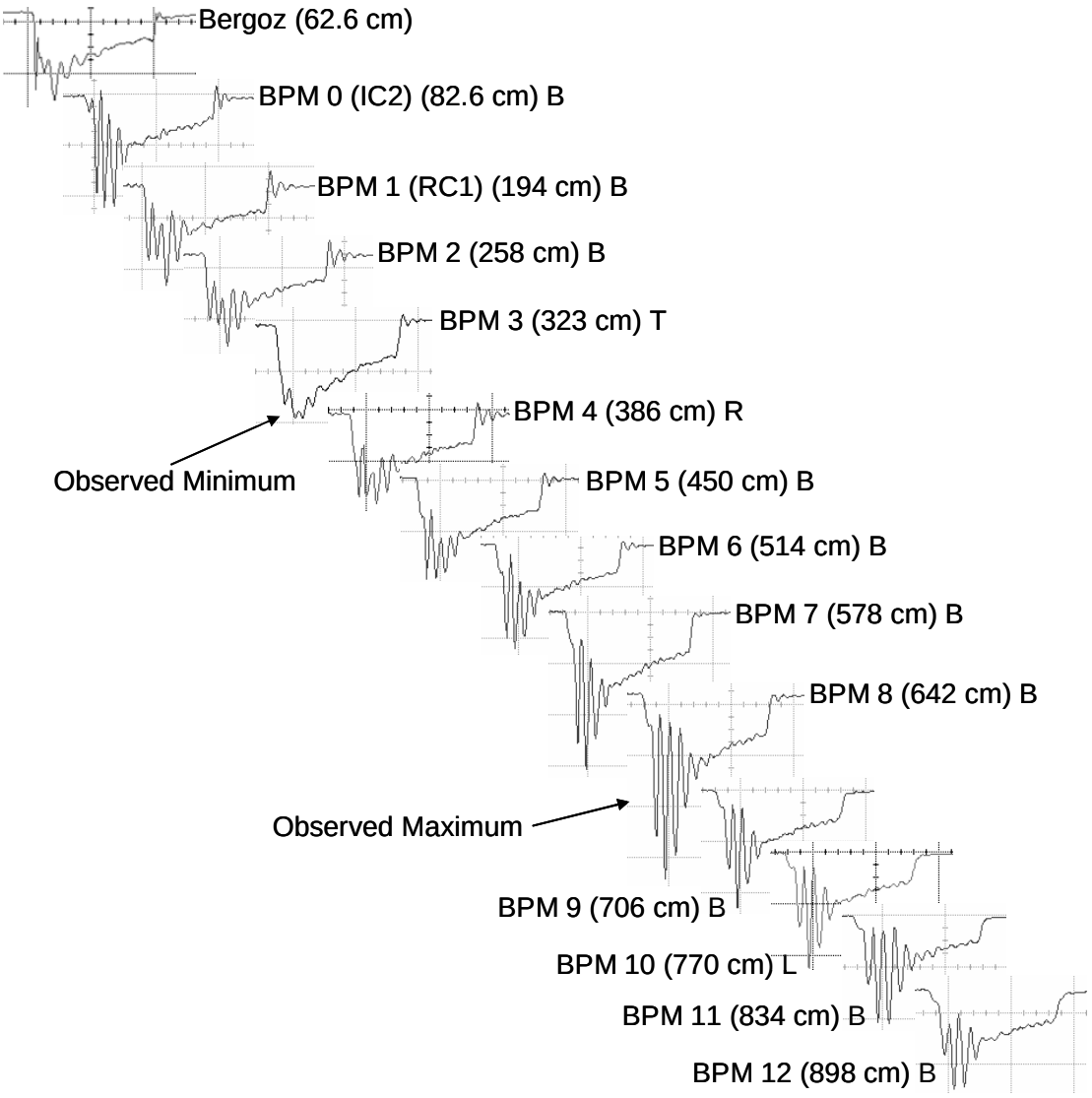

Fig. 72. UMER Measurements (3-31-04). Bias Voltage 60 V, std. 85 mA settings otherwise. BPM Electronics Set #0 (new electronics) used for all BPM measurements.

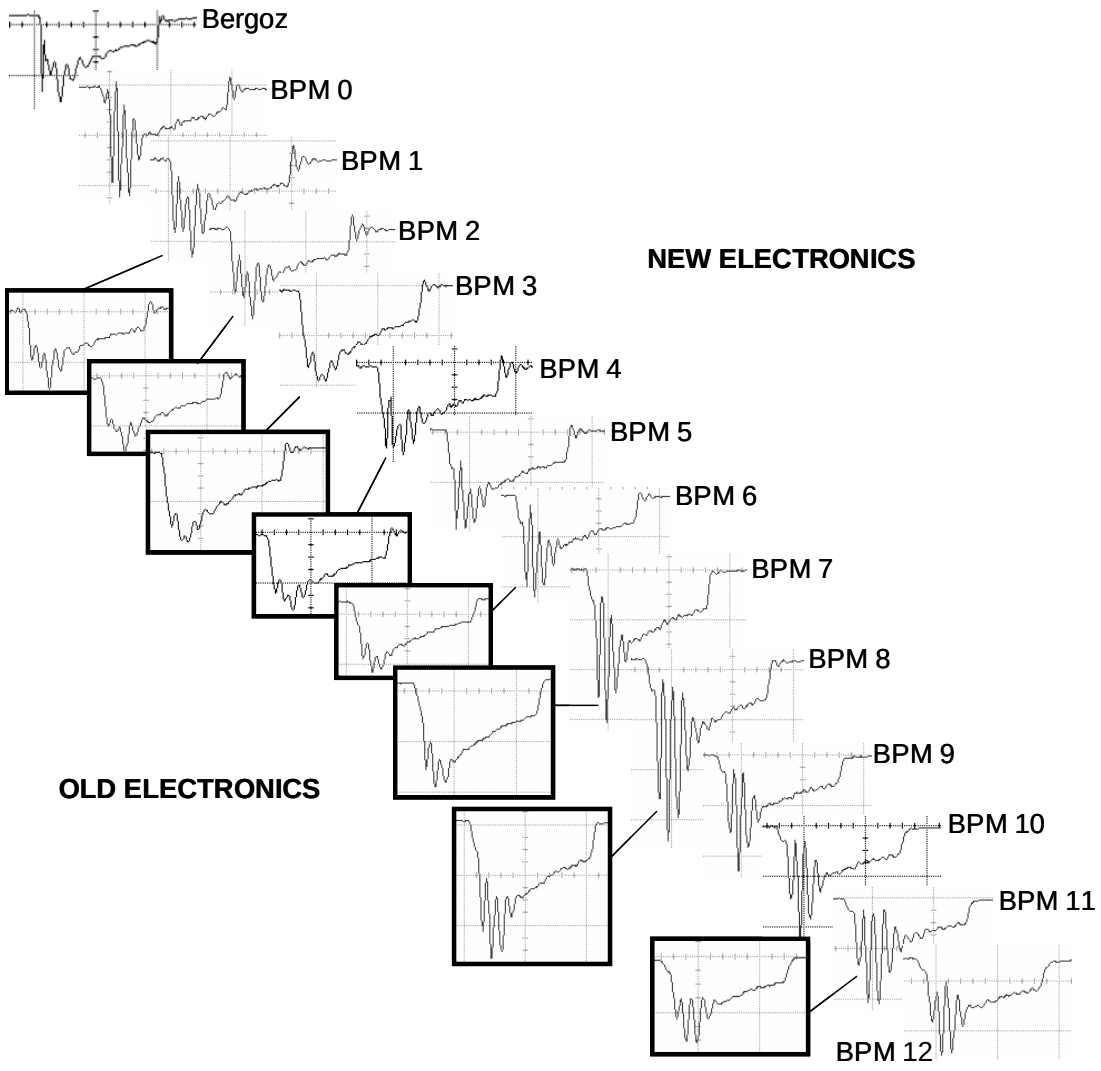

Fig. 73. UMER Measurements (3-31-04). Comparison of Old and New Electronics. Bias Voltage 60 V, std. 85 mA settings otherwise. Old Electronics show less ringing than New Electronics. Both sets show the same trend of decay, growth, decay in the "modulation"

changes in solenoid and Helmholtz coil currents tended to "flatten" the beam pulse, probably due to scraping of higher-current (and therefore wider) portions of the beam against the beam pipe. The remaining issues were to determine the source of the modulation, and to understand the evolution of that modulation.

4.3.2. Source of Modulation

As shown in Fig. 71, between a bias voltage of 0 V and 50 V, the pulse shape is approximately rectangular. The "bump" is present on the trailing edge of the beam, and decreases slowly with increasing bias voltage. The flat top does exhibit "reverse droop," which is indicative of the beam impacting on BPM plates due to mis-steering. Between bias voltage values of 50 V and 66 V, the average beam current falls quickly with increasing bias voltage, with the pulse exhibiting a sudden strong modulation followed by severe droop. At a bias voltage of 66 V, the beam is essentially undetectable with BPMs, and barely visible on the phosphor screens. The modulation frequency observed is approximately 115 MHz, found by measuring the period at the strongest part of the modulation. However, the spacing between adjacent peaks in the modulation becomes smaller near the head of the beam, so that the modulation frequency is higher towards the beam head, and lower towards the beam tail (Fig. 74). Varying the cathode heater voltage, solenoid, and quadrupoles had no effect on the frequency, and only the bias voltage affected the strength of the modulation.

The suggestion to try to explain this modulation as a triode effect in the UMER gun was first proposed by Y. Cui, based on his experience with a similar gun

used on the Long Solenoid Experiment at Maryland [33,82]. No pulsed power system produces ideal, rectangular output pulses. Instead, the pulses typically have overshoot, ringing at the head and tail, and droop during the pulse. In UMER, the cathode pulse is applied between the grid and cathode (Fig. 75). Since amplification occurs in triodes by applying voltages across the grid-cathode gap, to which the triode current is very sensitive, any nonideal structure in the cathode pulse will be amplified, producing similar, though much more pronounced nonideal structure in the beam pulse. Thus, in UMER, the current produced by the gun in triode amplification mode will be

$$I_T(t) = K_T\left[\left(PV(t) - BV\right) + \frac{10kV + PV(t) - BV}{\mu}\right]^{3/2} \pi r_c^2 T_g T_a , \qquad (92)$$

where K_T is the triode constant from Eq. (73), $PV(t)$ is the cathode pulser voltage as a function of time, BV is the bias voltage, μ is the amplification factor, πr_c^2 is the area of the cathode (and therefore the cross-sectional area of the beam, assuming ideal Pierce focusing), T_g is the transmissivity of the grid (0.66), and T_a is the transmissivity of the anode grid (0.87) (See Fig. 76). Note that the single grid voltage V_G of Eq. (72) referred to the potential at the grid relative to the potential at the cathode, and therefore is the sum of the cathode pulser voltage and the bias voltage in UMER. Similarly, the single anode voltage V_A of Eq. (72) is the potential at the anode relative to the potential at the cathode, and therefore in UMER is the sum of the cathode pulser voltage, the bias voltage, and the 10 kV accelerating voltage. The sign convention for the bias voltage and the cathode pulser voltage in Eq. (92) and Fig. 75 reflect the functions of these voltages. The bias voltage serves to suppress

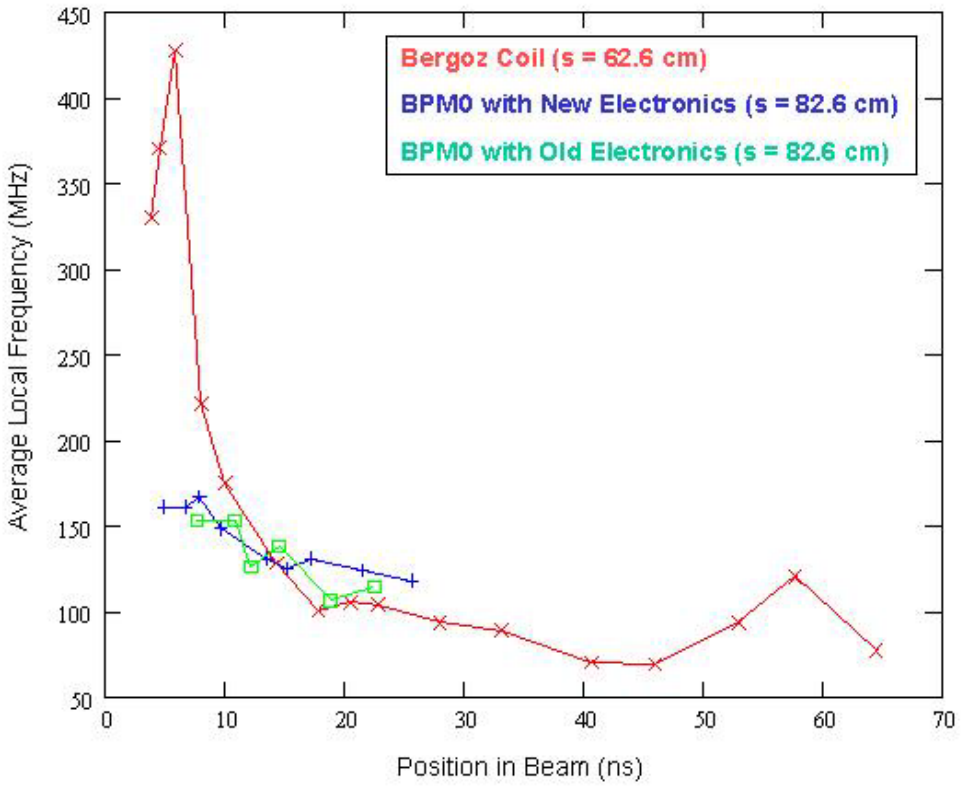

Fig. 74. UMER data 4-9-04 -- frequency of modulation vs. position in beam. 100 mA nominal beam settings, 60 V bias voltage, actual beam current ~ 25 mA

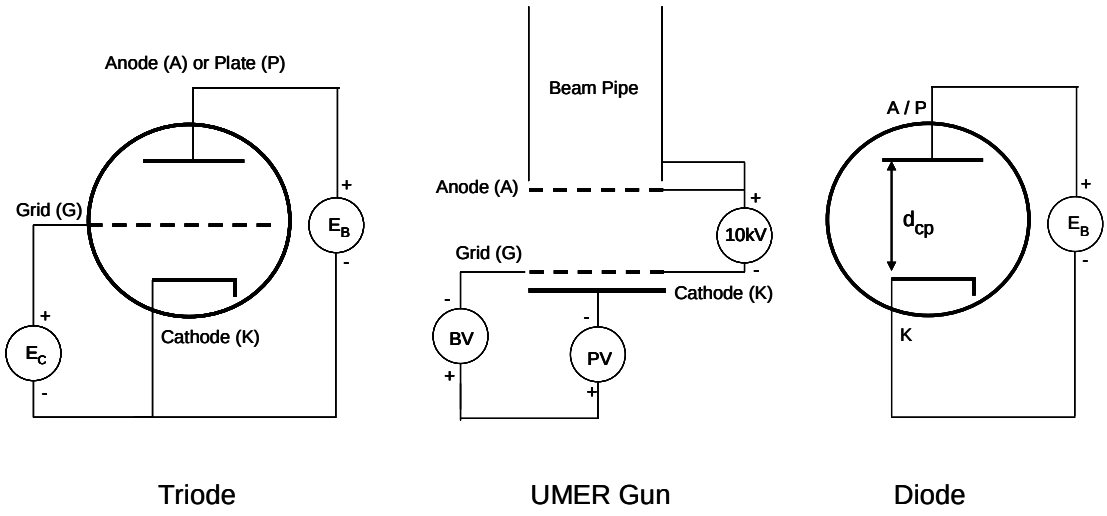

Fig. 75. Comparison of the UMER gun with a vacuum diode and triode.

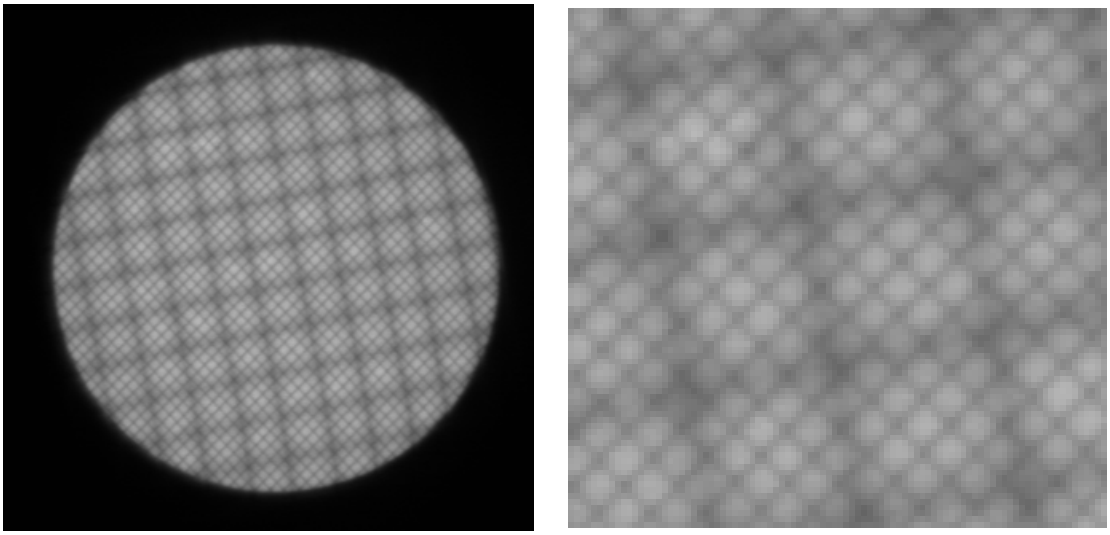

Fig. 76. Visible light image of hot cathode in UMER. Shadow of grid mesh (fine) and anode mesh (coarse) are visible [25].

emission from the cathode by holding the grid at a negative potential relative to the cathode, but is quoted on the UMER controls as a positive number. Similarly, the pulser voltage is generally quoted as a positive number, but serves to make the grid less negative with respect to the cathode during the cathode pulse.

Eq. (92) holds as long as the gun is in triode amplification mode. If at any time the value of current predicted by Eq. (92) exceeds the Child-Langmuir limit, the triode will be in saturation. For the UMER gun, the Child-Langmuir limit is given by

$$I_D(t) = K_D\left[10kV + PV(t) - BV\right]^{3/2} \pi r_c^2 T_g T_a , \tag{93}$$

with

$$K_D = \frac{2.335\times 10^{-6}}{d_{ca}^2} , \tag{94}$$

where d_{ca} is the distance from cathode to anode. Again, note that the potential difference of interest for the Child-Langmuir equation is that between the cathode and anode, which in UMER must take into account the cathode pulser voltage and the bias voltage. In practice, however, the inclusion of the pulser voltage and bias voltage provides a correction of only about 1% in the beam current.

With an assumed, but reasonable shape for the cathode pulser voltage (Fig. 77), this model explains all the observed structure on the beam pulse (Fig. 78). At small values of the bias voltage, the triode equation predicts a much higher current than the diode equation, so the gun is in saturation, and the output pulse shape predicted by the triode equation is clipped at the space charge limit. (Note that at *very* small values of bias voltage, the field from the anode, penetrating the grid mesh

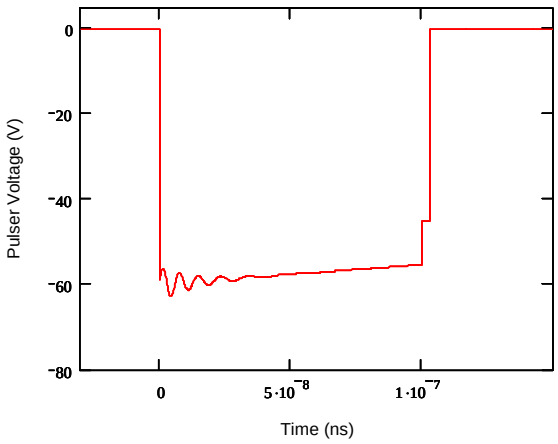

Fig. 77. Assumed pulser voltage. Ringing, droop, and "step" are chosen to reproduce observed beam pulse shape. Ringing and droop are common in pulsed circuits, but the source of the step is unknown, but accounts for the "bump" discussed in Chapter 3. Pulser voltage used (not including step) is given by

$$-60\exp(-0.5\times10^{6}t)+3\exp(-7\times10^{7}t)\sin(1300\times10^{6}\exp(-10^{7}t)t)$$

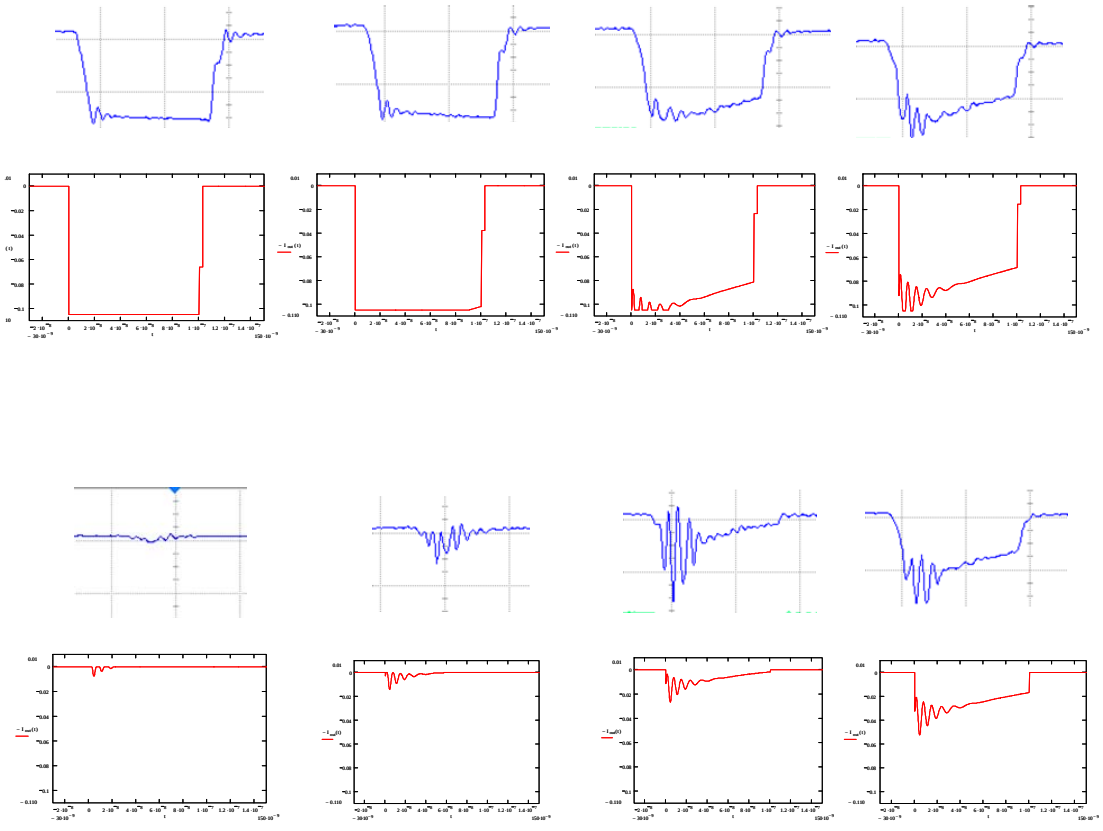

Fig. 78. Comparison of triode calculation to measured beam profile for several bias voltage values. Top left BV ~ 0 V; bottom left BV ~ 70 V

and influencing the cathode, will prevent the cathode from reaching cutoff at all, and the beam will be continually on at low current but with a higher-current phase during the cathode pulse. This condition is not obvious from BPM traces, as the effect is to move the entire trace, including the background level, to higher current. However, it is very obvious from looking at phosphor screens, which will show a bright region where the cathode is failing to reach cutoff, causing part of the beam to be DC.) As the bias voltage is increased, the current predicted by the triode equation is decreasing, but still exceeds the space charge limit, and is therefore still clipped. Note that the "bump" serves as a marker below the space charge limit, and the model correctly predicts its decreasing amplitude with increasing bias voltage. As the bias voltage is increased further, the modulation at the head of the pulse and the amplified droop at the tail become visible. Note that the modulation is being clipped by the space charge limit. Continuing to increase the bias voltage brings the entire pulse well below the space charge limit, so that the effects of all the structure on the cathode pulse are now reflected in the beam itself. Note that in the actual data, the modulation appears to increase in magnitude. This enhancement is probably due to circuit ringing in the BPM electronics. Further increase in the bias voltage brings the gun into triode cutoff, so that no current is being produced.

Although the triode model reproduces all the key features of the observed beam pulse shape, obtaining an exact quantitative match between the model and the data is more difficult, for several reasons. First, the exact pulse shape applied to the cathode is unknown. The pulse shape used in the model described here was an assumed pulse shape, with a functional form that was found to give good agreement

to the data when used in the triode model. Also, the amplification factor of the triode is believed to change as the bias voltage increases and brings the system towards cutoff. This is typical in triodes, and especially in triodes exhibiting *Insel Bildung* [70]. Unfortunately, it is not clear how to predict this change, and therefore the details of the beam pulse shape between 50 V and cutoff cannot be predicted exactly. Finally, the triode model discussed here does not take into account circuit ringing in the BPMs, which will have an effect on the observed beam pulse. Nevertheless, it seems clear that triode amplification in the UMER gun is responsible for the onset of the observed modulation.

4.3.3 Evolution of Modulated Beam in UMER

The proposal that this effect might be described in terms of space charge wave propagation was first proposed by I. Haber [83]. This is consistent with prior observations which showed that a perturbation in velocity or current introduced onto the beam would relax by production of a forward-traveling "fast wave," and a backward-traveling "slow wave," and that these waves travel in the beam frame at the sound speed

$$c_0 = \sqrt{\frac{qg\lambda_0}{4\pi\varepsilon_0 m\gamma^5}}\,. \qquad (95)$$

This is the same sound speed, which governs the beam end erosion of a rectangular beam pulse, as described in Chapter 3. (The production and evolution of discrete perturbations will be discussed in detail in Chapter 5.)

To study this modulation quantitatively, it was necessary to define a measure of the strength of modulation. Because the modulation is superimposed over a

nonuniform beam shape, and because the amplitude and frequency of the modulation are changing along the pulse, it was not clear how to establish a "zero" line about which the modulation amplitude could be measured. Instead, the vertical distance between the "deepest valley" to the "highest adjacent peak" was used. Although the BPMs can in principle be calibrated to give currents in amperes [28], this calibration was not established at the time of the experiments described in this chapter. The signal produced on individual BPM channels will vary with transverse steering of the beam. In order to take this into account, the measured depth of modulation was normalized by dividing it by the peak amplitude in the pulse, and then averaging the result over all available BPM channels. Figure 79 illustrates this measure, called the "average normalized modulation depth," or ANMD.

With this measure defined, ANMD values were extracted from BPM data and plotted against distance traveled by the beam. For these measurements, two beam configurations were used. The first used the 85 mA aperture and 85 mA beam transport settings, while the second used the 100 mA (full) aperture and 100 mA beam transport settings. In all cases, a bias voltage of 60 V was used, as this was found to produce the most significant modulation. Note that although the 85 mA and 100 mA settings were used, the actual beam currents, measured near the center of the beam, were approximately 43 mA and 25 mA, respectively. (These two beams will be denoted as the 85/43 mA beam and the 100/25 mA beam.) A reduction in beam current is expected because of the action of larger bias voltages in suppressing emission from the cathode. It is not entirely clear, however, why the current would have been reduced more in the case of the 100 mA beam settings compared to the 85

Measure of Modulation Strength: Average Normalized Modulation Depth

1) “Modulation Depth” – Distance from “deepest valley” to “highest adjacent peak”

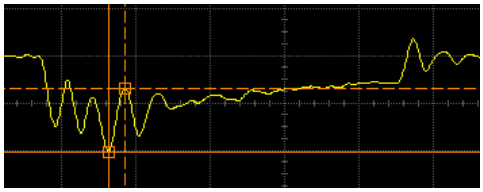

2) “Normalized” – Divide “Modulation Depth” by “Peak Amplitude”

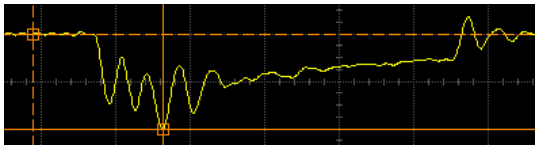

3) “Averaged” – Average over the values from each channel on the BPM

Fig. 79. Average Normalized Modulation Depth.

mA settings, but this is probably due to beam loss due to misfocusing at the reduced beam currents. The plots of ANMD as a function of distance traveled from the cathode are shown in Figs. 80 and 81.

The exact shape of the modulation on the beam in these experiments is complicated, with its frequency and amplitude changing during the beam pulse. In addition, the background beam level is varying during the pulse as well. Instead of this complicated shape, assume the modulation consisted of a simple cosine wave applied to a uniform background current. In this case, we would assume by analogy with the evolution of perturbations in intense beams that the modulation would split into a forward-traveling wave and a backward-traveling wave, described by

$$A(t,z) = \cos(\omega t - kz) + \cos(\omega t + kz)\,, \tag{96}$$

where k is the wave number associated with the spatial frequency of the modulation on the beam. These waves would travel past each other at the sound speed in the beam, interfering constructively and destructively. The result would be that the modulation would be seen to alternately disappear and reappear (Fig. 82a). When the amplitude is watched at a particular point, the value of the function there will vary as a cosine function of time with a frequency ω (Fig. 82b). However, the measure of modulation strength we defined is not the amplitude of the modulation, but rather depends on the difference in height between the crest and the trough. This value is always positive, and therefore scales roughly as the absolute value of the cosine of ωt (Fig. 82c). Because the beam is traveling in the laboratory frame, an evolution of the beam in time will be observed as an evolution in space, and ωt can be replaced by $\frac{\omega s}{c\beta}$, where s is the distance traveled in the laboratory frame.

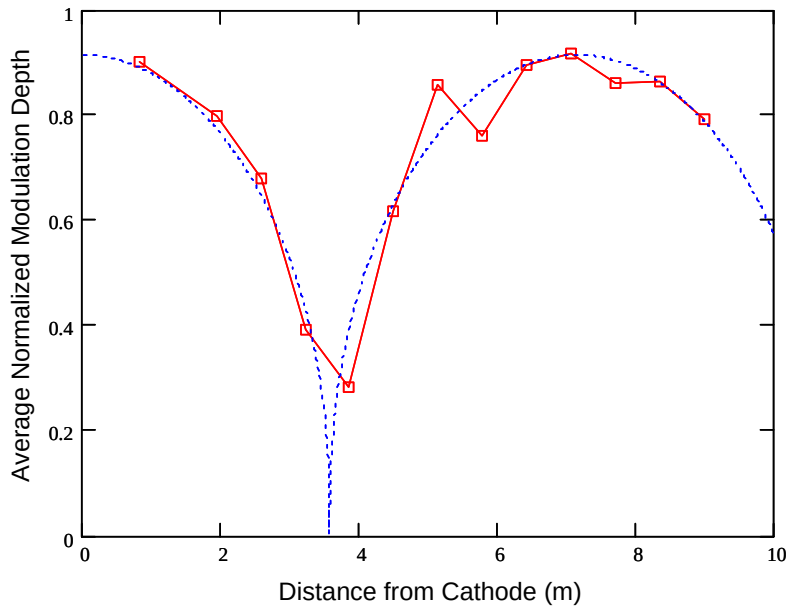

Fig. 80. Change in ANMD of modulation during travel along UMER beamline. 85 mA settings were used. Fit is:

$$ANMD(s) \approx \left|0.915(\cos(0.44s))^{0.4}\right|$$

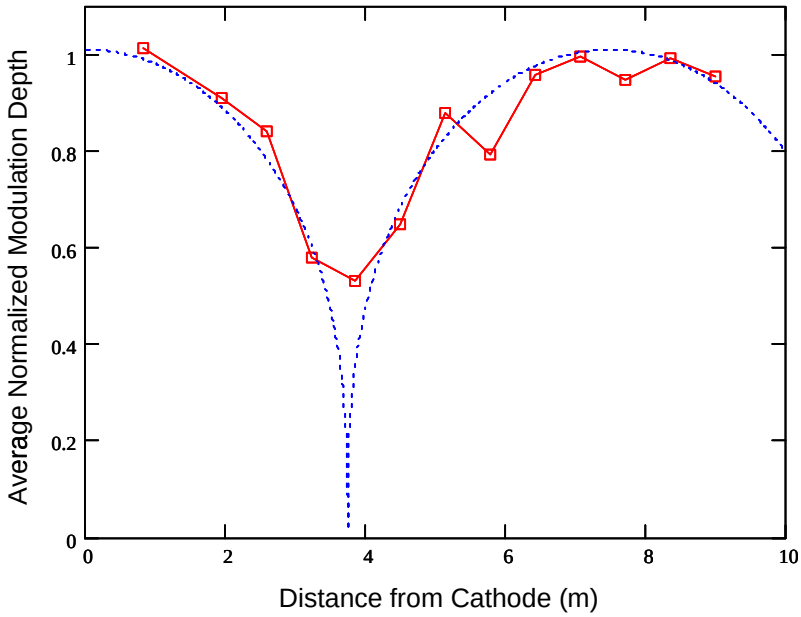

Fig. 81. Change in ANMD of modulation during travel along UMER beamline. 100 mA settings were used. Fit is

$$\left|1.01(\cos(0.42x))^{1/3}\right|$$

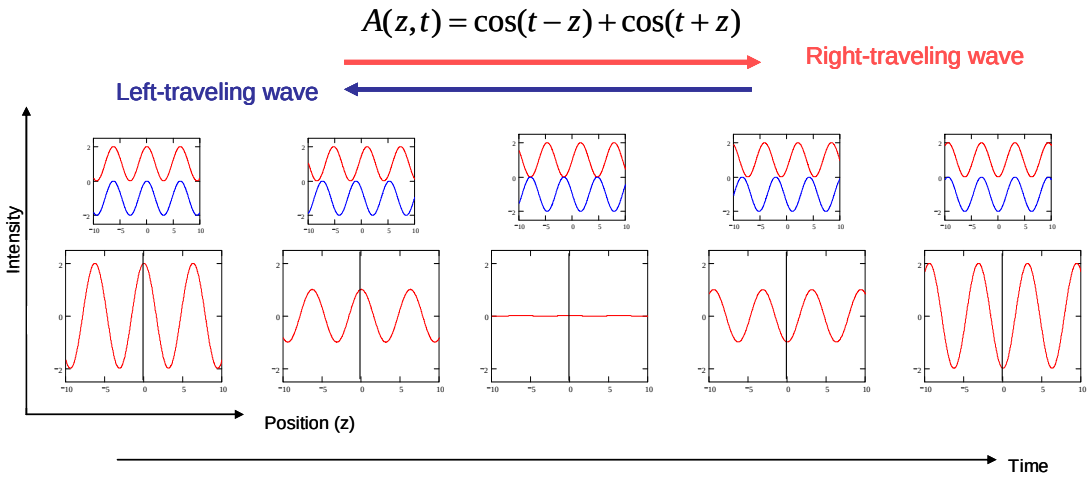

Fig. 82a. Interference of waves.

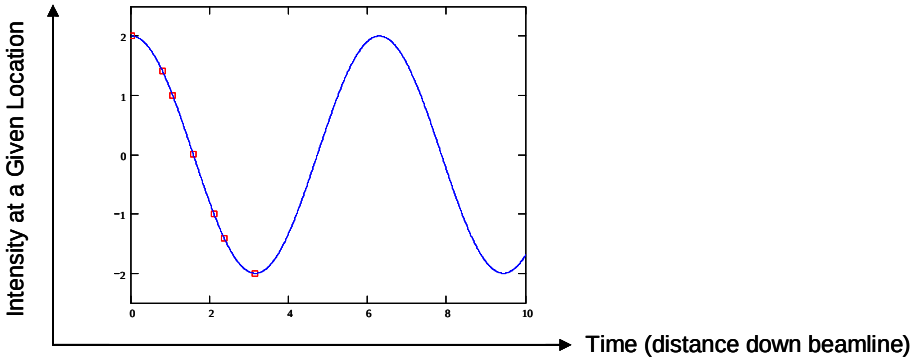

Fig. 82b. Resulting measured amplitude for fixed location in beam.

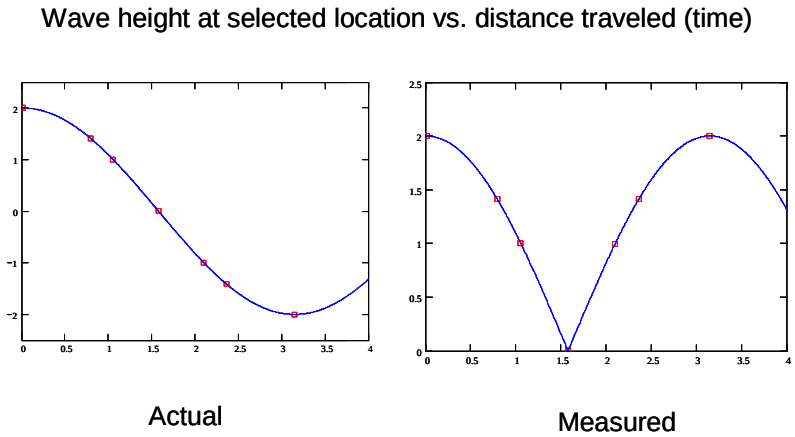

Fig. 82c. Result of measurement technique using absolute value of observed amplitude.

To determine the value of $\frac{\omega}{c\beta}$, curves were fit to the data, as shown in Figs. 80 and 81. Initially, the absolute value of a cosine function was tried. It was found, however, that such curves didn't match the curvature of the data points, but that raising the absolute value of a cosine function to a fractional power would produce a curve which matched exactly. This is a result of the way the ANMD was defined. First, the difference in height between the highest crest and the adjacent trough was found. This is not the maximum amplitude of the modulation, but rather twice the maximum amplitude. Then, this value was divided by the difference in height between the deepest trough and the zero-current level. This value, in turn, is not the background beam current, but the sum of the background beam current with the maximum amplitude of the modulation. The ANMD is therefore actually given by

$$ANMD = \left\langle \frac{2A_{\max}}{A_0 + A_{\max}} \right\rangle_{allchannels}, \tag{97}$$

where $A_{\max}$ is the amplitude of the strongest part of the modulation, A_0 is the signal level present without modulation, and the ratio is averaged over all available BPM channels. For the simple case of a uniform pedestal with counter-propagating cosine waves, the ANMD would be

$$ANMD = \left\langle \frac{2\left[a\cos(t-x) + a\cos(t+x)\right]}{A_0 + \left[a\cos(t-x) + a\cos(t+x)\right]} \right\rangle_{allchannels}. \tag{98}$$

Note that the ANMD becomes zero when the counter-propagating waves exactly cancel out. This is the same condition that gives the null in the curve of absolute value of cosine. Therefore, even though the functional form of the ANMD and

absolute value of cosine curves will differ, the interpretation of the null points (and the cosine arguments) is identical.

From the fitted curves shown in Figs. 80 and 81, the values of $\frac{\omega}{c\beta}$ for the 85/43 mA case and the 100/25 mA case are found to be 0.44 m^{-1} and 0.42 m^{-1}, respectively, and the values of ω are $2.64\times10^{7}\,s^{-1}$ and $2.52\times10^{7}\,s^{-1}$. The assumed expression for the modulation, Eq. (96), also contains a spatial term kz. In the same way that the beam's movement causes the "time" term ωt to be observed as a "spatial" term in the lab, the "spatial" term kz is observed in the lab as a "time" quantity, the modulation frequency. In particular, the spatial wave number k can be rewritten as $\frac{2\pi f}{c\beta}$, where f is the observed frequency of modulation in the laboratory frame. The frequency is actually a function of position in the beam, but since only one null is observed, and since the ANMD is measured at the location of peak modulation intensity in the beam, we can simply use the frequency corresponding to this location, which is approximately 115 MHz. Thus, the value of k is approximately 12.0 m^{-1}. Note that a single value of k can be specified for both beam current settings, because the frequency of modulation is defined by ringing in the pulser circuit, which is insensitive to beam current. The phase velocity of the fast and slow waves is then given by

$$v_p = \pm\frac{\omega}{k}. \tag{99}$$

The value of the phase velocity in the two cases is then $\pm 2.193\times10^{6}\ m/s$ for the 85/43 mA beam, and $\pm 2.094\times10^{6}\ m/s$ for the 100/25 mA beam. These values are

approximately what would be expected in the UMER beam (Table 9). The sound speed in intense beams is a measure of gI, the product of the geometry factor and the beam current. The geometry factor is a function of beam current, as discussed in Chapter 3. Unfortunately, in the modulated beams being considered here, it is not clear how to exactly measure the beam current, due to the strong modulation, the varying modulation amplitude, and the varying background current. The most that can be said is that the measured sound speeds agree fairly well with those predicted at the various current levels found in the beams.

4.3.4 Velocity Modulation and Current Modulation

In this discussion, we have assumed that the forward-traveling and backward-traveling space charge waves are of equal magnitude. This is a good assumption when the initial perturbation or modulation is in current (density) only, but may fail if velocity modulation is present also. It is therefore useful to know the relative strengths of the velocity and current modulations in the case of triode-amplified pulser ringing in the UMER gun. We can estimate these strengths using the triode model introduced here for the UMER gun, along with the inferred pulser voltage. The electrons in UMER are nonrelativistic, and so the beam voltage V_0 is related to the beam velocity v_0 by

$$v_0 = \sqrt{\frac{2qV_0}{m}} . \tag{100}$$

Any variation in the beam voltage will produce a variation in the beam velocity, according to

	25 mA	43 mA	85 mA	100 mA
Geometry Factor	*3.191*, 4.191	*2.648*, 3.648	*1.967*, 2.967	*1.804*, 2.804
Wave Speed (Mm/s)	*1.38*, 1.581	*1.649*, 1.935	*1.998*, 2.453	*2.075*, 2.587

Table 9. Geometry factor and wave speed calculated for several currents. Calculated geometry factors include dependence on beam current. Italicized values used alpha of 0, non-italicized values used alpha of 1.

$$\Delta v = \sqrt{\frac{q}{2mV_0}}\Delta V \,. \tag{101}$$

Following the notation of [58], we say that the initial strength of a small velocity perturbation or modulation v_1 is related to the unperturbed or unmodulated velocity v_0 by

$$v_1(0,t) = \delta v_0 f(t)\,, \tag{102}$$

where δ is a small quantity specifying the strength of the perturbation, and $f(t)$ is a function, varying between 0 and 1, specifying the shape of the perturbation. The maximum initial velocity perturbation and the unperturbed velocity therefore specify the perturbation strength:

$$\frac{v_1\big|_{\max}}{v_0} = \delta \,. \tag{103}$$

This means that in our case, the velocity perturbation strength is also given by

$$\delta = \frac{\Delta v\big|_{\max}}{v_0} = \frac{\Delta V\big|_{\max}}{2V_0} \,. \tag{104}$$

Because electrons generated at the cathode must travel through the grid, and through the anode to exit the gun, the total beam voltage is

$$V(t) = 10kV + PV(t) - BV \,. \tag{105}$$

If we only consider the time when the gun is producing beam, and we treat the pulser voltage as the sum of a DC component PV_0 with a sinusoidal component ΔPV, we can write the unperturbed voltage as

$$V_0 = 10kV + PV_0 - BV\,, \tag{106}$$

so that the strength of the voltage perturbation is

$$\delta = \frac{\Delta PV\big|_{\max}}{2\left[10kV + PV_0 - BV\right]}. \tag{107}$$

The maximum amplitude of the voltage modulation on the cathode pulse shown in Fig. 77 was 3 V. This inferred cathode pulse produced fairly good agreement with the observed modulation. This gives a value for δ of approximately 0.00015.

A similar procedure can be used to find the current perturbation strength η, defined, like δ, as the ratio of the maximum value of the initial perturbation current to the unperturbed current:

$$\frac{i_i\big|_{\max}}{i_0} = \eta. \tag{108}$$

The current in our triode is given by

$$I = K_T{}'\left(PV(t) - BV + \frac{10kV + PV(t) - BV}{\mu}\right)^{3/2}, \tag{109}$$

where $K_T{}'$ is the product of the triode constant of Eq. (73) with the area of the cathode, the transmissivity of the grid, and the transmissivity of the anode mesh. For simplicity, the pulser voltage and bias voltage in the anode term may be neglected, as they are on the order of volts or tens of volts. Variation in the pulser voltage results in a variation in the beam current; the maximum value of current variation is given approximately by

$$\Delta I\big|_{\max} \approx K_T{}'\frac{3}{2}\left(PV_0 - BV + \frac{10kV}{\mu}\right)^{1/2}\Delta PV\big|_{\max}, \tag{110}$$

so that the current perturbation strength is given by

$$\eta = \frac{\Delta I\big|_{\max}}{I} \approx \frac{3}{2}\left(PV_0 - BV + \frac{10kV}{\mu}\right)^{-1}\Delta PV\big|_{\max}. \tag{111}$$

This gives a value for η of approximately 0.41. Clearly, the current (density) modulation dominates over the velocity modulation in the UMER gun, so our assumption of forward-traveling and backward-traveling waves of approximately equal magnitudes is valid.

4.4. Conclusion

The UMER gun was intended for operation in the space charge limited regime, at operating points chosen to provide stable beam current and a rectangular pulse shape. When operated far from these chosen points, the gun exhibits a series of effects that produce beams with transverse and longitudinal structure, and average current levels that can exceed expected values. These effects can be explained by treating the UMER gun as a Pierce-focusing triode. One of these effects produces a modulated beam. When this beam is allowed to propagate in the UMER beamline, the modulation breaks into a forward-traveling and a backward-traveling space charge wave, which interfere, causing the modulation to appear and disappear as the beam moves through UMER. While this effect produces beam behavior which on the surface seems very different from that produced by discrete perturbations, the underlying physics is identical. In the next Chapter, we take up the issue of production and evolution of discrete perturbations in intense beams.

Chapter 5: Photomodulation and Perturbations

5.1. Introduction

One area of concern and interest for the design of beam transport and acceleration systems, particularly those propagating intense beams over long distances, is the generation and propagation of space charge waves in beams. These waves may originate from localized variations in the current density or velocity in a beam, which we will refer to as perturbations, regardless of their strength. There are a number of sources of perturbations and space charge waves, some intended and some unwanted. In longitudinal focusing systems, misfocusing and timing errors can generate unwanted waves due to over- or under-correction of beam expansion [84]. In photocathode systems, fluctuations of drive laser intensity can also create perturbations and waves. These may be unwanted [85-87], or may be used deliberately to create structure on the beam [88-90]. If the laser pulse is short enough, the resulting beam may even exceed the space charge limit [91]. In addition, deliberate use of applied perturbations gives flexibility in the selection of beam pulse shape, since any given pulse shape can be built from suitable perturbations.

Perturbations generated by any mechanism will evolve under space charge forces, in general by launching space charge waves. These waves may grow or decay under the influence of the resistive wall instability [1,87,92-94]. Perturbations may also have effects on the energy spread (longitudinal emittance in a beam) [95]. Deliberate application of perturbation-generated space charge waves is also being

investigated for use as a beam diagnostic [96,97]. In addition, under certain conditions, nonlinear effects have been observed, to include solitary wave propagation [98-101].

Once perturbations have been generated, and have evolved under space charge forces, the resulting features will be "frozen in" as the beam is accelerated to high energy. These features may then generate electromagnetic radiation through interactions with changing electric or magnetic fields or boundary conditions. Depending on the application, this radiation may be wanted [88-90] or unwanted [85].

Many experiments have been done at Maryland and elsewhere to study effects of perturbations in beams [93-97,99,100,102-105]. In order to generate perturbations, a way is needed to modulate beam current or velocity on a scale fast compared to the overall pulselength of the beam. This requirement for fast modulation prevents the use of certain control mechanisms, such as varying cathode temperature or accelerating potential[3], from being useful for this application. Instead, generation of perturbations has normally been accomplished by applying a voltage pulse across the beam. This can be implemented by use of a stub on the pulse forming line used to provide the gating voltage applied between the cathode and grid, or by a pulser connected to parts of the beam transport structure, such as electrostatic quadrupoles [96] or induction modules, farther downstream. All of these techniques provide modulation both of particle number (current) and particle velocity within the beam.

Recently, research has been conducted at Maryland on generation of beams using photoemission and thermionic emission simultaneously [91,106-109]. As part

[3] In UMER, the accelerating potential is DC. In principle it could be used to modulate the beam, but not without a major overhaul of the gun electrical systems.

of this research, this process has been used to produce perturbations generated by photoemission within longer beams generated by thermionic emission [108]. However, the system used was limited in its capabilities, as it was only able to produce a single perturbation at the center of the thermionic beam. This prevented it from being used to perform a number of interesting experiments involving multiple perturbations and perturbations in different locations.

As an extension of work being done on UMER on longitudinal effects in intense beams, and work being done by a colleague on modulation of electron beams at the cathode for generating terahertz radiation [88-90], it was decided to combine efforts and modify an existing but unused design for generating modulated electron beams by creating a train of drive laser pulses. With additional improvements in the triggering and timing system, a flexible, robust, simple system was implemented to produce multiple perturbations with variable timing anywhere within the 100 ns thermionic pulse in UMER [80].

This chapter will discuss the design and operation of this system, will present a theoretical framework for understanding the evolution of perturbations and waves in intense beams, and will show the results of a number of experiments conducted using this system.

5.2. Apparatus for Generating Multiple Perturbations

When operating as a conventional thermionic source, electrons produced at the cathode are prevented from escaping by a bias voltage applied between the cathode and grid [80]. A negative pulse applied to the cathode allows electrons produced there to overcome the potential of the grid, after which they are accelerated

out of the gun (Fig. 83). This pulse is nominally 100 ns long, but can be adjusted by changing the length of the pulse forming line which constitutes the heart of the main UMER pulser. In order to generate perturbations through photoemission, it is necessary to first generate an appropriate series of laser pulses, and then to ensure that they arrive at the cathode timed to coincide with the arrival of the cathode pulse. If the former is not done correctly, there will be no generation of photoelectrons, and if the latter is not done correctly, any photoelectrons which are generated will not be accelerated. The next three sections will deal with these problems of producing and correctly timing the optical pulse train, and operation of the system.

5.2.1. Optical Modulation

In order to produce a train of light pulses from a single source, with variable relative intensity and timing, a system of polarizing beamsplitters and delay lines was built [80]. This system was able to produce a pulse train of up to four pulses of 266 nm light, with the amplitude of each pulse being independently adjustable. The time delay between the first and last pair of pulses was variable, while the delay within the first and last pair of pulses was fixed. When configured for maximum delay, 43 ns separated the first and last pulse (Fig. 84).

The light source used to generate photoemission in this system was a single Continuum Minilite Nd:YAG laser, which produces a 5 ns pulse of 1064 nm light (Fig. 85). For compatibility with the available optics, the light was shifted into the UV at 266 nm by two stages of frequency doubling using second harmonic generation crystals. A pair of dichroic mirrors were used to reject any light with wavelength other than 266 nm, and the output was sent through a telescope used to increase laser

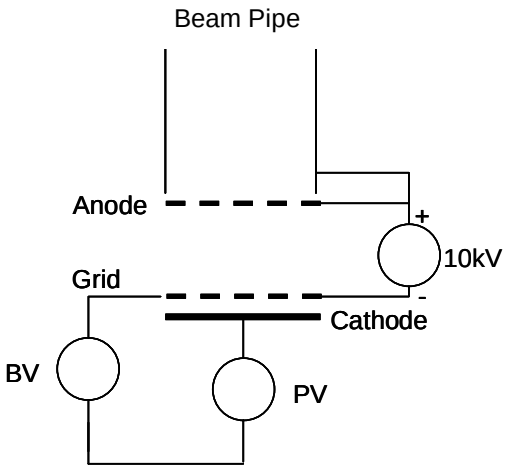

Fig. 83. UMER electronics configuration (simplified). Electrons produced at the cathode are prevented from escaping by a grid with is biased negatively relative to the cathode by a bias voltage supply (BV). When the UMER pulser (PV) is triggered, the cathode potential is lowered, allowing electrons to escape and be accelerated towards the anode, which is biased positively to the grid [80].

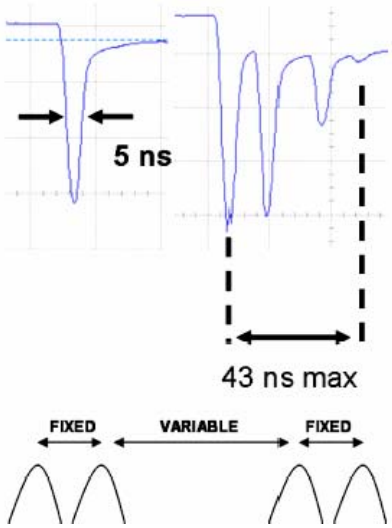

Fig. 84. Optical Pulse Train. Each pulse had a width of 5 ns, and each train consists of up to four pulses, with a maximum spacing of 43 ns. In our system, the delay between the second and third pulses was variable, while the other delays were fixed [80].

spot size in order to prevent damaging optical components. The remaining optics were at a slightly higher level, and a pair of mirrors was used to bring the light into that plane.

Once in the correct plane, the laser was sent into the system of beam splitters and delay lines (Fig. 86). That light is first sent through a half wave plate, which allows its polarization to be rotated. The resulting polarization angle governs what fraction of the light is reflected from the first polarized beam splitter, and how much is transmitted. The light which is transmitted is sent along one delay arm, while the light which is reflected is sent along another delay arm of different length. Included in each delay arm is a quarter wave plate. During one complete transit of the delay arm, the light will pass twice through the quarter wave plate. This will convert the polarization of the light from transmitting to reflecting, and vice versa. Because of this change in polarization, the light traveling along the two paths will be recombined by the first beamsplitter so that the initial 5 ns laser pulse will be split into two 5 ns laser pulses separated in time by the difference in the travel times along the two delay arms. To provide a pulse train of four pulses, a second stage, identical to the first stage just described, is used to split each of the two pulses from the first stage into two more, for a total of four pulses (Fig. 87).

A number of control points exist in the system. The laser output can be directly increased or reduced, which will affect the entire pulse train uniformly. Since the half wave plates govern how much light is sent along the short and long delay lines in each stage, they can be used to control the relative intensity of each pulse in the pulse train independently, to include entirely eliminating selected pulses.

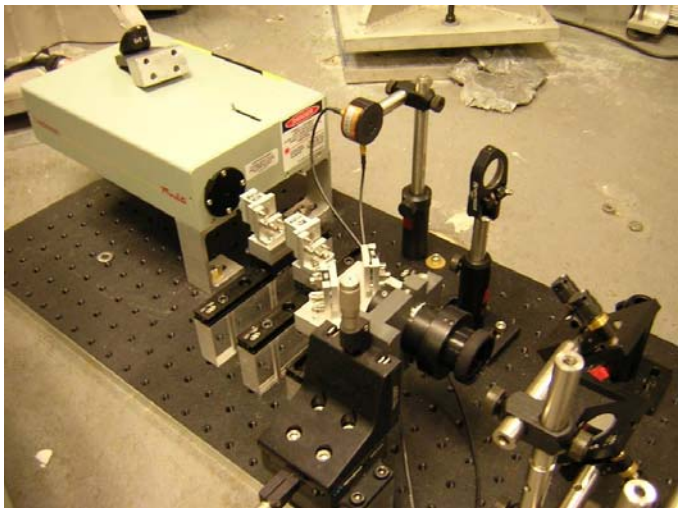

Fig. 85. Laser source arrangement [80].

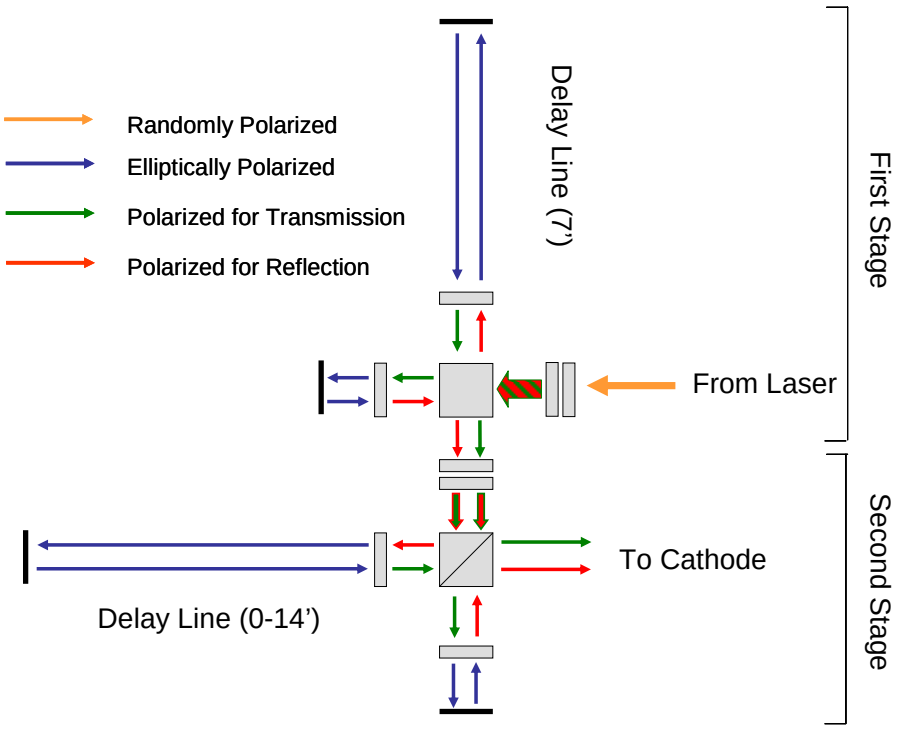

Fig. 86. Beamsplitter and delay line system. The system consisted of half wave plates (double rectangles), polarized beamsplitters (squares), quarter wave plates (single rectangles), and mirrors [80,110].

Reducing the number of pulses can also be accomplished by blocking chosen delay lines, or by changing the configuration of the system altogether. For example, to operate with only two pulses, the first stage could be removed and replaced with a single mirror (Fig. 88). By reducing the number of optical components the laser beam has to travel through, the optical power loss is reduced, and the number of photoelectrons generated at the cathode is increased.

To control pulse timing within the pulse train, the length of the delay lines can be adjusted. In our implementation, only one delay line was variable, consisting of a mirror mounted on a 4 m long optical rail (Fig. 89). The end mirror for the other delay arm was mounted on the base of one of the support columns for UMER (Fig. 90). The column provided the necessary rigidity to prevent accidental misalignments. Had both of the long delay arms been variable, full control over pulse spacing would have been possible.

A mirror in a New Focus "Flipper Mount" was used to switch the output of the optical modulation system between an Antel picosecond photodetector and the cathode (Fig. 85, Fig. 91). Using the Flipper Mount in this way allowed us to reliably alternate between measurements of the laser pulse shape and generation of photoelectrons without having to replace and realign any optical components.

Final optical transport to the cathode was accomplished by a series of mirrors which directed the laser light through a view port in the UMER beam pipe and onto a mirror located inside the beam pipe but below the path of the electron beam (Fig. 92). This final mirror, which had been installed for previous photoemission tests with UMER, directed the laser onto the cathode. Tests were carried out to ensure that the

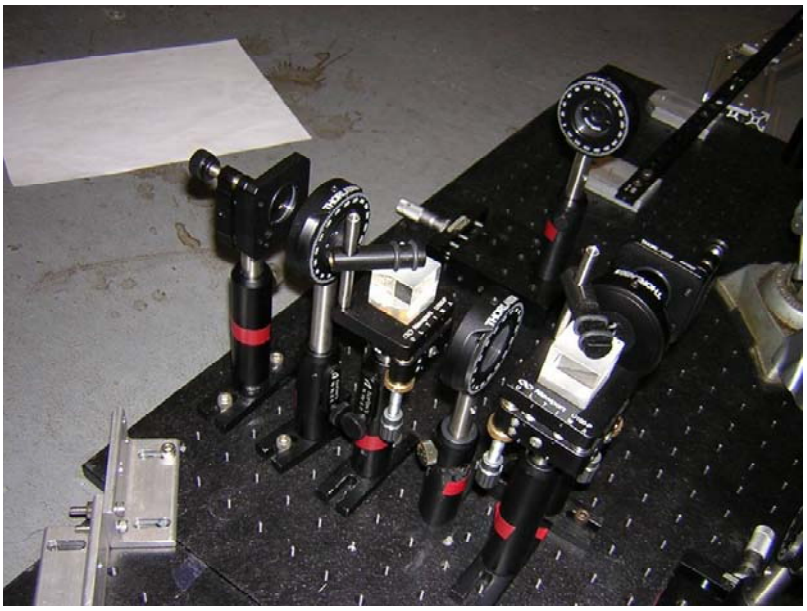

Fig. 87. Part of optical modulation system, showing beam splitters, wave plates, and mirrors. Optical track (variable delay arm) in upper right corner. Output to cathode exits the leftmost beamsplitter and travels towards the lower left corner [80].

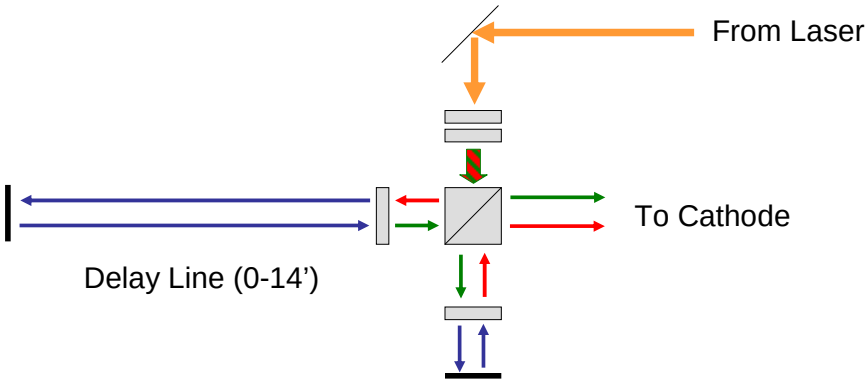

Fig. 88. Simplified optical modulation system for production of two pulses only.

Fig. 89. End mirror on variable delay arm.

Fig. 90. End mirror for second delay line.

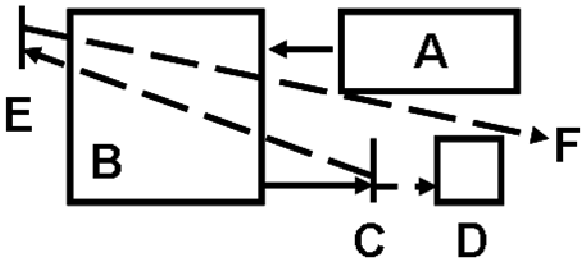

Fig. 91. Laser modulation system. Light from laser (A) enters beam splitter and delay line system (B) to produce four output pulses. Output reaches Flipper Mirror (C), and is either directed to detector (D), or is reflected off a mirror (E) and towards the cathode (F) [80].

final mirror was far enough below the electron beam to guarantee that it would have a negligible effect on the electron beam dynamics. A UV focusing lens placed just outside of the viewport was generally used to provide a tighter beam spot at the cathode, resulting in higher optical density and greater photoelectron generation.

5.2.2. Triggering

In normal thermionic operation, emission from the cathode is suppressed by a bias voltage, which holds the grid at a negative potential relative to the cathode. Electrons are only able to overcome this potential during a pulse applied to the cathode, which is nominally 100 ns long. Previous experiments with photoemission in UMER involved shorter optical path lengths, and did not allow arbitrary positioning of the photoemission pulse within the longer thermionic pulse (Fig. 6). If the triggering system previously used had also been used with our system, the increased phase delay between the trigger signal and the arrival of the laser at the cathode due to the increased optical path length of our more complicated system, along the inability to arbitrarily set the delay of the laser relative to the background thermionic pulse, would have cause the laser pulse to arrive at the cathode outside of the cathode pulse, preventing any photoelectrons generated from being accelerated. To overcome these problems, a redesigned trigger and timing system was developed, which allows an arbitrary delay to be set between the cathode pulse and the laser pulse [80].

As a thermionic emitter, the UMER cathode is designed to be heated in operation. This is not only necessary in order to generate electrons through thermionic emission (Eq. 12), but also to prevent surface contamination due to

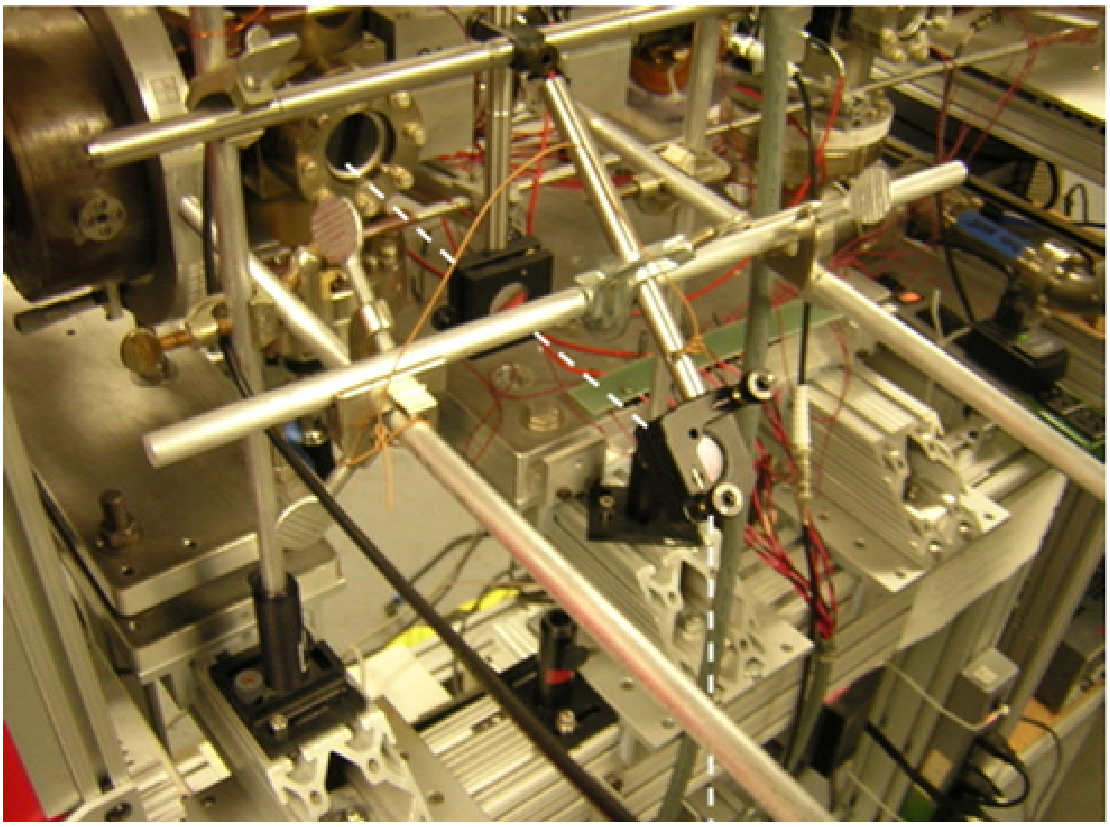

Fig. 92. Path of laser into beam pipe. Laser travels along dotted line and through the view port in the UMER beam line. A mirror behind the view port directs the laser onto the cathode, about 10 cm to the left [80].

residual gasses in the vacuum, which reduces the quantum efficiency of the cathode when generating electrons through photoemission. The heater on the Eimac Y-646B cathode used in UMER is designed to be supplied with approximately 1.3 A at 7 V in order to operate as a thermionic emitter [51]. However, the magnetic generated from the heater current is known to be detrimental to beam quality. Therefore, a variac is used to supply a variable-voltage AC signal to the cathode heater, and the UMER trigger system is phase locked to the nulls in the AC voltage, at which time the magnetic field disappears. The phase lock timing signal triggers a Berkeley Nucleonics BNC Model 500 Pulse Generator, which generally directly triggers the UMER cathode pulser at 10 - 60 Hz. The challenge with the multiple pulse photoemission system was to ensure that all the optical pulses arrived at the cathode simultaneously with the grid-cathode pulse. To accomplish this, the laser system was triggered first, with the gun pulser being triggered later after a suitable delay (Fig. 93). In this modified system, the BNC pulser was still phase locked to the nulls in the AC signal, but it triggered the laser flashlamp. When the laser flashlamp was activated, the flashlamp output trigger signal in turn triggered a Stanford Research Systems DG535 variable delay trigger source. The DG535 is capable of providing several outputs, with long but very precise delay times. One of these output channels was used to trigger the laser Q-switch after 150.000 μs. This is the delay between flashlamp activation and Q-switch activation recommended by Continuum for minimal laser timing and amplitude jitter. The second output from the DG535 was set to a nominal delay of 150.060 μs and used to trigger the UMER gun pulser. The relative delay of 60 ns was determined based on the intrinsic delay in the Q-switch

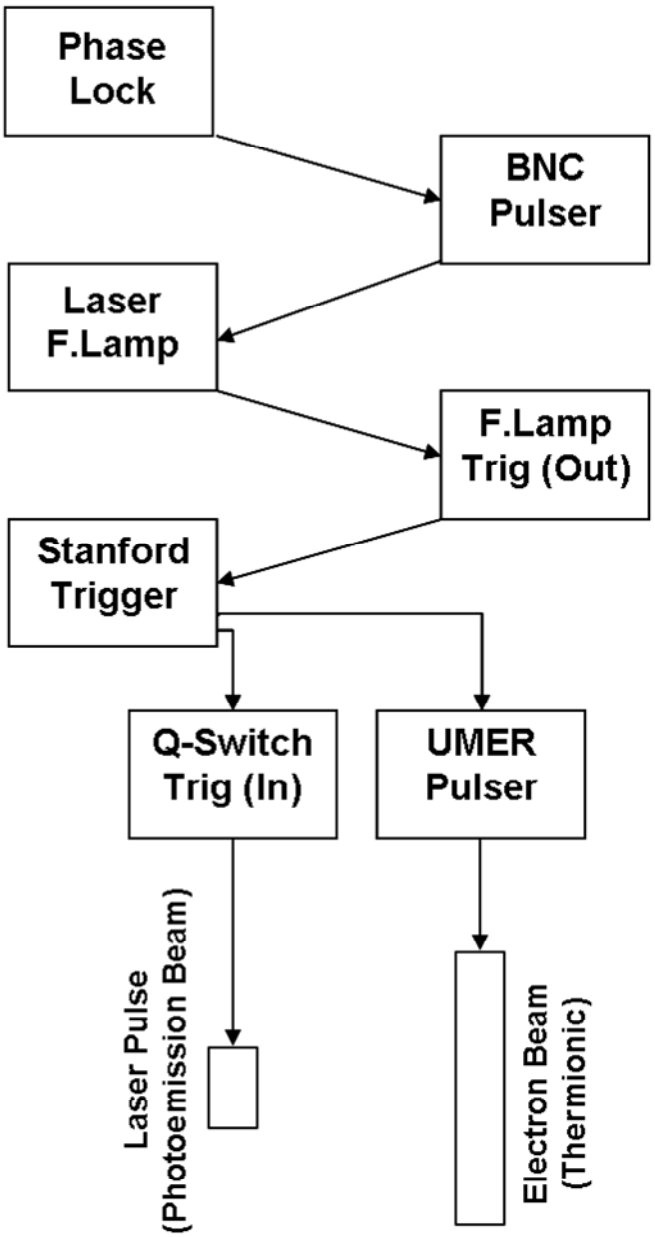

Fig. 93. Triggering system [80].

activation, the propagation time of the laser pulse(s) through the optical modulation system, and the intrinsic delay in the gun pulser. By changing this relative delay, the timing of the arrival of the laser pulse(s) at the cathode could be adjusted, allowing the photoemission pulse(s) to be placed anywhere within the thermionic background pulse.

5.2.3. Operation

To enable the laser pulses produced in the optical modulation system to be properly delivered to the cathode, it was necessary first to align the optical components with each other, and then to direct the output onto the cathode. Alignment within the optical modulation system was accomplished by using a fluorescing card to ensure that the UV light was centered on mirrors and lenses, and by selectively blocking delay lines to ensure that the light traveling along different paths arrived at the same location on all optical components. This alignment procedure was followed from the laser to the final mirror outside vacuum (Fig. 92). The remaining optical transport system was known as the "sextant" because of the similarity between its alignment procedure and the operation of the navigational instrument. For this final (coarse) alignment, the cathode heater was brought to normal temperature for full thermionic emission [80]. At this temperature, the cathode glows bright orange, and can be seen reflected off the mirror inside the beam pipe. Because the mirror in air is a UV mirror, it is transparent to visible light, and an operator can look through this mirror and the final UV lens to the image of the cathode reflected off the final mirror (Fig. 94). A fluorescing card was held over part of the cathode image, and the laser spot image was aligned with the visible portion of

the cathode (Fig. 95). Since the laser spot and the cathode image didn't necessarily have the same size or shape, the card would be repositioned to block different portions of the cathode image, and the operator was required to make a judgment call as to the overall alignment of the laser spot with the cathode image. For fine adjustment, the cathode heater power was reduced until a distinct photoemission peak was detected with the Bergoz FCT, and the height of this peak was maximized by walking the laser spot location. At this stage, the system was extremely sensitive to small adjustments in the laser spot location.

To maximize pulse shape flexibility, it was necessary to vary the current in the background thermionic pulse independently from the current generated by photoemission. In UMER, variation of the beam current when operating under standard thermionic emission conditions is accomplished by aperturing the beam while maintaining the electron gun in a stable, space charge limited mode of operation [111]. When operating the gun as a photoemission source, aperturing presents problems. Changing the aperture size would have reduced the laser spot size at the cathode. In addition, if the laser was not traveling along the line including the center of both the cathode and the aperture, the laser spot on the cathode could have changed shape and location as the aperture size was changed. To overcome these problems, the experiments described in this chapter were always carried out with the largest aperture. The background thermionic current was adjusted by changing the cathode heater power, which resulted in a relatively quick change in thermionic emission (Fig. 96). Operation at lower temperatures allows the cathode to become contaminated quicker, and prevents it from exuding barium onto its surface, which at

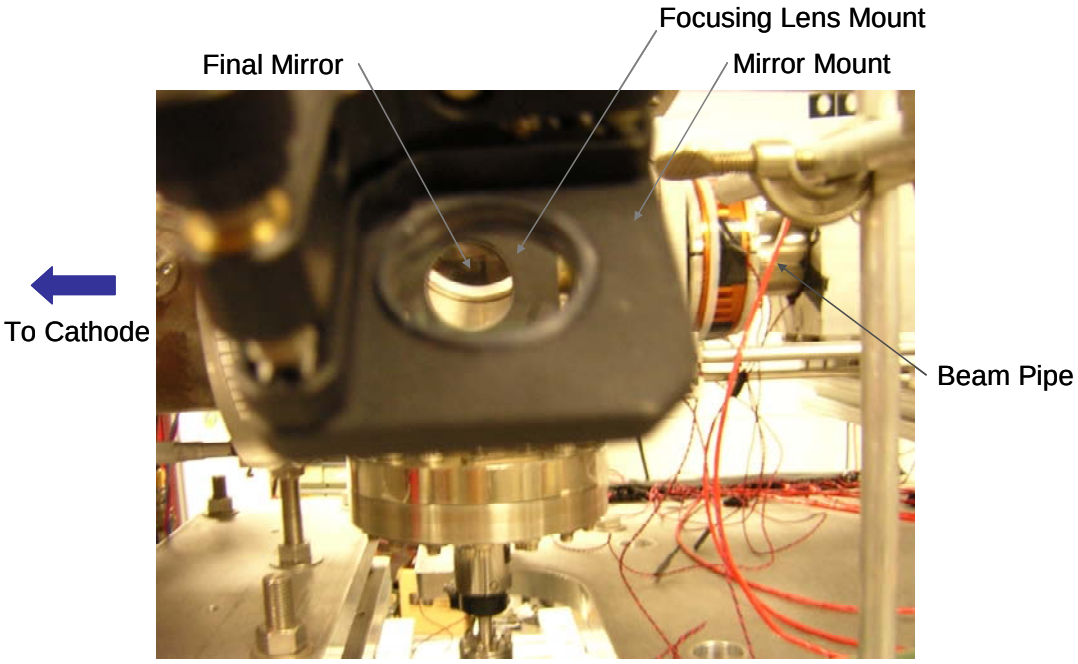

Fig. 94. The "Sextant."

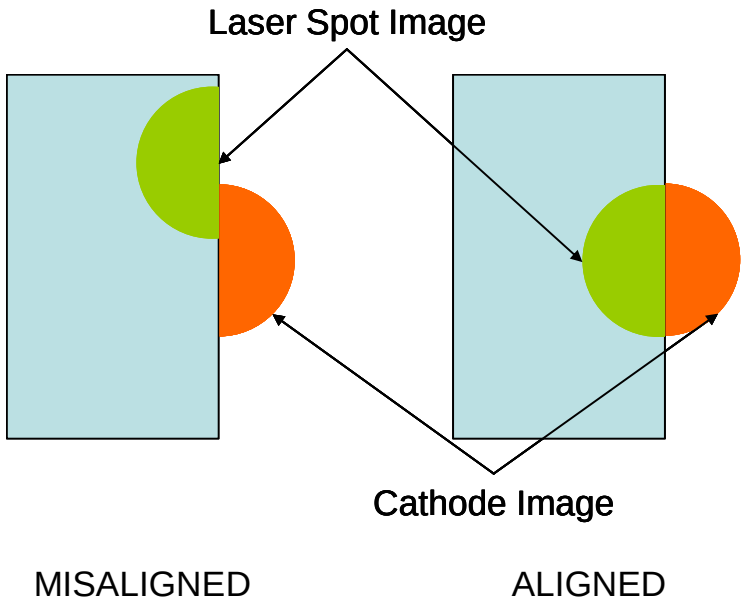

Fig. 95. Operation of the "Sextant."

higher temperatures allows the cathode to be continuously rejuvenating. As a result, there is a decrease in both the photoemission current (Fig. 37) and the thermionic current (Fig. 96, 97). The decay in quantum efficiency, resulting in a decrease in photoemission current on a time scale of tens of minutes, had been previously observed [91,106]. To rejuvenate the cathode after operating at reduced temperatures, the laser would be blocked and the cathode temperature would be increased to slightly above normal operating temperature for thermionic emission. After approximately 15 minutes at high temperature, the cathode would be fully rejuvenated.

Typically, after keeping the cathode temperature high for about 15 minutes, it would be reduced. As the cathode cooled towards its new equilibrium temperature, the thermionic emission current would fall, and several sets of data would be taken. Each of these data sets contained data from several locations along the beamline. As the cathode neared its new equilibrium temperature, the rate of change in the thermionic current would decrease, and another reduction in heater power would be made. Eventually, all thermionic emission would cease and only the photoemission beam would remain. As the quantum efficiency of the cathode decayed, this current would decrease. This final decay in current often took a long time, and to speed the process, the photoemission beam current would be reduced by reducing the laser power. After the full data set had been taken, the laser would be blocked and the cathode heater power increased to rejuvenate the cathode surface.

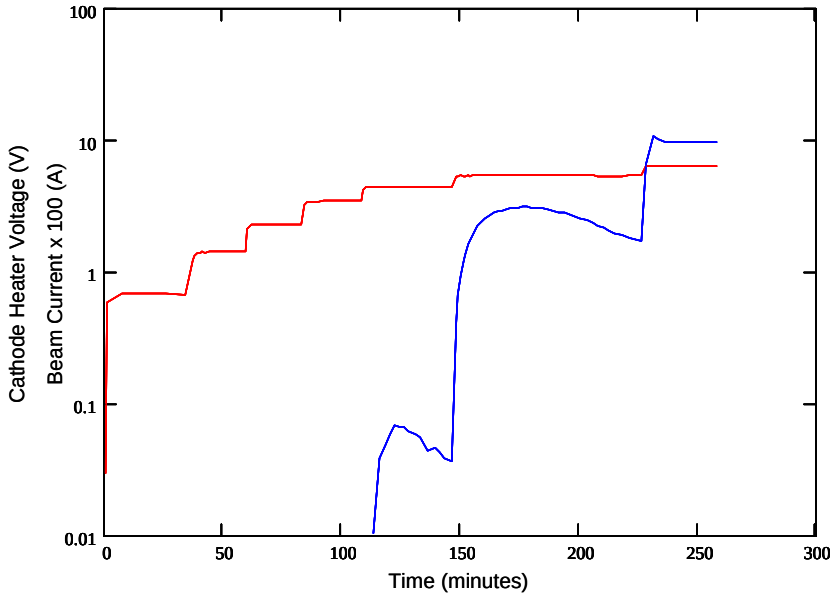

Fig. 96. Response of beam current (blue) to changes in cathode heater voltage (red).

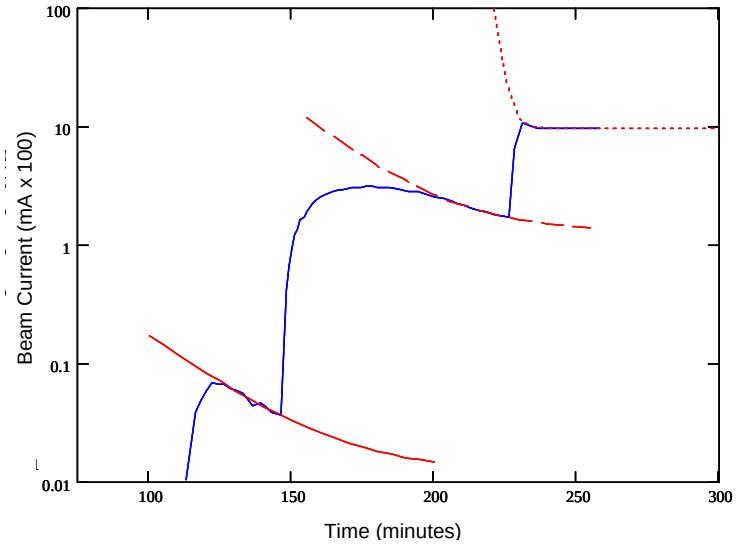

Fig. 97. The decay in thermionic current can be fit to exponential curves. These fits yield the following functional forms for cathode heater voltages of 4.41 V, 5.335 V, and 6.345 V, respectively (decay constants are quoted in units of 1/min):

$$I_{HV=4.41} = (0.098A)\exp(-0.041t) + (1.2\times10^{-4}\,A)$$

$$I_{HV=5.335} = (124.784A)\exp(-0.046t) + (0.013A)$$

$$I_{HV=6.345} = (1.173\times10^{40}\,A)\exp(-0.419t) + (0.096A)$$

5.3. Modes of Operation and Output Characteristics

In the UMER gun, several parameters can control the amount of current produced. Current may be limited by emission from the cathode, and this emission may be due to either thermionic emission or photoemission. In general, this is referred to as emission-limited operation, and in particular as temperature-limited or photoemission-limited operation depending on the method of generating electrons at the cathode. Temperature-limited operation is governed by Eq. (11), the Richardson-Dushman equation, while photoemission-limited operation is governed by [80]

$$i[A] = \frac{\lambda[\mu m]}{124} P[W] \cdot QE[\%], \tag{112}$$

where $i[A]$ is the current produced in Amperes, $\lambda[\mu m]$ is the wavelength of the light in microns, $P[W]$ is the power in Watts of the laser incident on the cathode, and $QE[\%]$ is the quantum efficiency of the cathode in percent. Emission-limited operation, of one sort or another, is possible in all electron sources. Because of the triode configuration of the UMER gun, the current produced may also be space charge limited and governed by the Child-Langmuir equation, or bias-voltage-limited and governed by the Triode law (see Chapter 4).

In the system for the production of perturbations described in this chapter, the gun was normally operated in emission-limited mode, with the main beam produced by thermionic emission and limited by cathode temperature, and the electrons in the perturbation produced by both thermionic emission and photoemission, and limited by both cathode temperature and laser power delivered to the cathode. Because the current was emission-limited, the increased current in the perturbation would remain

with the beam after it exited the gun. Operation in emission-limited mode allowed the pulse shape to be altered by changing the cathode temperature (Fig. 60) and the laser power independently. When the cathode temperature was increased so that the main beam emission was space charge-limited, the perturbation would not be seen. When the gun was operated at the transition between emission-limited and space charge-limited modes, an unusual effect occurred. Instead of increasing the beam current (as in emission-limited operation) or having no effect on the beam current (as in space charge-limited operation), the production of photoelectrons at the cathode actually resulted in a *decrease* in the current produced from the UMER gun (Fig 98). This unexpected phenomenon seems related to the "hump" in the current-vs-cathode temperature curve, which reflects the fact that the amount of current produced from the UMER gun actually exceeds the theoretical space charge limit during the transition from temperature-limited to space charge-limited operation. This effect was originally observed after the delivery of the UMER gun. A similar effect is observed in the current-vs-bias voltage curve. These effects are believed to be due to transverse focusing within the gun diode due to the Pierce geometry. This scenario is described in more detail in the context of bias-voltage-limited operation in Chapter 4.

Bias voltage effects can also be used to shorten the photoemission pulse. If the laser is used to produce photoelectrons at the cathode, timed to coincide with the

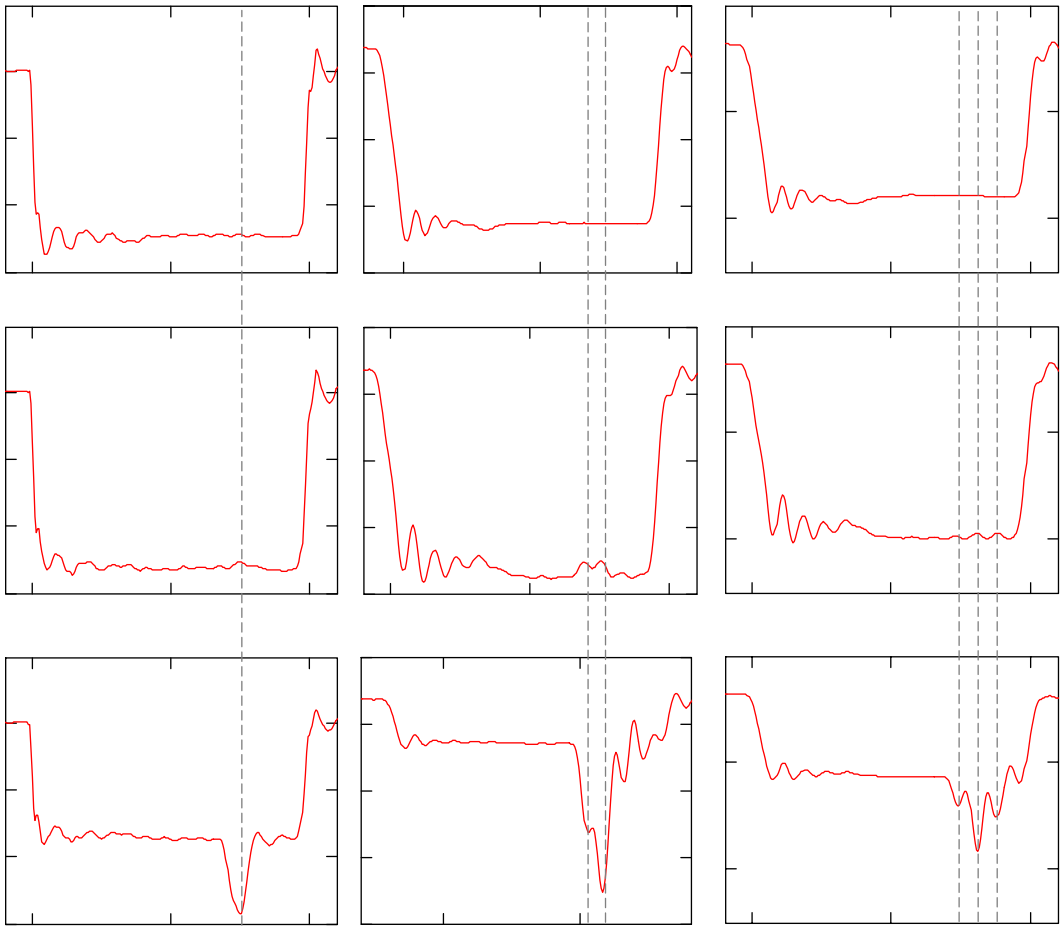

Fig. 98. Effect of photoelectron injection in the UMER gun. Current as a function of time is shown for one (left column), two (center column), and three (right column) perturbations produced when the gun is space charge limited (top row), in transition between space charge limited and emission limited (middle row), and emission limited (bottom row) [80].

cathode pulse, the electrons produced will see the plane of the grid[4] at a positive potential relative to the cathode, and will escape (Fig. 99). If the laser pulse is timed to fall outside the cathode pulse, the photoelectrons will see a negative potential at the grid, and will not escape from the cathode[5]. However, if the laser pulse is timed to coincide with the edge of the cathode pulse, the photoelectrons produced during the cathode pulse will escape, while those produced after the cathode pulse will not escape. This allows either the head or tail of the photoelectron pulse to be selected, and the rest of the photoelectron pulse to be deselected. The result is a shortening of the photoelectron pulse (Fig. 100).

Unfortunately, while emission-limited operation was required for generating observable perturbations, this required the cathode to be held at a temperature which was lower than its design temperature. As a result, the cathode became contaminated more easily, and the rate of barium replenishment to the surface was reduced. The net effect was a steady reduction in both the thermionic emission and photoemission, which caused the beam current to fall as time passed. This prevented the operation of the gun at predetermined current configurations. Instead, the current was allowed to continually fall, while data was taken at regular time intervals. While this allowed a

[4] In a triode or gridded gun, the grid itself may be kept at a slightly negative potential relative to the cathode to reduce the number of electrons striking the grid and therefore to maximize the number of electrons actually reaching the anode. Electron flow through the grid is still possible due to the leakage of electric field from the anode through the grid mesh and to the cathode. Thus, while the grid is still biased negatively, the space between the grid wires is at a higher potential than the cathode, allowing electron flow through that space. As a shorthand for this condition, we may say that the "plane of the grid" is at a positive potential.

[5] Electrons drawn *from the cathode* will not be able to escape under this condition. However, electrons drawn *from the control grid itself* will be accelerated and will leave the gun. The control grid in the UMER gun is 66% transparent, and therefore 34% of the light directed against the cathode is actually intercepted by the grid. The UV laser used in this experiment provides sufficient power and photon energy to produce photoelectrons from the control grid. This was observed experimentally as a faint glow on a phosphor screen in UMER while the cathode was illuminated with the UV laser, and the bias voltage was set to maintain the UMER gun in triode cutoff.

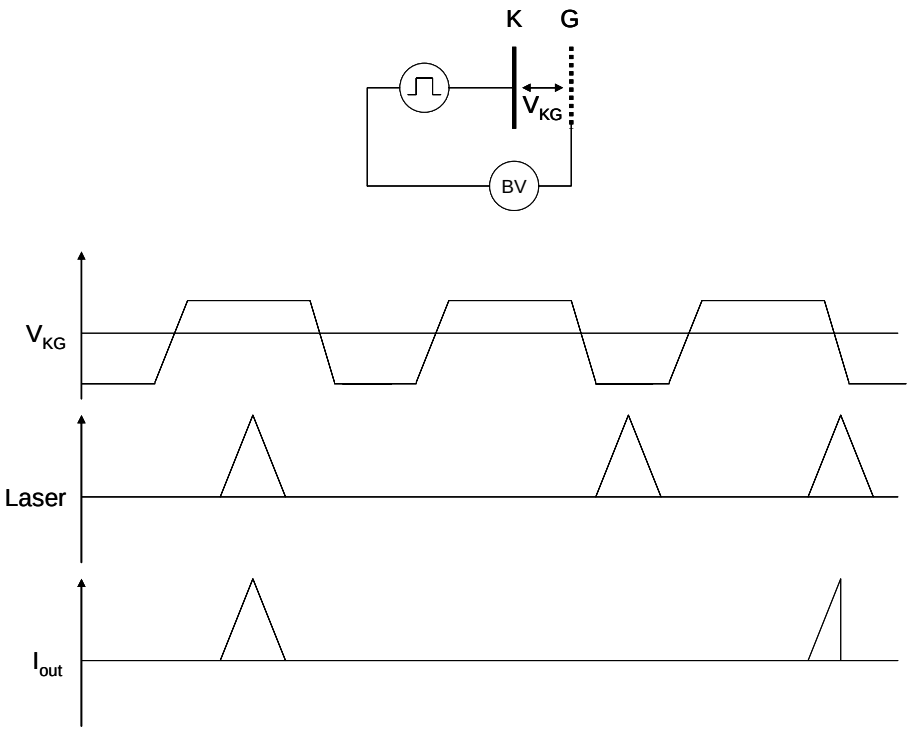

Fig. 99. Effect of relative timing of cathode pulses (top row) and laser pulse (middle row) on photoelectron current pulse length (bottom row). Cathode pulse as shown allows electrons to escape when V_{KG} is high and blocks electrons when V_{KG} is low.

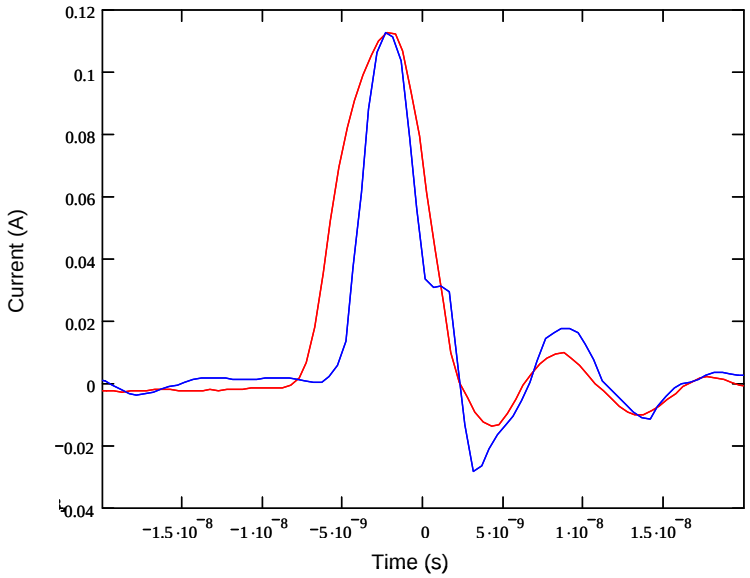

Fig. 100. Measured photoelectron currents; red trace is current when laser pulse coincides fully with cathode pulse and blue trace is current when laser pulse does not coincide fully with cathode pulse.

large parameter space to be investigated efficiently, it tended to generate data points that fell within "bands" when plotted on various axes, instead of data points that fell along a single curve (Figs. 101 - 103). The distribution of these data points defines allowed regions in the space of operating parameters of the system, which are bounded by limiting curves. These limiting curves are due to fundamental properties of the system.

For example, in the plot of peak perturbation current (I_P) as a function of flat top current in the main beam (I_{FT}) (Fig. 104), the data is seen to fall roughly in a diagonal band (Fig. 101). By definition, the peak perturbation current must equal or exceed the flat top current; therefore no data may fall below the line $I_P = I_{FT}$. In principle, the standard Child-Langmuir limit should hold for the main beam, as well as for the perturbations, which are not short compared to the length of the diode region in the UMER gun. This would prevent data from falling above the peak space charge current in the diode, which is approximately 0.104 A, so that $I_P \leq 0.104A$ and $I_{FT} \leq 0.104A$. However, in practice, operation near the space charge limit is complicated. For the main beam, transverse focusing effects due to the Pierce geometry of the gun must be considered. The effect of injecting photoelectrons at the cathode depends strongly on the level of the background flat top current as this current nears the theoretical space charge limit (Fig. 60). Additional lines may be drawn parallel to and above the line $I_P = I_{FT}$; the height of these lines above the line $I_P = I_{FT}$ is determined by the difference between the peak perturbation current I_P and the flat top current I_{FT}, which is the additional current *exiting* the gun due to

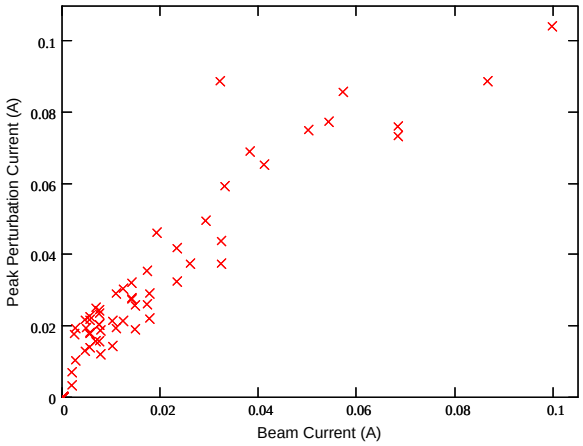

Fig. 101. Peak perturbation current vs. flat top current.

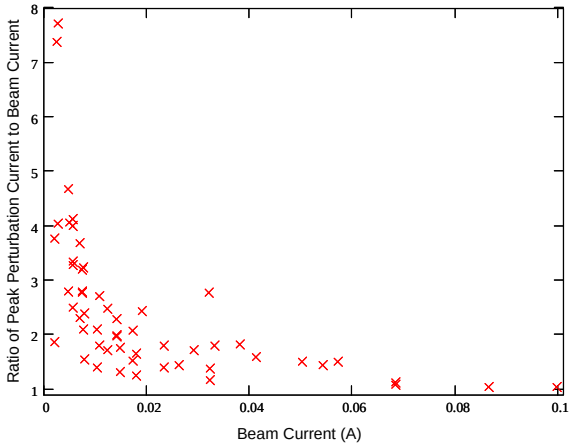

Fig. 102. Ratio of peak perturbation current to flat top current vs. flat top current.

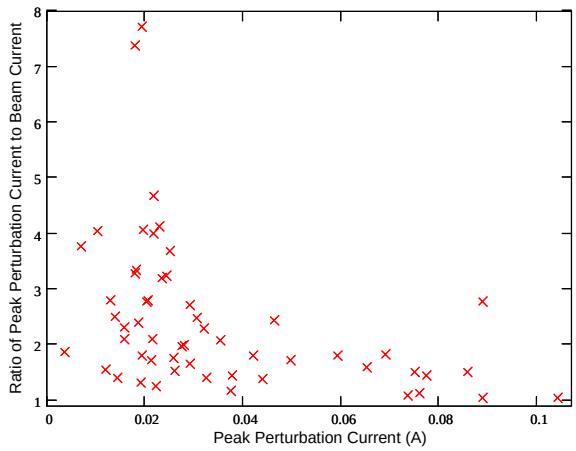

Fig. 103. Ratio of peak perturbation current to flat top current vs. peak perturbation current.

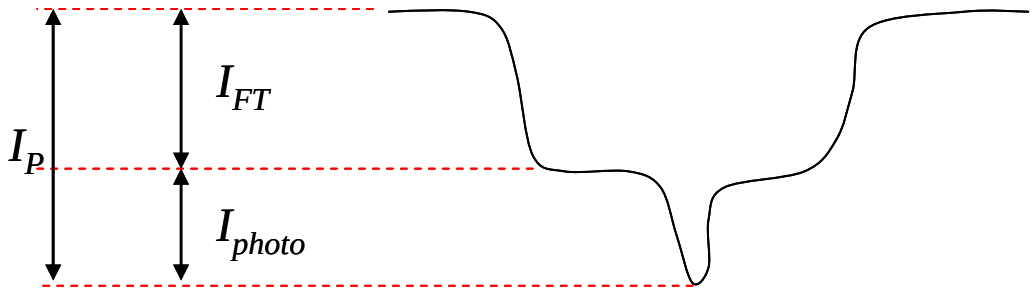

Fig. 104. Perturbation peak current (I_P), flat top current (I_{FT}), and photocurrent leaving the gun (I_{photo}).

photoemission at the cathode, I_{photo}. If the system is emission-limited, this current will be proportional to laser power absorbed at the cathode and cathode quantum efficiency, and will be given by Eq. (112). Therefore, for a given laser power and quantum efficiency, a given amount of photocurrent can be produced, and all data points generated with this configuration will fall along a particular line. The maximum laser power and optimal quantum efficiency available in the system defines another limiting curve, the photocurrent limit. If the sum of the photoelectron current produced at the cathode and the flat top current exceeds the space charge limit, a virtual cathode *may* form, with the excess current being reflected to the cathode. The onset of this condition depends on how close the flat top current is to the theoretical space charge limit. In actual operation, the quantum efficiency decreased as the experiment progressed, so that the actual operating point would not travel along a single photocurrent curve, but rather would tend to cross these curves as the photocurrent produced at the cathode fell.

When these limiting curves are plotted along with the data, it is seen that the available peak perturbation current available at a given flat top current must fall within a region whose area is defined by the gun geometry, laser power, and cathode material (Fig. 105). In this figure, the theoretical space charge limit is shown; it must be recognized that the actual behavior of the perturbation near this value is complicated, and depends on transverse effects in the gun and on the value of the flat top current, and so this "limit" may hold in some cases and not in others. Note that most of the data points correspond to limiting peak photocurrents of 20 mA or 30 mA. The higher peak photocurrents tended to occur at higher beam currents, which

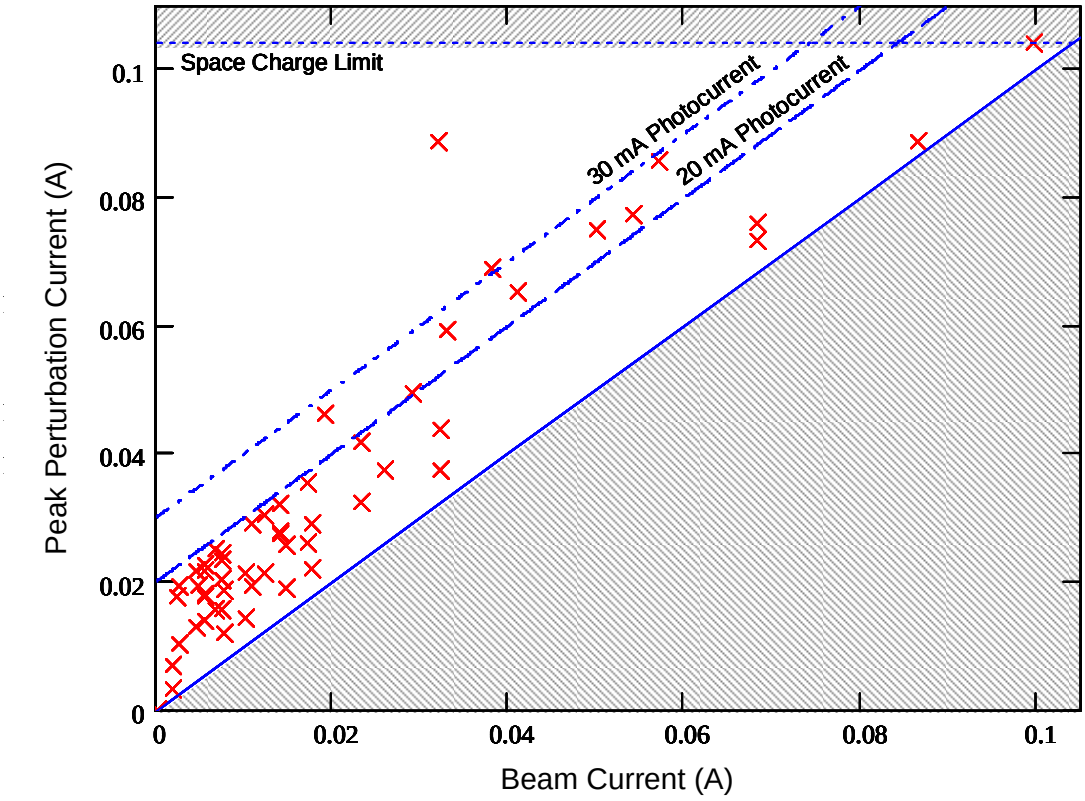

Fig. 105. Peak perturbation current vs. flat top current.

correspond to higher cathode temperature and therefore higher quantum efficiency of the cathode. At lower beam currents, the cathode had to be operated at lower temperatures, resulting in reduced quantum efficiency, and therefore reduced peak photocurrents. Note also the single outlier point at $I_{FT} \approx 30mA$. This data point appears as an outlier in most of the plots. This is most likely due to a calculation error, but it is not clear what the source of this error was.

A similar procedure can be used to explain the data when plotting the ratio of peak perturbation current to flat top current (I_P / I_{FT}) as a function of the flat top current I_{FT} (Fig. 102). By definition, the peak perturbation current must equal or exceed the flat top current, so that $I_P / I_{FT} \geq 1$. This defines the first prohibited region. Since the perturbation pulse length is not short compared to the length of the diode region in the UMER gun, the Child-Langmuir limit would generally apply, so that $I_P \leq 0.104A$, or

$$\frac{I_P}{I_{FT}} \leq \frac{0.104A}{I_{FT}}. \tag{113}$$

This defines the limiting curve due to space charge. However, the actual behavior of the beam when this current is approached is complicated, depending on the value of the beam flat top current, and so this "limit" may not hold in all cases. This equation, and the requirement that $I_P / I_{FT} \geq 1$, define the theoretically accessible parameter space. However, an additional constraint is imposed by the peak photoelectron current produced from the cathode. For emission-limited operation, the peak perturbation current for a given flat top current and photocurrent is

$$I_P = I_{FT} + I_{photo}, \tag{114}$$

so that

$$\frac{I_P}{I_{FT}} = 1 + \frac{I_{photo}}{I_{FT}}. \tag{115}$$

For a given laser power and quantum efficiency, the photocurrent is determined, and all data will fall along the curve defined by Eq. (115). For fixed laser power and quantum efficiency, increasing the flat top current will move the operating point along the photocurrent curve until that curve intersects the space charge limit curve. At this point, the effect of continuing to increase the flat top current will depend on how close that current is to the theoretical space charge limit in the diode.

For a given system, a peak value for I_{photo} exists as a function of maximum laser power and optimum quantum efficiency, and with that value Eq. (115) defines the photocurrent limit for the system. When these limiting curves are plotted (Fig. 106), an available parameter space is found as a function of machine geometry, laser power, and cathode material and condition. Note that as before, at lower flat top currents, the maximum photocurrent was approximately 20 mA, while at higher beam currents, a photocurrent of 30 mA was achievable. Note also the presence of the erroneous data point at $I_{FT} \approx 30mA$, discussed previously, and the data point at the origin, which is due to an error in the graphing program used to generate this plot.

Finally, a similar analysis is possible to explain the graph of the ratio of peak perturbation current to flat top current (I_P/I_{FT}) as a function of peak perturbation current (I_P) (Fig. 103). As before, the requirement that $I_P/I_{FT} \geq 1$ defines the first inaccessible region. Also, from Eq. (114), a curve

$$\frac{I_P}{I_{FT}} = \frac{1}{1 - \frac{I_{photo}}{I_P}} \tag{116}$$

can be defined for a given value of photocurrent *exiting* the gun (I_{photo}). When I_{photo} is set equal to its maximum value for a given laser power and quantum efficiency, this curve defines the photocurrent limit on the I_P / I_{FT} vs. I_P plane. In this plane, the space charge limit would serve to limit the operating parameters to $I_P \leq 0.104A$ (Fig. 107).

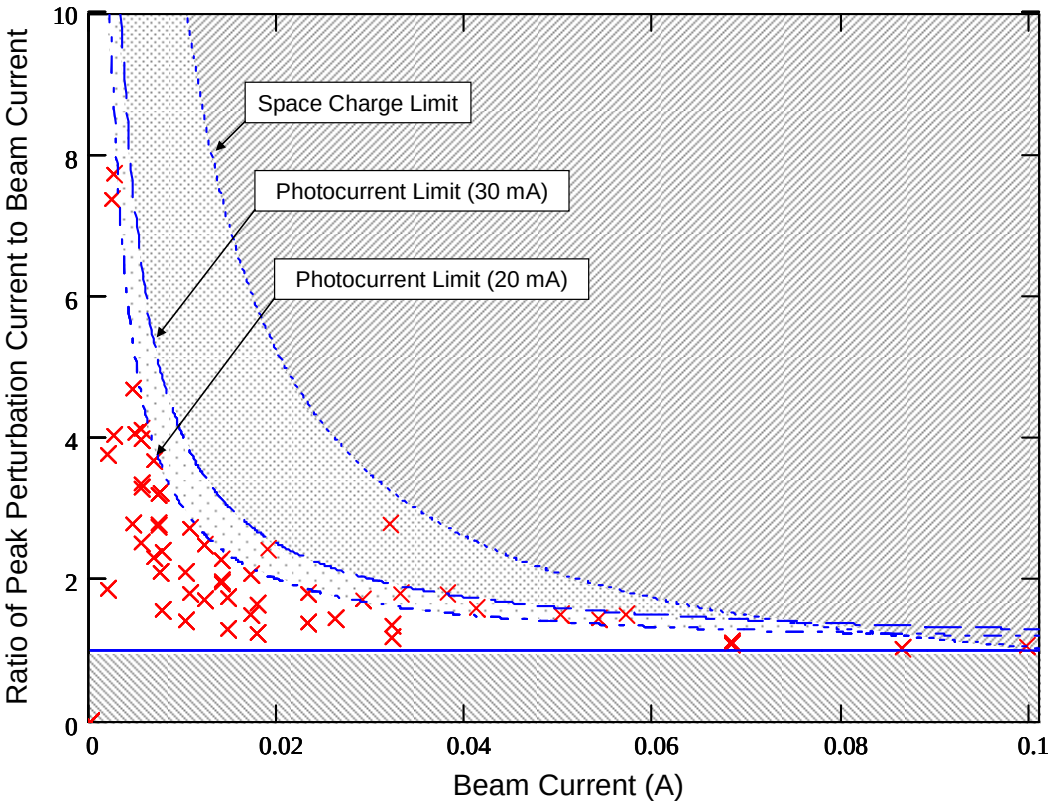

Fig. 106. Ratio of peak perturbation current to flat top current vs. flat top current.

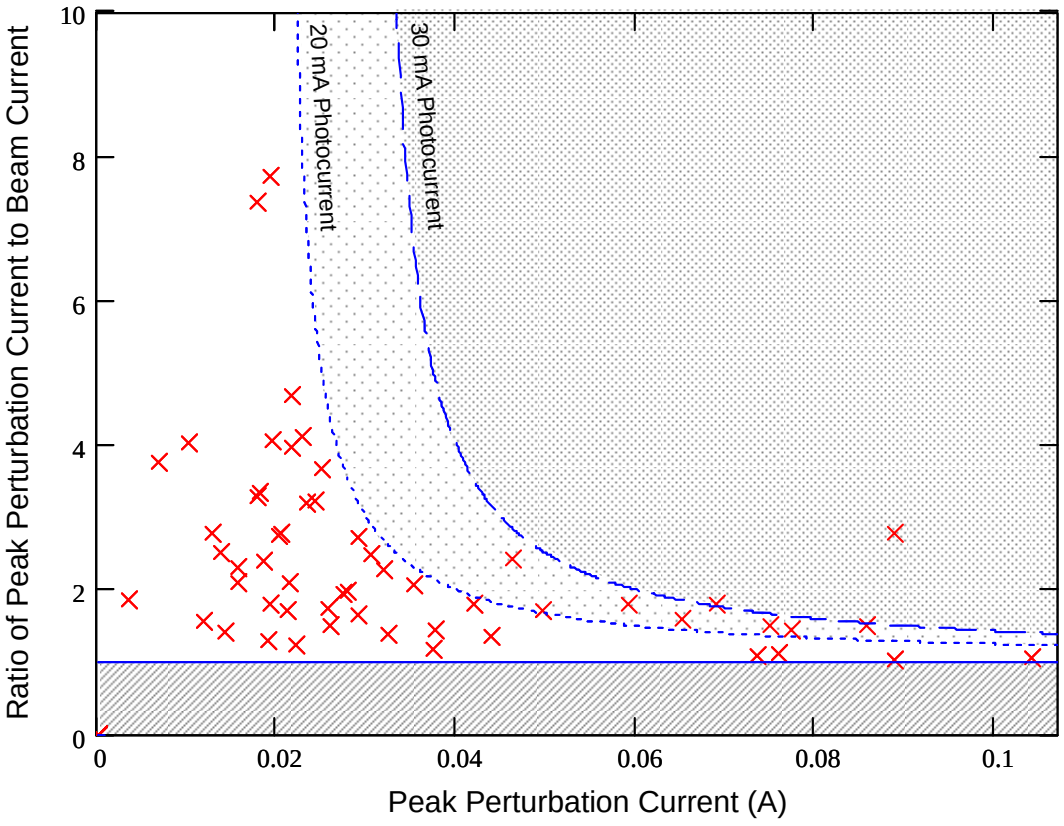

Fig. 107. Ratio of peak perturbation current to flat top current vs. peak perturbation current.

5.4. Conclusions

In this chapter, we described the design and operating characteristics of a system to produce a train of perturbations in a beam by using combined thermionic emission and photoemission from the UMER dispenser cathode. Unlike previous experiments using combined thermionic emission and photoemission, this system allows the perturbations to be placed anywhere within the main beam, to place perturbations of different strengths at several locations in the beam simultaneously, and to assemble more complicated perturbation shapes. All of these features are potentially useful for enhanced beam control and diagnostics. In addition, the system described could be installed on many existing accelerators to greatly increase system flexibility at minimal cost.

However, the system described above can be improved in several ways. The optical components used in this system were largely those on hand at the beginning of the experiment. The laser and optical elements in future experiments should be designed to optimize photocurrent, taking into account the effect of laser frequency, optical losses, and optical component damage thresholds. In this experiment, these factors were not optimized and as a result we often had difficulty delivering enough laser power to the cathode to produce desired photocurrent levels. In addition, redesigning the system to use non-polarized optical components may be possible, and may ease design constraints. Limitations were also imposed by the UMER cathode, which was designed to be operated at the high temperatures needed for thermionic emission. For our purposes, a dispenser photocathode optimized for lower temperature operation would allow for less decay in quantum efficiency and

thermionic emission, and provide more stable operation in the emission-limited regime. Also, operation would become more reliable and reproducible if the cathode heater supply variac were replaced with a more stable supply. Finally, the laser power damage threshold of the UMER cathode should be determined using spare cathodes.

Chapter 6: Conclusions

All beams of interest are dominated by space charge forces when first created. These space charge forces can cause longitudinal instabilities and nonlinear effects. Space charge also couples these longitudinal effects into the transverse dynamics of a beam. Even after a beam is accelerated to high enough energy that it is no longer dominated by space charge forces, the results of its early evolution are still present and can cause unintended effects, such as energy and density variation along the beam and production of electromagnetic radiation. Depending on the intended use of the beam, these effects may be good or bad.

The most fundamental result of longitudinal space charge forces is an increase in beam length. Several models exist to describe this increase under different conditions. For beams that have a parabolic longitudinal beam profile, the longitudinal envelope equation can be used. This equation is analogous to the well-known transverse envelope equation. Our experiments have shown that this model accurately describes the longitudinal expansion of parabolic beams in UMER. The RMS form of the longitudinal envelope equation can also be shown to describe, at least approximately, the increase in RMS length of beams which are initially rectangular.

The longitudinal envelope equation is valid for space charge dominated or emittance dominated beams, with or without longitudinal focusing. For beams where emittance may be neglected, and in the absence of longitudinal focusing, the one-

dimensional cold fluid model can be used to describe longitudinal beam expansion. The cold fluid model shows that for the special case of a beam with an initial rectangular pulse shape, the beam will expand by erosion from the beam ends. The characteristic time for this erosion is governed by the sound speed in the beam. Experiments performed on UMER agree very well with this model, although transverse effects can affect the beam expansion under certain conditions.

UMER was originally intended to operate with parabolic and rectangular beams, but by modifying the gun operation, a host of more exotic pulse shapes can be created. The UMER gun can be run in space charge limited, temperature limited, triode amplification, and photon limited modes, and in combinations of these modes. Each mode or combination of modes naturally produces different pulse shapes and properties for the UMER beam, which provides a flexibility not found on any other charged particle beam system. These novel pulse shapes are useful for studying longitudinal effects, and may have application to improved diagnostics and beam control. For example, by operating the UMER gun in triode amplification mode, the inherent ringing and imperfections in the cathode voltage pulse will be amplified, producing a sinusoidal modulation on the beam. This modulation will split into a forward-traveling wave and a backward-traveling wave, each of which travels at the sound speed. As a result, the two waves will interfere as the beam travels through the UMER transport system, and the modulation will be observed to disappear and reappear. The triode nature of the UMER gun can also be used to explain some of its unexpected behavior.

To produce novel beam shapes with more flexibility, a system was developed to produce a train of laser pulses. These laser pulses can be directed against the UMER cathode, producing a train of perturbations due to photoemission. The relative amplitude and timing of the perturbations can be easily adjusted. By combining these perturbations, more complex pulse shapes can be assembled. Individually, these perturbations split into forward-traveling and backward-traveling space charge waves, each traveling at the sound speed. This is the same physical mechanism that results in the space charge wave interference effects of Chapter 4. This shows that the evolution of beams which are superficially very different may often be explained by identical underlying physics.

Longitudinal dynamics of intense beams is an extremely rich field, and much work remains to be done. Longitudinal expansion of the beam in UMER will require development of a longitudinal focusing system. In order to optimize this system, detailed measurements of beam velocity evolution must be made, using the energy analyzers now under development. Space charge waves hold promise as beam diagnostic techniques, but preliminary results from the multiple perturbation system indicate that there are many unanswered questions. In addition, it is becoming increasingly apparent that the details of gun operation have a significant affect on the beam dynamics, and are in need of further study.

Appendix A: Longitudinal Electric Field.

In this section, we will review the longitudinal electric field, which drives longitudinal expansion of intense beams and participates in the propagation of space charge waves. We will see how it is affected by boundary conditions, and how its description involves information about the relationship between beam geometry, beam pipe geometry, and beam density variations. We will also make some hypotheses about stored energy and beam evolution.

A.1. Standard Derivation of Longitudinal Electric Field

The derivation of the longitudinal electric field normally begins by assuming an axisymmetric beam, on-axis in the center of a cylindrical, perfectly-conducting beam pipe [1,92,112]. The beam radius is a, the beam pipe radius is b, and the local line charge density is $\lambda(z)$ at the location z in the beam (Fig. A1). Faraday's Law states that

$$\oint \vec{E} \cdot d\vec{l} = -\frac{\partial}{\partial t} \int \vec{B} \cdot d\vec{S} \,. \qquad \text{(A1)}$$

If we are in the beam frame, there is no current flow and no magnetic field is generated. Faraday's law becomes

$$\oint \vec{E} \cdot d\vec{l} = 0 \,. \qquad \text{(A2)}$$

If we apply Eq. (A2) to the loop shown in Fig. A1, the radial electric fields inside (E_r^{inside}) and outside ($E_r^{outside}$) the beam are related to the longitudinal electric field $E_z(r)$ a distance r from the beam axis by

$$\int_{z}^{z+\Delta z} E_z(r)dz + \int_{r}^{a} E_r^{inside}(z+\Delta z)dr' + \int_{a}^{b} E_r^{outside}(z+\Delta z)dr'$$

$$+0+\int_{b}^{a} E_r^{outside}(z)dr' + \int_{a}^{r} E_r^{inside}(z)dr' = 0\,. \qquad \text{(A3)}$$

The zero in Eq. (A3) refers to the electric field in the beam pipe, which is assumed to be a perfect conductor. In this section, primes will be used to denote variables of integration rather than differentiation. From Gauss' Law, the radial electric fields inside and outside the beam can be found to be

$$E_r^{inside}(r') = \frac{\lambda}{2\pi\varepsilon_0}\frac{r'}{a^2} \qquad \text{(A4)}$$

and

$$E_r^{outside}(r') = \frac{\lambda}{2\pi\varepsilon_0 r'}\,. \qquad \text{(A5)}$$

Combining Eqs. (A3), (A4), and (A5) and taking $\Delta z \to 0$ gives the local longitudinal electric field,

$$E_z(r) = -\frac{1}{4\pi\varepsilon_0\gamma^2}\left(\left[1-\frac{r^2}{a^2}+2\ln\left(\frac{b}{a}\right)\right]\frac{\partial\lambda}{\partial z} - \frac{2\lambda}{a}\left[1-\frac{r^2}{a^2}\right]\frac{\partial a}{\partial z}\right) \qquad \text{(A6)}$$

or

$$E_z(r) = -\frac{1}{4\pi\varepsilon_0\gamma^2}\left[1-\frac{r^2}{a^2}-\frac{2\lambda}{a}\left[1-\frac{r^2}{a^2}\right]\frac{\partial a}{\partial\lambda}+2\ln\left(\frac{b}{a}\right)\right]\frac{\partial\lambda}{\partial z}\,. \qquad \text{(A7)}$$

Relativistic effects have been included in Eqs. (A6) and (A7) by dividing by γ^2. Eq. (A7) shows that the longitudinal electric field depends on the rate of change of line charge density with distance along the beam, and on a geometry factor

$$g = \alpha + 2\ln\left(\frac{b}{a}\right) = 1 - \frac{r^2}{a^2} - \frac{2\lambda}{a}\left[1 - \frac{r^2}{a^2}\right]\frac{\partial a}{\partial \lambda} + 2\ln\left(\frac{b}{a}\right). \qquad \text{(A8)}$$

Note that the geometry factor serves to couple the longitudinal and transverse physics of the beam. This derivation only holds in the "long-wavelength" approximation where the wavelength or characteristic length l of any disturbance in the beam's line charge density is much larger than the Lorentz-contracted beam pipe radius,

$$l >> \frac{b}{\gamma}. \qquad \text{(A9)}$$

In UMER, this length corresponds to a frequency of 1.2 GHz.

The beam radius is generally assumed to be constant, with any variation in line charge density occurring as a change in volume charge density. With this assumption, the geometry factor takes the form

$$g = \alpha + 2\ln\left(\frac{b}{a}\right) = 1 - \frac{r^2}{a^2} + 2\ln\left(\frac{b}{a}\right). \qquad \text{(A10)}$$

As a result, the value of α varies from 1 on axis to 0 at the beam edge, causing the longitudinal electric field to be greater in the center of the beam. For simplicity, it is useful to take a single value for α; some take 1, which gives the worst case for longitudinal expansion [92], while others use 0.5 as an average over the beam radius [113].

Others assume that the volume charge density

$$\rho = \frac{\lambda}{\pi a^2} \qquad \text{(A11)}$$

is a constant, and that changes in the local line charge density are coupled with changes in the local beam radius [53]. This gives a geometry factor of the form

$$g = \alpha + 2\ln\left(\frac{b}{a}\right) = 2\ln\left(\frac{b}{a}\right), \tag{A12}$$

or $\alpha = 0$. This geometry factor is uniform across the beam radius. These two cases ($a = const$ and $\rho = const$) can be considered opposite extremes, as illustrated in Fig. A2.

Under what circumstances is each picture actually valid? When a beam is transversely emittance dominated ($\chi_T \approx 0$), the beam radius will generally be independent of beam current and $\alpha = 1 - \frac{r^2}{a^2}$; when a beam is transversely space charge dominated ($\chi_T \approx 1$), the volume charge density in the beam will generally be independent of beam current, and $\alpha = 0$ [1,53]. This can be shown by using the matched transverse envelope equation,

$$k_0^2 R = \frac{K_T}{R} + \frac{\varepsilon^2}{R^3}. \tag{A13}$$

When the beam is emittance dominated, space charge can be neglected ($K_T \to 0$) and the beam radius is given by

$$R = \sqrt{\frac{\varepsilon}{k_0}}. \tag{A14}$$

Neither the transverse emittance ε nor the transverse focusing k_0 depends on beam current, and therefore the beam radius R is also independent of beam current. Thus, any change in beam current or line charge density will be a result of a change in the volume charge density in the beam. On the other hand, in a space charge dominated beam where emittance is negligible ($\varepsilon \to 0$), the beam radius is given by

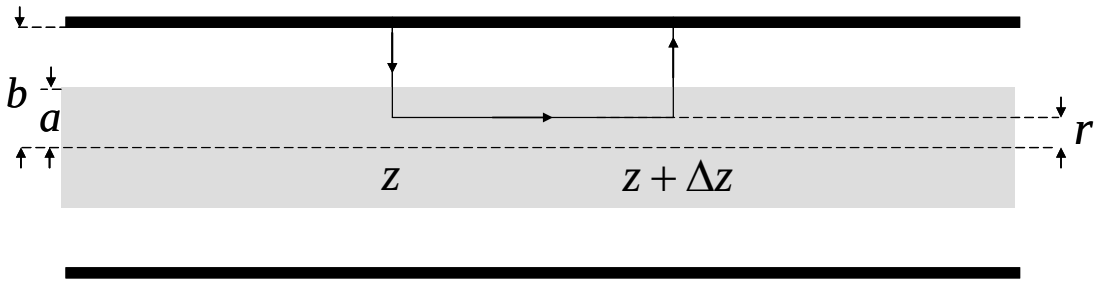

Fig. A1. Configuration used to derive longitudinal electric field.

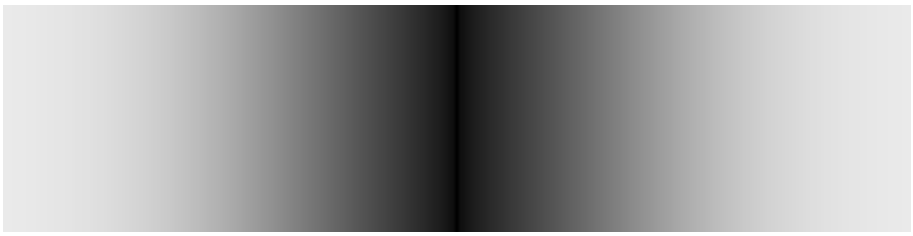

Constant Radius, Varying Volume Charge Density

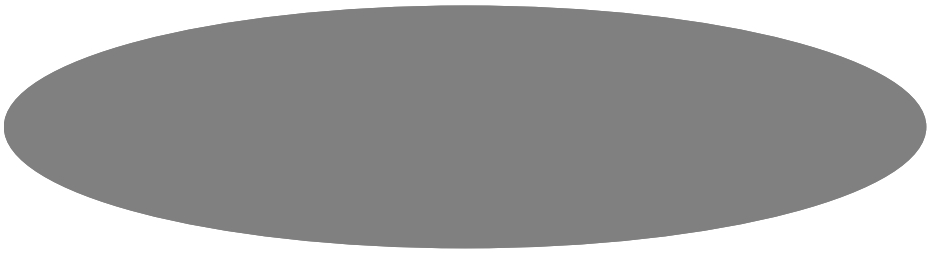

Constant Volume Charge Density, Varying Radius

Fig. A2. Physical models providing different values of α.

$$R = \sqrt{\frac{K_T}{k_0^2}} \tag{A15}$$

or

$$R = \sqrt{\frac{Iq}{2\pi\varepsilon_0 mc^3\beta^3\gamma^3 k_0^2}}\,. \tag{A16}$$

But the beam current and volume current density are related by

$$\rho = \frac{I}{c\beta\pi R^2}\,. \tag{A17}$$

Both Eqs. (A16) and (A17) relate beam current I and beam radius R; combining them gives a relation for the volume charge density

$$\rho = \frac{2\varepsilon_0 mc^2\beta^2\gamma^3 k_0^2}{q} \tag{A18}$$

which shows that the volume charge density should be independent of beam current in an intense beam. This is consistent with what is normally seen in simulations of intense beams [53].

However, this view breaks down when the origin of the beam is considered. In UMER, the beam is generated from a cathode, which has a fixed radius. When the beam is generated by thermionic emission, or photoemission when the entire cathode is illuminated, the beam radius will be identical to the cathode radius. Any variation in beam current *must* therefore occur through a variation in the beam volume charge density. This would have to be the case even in an intense beam, where the current variation would be expected to occur through variation of the beam radius. This suggests that, for an intense beam, a relaxation may occur from a state in which the radius is constant to a lower energy one in which the volume charge density is

constant. Such a relaxation is reasonable, since the timescale for transverse changes in the beam is much faster than the timescale for longitudinal changes in the beam, and so we might expect that a beam created with varying volume charge density but constant radius would quickly react to the presence of transverse focusing by adjusting its radius to achieve a transverse force balance. This would occur so quickly that any longitudinal changes in the beam during the same time interval would be negligible. Note that this would require a nonzero transverse mismatch, initially invalidating the assumptions made in deriving Eq. (A18). This explains how the beam could initially be best described by a model normally used for emittance dominated beams while the actual beam was space charge dominated. The relaxation proposed here may be indirectly observed as a variation in the geometry factor, or directly observed by measuring the beam's volume charge density as a function of transverse and longitudinal dimensions in the beam.

A.2. More Effects of Boundary Conditions and Focusing

In the discussion above, we assumed ideal conducting cylindrical beam pipes and no focusing. In this section we briefly mention some of the results when these assumptions don't hold.

To include effects of wall resistance and inductance in the model we have been using, the calculation proceeds as in Eq. (A3) except that the electric field in the wall E_w is assumed to be nonzero [114]. When this is done, the longitudinal electric field becomes

$$E_z = E_w - \frac{g}{4\pi\varepsilon_0\gamma^2}\frac{\partial\lambda}{\partial z}. \qquad \text{(A19)}$$

When the wall resistance per unit length r_w and the wall inductance per unit length l_w are included, this becomes

$$E_z = -r_w \beta^2 c^2 \lambda + l_w \beta^2 c^2 \frac{\partial \lambda}{\partial z} - \frac{g}{4\pi\varepsilon_0 \gamma^2} \frac{\partial \lambda}{\partial z}. \qquad \text{(A20)}$$

It can be seen from Eq. (A20) that the wall resistance has a defocusing effect because it adds to the (already defocusing) space charge term. A more pronounced effect is the "resistive wall effect," which can cause growth in space charge waves [1,92,93]. The wall inductance has a focusing effect on the beam because it is in the opposite direction from the defocusing space charge force term. Inductive loading of beam pipes was even proposed as a method of longitudinal focusing [115]. Note that the inductive and space charge terms both depend on $\frac{\partial \lambda}{\partial z}$, so that they could be written as a single term

$$-\frac{g_I}{4\pi\varepsilon_0 \gamma^2} \frac{\partial \lambda}{\partial z} \qquad \text{(A21)}$$

where

$$g_I = l_w \beta^2 c^2 4\pi\varepsilon_0 \gamma^2 - g \qquad \text{(A22)}$$

is an effective geometry factor taking into account inductive effects. When the inductive effects exceeded the space charge effects, the beam would experience net focusing and the effective geometry factor would become negative. In general, negative geometry factors are used to take into account external focusing [84].

Finally, cylindrical beams and beam pipes have been assumed throughout. In UMER, the actual beam is not cylindrical because of the use of quadrupole focusing. Because the longitudinal evolution of the beam is on a timescale which is much

longer than that of the transverse variation of the beam, it is usually assumed that these breathing oscillations can be neglected, and the beam treated as cylindrical with its average radius. However, for some applications other geometries are more appropriate, and a formulation similar to that used above can be developed to take the new geometry into account. (For example, see [92,116].)

A.3. Geometry Factor for Bunched Beams

The geometry factor derivations shown above are, by their nature, local. If the relationship between beam shape and charge density varies along the length of the beam, the geometry factor will vary as well. Therefore, these derivations are best used in the study of space charge wave propagation along a beam, which is discussed in Chapters 4 and 5. A geometry factor also arises in the longitudinal envelope equation, and is normally assumed in the literature to be identical to the geometry factor discussed above. However, the longitudinal envelope equation is not intended to apply to a specific, small region of the beam, but rather to the overall beam length. Therefore, it is reasonable that the local derivations of the geometry factor presented above may not be appropriate for use in envelope equations.

This topic was studied in detail by Allen, Brown, and Reiser [1,117,118]. They found that a uniformly-populated ellipsoid, which in free space yields a parabolic line charge distribution and space charge forces which vary linearly with position, will not in general yield linear forces when inside a conducting beam pipe. For bunch lengths that are long compared to the beam pipe diameter, the space charge fields become increasingly nonlinear at the beam ends. The image charges in the conducting beam pipe cause the field lines to become more radial than they would be

in free space, with the result that radial defocusing forces are increased while longitudinal defocusing forces are decreased. Because the longitudinal electric field is no longer linear with position in long beams, a longitudinal electric field of the form

$$E_z = -\frac{g}{4\pi\varepsilon_0\gamma^2}\frac{\partial\lambda}{\partial z}, \tag{A23}$$

which yields linear fields for parabolic beams with the line charge distribution

$$\lambda(z) = \lambda_0\left(1-\frac{z^2}{z_m^2}\right) \tag{A24}$$

is no longer appropriate unless the geometry factor g is allowed to be a function of position in the beam. If this is done, and g is averaged over position in the beam, a single approximate value for the geometry function can be found. For beams where the length is much greater than the beam pipe size, this geometry factor reaches the asymptotic value

$$g_b \approx 0.67 + 2\ln\left(\frac{b}{a}\right), \tag{A25}$$

where b is the beam pipe radius and a is the maximum beam radius.

Note that this expression for the geometry factor is only expected to hold in an average, global sense for bunched beams, as when used in the longitudinal envelope equation. The conventional descriptions of the geometry factor, discussed in the previous sections, are still expected to hold for wave propagation within beams. To distinguish between these two geometry factors, we will use the subscript "b" to refer to the geometry factor for bunched beams, as shown in Eq. (A25).

Appendix B: Notes on Calculations and Error Estimation.

B.1. Longitudinal Expansion

Processing for the parabolic beam expansion data shown above was done in Mathcad spreadsheets written for that purpose. The first fifty and last fifty data points were averaged to establish a zero-current level. The peak current was determined, and the 50% (for FWHM) or 10% (for 10%-10% length) current values were calculated. The intersections of these 50% or 10% current lines with the interpolated data were calculated for the head and tail of the beam. The location of these intersections in time was determined, and the difference of these values at the head and tail was calculated. These values are the FWHM (50%-50%) or 10%-10% beam lengths. Error was found from two sources. The first was the sampling rate of the data, typically 0.5 ns. In addition, the standard deviation of the value of the first fifty data points in each data set was calculated, and used as a measure of the noise inherent in the measurement due to EMI, etc. This error was then propagated through a series of calculations intended to carefully convert it from an error in y into an error in x, and then added to the 0.5 ns error to determine an overall error estimate. The statistical component was almost always negligible.

For rectangular beam expansion experiments, beam radius was determined from phosphor screen images by software developed by R. Feldman. Because the CCD cameras used on UMER were not synched to the beam repetition rate, the images recorded on the cameras actually consisted of two separate images, with the lines of the two images interlaced. R. Feldman developed software to extract and smooth a single image from the CCD camera data, and calculate the RMS beam

radius in x and y, measured in number of pixels. Conversion was then made to millimeters by determining the size in number of pixels of the phosphor screen mounting plate, for which the physical size is known. Based on the variation in measured radius in Fig. 62, the error in RMS radius measurements is approximately 3%.

Rectangular beam measurements described in section 3.5.1 were found by measuring the difference in the 0% and 100% levels at the head and at the tail. Because of nonideal pulse shape, some judgment was required to make this determination. The 20% and 80% current levels at the head and tail were then calculated, and the x-location or time of the data point nearest each of these levels in any given data set was taken to be the time location at which the 20% or 80% current level was reached. This introduced some error, which was quoted as the sampling rate of the data, typically 0.5 ns. This is probably excessive, and 0.25 ns would probably have been a more appropriate value, but the more conservative estimate was retained. The various lengths were determined by subtracting various time locations; for example, the 20%-80% rise time (head) was determined by subtracting the determined time at which the beam reached the 20% current level at the beam head from the determined time at which the beam reached the 80% current level at the beam head (see Fig. 42). The resulting error is found by adding the errors at each level in quadrature, typically giving a (very conservative) error of 0.7 ns.

Data analysis for section 3.5.2 proceeded as described in section B3.

B.2. Triode Effects

Issues relating to calculation of Average Normalized Modulation Depth are discussed in Chapter 4. The modulation frequency as a function of position in the beam shown in Fig. 74 was calculated using the raw data for a modulated beam, measured on the first Bergoz FCT, with the new electronics at BPM 0, and with the old electronics at BPM 0. The distance between adjacent troughs and crests in the modulation waveform was measured, and used to generate a "frequency." This frequency was halved (because it was measured from trough to crest, not from crest to crest). The new frequency was recorded as being the frequency of modulation at the location half way between the original crest and trough used for the measurement. This was repeated for all visible crest-trough pairs.

B.3. Perturbations

Measurements were made directly on the raw data traces, without any correction for tilt due to the beam impacting on BPM plates. Tilt correction was only used to generate plots that could be overlaid.

Current levels refer to average beam current in the flat top, as found by overlaying a horizontal line onto the current trace. Where the current varied significantly along the flat top, the average current level in the vicinity of the perturbations was used. Error in the flat top current refers to the ringing seen on the flat top. Averaging and error estimates were made by best-call positioning of a horizontal line in a Mathcad worksheet ("BZ-baseline" and "BZ-baseline-mod1"), and relied on eyeball judgments.

Head and tail rise and fall times were found by local calculation at the head and tail, eliminating the need for removing tilt. The differences between the base levels and the flat top levels at head and tail were measured, and the height of the 80% and 20% levels were calculated from these measurements. Eyeball judgments were used to find the flat top and base levels due to presence of ringing. Because the data is discrete, the data points with y-values closest to the calculated 80% and 20% levels were used. This introduced an error of 0.7 ns, which is due to the 0.5 ns spacing of the two data points, added in quadrature.

80%-20% rise and fall times were used to determine the geometry factors in the ends, assuming that the cold fluid model applies and that the 80%-20% rise and fall times were zero at the cathode, and using the flat top current. The rise and fall times, with error bars, were plotted in the Mathcad worksheet "CFM-multipulse-temp." Theoretical plots of fall times and rise times were overlaid on this data, and the geometry factors varied until the projected line coincided with the rise or fall time. The geometry factor was then varied to intersect the upper level of the error bar; the difference between the true geometry factor and the high geometry factor was used as the error in the geometry factor. Additional error is introduced (although not included in the error estimate) because the fit is through a single point. However, previous experiments with longitudinal expansion show that this procedure is acceptable so long as the location of the measurement is distant from the cathode, and assuming that the BPMs are working correctly.

Appendix C: Historical Background.

The most advanced charged particle beam systems of today are the direct descendents of the experimental electrical apparatus of the 19th century. The development of these high-voltage systems from then to the present day parallels much of the history of physics and electrical engineering over the last one-and-a-half centuries.

In a sense, charged particle beam devices can be traced to the light bulb itself. In his studies with the incandescent lamp, Edison noted that carbon was being transferred from the filament to the inside of the evacuated glass bulb [119]. He reasoned that if carbon was passing across the vacuum, then perhaps some of the current was as well. He inserted an additional electrode, and found that this was in fact the case. Thus the "Edison Effect" was discovered, better known today as thermionic emission. Edison never saw the full significance of this discovery, although he did patent an "Electrical Indicator" that made use of it (Fig. C1) [120]. It wasn't until the development of the Fleming Valve or thermionic diode in 1904 that the effect became useful. The diode was followed quickly by de Forest's Audion, or triode in 1907 (Fig. C2) [121]. The triode, in turn, was followed by a series of progressively more sophisticated vacuum tubes designed to accomplish specialized tasks, such as the magnetron and klystron for radar, the traveling wave tube for communications, and the image orthicon for television[4,70,74]. This growth was especially rapid during the 1940's, when military requirements for communications, radar, and countermeasures drove innovation in vacuum tubes and

(No Model.)

T. A. EDISON.

ELECTRICAL INDICATOR.

No. 307,031. Patented Oct. 21, 1884.

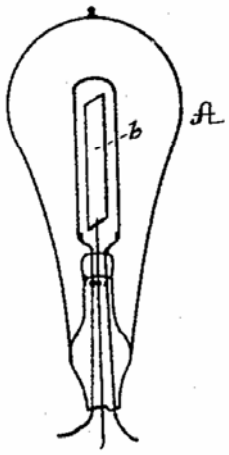

I have discovered that if a conducting substance is interposed anywhere in the vacuous space within the globe of an incandescent electric lamp, and said conducting substance is connected outside of the lamp with one terminal, preferably the positive one, of the incandescent conductor, a portion of the current will, when the lamp is in operation, pass through the shunt-circuit thus formed, which shunt includes a portion of the vacuous space within the lamp. This current I have found to be proportional to the degree of incandescence of the conductor or candle-power of the lamp.

Fig. C1. Edison patent for use of "Edison Effect."[120]

No. 879,532. PATENTED FEB. 18, 1908.

L. DE FOREST.

SPACE TELEGRAPHY.

APPLICATION FILED JAN. 29, 1907.

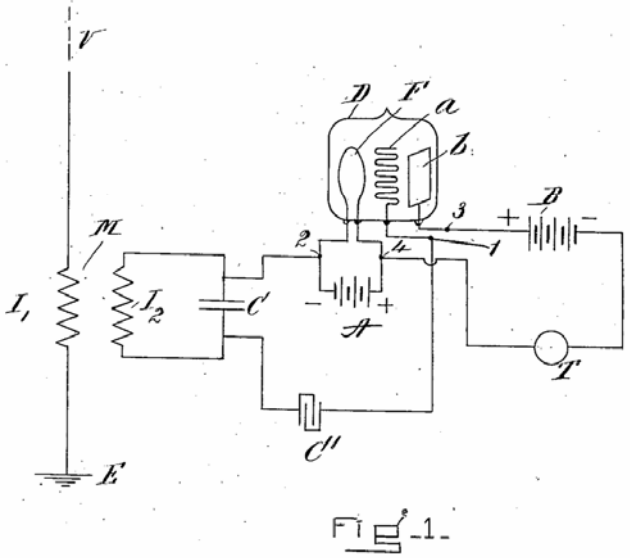

Fig. 1.

Fig. C2. A DeForest patent on the "audion." [121]

pulsed power systems. Many of these innovations directly aided the development of high energy accelerators in the years that followed [122].

The late 19th and early 20th centuries also saw the application of high-voltage, low-pressure tubes to basic physics research [123]. Cathode rays, carrying charge and able to be deflected by electric and magnetic fields, allowed direct experiments with the electron. At higher voltages, cathode rays were able to ionize residual gas in the tubes. The positive ions thus produced were naturally drawn towards the negative cathode, and could be observed by drilling holes, or canals, through the cathode. These "canal rays" which emerged on the other side of the cathode could be observed with phosphorescent screens and deflected by magnetic and electric fields in a similar way as cathode rays. Even higher voltages allowed the production of X-rays, discovered by Roentgen in 1895. The discovery of natural radiation by Becquerel in 1896 and the development of suitable detectors allowed the structure of the nucleus to be probed directly. Natural radiation from radioactive sources and from cosmic rays was used to transmute the elements and to discover fundamental particles such as the neutron and the positron. In the late 1920's and early 1930's, particles accelerated by high voltage and RF techniques began to supplant natural radioactivity for many investigations into basic physics [124]. In 1932 Cockcroft and Walton transmuted lithium nuclei by 120 keV proton beams. In the decades that followed, the push for higher and higher energy beams for nuclear and particle physics spawned a plethora of increasingly larger and more complicated accelerators.

More recent developments have focused on beam current and quality. Higher beam current allows greater output power from microwave tubes or more reactions in colliders. For certain devices, such as free-electron lasers (FELs) [71,125], high quality, low emittance beams are critical [3]. Higher currents and better quality in beams tend to cause them to be dominated by space charge forces, and many novel accelerator applications now under development find space charge to be a limiting factor. For example, space charge can impose limits on attempts to modulate a beam directly at the cathode, which is one approach being investigated for terahertz sources [126]. Often, space charge effects are only significant when a beam is first created, and become less prominent as it is accelerated. However, some proposed applications of charged particle beams, such as Heavy Ion Inertial Fusion (HIF), will require beams that are dominated by space charge throughout their lifetimes [127]. In HIF, beams of heavy ions such as bismuth will be accelerated to billions of electron volts and used to heat and compress targets of deuterium and tritium to produce controlled nuclear fusion. Although these beams will be accelerated to high energy, the rest masses of the heavy nuclei used are so large that the beams will not reach relativistic velocities. The accelerators used with HIF are expected to be of the induction linac type [127]. The dynamics of very intense beams, such as those for use with HIF, are very complicated, and largely unexplored. The investigation of these intense beams is the motivation for building UMER, and for the research described in this dissertation.

Bibliography

[1] M. Reiser, *Theory and Design of Charged Particle Beams*, Wiley: New York (1994)

[2] J.R. Pierce, *Theory and Design of Electron Beams*, Van Nostrand: Princeton (1954).

[3] P.G. O'Shea, Personal Communication.

[4] J.F. Gittins, *Power Travelling-WaveTubes*, American Elsevier: New York (1965).

[5] G. Caporaso and Y.J. Chen, Personal Communication.

[6] P.G. O'Shea et al., Nucl. Instrum. and Meth. A **464** (2001) 646-652.

[7] R. Kishek, et al., Phys. Plasmas **10**, 5 (2003).

[8] W.C. Turner, et al., Proc. 1989 Particle Accelerator Conference.

[9] J.T. Weir, et al., Proc. 1999 Particle Accelerator Conference.

[10] P.A. Seidl, et al., "Progress in the High Current Experiment (HCX) February - July 2002," LBNL-51476, Sept. 12, 2002. Online: repositories.cdlib.org/lbnl/LBNL-51476 (Dec. 19, 2004).

[11] S. Henderson, et al., "SNS Parameters List," SNS 100000000-PL0001-R11, May 2004. Online: http://www.sns.gov/documentation/100000000-PL0001-R11.pdf (Dec. 19, 2004).

[12] S. Nath, et al., Proc. 2003 Particle Accelerator Conference.

[13] R. Witkover, et al., Proc. Proc. 1999 Particle Accelerator Conference.

[14] E.P. Gilson, et al., Laser and Particle Beams **21**, 549-552 (2003).

[15] R.C. Davidson, et al., "Paul Trap Simulator Experiment (PTSX)," Fusion Summer Study, Snowmass, Colorado, July 8-19, 2002. Online: w3.pppl.gov/~egilson/PTSX/PTSX_Snowmass.pdf (Dec. 19, 2004).

[16] V. N.Litvinenko, et al., Proc. 1995 Particle Accelerator Conference.

[17] P. Wang, et al., Proc. 2001 Particle Accelerator Conference.

[18] D.X. Wang, et al., Proc. 1993 Particle Accelerator Conference.

[19] M. Reiser, et al., Proc. 1999 Particle Accelerator Conference.

[20] P.G. O'Shea, "The Quest for Bright Beams" (2004).

[21] FM Technologies, Inc., *10 kV Electron Gun Manual*, April 2000.

[22] J.R. Pierce, Journal of Applied Physics **11** 548-554 (1940).

[23] D. Feldman, Personal Communication.

[24] W.W. Zhang et al., Phys. Rev. ST Accel. Beams **3**, 122401 (2000).

[25] R. Kishek, "HIF Research on the University of Maryland Electron Ring (UMER)," Proc. 2004 Intern. Symp. Heavy Ion Fusion.

[26] Online: http://www.bergoz.com/fct/d-fct.htm (Jan. 6, 2005).

[27] Online: http://www.ipr.umd.edu/ebte/ring/ (Dec. 21, 2004).

[28] B.Quinn et al., Proc. 2003 Particle Accelerator Conference.

[29] Y. Zou, Master's Thesis, University of Maryland, Sept. 29, 1998.

[30] R.E. Shafer, "Beam Position Monitoring," AIP Conference Proceedings 249, vol. 1 (1992).

[31] Y. Li, "Resistive Beam Position Monitor," UMER Technical Note UMER-040998-YL, E-Ring Technical Note E-RING-98-19, April 9, 1998.

[32] H. Li et al., Proc. 2003 Particle Accelerator Conference.

[33] Y. Cui, Doctoral Dissertation, University of Maryland, 2004.

[34] Y. Cui et al., "Coherent Error Study in a Retarding Field Energy Analyzer," Nuclear Instruments and Methods A, accepted for publication (2004).

[35] Y. Zou et al., "Energy Spread Growth in Low Energy Intense Electron Beam," Nuclear Instruments and Methods A, accepted for publication (2004).

[36] Y. Zou et al., "Observation of anomalous increase of longitudinal energy spread in a space charge dominated electron beam," Physical Review Letters, submitted (2004).

[37] Y. Cui et al., Phys. Rev. ST Accel. Beams **7**, 072801 (2004).

[38] Y. Cui et al., Rev. Sci. Instrum. **75** (8), 2736 (2004).

[39] Y. Zou et al., Phys. Rev. ST Accel. Beams **6**, 112801 (2003).

[40] L. Smith, et al., *ERDA Summer Study of Heavy Ions for Inertial Fusion: Final Report*, LBL-5543, Appendix 6-4, December 1976.

[41] D. Neuffer, IEEE Trans. Nucl. Sci. **NS-26**, No. 3 (1979).

[42] David Neuffer, "Extentions of the Longitudinal Envelope Equation," FERMILAB-TM-1993, April 1997.

[43] J.R. Harris, Unpublished Report (2003).

[44] M. Reiser, Personal Communication (2003).

[45] J. R. Harris, Master's Thesis, University of Maryland (2002).

[46] Nathan Brown and Martin Reiser, Particle Accelerators, Vol. 43(4), pp. 231-233, 1994.

[47] Ivan S. Sokolnikoff and Elizabeth S. Sokolnikoff, *Higher Mathematics for Engineers and Physicists*, MacGraw-Hill, New York, 1941, p. 272.

[48] J.G. Wang, D.X. Wang, and M. Reiser, Nucl. Instrum. and Methods A **316**, p. 112-122, 1 June 1992.

[49] J.G. Wang, D.X. Wang, and M. Reiser, Appl. Phys. Lett. **62** (6), 2 February 1993.

[50] D.X. Wang, J.G. Wang, D. Kehne, and M. Reiser, Appl. Phys. Lett. **62** (25), 21 June 1993.

[51] FM Technologies, Inc., *10 kV Electron Gun Manual* (2000).

[52] B. Quinn, personal communication.

[53] I. Haber, personal communication.

[54] D. Feldman, et al., Proceedings of the 2001 Particle Accelerator Conference.

[55] M. Reiser, Personal Communication, 19 Aug. 2001.

[56] Y. Zou et al., Phys. Rev. Lett. **84** (22), 29 May 2000, p. 5138.

[57] H.W. Liepmann and A. Roshko, *Elements of Gasdynamics*, Wiley, New York, 1967.

[58] Dunxiong Wang, Doctoral Dissertation, University of Maryland (1993).

[59] A. Faltens, E.P. Lee, and S.S. Rosenblum, J. Appl. Phys. **61** (12), 15 June 1987, p. 5219

[60] G. Emanuel, *Analytical Fluid Dynamics*, CRC, Boca Raton, 2001.

[61] A.H. Shapiro, *The Dynamics and Thermodynamics of Compressible Fluid Flow*, Vol. II, Ronald, New York, 1954.

[62] L.D. Landau and E.M. Lifshitz, *Fluid Mechanics*, Pergamon, London, 1959.

[63] D.D.-M. Ho, S.T. Brandon, and E.P. Lee, *Particle Accelerators*, Vol. 35, 1991, pp. 15-42.

[64] A. Faltens, E.P. Lee, and S.S. Rosenblum, J. Appl. Phys **61** (12), 15 June 1987.

[65] D.X. Wang, J.G. Wang, and M. Reiser, Phys. Rev. Lett. **73** (1) 4 July 1994

[66] J.R. Harris et al., Proc. 2003 Particle Accelerator Conference.

[67] R. Baartman, "Form Factor *g* in Longitudinal Space Charge Impedance," June 1992. Online: http://www.triumf.ca/people/baartman/dn/ (July 8, 2005).

[68] J.R. Harris, et al., Proc. 2005 Particle Accelerator Conference.

[69] S. Bernal, et al., Proc. 2003 Particle Accelerator Conference.

[70] K.R. Spangenberg, *Vacuum Tubes*, McGraw-Hill: New York (1948).

[71] C.A. Brau, *Free-Electron Lasers*, Academic Press: Boston (1990).

[72] C.D. Child, Phys. Rev. **32**, 492-511 (1911).

[73] F.E. Terman, Electronic and Radio Engineering, 1955. (New York: McGraw-Hill).

[74] Curtis L. Hemenway, Richard W. Henry, and Martin Caulton, *Physical Electronics*, Wiley: New York (1962).

[75] L. Tonks, Phys. Rev. **30** 501-511, October 1927.

[76] R. A. Chipman 1935 *Proc. Phys. Soc.* **47** 1042-1059

[77] R A Chipman 1939 *Proc. Phys. Soc.* **51** 566-574

[78] Federal Telephone and Telegraph Corporation. *Reference Data for Radio Engineers*, 3rd Ed. New York: Knickerbocker. 1949.

[79] S. Bernal, personal communication

[80] J. Neumann, et al., Rev. Sci. Instrum. **76**, 1 (2005).

[81] Agust Valfells, personal communication.

[82] Y. Cui, personal communication, 3/31/04.

[83] I. Haber, personal communication, 4/2/04.

[84] A. Friedman, et al., 42nd Annual Meeting of the APS-DPP, Quebec City Oct. 23-27, 2000.

[85] Z. Huang, M. Borland, P. Emma, J. Wu, C. Limborg, G. Stupakov, J. Welch, Phys. Rev. ST Accel. Beams **7** (2004).

[86]A.M. Weiner, Rev. Sci. Instrum. **71**, 5 (2000).

[87] H. Suk, et al., J. Appl. Phys **86**, 3 (1999)

[88]J. Neumann, R. Fiorito, H. Freund, P. O'Shea, G.L. Carr, H. Loos, T. Shaftan, B. Sheehy, Y. Shen, Z. Wu, Proc. 2004 Free-Electron Laser Conf, Trieste, Aug. 29 - Sept. 3, 2004.

[89] J. Neumann, P.G. O'Shea, D. Demske, R. Fiorito, G.L. Carr, H. Loos, T. Shaftan, B. Sheehy, Z. Wu, Proc. 2003 Part. Accel. Conf. Portland, Oregon, May 12-16, 2003. IEEE Cat. Number 03CH37423C.

[90] J.G. Neumann, P.G.O'Shea, D. Demske, W.S. Graves, B. Sheehy, H. Loos, G.L. Carr, Nucl. Instrum. and Methods A **507** (2003) 498-501.

[91] Agust Valfells, D.W. Feldman, M. Virgo, P.G. O'Shea, Y.Y. Lau, Phy. Plasmas **9**, 5 (2002).

[92] V. Kelvin Neil and Andrew M. Sessler, Rev. Sci. Instrum. **36** (4), 429 (1965).

[93] J.G. Wang, H. Suk, and M. Reiser, Phys. Rev. Lett. **79**, 6 (1997).

[94] J.G. Wang and M. Reiser, Phys. Plasmas **5**, 5 (1998).

[95] H. Suk, J.G. Wang, Y. Zou, S. Bernal, and M. Reiser, Proc. 1997 Part. Accel. Conf., Vancouver, B.C., 12-16 May 1997. IEEE Cat. Number 97CH36167.

[96] F.M. Bieniosek, S. Eylon, A. Faltens, A. Friedman, J.W. Kwan, M.A. Leitner, A.W. Molvik, L. Prost, P.K. Roy, P.A. Seidl, G. Westenkow, Proc. 2004 Intern. Symp. Heavy Ion Inertial Fusion, Princeton, New Jersey, June 7-11, 2004.

[97] J.G. Wang and M. Reiser, Rev. Sci. Instrum. **65**, 11 (1994).

[98] H. Suk, et al., Phys Plas **3**, 2 (1996).

[99] J.G. Wang, Y. Zou, H. Suk, and M. Reiser, Proc. 1999 Part. Accel. Conf., New York City, March 29 - April 2, 1999. IEEE Cat. Number 99CH36366.

[100] Y. Zou, J.G. Wang, H. Suk, and M. Reiser, Phys. Rev. Lett. **84**, 22 (2000).

[101] J. Bisognano, et al., IEEE Trans. Nucl. Sci. **NS-28**, 3 (1981).

[102] J.G. Wang, D.X. Wang, and M. Reiser, Phys. Rev. Lett. **71**, 12 (1993).

[103] J.G. Wang, D.X. Wang, D. Kehne, and M. Reiser, Proc. 1993 Part. Accel. Conf., Washington, D.C., May 17-20, 1993. IEEE Cat. Number 93CH3279-7.

[104] J.G. Wang, H. Suk, D.X. Wang, and M. Reiser, Phys. Rev. Lett. **72**, 13 (1994).

[105] J.G. Wang, D.X. Wang, H. Suk, and M. Reiser, Phys. Rev. Lett. **74**, 16 (1995).

[106] D.W. Feldman, A. Valfells, J. Neumann, J. Harris, B. Beaudoin, P.G. O'Shea, Proc. 2001 Part. Accel. Conf., Chicago, Illinois, June 18-22, 2001. IEEE Cat. Number 01CH37268.

[107] K.L. Jensen, D.W. Feldman, and P.G. O'Shea, Appl. Phys. Lett. **85**, 22 (2004).

[108] Y. Huo, Master's Thesis, University of Maryland (2004).

[109] Patent(s) Pending. University of Maryland Invention Disclosure PS-2003-073.

[110] J.R. Harris, et al., "Space charge Effects for Prebunched Electron Beam Light Sources," 2004 Directed Energy Professional Society Symposium, Unpublished (2004).

[111] S. Bernal, B. Beaudoin, Y. Cui, M. Glanzer, T.F. Godlove, J. Harris, M. Holloway, I. Haber, R.A. Kishek, W.-T. Lee, H. Li, D. Lamb, B. Quinn, M. Quirus, M. Reiser, A. Valfells, M. Walter, M. Wilson, R. Yun, Y. Zou, P.G. O'Shea, Nucl. Instrum. and Methods A **519** (2004) 380-387.

[112] I. Haber, Oral Presentation, University of Maryland, May 5, 2004.

[113] A. Faltens, et al., J. Appl. Phys. **61** (12), 5219 (1987).

[114] O. Boine-Frankenheim. Online: http://www-linux.gsi.de/~boine/vorlesung/skript/html/node22.html. (Feb. 13, 2005)

[115] L. Smith, *ERDA Summer Study of Heavy Ions for Inertial Fusion*, Appendix 6-4. LBL-5543. Dec. 1976.

[116] C.E. Nielsen and A.M. Sessler, Rev. Sci. Instrum. **30** (2), 80 (1959).

[117] C.K. Allen, et al., Part. Accel. **45**, 149 (1994).

[118] C.K. Allen and M. Reiser, Phys. Rev. E **55** (6) 7591 (1997).

[119] Online: http://www.ieee-virtual-museum.org/collection/tech.php?id=2345876&lid=1 (July 8, 2005)

[120] U.S. Patent 307,031, Oct. 21, 1884.

[121] U.S. Patent 879,532, Feb. 18, 1908

[122] For example, Glascoe and Lebacqz, *Pulse Generators*, MIT Radiation Laboratory Series, McGraw-Hill: New York (1951).

[123] M. Born, *Atomic Physics*, Dover: New York (1989)

[124] S.Y. Lee, *Accelerator Physics*, World Scientific: Singapore (1999).

[125] P.G. O'Shea and H.P. Freund, Science **292** 1853-8 (2001)

[126] J.G. Neumann, et al., Nucl. Instrum. and Meth. A **507** (2003) 498-501.

[127] C.M. Celata, et al., Phys. Plasmas **10**, 5 (2003)